Searches for Electroweak Production of Supersymmetric Particles in Compressed Mass Spectra with the ATLAS Detector in LHC Run 2

Michael Holzbock

München 2020

Searches for Electroweak Production of Supersymmetric Particles in Compressed Mass Spectra with the ATLAS Detector in LHC Run 2

Dissertation an der Fakultät für Physik
der
Ludwig-Maximilians-Universität München

vorgelegt von
Michael Holzbock
geboren in München

München, den 30.09.2019

Erstgutachter: PD Dr. Alexander Mann
Zweitgutachter: PD Dr. Oliver Kortner
Tag der mündlichen Prüfung: 13.11.2019

Zusammenfassung

Trotz des Erfolgs des Standardmodells der Teilchenphysik weisen zahlreiche Hinweise auf das Vorhandensein neuer Phänomene hin, die in diesem theoretischen Rahmen nicht enthalten sind. Ein vielversprechender Kandidat für die Einführung von Physik jenseits des Standardmodells ist die Theorie der Supersymmetrie. Diese sagt die Existenz eines supersymmetrischen Partners für jedes Teilchen im Standardmodell voraus.

Diese Arbeit beschäftigt sich mit der Suche nach elektroschwacher Produktion supersymmetrischer Teilchen mit komprimierten Massenspektren. Die Suche verwendet $139\,\mathrm{fb}^{-1}$ an Daten aus Proton-Proton-Kollisionen, die bei einer Schwerpunktsenergie von $\sqrt{s} = 13\,\mathrm{TeV}$ mit dem ATLAS-Detektor in Run 2 des Large Hadron Colliders aufgezeichnet wurden. Die selektierten Ereignisse zeichnen sich durch fehlenden transversalen Impuls, zwei entgegengesetzt geladene Elektronen oder Myonen mit geringem Transversalimpuls und hadronischer Aktivität durch Abstrahlungen des Parton-Ausgangszustandes aus. Eine Erweiterung der Analyse wird vorgestellt, um auch Ereignisse mit niedrigerem fehlenden Transversalimpuls zu berücksichtigen, womit die Sensitivität der Suche verbessert wird. Die Erweiterung der Messung von Myon-Rekonstruktionseffizienzen zu noch geringeren Transversalimpulsen der Myonen ermöglichen auch das Testen von Signalen mit sehr komprimierten Massespektren, in denen sich die supersymmetrischen Zustände in der Masse nur um mehrere hundert MeV bis einige GeV unterscheiden.

Die Daten weisen keine signifikanten Abweichungen von den Standardmodellvorhersagen auf. Die Ergebnisse werden daher in Form von Masseausschlussgrenzen für Modelle der Higgsino- und Sleptonproduktion interpretiert. In diesen ist das leichteste supersymmetrische Teilchen ein Neutralino, welches eine ähnliche Masse wie ein Chargino und ein schwereres Neutralino beziehungsweise ein Slepton aufweist. Im Higgsino-Modell können Neutralinos bis zu einer Masse von $162\,\mathrm{GeV}$ ausgeschlossen werden. Insgesamt erlauben die Ergebnisse, Massendifferenzen zwischen dem leichtesten und schwereren Neutralino von bis zu maximal $53\,\mathrm{GeV}$ und bis zu minimal $2.6\,\mathrm{GeV}$ auszuschließen. Die unteren Grenzen für Slepton-Massen werden auf bis zu $256\,\mathrm{GeV}$ erweitert, zudem können Massendifferenzen von bis zu maximal $29\,\mathrm{GeV}$ und bis zu minimal $590\,\mathrm{MeV}$ zwischen den Sleptonen und Neutralinos ausgeschlossen werden.

Abstract

Despite the success of the Standard Model of particle physics, numerous hints indicate the presence of new phenomena, not contained in this theoretical framework. A promising candidate to introduce physics beyond the Standard Model is Supersymmetry, which predicts the existence of a supersymmetric partner for each of the Standard Model particles.

This thesis presents searches for the electroweak production of supersymmetric particles with compressed mass spectra. The searches use $139\,\text{fb}^{-1}$ of proton–proton collision data recorded by the ATLAS detector at a center-of-mass energy $\sqrt{s} = 13\,\text{TeV}$ in Run 2 of the Large Hadron Collider. Selected events are characterized by missing transverse momentum, two same-flavor, oppositely charged leptons with low transverse momentum, and hadronic activity from initial-state radiation. Dedicated event selections extend the analysis towards lower transverse momenta to enhance the sensitivity reach of the searches. The extension of the muon reconstruction efficiency measurements towards lower transverse momenta allows to probe also the very compressed regime, in which the supersymmetric states differ in mass by several hundreds of MeV to a few GeV.

No significant deviations from the Standard Model predictions are found in the data. The results are interpreted in terms of mass exclusion limits for simplified models of higgsino and slepton production, in which the lightest supersymmetric particle is a neutralino with similar mass to a chargino and a heavier neutralino, or to a slepton. In the higgsino model, neutralino masses up to 162 GeV are excluded. Excluded mass splittings between the lightest and heavier neutralino range from 53 GeV down to 2.6 GeV. Lower limits on slepton masses are extended up to 256 GeV, where mass splittings between the slepton and the neutralino from up to 29 GeV down to 590 MeV can be excluded.

Remember kids, the only difference between screwing around and science is writing it down.

<div align="right">MYTHBUSTERS</div>

Contents

1 Introduction

The aim of fundamental research is to derive a consistent understanding and description of nature, and its underlying principles. In elementary particle physics this means to find out what the universe actually is made from at the smallest scales and how these fundamental constituents interact with each other. To study these interactions, it has proven as prospering to collide particles with each other or on stationary targets. In case the energies involved are large enough, the innermost structures of matter are revealed and the outcome of their interactions can be detected. Analyzing this outcome can then give insights into the nature of the underlying physics. Increasing collision energies allowed the production of unknown, heavier particles in these interactions, and hence the confirmation or falsification of theoretical models describing them. Altogether this in principle simple idea of a collide-and-detect experiment contributed significantly to the formulation of a self-consistent theory for particle interactions, referred to as the Standard Model (SM) of particle physics, over the last decades. The world's current most powerful particle accelerator is the Large Hadron Collider (LHC) hosted by the research area at CERN (derived from *Conseil européen pour la recherche nucléaire*), which was established in 1954 and is located near Geneva, Switzerland. Over the years, CERN hosted a variety of particle accelerators and detectors, by which numerous scientific achievements were made, in particular the discoveries of the W and Z bosons in the UA1 and UA2 experiments in 1983 [1, 2]. Predicted by the electroweak theory of Glashow, Weinberg and Salam [3] their discovery represented a confirmation of one of the cornerstones of the SM. The discovery of the Higgs boson in 2012 with the ATLAS and CMS detectors at the LHC [4, 5] completed the SM by adding its last missing ingredient. Although the SM is valid up to arbitrarily large energies and withstood all experimental tests to date, it is a general consensus that it should be viewed as a low-energy approximation of some underlying, more fundamental theory.

Numerous hints, for instance from cosmological observations, indicate the presence of physics beyond the Standard Model (BSM), i.e. new particles and interactions not contained in the current theory. By far the best-studied extension of the SM is supersymmetry (SUSY), which introduces a new symmetry linking fermions and bosons. Strong arguments suggest that new particles predicted by SUSY should be accessible at LHC energies and would result in clearly visible, new signatures. Despite high expectations, no significant deviations from the SM predictions were found in the LHC dataset of the first round of data-taking between 2009 and 2013. Also in the first part of the dataset of the second run, which uses even higher collision energies, no striking candidates for new physics were found so far. Consequently, the present situation in the field of particle physics differs from the one in previous decades. These have been governed by a fruitful interplay between theorists and experimentalists. On the one side theoretical hints pointed out what to look for in experiments, such as the predictions of the W and Z bosons. On the other side, experimental observations dictated how theory had to be adjusted, for instance the energy spectrum of the electron in the beta decay necessitated the introduction of the neutrino. In the past, the road for particle physics at the LHC was

somewhat clear: validate and complete the SM with the Higgs boson, and potentially pick up signs of BSM physics at the TeV scale. The absence of new phenomena so far put the field into an unfamiliar state: to address the open questions of particle physics and advance its theoretical framework, experimental evidence for new physics is required but it is less clear how this new physics may be realized in nature.

A potential realization is given in terms of compressed mass spectra, in which the new physics states are close or nearly-degenerate in mass. Such scenarios are characterized by low-energetic particles in the final state, are thus challenging to access experimentally and can evade current constraints from colliders. Models with compressed mass spectra can be easily realized in the framework of SUSY, while they keep at the same time many of the features that made SUSY such an attractive BSM candidate. Although it has lost some of its former popularity, it is hence still a viable guideline to design and optimize a search for new physics. Furthermore, the direct production of the particles under study is mediated via the electroweak interaction, and consequently occurs at a low rate. In conjunction with refined reconstruction and selection criteria, the full dataset of the second data-taking period of the LHC provides enough statistics to probe now also signals with low production cross section.

This thesis presents a search for supersymmetric partners of the Higgs boson, as well as SUSY partners for the leptons of the first and second generation with the ATLAS experiment. Chapter 3 introduces the LHC and the ATLAS detector. The measurements of muon reconstruction efficiencies, required to extend the sensitivity of the search towards very compressed scenarios are presented in Chapter 4. Event selection, background estimation and results of the search are described in Chapter 5, followed by a brief conclusion in Chapter 6.

2 Theory

Elementary particles and their interactions are described by the SM of particle physics. This chapter reviews its particle content and introduces the key concepts of the underlying framework. Afterwards immanent shortcomings of the SM are presented that motivate the introduction of new physics in the theory. SUSY, a promising extension of the SM to overcome these shortcomings, is reviewed and the supersymmetric models, the context in which the presented search for new physics was performed, are established.

2.1 The Standard Model of Particle Physics

Loosely speaking, the SM describes matter as spin-$\frac{1}{2}$[†] particles that interact via the exchange of spin-1 gauge bosons. In this manner three of the four known fundamental forces are described by the SM: the electromagnetic, weak and strong force. Technically, the SM is a non-Abelian Yang–Mills-type gauge theory [6] based on the group

$$SU(3)_C \times SU(2)_L \times U(1)_Y \,, \tag{2.1}$$

where the subscripts C, L and Y denote the associated quantum numbers color, weak isospin and hypercharge, respectively. Strong interactions are described by the $SU(3)_C$ gauge group, while electromagnetic and weak forces are unified into the electroweak interaction governed by $SU(2)_L \times U(1)_Y$. The SM is formulated in the mathematical language of Quantum Field Theory, i.e. via the description of quantized relativistic fields. Particles can then be imagined as excitations of these fields [7].

2.1.1 Particle Content

In the SM particles are classified with respect to their spin and the interactions they participate in. Particles that form matter are fermions with spin $\frac{1}{2}$ and categorized into quarks and leptons. Leptons are only charged under the electroweak, whereas quarks additionally couple via the strong interaction, i.e. carry strong charge usually denoted as color. Three different types of colors are known and denoted as *red*, *green* and *blue*. Hence there are three identical replicas of every quark only differing by their color. Except in extreme conditions as for example present in a quark–gluon plasma [8] quarks are not free but are confined in compound colorless $q\bar{q}$ (meson) and qqq (baryon) states such as pions and protons. Quarks carry fractions of the electric charge e that classifies them as *up*-type $(+\frac{2}{3}e)$ or *down*-type $(-\frac{1}{3}e)$ quarks. Six different flavors of quarks are known and grouped into three generations with one *up*- and one *down*-type quark each: (u, d), (c, s) and (t, b). These three quark generations are matched by three generations in the lepton sector where a charged lepton is

---

[†] Natural units, $\hbar = c = 1$, are used throughout this thesis.

Fermions			Quarks			Leptons		**Bosons**			
			$Q[e]$	Mass		$Q[e]$	Mass			$Q[e]$	Mass
Generation	I	u	$+\frac{2}{3}$	$2.3\,\text{MeV}$	ν_e	0	$\approx 0\,\text{eV}$	spin 1	gluon	0	0
		d	$-\frac{1}{3}$	$4.8\,\text{MeV}$	e	-1	$511\,\text{keV}$		Z	0	$91.2\,\text{GeV}$
	II	c	$+\frac{2}{3}$	$1.28\,\text{GeV}$	ν_μ	0	$\approx 0\,\text{eV}$		$W^\pm$	± 1	$80.4\,\text{GeV}$
		s	$-\frac{1}{3}$	$95\,\text{MeV}$	μ	-1	$105\,\text{MeV}$		γ	0	0
	III	t	$+\frac{2}{3}$	$173\,\text{GeV}$	ν_τ	0	$\approx 0\,\text{eV}$	spin 0	H	0	$125.7\,\text{GeV}$
		b	$-\frac{1}{3}$	$4.18\,\text{GeV}$	τ	-1	$1.78\,\text{GeV}$				

Table 2.1: Fermionic and bosonic particle content of the SM. Masses are taken from Ref. [9] and rounded to three significant digits if available. Each fermion has an anti-fermion counterpart with the same mass but opposite charge.

associated with an uncharged, massless neutrino[†]: (e, ν_e), (μ, ν_μ) and (τ, ν_τ). All fermions have an associated anti-particle with the same mass but opposite charges. The force carriers are bosons with spin 1. The strong interaction is mediated via eight massless gluons that carry one color and one anti-color themselves. In addition to the massless photon γ, three heavy gauge bosons — the two charged W^+, W^- and the neutral Z boson — are associated with the electroweak interaction. Fermion and gauge boson masses arise from the interaction with an additional spin-0 particle: the Higgs boson which was discovered recently at the LHC [4, 5]. A summary of the particle content in the SM is given in Table 2.1.

2.1.2 Key Concepts

The development and structure of the SM was driven by the findings made in experiments, e.g. the parity-violating nature of the weak interaction. In the following some of the key concepts used in the SM to describe the phenomena observed in nature in a self-consistent way are described, following mostly Ref. [10].

Gauge Invariance

In the description of elementary particle states some degrees of freedom exist [11]. These can be imagined as kind of an internal space in which the particles can be rotated without changing the physics outcome. Requiring that the Lagrangian density — in the following just denoted as the Lagrangian — is locally invariant under such symmetry transformations generates the interactions of the fermions with the gauge bosons. A common and illustrative example is the theory of quantum electrodynamics (QED). The Lagrangian for a free fermion field ψ with mass m is given by

$$\mathcal{L}_0 = \bar{\psi}(i\gamma^\mu \partial_\mu - m)\psi \tag{2.2}$$

[†] Non-zero neutrino masses can be accounted for by extension of the SM, as discussed below.

where $\bar{\psi} = \psi^\dagger \gamma^0$ and γ^μ are the Dirac matrices. The Lagrangian in the above equation is invariant under a global $U(1)$ transformation

$$\psi(x) \rightarrow \psi'(x) = e^{i\alpha}\psi(x)\,, \tag{2.3}$$

where α is a real number. Requiring the Lagrangian to be invariant also under local transformations $\alpha(x)$ necessitates the presence of a vector field A_μ and to replace the derivative in the Lagrangian with the covariant derivative

$$\partial_\mu \rightarrow D_\mu = \partial_\mu + ieA_\mu\,, \tag{2.4}$$

where e is the coupling to the gauge field and can be identified with the elementary charge. This results in a Lagrangian invariant under the transformations

$$\psi(x) \rightarrow \psi'(x) = e^{i\alpha(x)}\psi(x)\,,$$
$$A_\mu(x) \rightarrow A_\mu(x)' = A_\mu(x) - \frac{1}{e}\partial_\mu\alpha(x)\,,$$

which form the electromagnetic gauge group $U(1)_{em}$. The now invariant Lagrangian contains an interaction term for the fermions and the gauge field: $e\bar{\psi}\gamma^\mu\psi A_\mu$. After adding the field-strength tensor $F_{\mu\nu} = \partial_\mu A_\nu - \partial_\nu A_\mu$ to consider the dynamics of the vector field itself, the final Lagrangian reads

$$\mathcal{L} = \bar{\psi}(i\gamma^\mu D_\mu - m)\psi - \frac{1}{4}F_{\mu\nu}F^{\mu\nu}\,. \tag{2.5}$$

This is the Lagrangian for QED and describes the interaction of charged matter with photons. Gauge invariance can also be related to conservation laws via Noether's theorem [12]. It states the existence of a conserved quantity — electromagnetic charge in the example above — for every global transformation under which the Lagrangian is invariant.

In the case of non-Abelian symmetry transformations, as described by $SU(n)$ groups where $n \geq 2$, the requirement of local gauge invariance leads to additional phenomena for the gauge fields. Considering a multiplet of n fermion fields $\Psi = (\psi_1, \ldots, \psi_n)^T$ a global transformation reads

$$\Psi(x) \rightarrow U(\alpha_1, \ldots, \alpha_N)\Psi(x)\,, \tag{2.6}$$

where the unitary $n \times n$ matrix is parametrized by N real parameters α_a. The set of transformations U forms a group and each element can be expressed in terms of the generators of the group T^a as

$$U(\alpha_1, \ldots, \alpha_N) = \exp(i\alpha_a T^a)\,. \tag{2.7}$$

There are $n^2 - 1$ generators for a $SU(n)$ group [7] and they satisfy commutation relations with each other

$$[T^a, T^b] = if^{abc}T^c\,, \tag{2.8}$$

where the structure constants f^{abc} are real numbers and characterize the group. To make the Lagrangian invariant under local transformations, i.e. with space-time dependent parameters $\alpha_a(x)$, a covariant derivative has to be defined that introduces a vector field $\mathbf{W}_\mu$ with coupling g that can be expanded in terms of the generators to give

$$\partial_\mu \rightarrow D_\mu = \partial_\mu - igT^a W_\mu^a\,. \tag{2.9}$$

(a) quark–gluon   **(b)** triple-gluon   **(c)** quartic-gluon
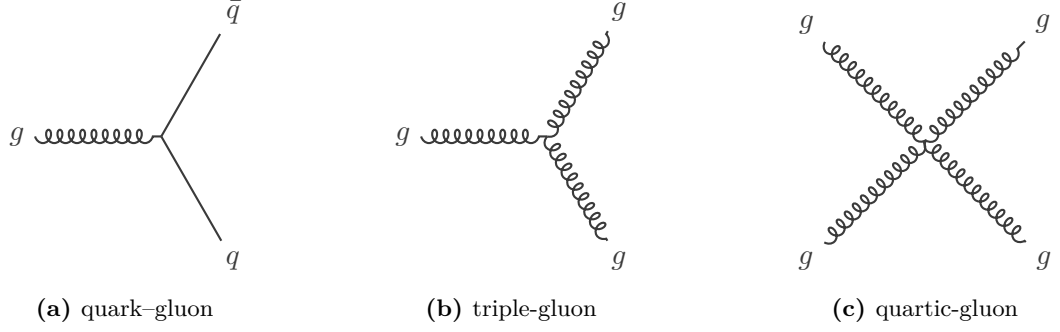
Figure 2.1: Standard vertices of QCD. The colors of quarks and gluons are not shown to give a better overview, i.e. these vertices are present for every allowed combination of colors.

Hence a set of N gauge fields W_μ^a enters the theory that transform with infinitesimal $\alpha_a(x)$ as

$$W_\mu^a \to W'^a_\mu = W_\mu^a + \frac{1}{g}\partial_\mu\alpha^a + f^{abc}W_\mu^b\alpha^c \,, \tag{2.10}$$

where the term with f^{abc} introduces the non-Abelian nature into the theory. These fields then induce an interaction term of the form

$$\mathcal{L}_{\text{int}} = g\bar{\Psi}\gamma^\mu \mathbf{W}_\mu\Psi \tag{2.11}$$

in the Lagrangian. Analogous to the photon field the kinematics of the gauge fields are obtained by adding a generalization of the field-strength tensor to the Lagrangian

$$\mathcal{L}_W = -\frac{1}{4}F_{\mu\nu}^a F^{a,\mu\nu} \,, \tag{2.12}$$

where $F_{\mu\nu}^a = \partial_\mu W_\nu^a - \partial_\nu W_\mu^a + gf^{abc}W_\mu^b W_\nu^c$. Besides terms quadratic in the W fields to describe the free propagation of gauge bosons, the Lagrangian above contains also cubic and quartic terms that represent self-interactions of the gauge fields.

An example for this is quantum chromodynamics (QCD), the gauge theory of the strong interaction, in which gluons couple also to each other. QCD is described by the $SU(3)_C$ part of the SM gauge group where the subscript denotes that the symmetry is associated with the three-fold "color space" of the quarks. The generators of this group are represented by the eight Gell-Mann matrices λ_a. Each quark is arranged in a color triplet $q = (q_r, q_g, q_b)^T$ so that a transformation in color space is given by

$$q \to q' = \exp\left(ig_s\alpha_a\frac{\lambda_a}{2}\right)q \,, \tag{2.13}$$

where g_s is the strong coupling constant. In analogy to the fine-structure constant, g_s often expressed in terms of $\alpha_s = g_s^2/(4\pi)$. Requiring local gauge invariance under these transformations gives rise to the eight gluon fields G_μ^a (with $a = 1, \ldots, 8$) and quark–gluon interaction terms of the form $g_s\bar{q}\gamma^\mu\frac{\lambda^a}{2}qG_\mu^a$. The kinematics of the gluon fields enter the Lagrangian via the gluon field tensor $G_{\mu\nu}^a = \partial_\mu G_\nu^a - \partial_\nu G_\mu^a + g_sf^{abc}G_\mu^b G_\nu^c$. The resulting cubic and quartic terms in the gluon fields correspond to triple and quartic gluon self-interactions. The vertices

of these interactions are shown in Figure 2.1. This gluon self-interaction is also the origin of the phenomenon called *asymptotic freedom* [13]. Due to the presence of virtual gluon bubbles in the gluon propagator (see Figure 2.2a) "anti-screening" of color makes the strong coupling weak at small distances. This is reversed at larger distances where the stronger coupling leads to the hadronization of quarks and gluons, as with increasing distance new quark–antiquark pairs can be generated. In this process known as *confinement*, the colored quarks and gluons form colorless hadrons in the final state. These can then be reconstructed as so-called jets in a particle detector.

Although the principle of gauge invariance is very successful to derive interactions and their structure it cannot account for massive gauge bosons because potential mass terms such as $\frac{1}{2}m^2 W_\mu^a W^{a,\mu}$ do not leave the Lagrangian invariant and thus would break the gauge symmetry. The gauge bosons of the weak interaction are observed to be massive which breaks the $SU(2)_L \times U(1)_Y$ symmetry of the SM and hence a mechanism how this breaking occurs is needed.

Electroweak Gauge Interactions

In the weak interaction the electron can be transformed into a neutrino via charged currents. This indicates the presence of a symmetry between those states and motivates to arrange the fields as doublets

$$\Psi = \begin{pmatrix} \psi_{\nu_e} \\ \psi_e \end{pmatrix} \quad \text{or} \quad \begin{pmatrix} \nu_e \\ e \end{pmatrix}. \tag{2.14}$$

Transformations in this internal space are described by the $SU(2)$ group whose generators are the Pauli matrices σ^a with $i = 1, 2, 3$ and which are of the form

$$\begin{pmatrix} \nu_e \\ e \end{pmatrix}' = \exp\left(i\alpha^a \frac{\sigma^a}{2}\right) \begin{pmatrix} \nu_e \\ e \end{pmatrix}, \tag{2.15}$$

with real parameters α^a. As the weak interaction acts differently on right- and left handed states this has to be accounted for in the symmetry transformations. The left- and right-handed components of a Dirac field ψ are projected out via

$$\psi_L = \frac{1 - \gamma_5}{2}\psi, \qquad \psi_R = \frac{1 + \gamma_5}{2}\psi, \tag{2.16}$$

where $\gamma^5 = i\gamma^0\gamma^1\gamma^2\gamma^3$, and are described by different representations of $SU(2)$. The quantum number associated with this symmetry is called weak isospin I with its third component labeled I_3. The left-handed fields of the SM have $I = \frac{1}{2}$ and form doublets

$$\begin{pmatrix} \nu_e \\ e \end{pmatrix}_L, \begin{pmatrix} u \\ d \end{pmatrix}_L, \quad \begin{pmatrix} \nu_\mu \\ \mu \end{pmatrix}_L, \begin{pmatrix} c \\ s \end{pmatrix}_L, \quad \begin{pmatrix} \nu_\tau \\ \tau \end{pmatrix}_L, \begin{pmatrix} t \\ b \end{pmatrix}_L, \tag{2.17}$$

where the upper components have $I_3 = \frac{1}{2}$ and the lower components $I_3 = -\frac{1}{2}$. The right-handed fields transform as singlets

$$e_R, u_R, d_R, \quad \mu_R, c_R, s_R \quad \tau_R, t_R, b_R, \tag{2.18}$$

and are invariant under weak isospin transformations, i.e. they do not couple to the weak interaction. Right-handed neutrinos have not been observed and are thus not part of the SM.

The treatment described above assumes massless fermions, as in such a chiral theory mass terms of the form $\bar{\psi}\psi = \bar{\psi}_L\psi_R + \bar{\psi}_R\psi_L$ mix left- and right-handed fields and thus would break the gauge invariance. Moreover the different charges of the fermions are not considered, however it is not possible to treat the weak and electromagnetic interactions as independent gauge theories [11]. In the Glashow–Weinberg–Salam theory [3, 14] the weak and electromagnetic interactions originate from an electroweak Lagrangian that is invariant under local gauge transformations of the direct group product $SU(2)_L \times U(1)_Y$ in which the electromagnetic gauge group $U(1)_{em}$ appears as subgroup. The $U(1)_Y$ part in the gauge group corresponds to a multiplication of a phase factor $e^{i\alpha Y/2}$, where Y denotes the weak hypercharge and is related to the charge Q of the fields via the Gell-Mann–Nishijima [15, 16] relation

$$Q = I_3 + \frac{Y}{2}\,. \tag{2.19}$$

The group $SU(2)_L \times U(1)_Y$ comprises one vector field B_μ and three vector fields W_μ^a associated with the generators of $U(1)$ and $SU(2)$, respectively. Similarly two coupling constants g_1 and g_2 are introduced. As the gauge bosons of the weak interaction are massive, the electroweak symmetry has to be broken. This is described by the Brout–Englert–Higgs mechanism [17–19]. The SM considers one isospin doublet of complex scalar fields

$$\Phi(x) = \begin{pmatrix} \phi^+(x) \\ \phi^0(x) \end{pmatrix}\,, \tag{2.20}$$

with hypercharge $Y = 1$, usually denoted as Higgs doublet. The associated Lagrangian is written as

$$\mathcal{L}_{\mathrm{H}} = (D_\mu\Phi)^\dagger(D^\mu\Phi) - V(\Phi)\,, \tag{2.21}$$

with the covariant derivative D_μ defined as

$$D_\mu = \partial_\mu + ig_1\frac{1}{2}B_\mu - ig_2\frac{\sigma^a}{2}W_\mu^a\,, \tag{2.22}$$

and a gauge invariant potential $V(\Phi)$

$$V(\Phi) = -\mu^2\Phi^\dagger\Phi + \frac{\lambda}{4}(\Phi^\dagger\Phi)^2 \tag{2.23}$$

that induces the self-interaction of the Higgs boson with positive, real parameters μ^2 and λ. This potential has the form of a "Mexican hat" and has a minimum for field configurations satisfying $\Phi^\dagger\Phi = 2\mu^2/\lambda$, which should be occupied by the vacuum, the ground state of the theory with minimal potential energy of the field. The vacuum selects one of these configurations so that the Higgs field receives a vacuum expectation value (VEV)

$$\langle\Phi\rangle = \frac{1}{\sqrt{2}} \begin{pmatrix} 0 \\ v \end{pmatrix} \quad \text{where} \quad v = \frac{2\mu}{\sqrt{\lambda}} \approx 246\,\mathrm{GeV}\,. \tag{2.24}$$

which represents a suitable rotation of the Higgs doublet given in Equation (2.20). This expression is not invariant under the $SU(2)_L \times U(1)_Y$ symmetry transformations so that the

symmetry is spontaneously broken; the ground state does not share the symmetry with the Lagrangian [13]. The parameter v also defines the typical energy scale of the electroweak theory called *electroweak scale*. The Higgs doublet can be re-written in terms of excitations of the vacuum

$$\Phi(x) = \frac{1}{\sqrt{2}} \begin{pmatrix} \phi_1(x) + i\phi_2(x) \\ v + H(x) + i\chi(x) \end{pmatrix}, \tag{2.25}$$

where H, χ, ϕ_1 and ϕ_2 are real scalar fields with zero VEV. The Higgs potential then becomes

$$V = \mu^2 H^2 + \frac{\mu^2}{v} H(H^2 + \chi^2 + \phi_1^2 + \phi_2^2) + \frac{\mu^2}{4v^2}(H^2 + \chi^2 + \phi_1^2 + \phi_2^2)^2, \tag{2.26}$$

and reveals that H represents a neutral scalar particle with mass $M_H = \sqrt{2}\mu$. No mass terms exist for the other three fields, which is in agreement with the Nambu–Goldstone theorem [20], postulating the existence of a massless particle for every spontaneously broken continuous symmetry. By a local $SU(2)_L$ transformation these massless particles can be gauged away such that in the so-called unitary gauge the Higgs doublet involves only the physical field H

$$\Phi(x) = \frac{1}{\sqrt{2}} \begin{pmatrix} 0 \\ v + H(x) \end{pmatrix}. \tag{2.27}$$

Now the Higgs potential is given by

$$V = \frac{M_H^2}{2} H^2 + \frac{M_H^2}{2v} H^3 + \frac{M_H^2}{8v^2} H^4, \tag{2.28}$$

which contains cubic and quartic self-interactions of the Higgs proportional to M_H^2. The kinematic term $(D_\mu \Phi)^\dagger (D^\mu \Phi)$ in the Higgs Lagrangian $\mathcal{L}_H$ yields couplings between the Higgs and the gauge fields as well as mass terms for the gauge bosons

$$\mathcal{L}_H \propto \frac{v^2}{8} \left[g_2^2 (W_\mu^1)^2 + g_2^2 (W_\mu^2)^2 + (-g_2 W_\mu^3 + g_1 B_\mu)^2 \right]. \tag{2.29}$$

This term can be expressed in terms of the "physical" fields $W_\mu^\pm, Z_\mu$ and A_μ given by

$$W_\mu^\pm = \frac{1}{\sqrt{2}}(W_\mu^1 \mp W_\mu^2) \quad \text{with mass } \mathrm{M}_W = \frac{g_2}{2} v,$$

$$Z_\mu = \frac{1}{\sqrt{g_1^1 + g_2^2}}(g_2 W_\mu^3 - g_1 B_\mu) \quad \text{with mass } \mathrm{M}_Z = \frac{\sqrt{g_1^2 + g_2^2}}{2} v,$$

$$A_\mu = \frac{1}{\sqrt{g_1^1 + g_2^2}}(g_1 W_\mu^3 + g_2 B_\mu) \quad \text{with mass } \mathrm{M}_A = 0,$$

that represent the massive weak gauge bosons $W^\pm, Z$ and the massless photon γ, respectively. The change of basis from (W_μ^3, B_μ) to (Z_μ, A_μ) [7] can also be expressed in terms of the electroweak mixing angle θ_w via

$$\begin{pmatrix} Z_\mu \\ A_\mu \end{pmatrix} = \begin{pmatrix} \cos\theta_w & \sin\theta_w \\ -\sin\theta_w & \cos\theta_w \end{pmatrix} \begin{pmatrix} W_\mu^3 \\ B_\mu \end{pmatrix} \quad \text{where} \quad \cos\theta_w = \frac{g_2}{\sqrt{g_1^2 + g_2^2}} = \frac{\mathrm{M}_W}{\mathrm{M}_Z}. \tag{2.30}$$

Not only the $W^\pm$ and Z bosons get their masses from the spontaneous symmetry breaking but also the fermions acquire mass by gauge-invariant Yukawa interactions with the Higgs field. For one generation of fermions the terms in the Lagrangian reads

$$\mathcal{L}_Y \propto -\lambda_\ell \bar{L}_L \Phi \ell_R - \lambda_d \bar{Q}_L \Phi d_R - \lambda_u \epsilon^{ab} \bar{Q}_{L,a} \Phi_b^\dagger u_R + \text{h.c.}\,, \tag{2.31}$$

where $L_L = (\nu_L, \ell_L)^\text{T}$ and $Q_L = (u_L, d_L)^\text{T}$ are the left-handed lepton and quark doublets respectively, with dimensionless Yukawa couplings λ_f. The VEV v of the Higgs field then gives rise to fermion masses m_f: In the unitary gauge the contribution to the Lagrangian of a fermion field ψ_f is of the form

$$\mathcal{L}_Y \propto -m_f \bar{\psi}_f \psi_f - \frac{m_f}{v} \bar{\psi}_f \psi_f H \quad \text{with } m_f = \frac{1}{\sqrt{2}} \lambda_f v\,, \tag{2.32}$$

that exhibits explicit fermion mass terms and interactions between the fermions and the Higgs field proportional to their masses. In case additional quark generations are introduced, additional coupling terms that mix generations can be added. These are described by the Cabibbo–Kobayashi–Maskawa matrix V_{ij} [21, 22] whose off-diagonal entries quantify transition probabilities between quark generations mediated by the weak interaction. There are no transitions between lepton generations in the SM due to the absence of right-handed neutrinos [7]. This also does not allow for neutrino mass terms as they would require terms of the form

$$\mathcal{L}_Y \propto -\lambda_\nu \epsilon^{ab} \bar{E}_{L,a} \Phi_b^\dagger \nu_R + \text{h.c.}\,. \tag{2.33}$$

However, the observation of neutrino oscillations [23] requires at least one neutrino generation to have a non-zero mass. The neutrino mixing is described by the Pontecorvo–Maki–Nakagawa–Sakat matrix [24] and the neutrinos acquire masses e.g. by the see–saw mechanism [25].

Renormalization

To derive the characteristics of a particular process of interest, e.g. its cross section, roughly speaking all possible ways to get from the initial to the final state have to be considered by calculating their amplitudes. At lowest order ("tree-level") the least amount of vertices are involved and thus this represents the lowest order of the perturbative expansion. In this case the momenta of the internal lines are fixed by the momenta of the external particles. Higher-order corrections involve loop graphs, i.e. additional vertices and require that the momenta of the internal lines are integrated over. Each vertex is associated with a coupling constant that is usually smaller than 1 (except for the strong coupling α_s that can be larger than 1 where a perturbative treatment breaks down). Hence, the more additional vertices are involved, the less the loop corrections contribute to the total amplitude. The loops result in corrections for propagators (see Figures 2.2a and 2.2b) and vertices (see Figure 2.2c) with diverging momentum integrals for large loop momenta. These divergencies have to be regularized in order to obtain a meaningful theory. The aim of renormalization is to absorb the effect of quantum fluctuations that act on a much smaller scale than the actual problem in the parameters of the theory. Different approaches for this exist, e.g. in dimensional regularization
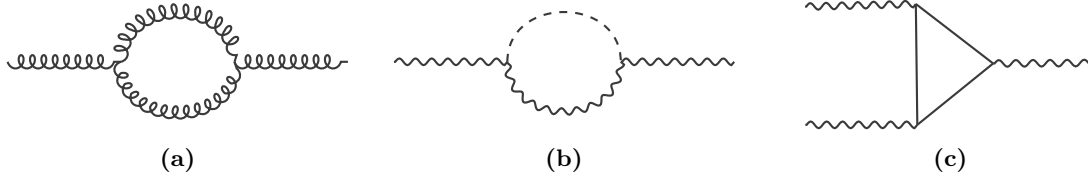
Figure 2.2: Example loop graphs for corrections of the gluon propagator (a), the W/Z propagator (b) and the vertex of three gauge bosons (c).

loop integrals are performed in $D = 4 - \epsilon$ dimensions where they converge. The would-be divergencies are then absorbed in the parameters of the Lagrangian such as masses and couplings. Afterwards the regulator is removed again by taking the limit $\epsilon \to 0$. Typically the renormalization schemes involve a renormalization scale μ that, roughly speaking, specifies the lower limit of loop momenta to be absorbed by the renormalized parameters. Renormalization group equations describe the running of the parameters with μ, which in the simple case of one mass m and one coupling g have the form

$$\mu \frac{\mathrm{d}}{\mathrm{d}\mu} g(\mu) = \beta(g(\mu)), \quad \mu \frac{\mathrm{d}}{\mathrm{d}\mu} m(\mu) = m(\mu)\gamma_m g(\mu). \tag{2.34}$$

The renormalization group functions β and γ_m can be expanded in the coupling and derived from the associated loop graphs. The proof that Yang–Mills theories with massive fields are renormalizable by t'Hooft and Veltmann [26] renders also the SM renormalizable and hence makes it computable to all orders.

2.1.3 Shortcomings

Despite its enormous success over the past decades to predict the outcome of particle physics experiments on a large scale of energies, there are numerous hints that the SM is only an intermediate step on a way to a more fundamental theory. On the one hand these hints are measurements that show a significant deviation from the SM prediction and cosmological observations that cannot be explained by the SM particles alone. On the other hand there are more aesthetic concerns, in particular about aspects that arise from loop corrections. These shortcomings motivate the introduction of extensions to the SM that address those open questions, typically by predicting new particles.

Anomalous Magnetic Moment of the Muon

One of the most outstanding and long known difference between experiment and the SM prediction is present in the measurement of the anomalous magnetic moment of the muon. The magnetic moment $\vec{M}$ and the intrinsic spin $\vec{S}$ of the muon are related by the gyromagnetic ratio g_μ via

$$\vec{M} = g_\mu \left(\frac{q}{2m} \right) \vec{S}, \tag{2.35}$$

where $g_\mu = 2$ is expected for a structureless spin-1/2 particle of mass m and charge q [27]. Small deviations from this value arise through quantum loop corrections and are parametrized
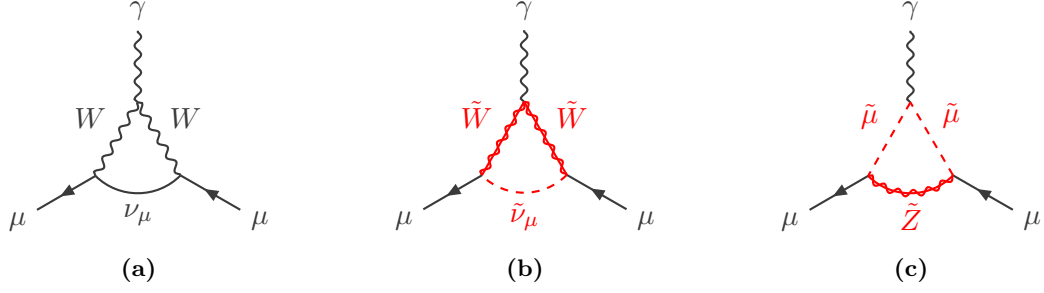
Figure 2.3: Weak (a) and supersymmetric loops (b, c) contributing to the muon anomalous magnetic moment. The supersymmetric particles are shown in red. Solid lines superimposed with wavy lines represent fermions with spin $1/2$ and dotted lines mark scalar particles.

by the anomalous magnetic moment

$$a_\mu = \frac{g_\mu - 2}{2}, \tag{2.36}$$

which can be measured and calculated to very high precision. Three classes of corrections can be distinguished: QED loops involving photons and leptons, weak loops involving the W, Z and Higgs bosons, and hadronic loops. An example Feynman diagram for a weak loop is shown in Figure 2.3a. Extensions of the SM may result in additional loop corrections to be considered in the lepton magnetic moment, that are typically proportional to m_ℓ [28], rendering the corrections for muons more sensitive to new physics than the corrections for electrons. The most recent measurement of a_μ was performed by the E821 experiment [27] using a uniform-field muon storage ring and found a deviation of a_μ from the SM prediction of

$$\Delta a_\mu = a_\mu^{\mathrm{exp}} - a_\mu^{\mathrm{SM}} = 268(63)(43) \times 10^{-11} \tag{2.37}$$

where the numbers in brackets are the errors are from experiment and theory prediction, respectively, which represents a discrepancy of 3.5 times the combined 1σ error [9]. New particles in the theory can address this deviation as they may result in additional diagrams that need to be considered. For example the presence of SUSY leads to diagrams containing so-called *superpartners* of the muon, the muon neutrino and the electroweak gauge bosons (see Figures 2.3b and 2.3c) that can account for the observed deviation [29].

Dark Matter

Another strong hint for physics beyond the SM is the presence of non-luminous and non-absorbing matter, consequently named Dark Matter (DM), in the universe. One of the most convincing evidences for DM originates from the observation of the rotation curves of galaxies. Considering the circular velocity $v(r)$ of an object within a galaxy such as a star, one expects from Newtonian dynamics

$$v(r) = \sqrt{\frac{GM(r)}{r}}, \tag{2.38}$$

where G is the gravitational constant and $M(r) = 4\pi \int \rho(r) r^2 \mathrm{d}r$ is the enclosed mass with the mass density profile $\rho(r)$ [31]. Hence $v(r)$ is expected to fall of as $1/\sqrt{r}$ beyond the optical
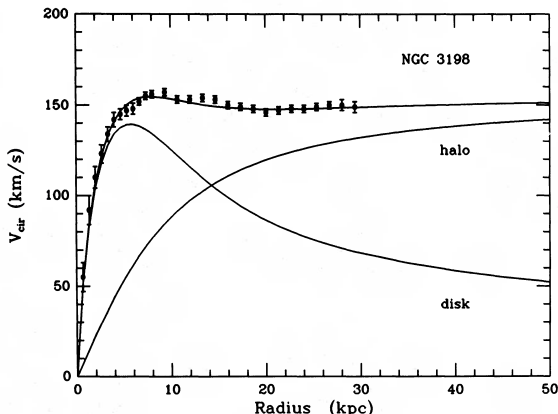
Figure 2.4: Rotation curve of the spiral galaxy NGC 3198. The solid line marked "disk" shows the expected curve assuming that only the visible stars contribute to the mass in the galaxy. The line marked "halo" represents the DM needed to reproduce the observed rotation curve. Figure taken from [30].

disc formed by the luminous matter of the galaxy. The observation that the velocity stays approximately constant at outer radii implies the presence of a *dark*, non-luminous halo with $M(r) \propto r$ and $\rho(r) \propto 1/r^{2\dagger}$ as shown in Figure 2.4. Evidence for DM is also given by numerous other astrophysical and cosmological observations such as the effect of gravitational lensing in the galaxy cluster Abell 1689 [32] and features in the anisotropy of the cosmic microwave background [33]. Thus the existence of DM is by now well established, which inevitably raises the question about its nature. Multiple experiments indicate that most DM should be non-baryonic and cold, i.e. non-relativistic [9]. Potential (cold) DM candidates must furthermore fulfill a set of criteria:

- Stable on cosmological timescales,

- Interact only very weakly with photons to appear as dark,

- Yield the right relic density in today's universe.

In the SM (extended by neutrino masses) the most promising candidate is the neutrino, that is however not abundant enough to be a dominant component of DM [31]. From the power spectrum of the cosmic microwave background [34] it can be concluded that most of the matter in the universe is actually formed by DM. This makes its nature one of the largest mysteries to date. SUSY models can be built to render a viable DM candidate that fulfills the requirements above. The capability to provide a solution to one of most important open questions is a major reason for the attractiveness of SUSY.

Fine Tuning

Although the renormalizabilty of the SM ensures that finite results are obtained for all higher-order corrections, loop corrections indicate that the masses of scalar particles have to be *fine tuned* over several orders of magnitude. While the masses of fermions and gauge bosons are protected by chiral and gauge symmetries, respectively [35], the Higgs squared mass parameter μ^2 receives corrections from Dirac fermion and scalar loops as shown in Figure 2.5.

$\dagger$ To keep the mass of the universe finite $\rho(r)$ has to fall off faster at some point.

Figure 2.5: One-loop quantum corrections to the Higgs mass parameter due to a Dirac fermion f (a) and a scalar particle S (b).

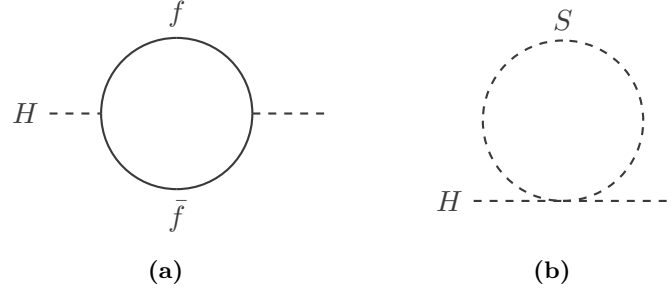If a fermion f couples to the Higgs boson with a term $-\lambda_f H \bar{f} f$ in the Lagrangian, the loop in Figure 2.5a yields a correction [36]

$$\Delta M_H^2 = -\frac{|\lambda_f|^2}{8\pi^2}\Lambda_{\mathrm{UV}}^2 + \dots , \tag{2.39}$$

where Λ_{UV} is an ultraviolet momentum cutoff to regulate the loop integral. The ellipsis represents terms proportional to the mass of the fermion m_f and grows only with $\ln \Lambda_{\mathrm{UV}}$. Λ_{UV} reflects the energy scale up to which the SM is assumed to be valid and new physics enters the theory. In any case the SM will break down at the reduced Plank scale $M_{\mathrm{P}} = \sqrt{1/8\pi G} = 2.4 \times 10^{18}\,\mathrm{GeV}$, where quantum-gravitation effects start to become relevant. In terms of the Lagrangian, the parameter μ^2 in the Higgs potential $V(\phi)$ is replaced by the "physical" one-loop corrected value $\mu_{\mathrm{phys}}^2 = \mu^2 + \Delta\mu^2$ where $\Delta\mu^2 \propto \Delta M_H$ [35]. The discovery of the Higgs boson implies that μ_{phys}^2 is of the order $(100\,\mathrm{GeV})^2$, while with a cutoff at M_{P} the quadratic divergencies in Λ_{UV}^2 yield corrections $\sim (10^{18}\,\mathrm{GeV})^2$. To leave μ_{phys}^2 at the observed value, large cancellations between the Lagrangian parameter μ^2 and the quantum correction $\Delta\mu^2$ would need to take place. This affects not only the Higgs mass, but the masses of all SM particles as these are generated by the VEV of the Higgs field which is related to μ^2 and hence also Λ_{UV}^2. Such a large amount of fine tuning is not considered as "natural" in a theory [37]. An appealing idea is that, similar as for fermions and gauge bosons, the Higgs mass is protected by some symmetry. Interestingly, loop corrections to μ^2 from a hypothetical scalar particle S (see Figure 2.5b) that couples to the Higgs via a term $-\lambda_S |H|^2 |S|^2$ in the Lagrangian come with the opposite sign

$$\Delta M_H^2 = \frac{\lambda_S}{16\pi^2}\Lambda_{\mathrm{UV}}^2 + \dots , \tag{2.40}$$

indicating such a symmetry may link fermions and bosons. Under the assumption that every SM fermion is accompanied by two complex scalars with $\lambda_S = |\lambda_f|^2$, i.e. same masses, the Λ_{UV}^2 contributions would cancel neatly. Such additional scalar particles are precisely the prediction of SUSY and would elegantly remove the need for any fine tuning of the Higgs mass. Partners of the SM fermions that differ only in spin would have been discovered long ago of course. Consequently SUSY, if it exists, must be a broken symmetry so that the SUSY particles acquire masses well above their SM counterparts.

2.2 Supersymmetry

SUSY [38–43] is one of the best studied candidates to extend the SM. Roughly speaking, it postulates a symmetry that relates bosons and fermions via transformations generated by an operator Q that turns a bosonic state into a fermionic state and vice versa [36]

$$Q\,|\text{Boson}\rangle = |\text{Fermion}\rangle\,, \quad Q\,|\text{Fermion}\rangle = |\text{Boson}\rangle\,. \tag{2.41}$$

As a result, every SM particle gets supersymmetric counterparts that differ in spin by $1/2$. The leptons and quarks get scalar superpartners denoted as *sleptons* and *squarks*, while the superpartners (spin $1/2$) of the gauge bosons and Higgs particles are labeled as *gauginos* and *higgsinos*, respectively. SUSY partners of the SM particles are marked with a tilde. For example, the gluino, the supersymmetric counterpart of the gluon g, is denoted as $\tilde{g}$.

The most elegant treatment of SUSY transformations involves the extension of space-time to *superspace* that in addition to the spacetime coordinates contains anticommuting fermionic coordinates θ and $\theta^\dagger$ [9]. Bosonic and fermionic states are combined and represented in a *superfield* $S(x^\mu, \theta, \theta^\dagger)$ which is a function of these coordinates. A description of this formalism would go beyond the scope of this thesis, but details can be found e.g. in Ref. [28].

It is appealing to extent the SM not more than necessary. The minimal supersymmetric extension of the Standard Model (MSSM) represents exactly such an extension, adding only the field content required for a consistent theory. Following mostly Ref. [36], the general concepts of SUSY, the structure of the MSSM and their implications are qualitatively introduced at a level relevant for the search presented in this thesis. More thorough discussions are presented in Refs. [28, 44].

2.2.1 Basic Concepts

The SM is based on two types of symmetries: internal symmetries reflected by the gauge group $SU(3)_C \times SU(2)_L \times U(1)_Y$ that do not affect the space-time properties of the particles [10] and space-time symmetries (translations, rotations and boosts) described by the Poincaré group. The basic idea of a supersymmetric SM is to embed the Poincaré group into some larger group which would serve as a more general framework.

Supersymmetry Algebra

Such an extension of the space-time symmetries is highly restricted by the Coleman–Mandula theorem [45], which loosely speaking states it is not possible to combine the Poincaré symmetry with other symmetries in a non-trivial way. Groups representing internal and global symmetries can thus only be realized as a direct product with the Poincaré group. These restrictions can be circumvented by the use of anticommuting spinors as generators. Thus the operator Q and its hermitian conjugate $Q^\dagger$ are spinors carrying spin angular momentum $1/2$ whose anticommuting relations have the following schematic form

$$\begin{aligned}
\left\{Q, Q^\dagger\right\} &= \sigma_\mu P^\mu\,, \\
\{Q, Q\} &= \left\{Q^\dagger, Q^\dagger\right\} = 0\,, \\
[P^\mu, Q] &= \left[P^\mu, Q^\dagger\right] = 0\,,
\end{aligned}$$

where P^μ is the four-momentum generator of space-time translations and σ_μ are the Pauli matrices. Together with the Poincaré algebra these relations form the SUSY algebra. The direct connection between the SUSY generators $Q, Q^\dagger$ and P^μ underlines that SUSY can indeed be understood as an extension of the space-time symmetries.

Supermultiplets

Similar to the lepton doublets in the $SU(2)_L$ group, particles and their superpartners form supermultiplets, which are irreducible representations of the SUSY algebra. As the SUSY generators Q and $Q^\dagger$ commute with the generators of gauge transformations, particles in the same multiplet are also in the same representation of the gauge group. Therefore, the bosonic and fermionic counterparts must have the same electric charges, weak isospin and color degrees of freedom, i.e. the same quantum numbers except the spin. The way to construct supermultiplets is restricted as each supermultiplet must contain an equal number of bosonic (n_B) and fermionic (n_F) degrees of freedom. The simplest form combines a two-component Weyl fermion $(n_F = 2)$ and a complex scalar field $(n_B = 2)$ into a *chiral* supermultiplet. The next-simplest form is to combine a massless[†] spin-1 boson $(n_B = 2)$ with a massless spin-1/2 Weyl fermion $(n_F = 2)$ into a *gauge* supermultiplet. Other possible, renormalizable combinations that yield $n_F = n_B$ are always reducible to chiral and gauge multiplets in case there is only one distinct copy of the SUSY generators $Q, Q^\dagger$ as presented here. Consequently, particles reside either in a chiral or gauge supermultiplet and the superpartners differ in spin by 1/2.

Supersymmetry Breaking

The squared mass operator $-P^2$ commutes with $Q, Q^\dagger$ as well as the rotation and translation operators. Thus it can be concluded that particles residing in the same supermultiplet must have equal masses. In this case the superpartners would have been discovered already. This means SUSY has to be a broken symmetry and the question about the nature of the symmetry breaking arises. A remarkable feature of unbroken SUSY is the cancellation of quadratic divergencies in Λ_{UV}, which stabilizes the masses of scalar particles such as the SM Higgs boson. These are present to all orders of perturbation theory even when the boson and fermion masses are not equal [28]. In order not to re-introduce quadratic divergencies, the relationships between the dimensionless fermion and boson couplings present in unbroken SUSY have to be maintained also in broken SUSY. Otherwise there would again be radiative corrections to the Higgs scalar mass of the form

$$\Delta m_H = \frac{1}{8\pi}\Big(\lambda_S - |\lambda_f|^2\Big)\Lambda_{\mathrm{UV}}^2 + \dots . \tag{2.42}$$

Thus it is common to consider only *soft* supersymmetry breaking that preserves the cancellations of quadratic divergencies. This means the Lagrangian can be written in the form

$$\mathcal{L} = \mathcal{L}_{\mathrm{SUSY}} + \mathcal{L}_{\mathrm{soft}} , \tag{2.43}$$

[†] For a renormalizable theory masses of gauge bosons have to be generated via spontaneous symmetry breaking.

	Supermultiplets		bosons	fermions	$SU(3)_C, SU(2)_L, U(1)_Y$
chiral	squarks, quarks	Q	$(\tilde{u}_L, \tilde{d}_L)$	(u_L, d_L)	$(\mathbf{3}, \mathbf{2}, +\frac{1}{6})$
		$\bar{u}$	$\tilde{u}_R^*$	$u_R^\dagger$	$(\bar{\mathbf{3}}, \bar{\mathbf{1}}, -\frac{2}{3})$
		$\bar{d}$	$\tilde{d}_R^*$	$d_R^\dagger$	$(\bar{\mathbf{3}}, \bar{\mathbf{1}}, +\frac{1}{3})$
	sleptons, leptons	L	$(\tilde{\nu}, \tilde{e}_L)$	(ν, e_L)	$(\mathbf{1}, \mathbf{2}, -\frac{1}{2})$
		$\bar{e}$	$\tilde{e}_R^*$	$e_R^\dagger$	$(\bar{\mathbf{1}}, \bar{\mathbf{1}}, 1)$
	Higgs, higgsinos	H_u	(H_d^+, H_d^0)	$(\tilde{H}_u^+, \tilde{H}_u^0)$	$(\mathbf{1}, \mathbf{2}, +\frac{1}{2})$
		H_d	(H_d^+, H_d^0)	$(\tilde{H}_d^+, \tilde{H}_d^0)$	$(\bar{\mathbf{1}}, \bar{\mathbf{2}}, -\frac{2}{3})$
gauge	gluon, gluino		g	$\tilde{g}$	$(\mathbf{8}, \mathbf{1}, 0)$
	W bosons, winos		$W^\pm, W^0$	$\tilde{W}^\pm, \tilde{W}^0$	$(\mathbf{1}, \mathbf{3}, 0)$
	B boson, bino		B^0	$\tilde{B}^0$	$(\mathbf{1}, \mathbf{1}, 0)$

Table 2.2: Field content of the MSSM. Chiral multiplets are defined in terms of left-handed Weyl spinors so that the conjugates of the right-handed quarks and leptons appear in the table. Only the first generation of the quark and lepton supermultiplet are shown. Table adapted from [36].

where $\mathcal{L}_{\text{SUSY}}$ contains the all gauge and Yukawa interactions and is invariant under SUSY transformations, and $\mathcal{L}_{\text{soft}}$ violates these. It is assumed that SUSY is spontaneously broken, i.e. the Lagrangian is invariant under SUSY transformations but the vacuum state of the underlying model is not. In this manner SUSY is hidden at low energies as it is the case for the electroweak symmetry. There is no consensus about the dynamics that cause the breaking of SUSY. Several models exists how a spontaneous symmetry breaking would be generated. Typically they assume that SUSY is broken in a "hidden sector" that is essentially decoupled from the visible sector containing the MSSM particles. The effects of SUSY breaking are then communicated by an unknown mechanism, often modeled as interactions of mediator particles residing in an additional messenger sector. In the absence of any knowledge about the exact nature of the SUSY breaking mechanism, it is practical to add terms to the Lagrangian that explicitly break SUSY such as scalar mass terms.

2.2.2 Structure of the Minimal Supersymmetric Standard Model

The MSSM represents a direct supersymmetrization of the SM. It is minimal in the sense that it contains the smallest number of new particle states and interactions while being consistent with phenomenology.

Field Content

The Higgs sector in the MSSM consists of two chiral supermultiplets H_u and H_d with hypercharge $Y = 1/2$ and $Y = -1/2$, respectively. To guarantee the cancellation of gauge anomalies [46], at least two Higgs supermultiplets are required with $Y = \pm 1/2$. Furthermore, Higgs supermultiplets with differing Y are also needed to give masses to both *up*-type

and *down*-type quarks (and the charged leptons). H_u and H_d contain complex scalar fields arranged as $SU(2)_L$ doublets labeled (H_u^+, H_u^0) and (H_d^-, H_d^0). The Higgs boson in the SM would then correspond to a linear combination of H_u^0 and H_d^0. The higgsinos, the fermionic superpartners to the Higgs scalars are arranged as $SU(2)_L$-doublet Weyl spinor fields and denoted as $(\tilde{H}_u^+, \tilde{H}_u^0)$ and $(\tilde{H}_d^-, \tilde{H}_d^0)$. The fields are listed in Table 2.2 along with the remaining fields of the MSSM.

The quarks and leptons are also arranged in chiral supermultiplets with their superpartners. There, the SM fermions are left-handed two-component Weyl spinors with spin $1/2$ and the superpartners complex spin-0 fields. Q contains the $SU(2)_L$-doublets $(\tilde{u}_L, \tilde{d}_L)$ and (u_L, d_L). The supermultiplets $\bar{u}$ and $\bar{d}$ contain the associated $SU(2)_L$-singlets $\tilde{u}_R^*$, $u_R^\dagger$ and $\tilde{d}_R^*$, $d_R^\dagger$, respectively. Likewise L contains the lepton and slepton doublets, as well as the corresponding singlets under $SU(2)_L$. The quark and lepton multiplets come, as usual, in three generations. Table 2.2 shows the representatives of the first generation. Squarks and sleptons do not carry chirality as they are spin-0 particles, hence the handedness label refers to the chirality of their superpartners to indicate their couplings. For example a right-handed slepton $\tilde{\ell}_R$ does not couple to a W boson while the left-handed slepton $\tilde{\ell}_L$ does.

The SM gauge bosons reside in gauge supermultiplets together with their fermionic counterparts. The QCD interactions are mediated by the gluon and its spin-1/2 color-octet superpartner, the gluino. The superpartners of the electroweak gauge fields $W^\pm, W^0$ and B^0 are labeled $\tilde{W}^\pm, \tilde{W}^0$ and $\tilde{B}^0$, and referred to as *winos* and *bino*, respectively.

Supersymmetry Interactions

In the SUSY formalism it is useful to introduce a function of the chiral superfields called *superpotential W* that describes all non-gauge interactions and that is used to build the final Lagrangian. In the MSSM it has the schematic (with suppressed gauge and family indices) form

$$W_{\text{MSSM}} = \bar{u}\mathbf{y_u}QH_u - \bar{d}\mathbf{y_d}QH_d - \bar{e}\mathbf{y_e}LH_d + \mu H_u H_d\,, \tag{2.44}$$

where the objects $H_u, H_d, Q, L, \bar{u}, \bar{d}, \bar{e}$ are the superfields corresponding to the chiral supermultiplets in Table 2.2. The parameters $\mathbf{y_u}, \mathbf{y_d}, \mathbf{y_e}$ are 3×3 matrices in family space and contain the Yukawa couplings. Most relevant for the phenomenology[†] is the $\mu H_u H_d$ term, which is the supersymmetric version of the Higgs boson mass in the SM. The expression results in terms for higgsino masses in the Lagrangian

$$\mathcal{L}_{\text{SUSY}}^{m_{\tilde{H}}} \propto \mu\Big(\tilde{H}_u^+ \tilde{H}_d^- - \tilde{H}_u^0 \tilde{H}_d^0\Big) + \text{c.c.}\,, \tag{2.45}$$

as well as Higgs mass terms

$$\mathcal{L}_{\text{SUSY}}^{m_H} \propto |\mu|^2 \Big(|H_u^0|^2 + |H_u^+|^2 + |H_d^0|^2 + |H_d^-|^2\Big)\,. \tag{2.46}$$

Roughly speaking μ parametrizes the mass in the Higgs sector of the MSSM and is consequently referred to as higgsino mass parameter.

The production and decay of sparticles in the MSSM are typically dominated by their gauge interactions. Consequently, these are of direct interest for phenomenology. Interactions

---

[†] the Yukawa couplings are known to be rather small, except for the third generation
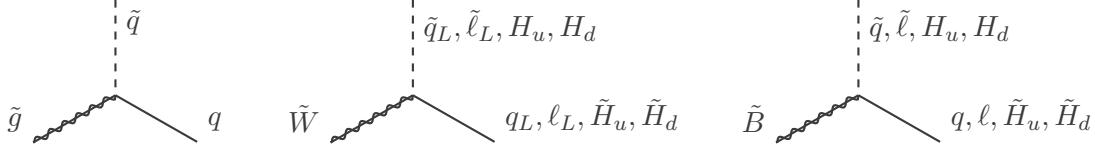
Figure 2.6: Couplings of the gluino, wino and bino to scalar-fermion pairs contained in the MSSM. The strength of the coupling is proportional to the coupling constant of the associated gauge group, e.g. bino vertices are proportional to g_1.

of the SM gauge bosons with the MSSM particles are determined completely by the gauge invariance of the Lagrangian. Furthermore, gauginos also couple to $(q, \tilde{q})$, $(\ell, \tilde{\ell})$ and $(H, \tilde{H})$ pairs as shown in Figure 2.6, which impacts the mass spectrum of the MSSM. The coupling strengths are proportional to the coupling constant of the associated gauge group.

R-Parity

In contrast to the SM, there are terms which can be added to the supersymmetric Lagrangian $\mathcal{L}_{\text{SUSY}}$ that are gauge-invariant and renormalizable but would violate lepton L or baryon B number conservation. Such terms would result for example in the proton decay via $p \to e^+ \pi^0$, which is constrained by lower limits on the proton lifetime from experiment, e.g. $\tau/\text{B}(p \to e^+ \pi^0) > 1.6 \times 10^{34}$ years [47]. To eliminate the possibility to add such terms to the Lagrangian a new, multiplicative symmetry called "R-parity" [48] is introduced

$$P_R = (-1)^{3(B-L)+2s} \,, \tag{2.47}$$

where s is the spin of the particle. From the definition it follows that all SM particles and the Higgs bosons ("particles") have even R-parity $P_R = +1$, while all squarks, sleptons, gauginos and higgsinos ("sparticles") have odd R-parity $P_R = -1$. In case R-parity is exactly conserved, sparticles and particles do not mix. Additionally the number of sparticles must be even at each interaction vertex. Thus the conservation of R-parity has fundamental phenomenological consequences:

- The lightest supersymmetric particle (LSP) is absolutely stable which makes it a viable candidate for DM in case it is electrically neutral.

- Except for the LSP, each sparticle must eventually decay into a final state with an odd number of LSPs.

- Sparticles are produced in even numbers at colliders.

The MSSM is defined to conserve R-parity. This is well-motivated due to the strong constraints on the proton decay and the attractiveness of having a DM candidate. This requirement can also be relaxed by e.g. allowing only lepton or baryon number violating terms but not both to avoid a potential proton decay. Such R-parity violating models [49] exhibit often a quite different phenomenology than the MSSM and are the basis for complementary SUSY searches.

Soft Supersymmetry Breaking

As the exact nature of SUSY breaking is not known, all possible terms that break SUSY softly are explicitly added to the Lagrangian in the MSSM. The associated parameters are:

- three gaugino mass parameters M_3, M_2, M_1 for the gluino, wino and bino;

- trilinear scalar couplings corresponding to Higgs–squark–squark and Higgs–slepton–slepton interactions; parametrized by $\mathbf{a_u}, \mathbf{a_d}, \mathbf{a_e}$ which are complex 3×3 matrices in family space;

- hermitian 3×3 matrices $\mathbf{m_Q^2}, \mathbf{m_{\bar{u}}^2}, \mathbf{m_{\bar{d}}^2}, \mathbf{m_L^2}, \mathbf{m_{\bar{e}}^2}$ governing squark and slepton mass terms;

- SUSY-breaking contributions to the Higgs potential m_{H_u}, m_{H_d}, b.

In total there are 105 parameters in the MSSM that do not have a counterpart in the SM [9], with most of them being added by the soft symmetry breaking. This huge parameter space makes the MSSM very flexible but also challenging to analyse. However, a lot of the introduced parameters imply flavor mixing or processes violating charge conjugation and parity symmetry (CP), on which there are strong experimental constraints. These potentially dangerous effects can be evaded if the soft symmetry breaking is assumed to be universal and flavor-blind. This means the matrices $\mathbf{m_i}$ are approximately diagonal so that processes inducing flavor-changing neutral current are suppressed up to the contribution of the trilinear couplings described by the $\mathbf{a_i}$ matrices. If those trilinear couplings are furthermore assumed to be proportional to the corresponding Yukawa coupling matrix, they are only relevant for the third generation squarks and sleptons. To avoid large CP-violating effects, it can be required that no new phases are introduced with the soft breaking parameters. The only CP-violating source is then the usual phase in the CKM matrix of the SM. The conditions above form the hypothesis of *soft supersymmetry-breaking universality*, that reduces the amount of free parameters in the MSSM significantly.

Mass Spectrum

Due to effects of the electroweak symmetry breaking the fields of the MSSM are in general not the mass eigenstates. Instead states with same electric charge, color and spin will mix [28].

Higgs Bosons In the MSSM the electroweak breaking mechanism is generalized to account for the two Higgs $SU(2)_L$-doublets in the theory. In a similar manner as in the SM, each doublet acquires a VEV

$$v_u = \left\langle H_u^0 \right\rangle, \quad v_d = \left\langle H_d^0 \right\rangle, \tag{2.48}$$

that are related to the VEV v in the SM by

$$v_u^2 + v_d^2 = v^2. \tag{2.49}$$

For phenomenology often the ratio of the two VEVs is considered and denoted as

$$\tan \beta \equiv \frac{v_u}{v_d}, \tag{2.50}$$

with $0 < \beta < \pi/2$ as v_u and v_d are taken to be positive by convention.

When the electroweak symmetry is spontaneously broken, the eight degrees of freedom contained in the two complex doublets become the three longitudinal modes of the massive Z and $W^\pm$ vector bosons, and five Higgs scalar mass eigenstates: the CP-even h^0 and H^0 (with $m_{h^0} < m_{H^0}$ by definition), the CP-odd A^0 and the charged H^+, H^-. The recently found $125\,\mathrm{GeV}$ scalar may then be identified with h^0.

Neutralinos and Charginos Also the gauginos and the higgsinos mix with each other to form particles called *electroweakinos*:

- The neutral higgsinos ($\tilde{H}_u^0$ and $\tilde{H}_d^0$) combine with the neutral gauginos ($\tilde{B}^0$ and $\tilde{W}^0$) to form four mass eigenstates $\tilde{\chi}_1^0, \tilde{\chi}_2^0, \tilde{\chi}_3^0, \tilde{\chi}_4^0$ refered to as *neutralinos*.

- The charged higgsinos ($\tilde{H}_u^+$ and $\tilde{H}_d^-$) and the charged gauginos ($\tilde{W}^+$ and $\tilde{W}^-$) combine to two charged mass eigenstates $\tilde{\chi}_1^\pm, \tilde{\chi}_2^\pm$ named *charginos*.

In both cases the indices mark the mass hierarchy of the electroweakinos, e.g. $m(\tilde{\chi}_1^\pm) < m(\tilde{\chi}_2^\pm)$. Usually the lightest neutralino $\tilde{\chi}_1^0$ is assumed to be the LSP as it is the only particle in the MSSM that can be a viable candidate for DM. The neutralino mixing is defined by the matrix

$$\mathbf{M}_{\chi^0} = \begin{pmatrix} M_1 & 0 & -g_1 v_d/\sqrt{2} & g_1 v_u/\sqrt{2} \\ 0 & M_2 & g_2 v_d/\sqrt{2} & -g_2 v_u/\sqrt{2} \\ -g_1 v_d/\sqrt{2} & g_2 v_d/\sqrt{2} & 0 & -\mu \\ g_1 v_u/\sqrt{2} & -g_2 v_u/\sqrt{2} & -\mu & 0 \end{pmatrix}. \tag{2.51}$$

The wino and bino mass parameters M_2 and M_1 originate from the explicit mass terms of the soft symmetry breaking while the entries $-\mu$ are the higgsino mass terms, see Equation (2.45). Entries proportional to g_1 and g_2 stem from the Higgs–higgsino–gaugino couplings shown in Figure 2.6. $\mathbf{M}_{\chi^0}$ can be diagonalized to obtain the neutralino masses. They can be expressed in terms of M_1, M_2, μ and $\tan(\beta)$ but the exact analytical solutions [50] are complicated and not very informative. Instead the mixing is usually evaluated in certain limits, in which one of the mass parameters is significant smaller than the other two, e.g. $M_1, M_2 \gg |\mu|$ or $M_2, |\mu| \gg M_1$. Here M_1, M_2 are taken to be real and positive, which can be ensured by an appropriate redefinition of the phases of $\tilde{B}^0$ and $\tilde{W}^0$, while the phase of μ stays a physical parameter. Neutralinos which are dominated by the higgsino, wino or bino component are referred to as higgsino, wino- and bino-like, respectively.

Likewise, the mixing of the charginos is described by the matrix

$$\mathbf{M}_{\chi^\pm} = \begin{pmatrix} \mathbf{0} & \mathbf{X}^T \\ \mathbf{X} & \mathbf{0} \end{pmatrix}, \quad \text{with} \quad \mathbf{X} = \begin{pmatrix} M_2 & g_1 v_u \\ g_2 v_d & \mu \end{pmatrix}. \tag{2.52}$$

The chargino masses $m(\tilde{\chi}_1^\pm), m(\tilde{\chi}_2^\pm)$ are then the double degenerate eigenvalues of the 4×4 matrix $\mathbf{M}_{\chi^\pm}^\dagger \mathbf{M}_{\chi^\pm}$ and depend on M_2, μ and $\sin 2\beta$.

Gluino Octet   There is no other color-octet fermion so that the gluino cannot mix with any other MSSM particle as the gauge group $SU(3)_C$ is unbroken. Consequently its mass arises solely from the gluino mass term in the soft symmetry breaking part of the MSSM Lagrangian

$$-\frac{1}{2}M_3\tilde{g}\tilde{g}\,, \tag{2.53}$$

so that the physical gluino mass is M_3 [28]. However M_3 is a running mass parameter and its value depends also on the renormalization scale.

Squarks and Sleptons   The largest set of new particles comes with the scalar superpartners of the SM fermions. In principle mixing can occur between all scalars of same electric charge, R-parity and color, also across families. This would result in a diagonalization problem of the 6×6 matrices for the

- *up*-type squarks $\tilde{u}_L, \tilde{c}_L, \tilde{t}_L, \tilde{u}_R, \tilde{c}_R, \tilde{t}_R$

- *down*-type squarks $\tilde{d}_L, \tilde{s}_L, \tilde{b}_L, \tilde{d}_R, \tilde{s}_R, \tilde{b}_R$

- charged sleptons $\tilde{e}_L, \tilde{\mu}_L, \tilde{\tau}_L, \tilde{e}_R, \tilde{\mu}_R, \tilde{\tau}_R$

and for the 3×3 matrix for the sneutrinos $\tilde{\nu}_e, \tilde{\nu}_\mu, \tilde{\nu}_\tau$. Under the assumption of universal soft symmetry breaking most of these mixing angles are very small. The first and second generation squarks and sleptons have negligible Yukawa couplings, thus they form seven nearly mass-degenerate pairs:

$$(\tilde{e}_R, \tilde{\mu}_R), (\tilde{\nu}_e, \tilde{\nu}_\mu), (\tilde{e}_L, \tilde{\mu}_L), (\tilde{u}_R, \tilde{c}_R), (\tilde{d}_R, \tilde{c}_R), (\tilde{u}_L, \tilde{c}_L) \text{ and } (\tilde{d}_L, \tilde{c}_L)\,.$$

As the squarks and sleptons of the third generation have a significantly larger Yukawa coupling, the left- and right-"handed" scalars combine to form distinct mass eigenstates

$$(\tilde{t}_L, \tilde{t}_R) \to (\tilde{t}_1, \tilde{t}_2), \quad (\tilde{b}_L, \tilde{b}_R) \to (\tilde{b}_1, \tilde{b}_2), \quad (\tilde{\tau}_L, \tilde{\tau}_R) \to (\tilde{\tau}_1, \tilde{\tau}_2),$$

where the index denotes the mass hierarchy as for the electroweakinos, i.e. $m(\tilde{t}_1) < m(\tilde{t}_2)$.

This concludes the particle spectrum of the MSSM. In total there are 32 distinct masses (including h^0 that may be identified with the SM Higgs boson) that correspond to particles yet to be discovered.

2.2.3 Implications

SUSY and the MSSM exhibit a couple of remarkable implications. Some of them are the main motivation why SUSY is thought to be realized at the electroweak scale, which would render at least part of the SUSY particles spectrum accessible at the LHC.
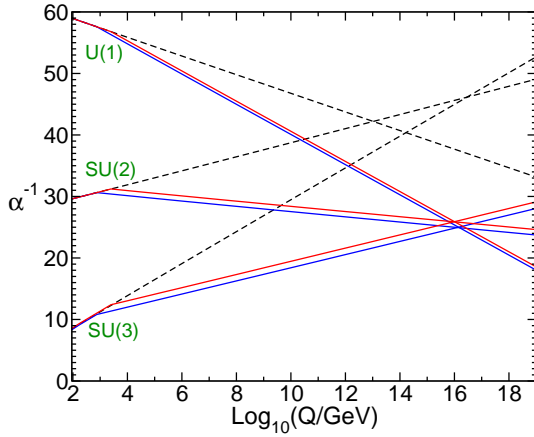
Figure 2.7: Renormalization group evolution including two-loop effects of the inverse gauge couplings in the Standard Model (dashed lines) and the MSSM (solid lines). The blue and the red lines reflect different assumptions about the sparticles masses (between 750 GeV and 2.5 TeV) and on the value of $\alpha_3(m_Z)$. Figure taken from [36].

Natural Supersymmetry

Although the quadratic divergences in Λ_{UV} vanish in a (broken) supersymmetric theory, additional corrections to the masses of scalar particles such as M_H remain. These are proportional to the masses appearing in the soft symmetry breaking and grow logarithmically with Λ_{UV}. If the largest mass scale in the soft terms is denoted as m_{soft}, these corrections have the form

$$\Delta M_H^2 = m_{\mathrm{soft}}^2 \left[\frac{\lambda}{16\pi^2} \ln(\Lambda_{\mathrm{UV}}/m_{\mathrm{soft}}) + \dots \right], \tag{2.54}$$

where λ stands schematically for dimensionless couplings. Large values of m_{soft} would clearly re-include notable corrections. To avoid unnatural amounts of fine tuning, the SUSY particles should consequently not be too far away from the weak scale. As naturalness can be understood as a rather aesthetic judgment, the amount of "allowed" fine tuning is a matter of taste. A widely accepted naturalness criterion [51] derives that parts of the supersymmetric particle spectrum should not be heavier than $\mathcal{O}(1\,\mathrm{TeV})$, and thus accessible at the LHC.

Unification of Coupling Constants

Another remarkable feature of the MSSM is the apparent unification of the gauge couplings [52]. As outlined in Section 2.1.2, the three gauge couplings g_i evolve with the renormalization scale Q. The running of the couplings is described by the renormalization group equations which depend on the particle content of the theory. Typically the quantities $\alpha_i = g_i^2/4\pi$ are considered, as their reciprocals α_i^{-1} run linearly with Q at one-loop order. For the SM these are shown as dashed lines in Figure 2.7. In principle the couplings evolve in a convergent direction towards higher energy scales and get close in the range $Q \sim 10^{13}$–10^{17} GeV but do not meet exactly. If one switches from the SM to the MSSM evolution equations at Q between 10^2 and 10^3 GeV, i.e. assuming SUSY to be realized at the weak scale, the gauge couplings unify with a notable precision at a scale $M_U \sim 1.5 \times 10^{16}$ GeV. The unification is not perfect as α_3 comes out slightly smaller than the common value of α_1 and α_2 at M_U, but this can easily be addressed to corrections due new particles that may exist near that scale. This approximate unification may be taken as a hint of some grand unification happening around the scale of M_U and indicates the MSSM could be the right way towards a more fundamental theory.

Gravitation

An arguably serious and unsatisfying flaw of SM is the absence of a description of the gravitational force. This is not a problem at the energies accessible with current particle colliders where the gravitational forces are completely negligible. A complete theory of elementary particle interactions should in any case also contain gravitation. SUSY can be linked to Einstein's general relativity which describes the gravitational force by requiring local, i.e. space-time dependent supersymmetry transformations. A consistent treatment of such supergravity [53] transformations necessitates the introduction of a massless spin-2 field that couples to the energy–momentum tensor for matter as in general relativity [28]. The quanta of this field are identified with gravitons and mediate the gravitational interaction together with the gravitinos, their spin-3/2 superpartners. Although such a theory is not renormalizable, the intrinsic connection between local SUSY transformation and gravitation is tantalizing and motivates that supergravity can be thought of as a low-energy limit of some more fundamental supersymmetric theory.

2.3 Search for Higgsinos and Sleptons in Compressed Mass Spectra

Recent constraints from the LHC place strong bounds on the presence of new particles at the TeV scale [54, 55]. Under the assumption that new states are nearly degenerate in mass, these constraints can be evaded while keeping a plethora of the features SUSY is known for. Such scenarios are challenging to access experimentally as their final states are characterized by *soft*, low-energy particles as depicted in Figure 2.8. If the states are too close in mass, the decay products will be too soft to pass the reconstruction thresholds. Consequently, the sensitivity of searches targeting compressed mass spectra is restricted to SUSY models that result in final-state objects with momenta of at least a couple of GeV. Two of such compressed SUSY scenarios have been considered in this thesis, namely the direct production of an electroweakino- and a slepton pair at the LHC, respectively.

Figure 2.8: Example configuration for a compressed mass spectrum. The three electroweakino states $\tilde{\chi}_2^0, \tilde{\chi}_1^\pm$ and $\tilde{\chi}_1^0$ are assumed to be very close in mass around μ. The decays into the LSP happen via offshell Z and W bosons. Those decay further into low-energetic leptons or pions, resulting in a final state characterized by very soft objects.
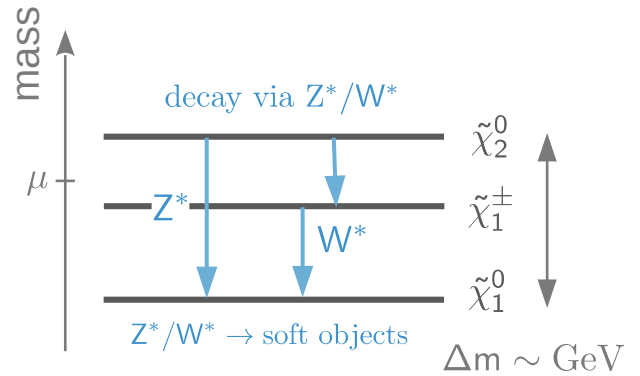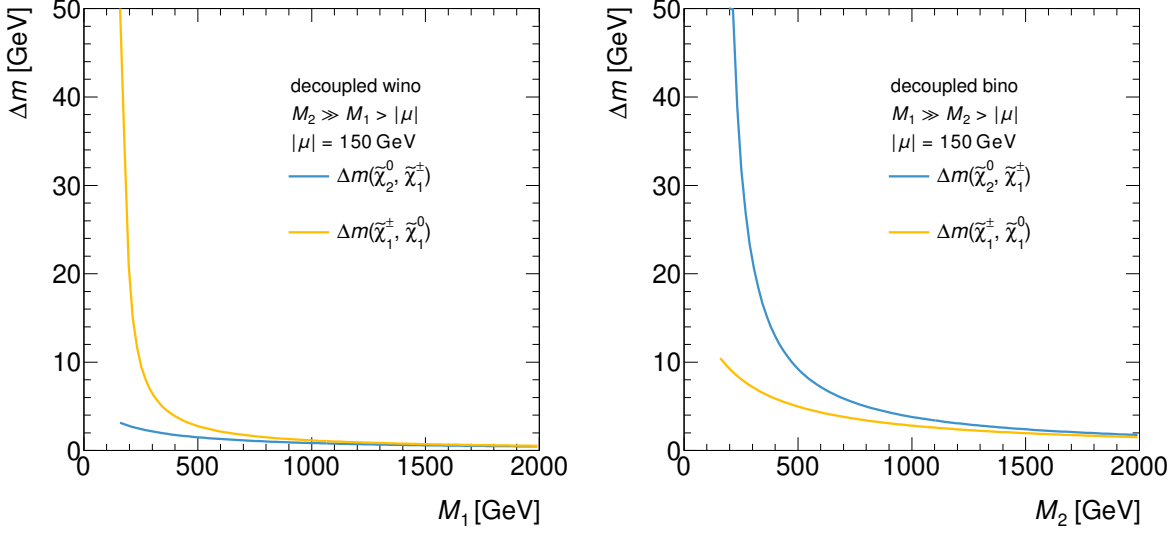
Figure 2.9: Higgsino mass splittings Δm assuming a decoupled wino (left) and a decoupled bino (right) under the assumption $\tan\beta \gg 1$.

2.3.1 Motivation

The first scenario is motivated by naturalness arguments [56] which suggest that $|\mu|$ is near the weak scale, while the bino and wino mass parameters could be much larger: $M_1, M_2 \gg |\mu|$. In such a configuration the three lightest electroweakinos are dominated by the higgsino component and result in a nearly mass-degenerate triplet of the $\tilde{\chi}_1^0, \tilde{\chi}_1^\pm, \tilde{\chi}_2^0$ states, consequently referred to as higgsinos. The mass splitting and the hierarchy between the individual states depends then on the relative sizes of M_1 and M_2, and also on their size relative to $|\mu|$. If either the wino or the bino mass parameter is assumed to be decoupled, the mixing matrices in Equations (2.51) and (2.52) can be evaluated to give approximate relations for the higgsino mass splittings [57]

$$M_1 \gg M_2 > |\mu| : \qquad\qquad M_2 \gg M_1 > |\mu| :$$

$$\left| m_{\tilde{\chi}_2^0} \right| - \left| m_{\tilde{\chi}_1^\pm} \right| \approx \frac{m_W^2 (1 \pm s_{2\beta})}{2(M_2 - |\mu|)} , \qquad \left| m_{\tilde{\chi}_2^0} \right| - \left| m_{\tilde{\chi}_1^\pm} \right| \approx \frac{m_W^2 t_{\theta_W}^2 (1 \mp s_{2\beta})}{2(M_1 + |\mu|)} , \qquad (2.55)$$

$$\left| m_{\tilde{\chi}_1^\pm} \right| - \left| m_{\tilde{\chi}_1^0} \right| \approx \frac{m_W^2 (1 \mp s_{2\beta})}{2(M_2 + |\mu|)} , \qquad \left| m_{\tilde{\chi}_1^\pm} \right| - \left| m_{\tilde{\chi}_1^0} \right| \approx \frac{m_W^2 t_{\theta_W}^2 (1 \pm s_{2\beta})}{2(M_1 - |\mu|)} , \qquad (2.56)$$

where the index $\pm$ corresponds to the sign of μ, m_W is the mass of the W boson, $s_{2\beta} \equiv \sin 2\beta$ and $t_{\theta_W} \equiv \tan\theta_W$. In the limit of $\tan\beta \gg 1$, the above relations can be further simplified as $(1 \pm s_{2\beta}) \approx 1$. For illustration purposes, Figure 2.9 shows the mass splitting between $\tilde{\chi}_2^0$ and $\tilde{\chi}_1^\pm$, and between $\tilde{\chi}_1^\pm$ and $\tilde{\chi}_1^0$ for $|\mu| = 150\,\text{GeV}$. Dependent on M_1 and M_2 respectively, mass splittings between tens of GeV down to $\mathcal{O}(1\,\text{GeV})$ arise.

Similar mass spectra are also predicted by *split supersymmetry* models [58, 59]. These models assume that only part of the SUSY spectrum is realized at the TeV scale, while the rest of the sparticles can be significantly heavier. In low-μ split SUSY [60] only μ remains
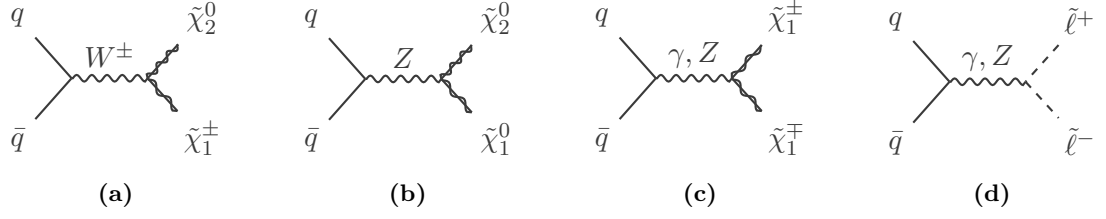
Figure 2.10: Dominant Feynman diagrams for the direct production of (a) to (c) electroweakino and (d) slepton pairs at the LHC.

around the weak scale with the rest of the SUSY breaking parameters pushed to a much larger scale $m_{\text{SUSY}} \sim 10^9 \, \text{GeV}$. It was shown that in such an arrangement the unification of gauge couplings still holds [61] and the lightest higgsino can form an adequate DM candidate [62], hence some the most striking implications of weak-scale SUSY are maintained. The naturalness problem may then have to be addressed differently, for instance by a cosmological relaxation of the weak scale [63]. At tree level the higgsino mass splittings are only between tens of keV and 1 MeV, but the radiative corrections are significant and can generate mass splittings up to $\mathcal{O}(\text{GeV})$ [64]. This places the particles produced in the decays on the edge of being reconstructable in the detector, rendering the presented search to a certain degree also sensitive to these kind of models.

The second scenario assumes the presence of light sleptons $\tilde{\ell}$ that are only slightly heavier than a bino-dominated LSP. A smuon $\tilde{\mu}$ and electroweakinos with masses up to $\sim 1 \, \text{TeV}$ can resolve the deviation in the anomalous magnetic moment of the muon in various settings of the MSSM [65]. Under the assumption of non-universal gaugino masses $M_1 < M_2 \ll M_3$, these models can also provide a viable DM candidate [66].

2.3.2 Production at the Large Hadron Collider

In the presented search the electroweakino and slepton pairs are assumed to be produced directly via electroweak processes. In principle higgsinos could also be produced indirectly via the production of more massive, strongly coupled particles such as squarks, which then subsequently decay into higgsinos [57]. This production mode would benefit from significant larger cross sections due to the strong coupling and color factors with respect to direct production which is at electroweak strength. However, in that case detailed statements about the particle spectrum and branching ratios of the strongly interacting particles are required. Furthermore, the strong constraints on squark and gluino masses indicate that indirect higgsino and electroweakino would contribute only minor. Consequently, only the direct production modes are considered, which allows the analysis be independent of the rest of the SUSY spectra. $\tilde{\chi}_2^0 \tilde{\chi}_1^\pm$, $\tilde{\chi}_2^0 \tilde{\chi}_1^0$ and $\tilde{\chi}_1^+ \tilde{\chi}_1^-$ pairs are produced via electroweak bosons in the s-channel from $q\bar{q}$ annihilation as shown in Figures 2.10a to 2.10c. Contributions from t-channels via squark exchange also arise due to the gaugino content in the electroweakinos, but are usually of lesser importance [36] and thus not shown. Slepton pairs are also produced in the s-channel via the neutral gauge bosons as depicted in Figure 2.10d. In both cases, the masses of the SUSY pairs are well above the Z- and W-boson mass, which makes the gauge bosons offshell in the production.

2.3.3 Simplified Models

The search was optimized and interpreted for both scenarios in terms of simplified models [67, 68]. Simplified models are designed to involve only a small number of new particles and interactions. They are described by the masses, production cross sections and branching ratios of the particles considered. In principle simplified models represent a "swath" in the MSSM parameter space and allow the analysis to focus on certain kinematics, such as compressed mass spectra. This means that instead of considering specific MSSM parameter configurations and the resulting mass spectra, the masses of the SUSY particles and their branching ratios are postulated directly. Further simplification takes place by giving only the SUSY particles appearing in the decay chain masses in a regime that renders them relevant at LHC energies. All other SUSY particles are assumed to be decoupled, i.e. set to much larger masses so they do not play any role in the model under consideration. The simplified models for the higgsino (involving only the three electroweakino states $\tilde{\chi}_2^0$, $\tilde{\chi}_1^0$ and $\tilde{\chi}_1^\pm$) and the slepton scenario (involving only $\tilde{e}_{L/R}, \tilde{\mu}_{L/R}$ and $\tilde{\chi}_1^0$) used in the analysis are presented in subsection 5.1.2.

3 Experiment

The data, i.e. the collision events analyzed in this thesis have been produced by the LHC and recorded with the ATLAS detector at CERN. This chapter describes how particles are accelerated and collided at the LHC, and gives an overview about the layout and detection principles of ATLAS. As simulated collision data are a key ingredient in many analysis activities, the required steps to generate simulated events are also reviewed.

3.1 The Large Hadron Collider

The LHC is a circular hadron–hadron collider hosted by CERN and located near Geneva, Switzerland. It is a synchrotron with a circumference of about 27 km, and can be operated with protons and heavy ions[†]. This thesis considers only proton–proton (pp) collision data, thus the description of the experimental setup focuses on this operation mode. To analyze the collisions produced by the LHC, four large detectors have been installed along the accelerator ring: ALICE, LHCb, CMS and ATLAS. Their respective locations are indicated in the scheme in Figure 3.1. In order to provide insights for a wide range of fundamental research, the experiments are individually designed and optimized for a specific purpose.

ALICE [69] investigates a prediction of QCD at sufficient high energy densities: the occurrence of a phase transition from conventional hadronic matter to a plasma of deconfined quarks and gluons, the so-called quark–gluon plasma [8].

LHCb [70] performs precision measurements of CP violation and rare decays of bottom and charm hadrons that may give hints for BSM physics.

The sister experiments ATLAS [71] and CMS [72] are both multi-purpose detectors, designed to cover many potential signatures and are targeted for SM measurements as well as searches for BSM physics. In general both detectors can address the same phase space, which enables to cross-validate their results.

In addition to these four large detectors, the three smaller experiments TOTEM [73], MoEDAL [74] and LHCf [75] address very specific research fields, such as precise measurements of the proton size.

As protons cannot be injected directly into the LHC, several steps of pre-acceleration are required. Economically these are performed by predecessing accelerators of the LHC that have been upgraded to cope with the demanding requirements of the LHC [77]. The protons originate from a bottle of hydrogen. The hydrogen is guided into a duoplasmatron [78], in which the electrons are stripped away from the hydrogen atoms by electric discharges in the gas between a hot cathode and an anode to form protons. These are then sent to a radio frequency (RF) quadrupole [79], a linear accelerator which focuses the particle beam and increases its energy to 750 keV. This beam is then injected into the linear accelerator Linac 2,

---

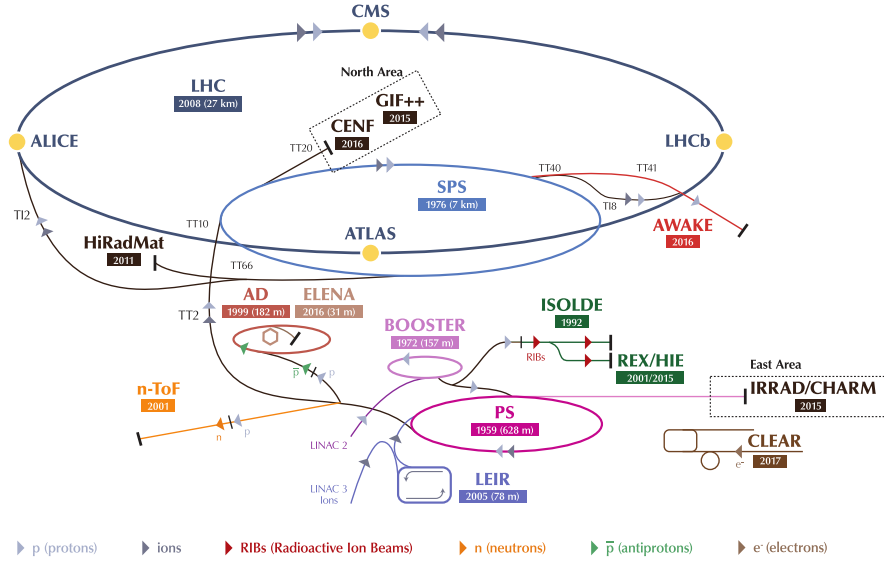[†] So far lead and xenon ions have been used.

Figure 3.1: Schematic illustration of the CERN accelerator complex, showing the acceleration chain the protons undergo before being injected into the LHC as well as the four large experiments around the storage ring. Experiments not directly related to the LHC are also shown for completeness. Figure adapted from [76].

in which the energy is increased to 50 MeV. The beam energy is then further increased step by step using a series of circular accelerators (the PS Booster PSB, the Proton Synchrotron PS and the Super Proton Synchrotron SPS) to 450 GeV, the injection energy of the LHC [80]. Within the LHC, the particles are accelerated to their final energy (6.5 TeV in Run 2). The complete accelerator chain for the protons is depicted in Figure 3.1.

The LHC is build of eight arcs and eight shorter straight sections that make up the ring-like structure of the accelerator. Within the LHC, two counter-rotating proton beams circulate in evacuated pipes and are brought to collision at four interaction points, where the large detectors have been installed. These interactions points are located in the straight sections, along with the facilities for injection, beam dumping and cleaning. In the arcs, dipole magnets built out of NbTi Rutherford cables produce magnetic fields that force the particles on a circular trajectory. To achieve a center-of-mass energy of 13 TeV, field strengths of more than 8 T are required. The electric currents needed to produce such high field strengths require the magnets to be operated in a superconducting state by cooling them to 1.9 K using superfluid helium. Furthermore, quadrupole magnets focus the beam to keep the particles close to the reference trajectory, they and are used to squeeze the beams on both sides of the interaction point to maximize the collision rate. In addition, multipole corrector magnets are used to optimize the beam trajectories. The acceleration itself is performed — as in most of the pre-accelerators — by RF cavities operating at 400 MHz (in the LHC), which increase the energy of the protons at each passage using electric fields. The energy gain provided by the cavity depends on the time of arrival of the particle. Loosely speaking, slower particles that reach the accelerating structure later than faster particles, gain more energy [81]. This does not only ensure that all particles in the beam have the same energy but also results in the bunch structure of the beam: instead of a continuous particle beam, the LHC collides bunches of

approximately 10^{11} protons each. The bunch-spacing, the time between the collision of two bunches, is 25 ns in the LHC, so that approximately 40 million collisions occur per second.

The performance of a collider is expressed in terms of the instantaneous luminosity L that for a synchrotron under simplifications such as assuming Gaussian bunch profiles is given by

$$L = \frac{N_b^2 n_b}{4\pi\sigma_x\sigma_y} f \,, \tag{3.1}$$

where N_b is the number of protons per bunch, n_b the number of bunches, σ_x and σ_y characterize the horizontal and vertical beam spread, and f represents the revolution frequency [9]. L can be understood as a measure of particle flow density and thus is desired to be large in order to maximize the collision rate. The design luminosity of the LHC is $1 \times 10^{34}\,\mathrm{cm}^{-2}\,\mathrm{s}^{-1}$, but more than twice of that was already reached during 2017 data-taking [82]. The size of the total dataset recorded at an experiment is denoted as the integrated luminosity L_{int} and given by the integral of L over time

$$L_{\mathrm{int}} = \int L \, \mathrm{d}t \,. \tag{3.2}$$

This dataset can then be searched for interesting signatures. Assuming a potential process of interest has the cross section σ, the number of expected events N_{exp} from this process in a dataset of size L_{int} is given by

$$N_{\mathrm{exp}} = \epsilon A \times \sigma \times L_{\mathrm{int}} \,, \tag{3.3}$$

where A and ϵ are the acceptance and efficiency of the applied selection, respectively. The acceptance accounts for signal events not entering the fiducial volume spanned by the analysis while the efficiency considers that not all signal events in this volume are reconstructed.

The LHC went into operation during 2008 [83] with first beam circulations. In general its operation is structured into Runs — multiple-year periods of data-taking — with only short shutdowns between the years within a Run to allow for small adjustments and repairs of the accelerator and detectors. More extensive improvements are performed in the long shutdowns between Runs, e.g. to replace or install new detector systems. During Run 1 (2009–2013) *pp* collision data was taken at center-of-mass energies of 7 TeV and 8 TeV, and a total integrated luminosity of approximately $28.5\,\mathrm{fb}^{-1}$ was delivered to ATLAS [84]. For Run 2 (2015-2018) the center-of-mass energy was increased to 13 TeV and about $156\,\mathrm{fb}^{-1}$ was delivered to ATLAS [85]. After a two-year long shutdown, Run 3 is scheduled for 2021–2023, eventually with another increase of the center-of-mass energy to 14 TeV and the target to record another $150\,\mathrm{fb}^{-1}$ [86]. Finally, the subsequent upgrade to the High Luminosity LHC [87] aims to record a dataset of up to $3000\,\mathrm{fb}^{-1}$ during another 10 years of data-taking.

3.2 The ATLAS Detector

The ATLAS experiment is a multipurpose particle detector and hosts a variety of detector technologies to measure as many physical quantities as possible for each collision. Combining the information from all subdetectors enables to fully reconstruct and explore the collision event such that a broad search and measurement program can be covered. This section summarizes the general requirements as well as the layout of the detector and its components,

and introduces the coordinate system used to describe the collision events. Specifications are generally taken from Ref. [71] except when stated otherwise.

3.2.1 General Layout and Detection Concept

ATLAS is interfaced with the LHC via the beam pipe. While the beam pipe has to be transparent for the particles produced in the collisions it must also be able to withstand the forces originating from the vacuum. To meet these requirements the beam pipe is made out of beryllium at the interaction point while stainless steel was used for its outer segments. Closest to the beam pipe the first detection layer, the Inner Detector (ID), measures particle tracks and provides vertex information. It is immersed in a magnetic field so that the particle momenta can be deduced from the bending of the tracks. The ID is made of lightweight material to minimize energy losses before the particles reach the next detector layer, the calorimeters. These measure the energy of particles by essentially absorbing them. In the electromagnetic calorimeter, electrons and photons are stopped by inducing showers of bremsstrahlung and electron–positron pairs. Hadrons will mostly pass the electromagnetic calorimeter without large energy deposits. They will be absorbed in the adjacent hadronic calorimeter by nuclear interactions and ionization processes with the calorimeter material. The outermost detection layer is formed by the Muon Spectrometer (MS) which records tracks of muons that traverse the calorimeters without leaving large energy deposits. Like the ID, the MS is immersed in a magnetic field to enable momentum measurements.

Sensitivity to particles that interact only weakly with the detector material, like neutrinos, can be inferred from transverse momentum imbalances. Hence, ATLAS covers nearly the full solid angle of 4π. For this purpose, the "barrel–endcap" layout was adapted in the detector design: in the central region the detector components are aligned as concentric cylinders (barrels) while in the forward region particles are detected by discs (endcaps), making ATLAS forward–backward symmetric with respect to the interaction point. A schematic illustration of the complete ATLAS detector and its components is depicted in Figure 3.2.

The high collision rate of the LHC does not allow to store all events permanently as the bandwidth of the write-out systems is limited. For that reason already at *online* level a decision has to be made whether an event is interesting for analysis or not. Triggers — electronics- and software-based systems — scan events for promising signatures and reduce the raw data rate to levels that allow for further processing [81]. Parts of the subdetectors are thus designed to have response times short enough to offer trigger capabilities in "real" time. In case of a positive trigger decision, the events are written to permanent storage and undergo the offline reconstruction, i.e. the building of physics objects such as jets from the measured detector signals.

As each of the colliding bunches consists of a large amount of protons, the recorded events will not only contain the signature of the hard-scattering processes that triggered the write-out but will also have contributions from several other, typically low-energy *pp* collisions, referred to as *pile-up*. In-time pile-up denotes contributions from collisions occurring in the same bunch crossing, while large signal integration times of some detector systems makes them sensitive also to collisions before or after the collision of interest, known as out-of-time pile-up. Other contributions come from thermal neutrons and photons filling the ATLAS cavern during the LHC operation (cavern background), and interactions of the proton bunches with
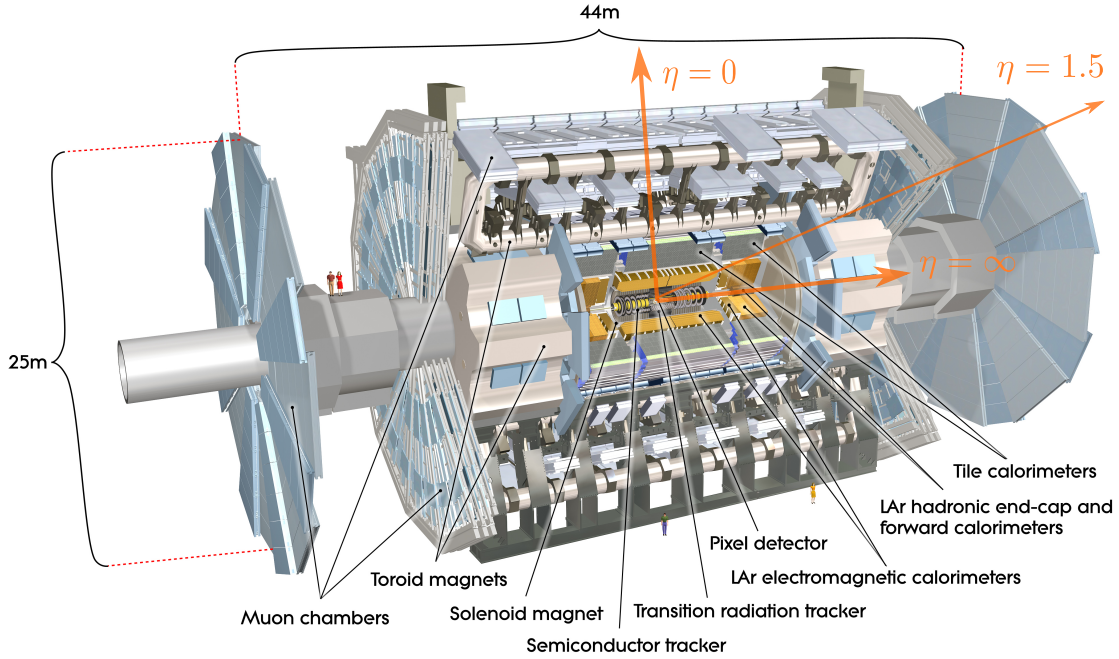
Figure 3.2: Schematic view of the ATLAS detector. The orange arrows indicate η-directions of 0, ∞ and 1.5, the end of barrel electromagnetic calorimeter. Figure adapted from [89].

the collimators (beam-halo events) and residual gas in the beam pipe (beam-gas events) [88]. These are mitigated by appropriate shielding or produce out-of-time signals and thus can be removed from the analysis.

3.2.2 ATLAS Coordinate System

To describe the detector layout and the objects reconstructed from the *pp* collisions, a dedicated, right-handed coordinate system was established and is used in ATLAS. The origin of the coordinate system is defined as the center of the detector, with the *z*-axis defined by the beam direction. The *x*–*y* plane is perpendicular to the beam so that the positive *x*-axis points from the interaction point (IP) towards the center of the LHC ring and the positive *y*-axis points upwards. In the transverse plane, cylindrical coordinates (r, ϕ) are used, with $\phi \in [-\pi, \pi]$ being the azimuthal angle measured around the beam axis. Longitudinal directions are given by the pseudorapidity η defined in terms of the polar angle $\theta \in [0, \pi]$ as $\eta = -\ln \tan(\theta/2)$. Some example values for η are illustrated in Figure 3.2. In the massless limit $(E \approx |\vec{p}|)$ the pseudorapidity is equivalent to the rapidity $y = 0.5 \ln[(E + p_z)/(E - p_z)]$, where E is the energy of the object and p_z its longitudinal momentum. Transverse momentum and energy are defined relative to the beam axis by $p_\mathrm{T} = p \sin \theta$ and $E_\mathrm{T} = E \sin \theta$, respectively. Angular distances ΔR are measured in terms of the rapidity by $\Delta R = \sqrt{(\Delta y)^2 + (\Delta \phi)^2}$. An important feature of this description is that it is independent of the longitudinal momenta of the initial interacting partons: as differences in y and for massless particles also in η are

invariant under Lorenz boosts along the z-axis, distances given ΔR are invariant as well.

3.2.3 Magnet System

One of the key requirements of ATLAS is to provide momentum measurements with good resolution in the trackers of the ID and the MS using the track curvature. The magnetic fields that bend the trajectories of charged particles are created by four superconducting magnets: a solenoid for the ID and three toroids for the MS. To operate in the superconductive state the magnets are cooled down to $4.5\,\mathrm{K}$ by a cryogenic system utilizing liquid helium. All magnets share a common design principle: minimizing the amount of material particles have to traverse before reaching the detector in order to mitigate effects from multiple-scattering that worsen the momentum resolution.

The central solenoid is formed by windings out of a NbTi conductor stabilized with aluminum inside an aluminum supporting cylinder. It is aligned to the beam axis and immerses the ID with an axial magnetic field of $2\,\mathrm{T}$ at the nominal operation current of $7730\,\mathrm{kA}$.

The toroids are made from a NbTi-based conductor winded into a doublet of pancake-shaped coils and embedded into stainless-steel vacuum vessels. Eight such coils in a race-track configuration form the barrel and the two endcap magnets of the MS. The barrel toroid provides a magnetic field of approximately $0.5\,\mathrm{T}$ in the central region. In the endcaps the magnetic field is about twice as large to ensure enough bending power also in the forward region, where the fraction of the transverse momentum with respect to the total momentum decreases.

3.2.4 Inner Detector

The ID records tracks of charged particles to provide information for vertex reconstruction and momentum measurements. For this purposes position measurements with high precision at a fine granularity are required while the detector components — being closest to the IP — have to be able to withstand the large amount of radiation originating from the collisions. To match these demands two semiconductor-based trackers, the pixel detector and the Silicon Microstrip Tracker (SCT), complemented by the Transition Radiation Tracker (TRT), a gaseous detector system, are used. Schematic illustrations of the whole ID and the mutual alignment of its subcomponents are shown in Figure 3.3. The trackers are permeated by the $2\,\mathrm{T}$ magnetic field produced by the solenoid. The ID provides tracking information in the range $|\eta| < 2.5$ and measures the transverse momenta of the tracks with a design resolution of $\sigma_{p_\mathrm{T}}/p_\mathrm{T} = 0.05\,\%\,p_\mathrm{T}/\mathrm{GeV} \oplus 1\,\%$. For Run 2 the ID did not provide any online trigger capabilities, which will however change in Run 3 with the installation of the Fast TracKer system in ATLAS [90]. In the following the three subsystems of the ID are briefly reviewed.

Pixel Detector   Pixels are the only possible geometry that is still operational in high rate environments like the IPs within the LHC and the resulting level of occupancy [10]. Therefore the innermost layer of the ATLAS detector is segmented into pixels of silicon, built as hybrids of sensors and readout electronics. The pixel detector provides about 92 million readout channels with a typical pixel size of $50\,\mathrm{\mu m} \times 400\,\mathrm{\mu m}$ that are arranged as two endcaps with three disc layers each and four barrel layers in the central region to cover the range up to
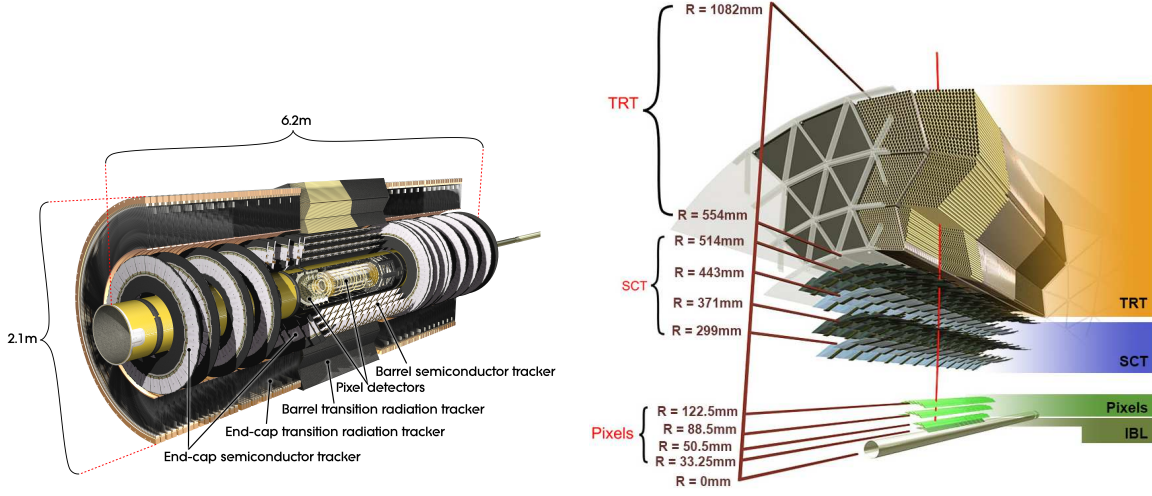
Figure 3.3: Schematic drawings of the ID and its components. Figures taken from [92, 93]

$|\eta| < 2.5$. The innermost central layer, the Insertable B-Layer (IBL) was installed between Run 1 and Run 2 together with a new beryllium beam pipe of smaller diameter and extended the ID to even smaller radii [91]. Along with reduced pixel sizes of $50\,\mu\text{m} \times 50\,\mu\text{m}$ on the IBL and further software improvements this additional layer notably increased the tracking and flavor-tagging performance [92].

Silicon Microstrip Tracker The second subsystem of the ID is formed by silicon semiconductor detectors aligned as strips. They are grouped as double layers of strips and by building them in "stereo" mode, i.e. with a small crossing angle between the two layers, a two-dimensional position information of a traversing particle can be obtained. In total the SCT has 6.3 million channels and provides tracking information in the range $|\eta| < 2.5$. The SCT modules are arranged to form four cylindrical double layers in the barrel and nine discs for each endcap so that a particle from the IP traverses four SCT layers [94], i.e. provides four space-point measurements. Strips in the barrel and the endcaps are aligned axially and radially, respectively, with a mean strip pitch of $80\,\mu\text{m}$. The stereo layer of strips in each SCT module has a crossing angle of $40\,\text{mrad}$.

Transition Radiation Tracker To enhance pattern recognition for track finding and the momentum resolution, the semiconductor trackers are complemented by the TRT at outer radii [71]. The TRT is operated like a drift chamber and consists of multiple layers of straw tubes filled with an argon-based gas mixture and interleaved with polypropylene as radiator material. The straws are made from polyimide foil with a $31\,\mu\text{m}$ diameter tungsten wire at the center working as anode. In the barrel region the straws are aligned parallel to the beam axis while radially orientated straws in the endcaps provide a total coverage up to $|\eta| < 2.0$. Although the intrinsic resolution of the straws of about $130\,\mu\text{m}$ is worse with respect to the inner silicon detectors the larger amount of hits (typically above 30) in conjunction with the lever arm due to the much larger geometrical size compensates for this. This subsystem also

enhances the electron-identification capabilities by measuring transition radiation emitted in the radiator material [95]. Photons from the transition radiation are absorbed in the gas inside the tubes which results in an output signal at the wires. As it is much more likely for electrons to radiate when passing the boundary of two media than for heavier particles such as pions, it can be used to discriminate those particles [96].

3.2.5 Calorimeters

The aim of calorimeters is to measure the energy contained in the showers induced by electrons, photons and hadrons. As electromagnetic showers occupy much smaller volumes than hadronic showers [81], the calorimeter system is separated into two parts: a liquid argon (LAr) electromagnetic calorimeter with fine granularity and adjacent hadronic calorimeters with coarser segmentation. The hadronic calorimeter system comprises a scintillator-tile calorimeter in the central region and LAr calorimeters in the endcaps. In addition, the LAr forward calorimeter covers the region close to the beam pipe, so that the total calorimeter coverage is up to $|\eta| = 4.9$. A schematic drawing of the calorimeters is shown in Figure 3.4a. All calorimeters are built in a "sandwich" design in which layers of passive absorber material alternate with active layers which produce the output signal. Consequently, only a fraction of the absorbed energy is measured, which has to be taken into account via calibrations. Information from all subsystems — at reduced granularity — are available to the online trigger system. The total thickness of the calorimeter of about 10 interaction lengths ensures a good containment of hadronic activity thus mitigating leakage to the MS, which would negatively impact muon reconstruction. The design energy resolutions are $\sigma_E/E = 10\,\%/\sqrt{E} \oplus 0.7\,\%$ in the electromagnetic and $\sigma_E/E = 50\,\%/\sqrt{E} \oplus 3\,\%$ in the hadronic calorimeter. In the following the subcomponents of the calorimeter system are discussed briefly.

Electromagnetic Calorimeter   The electromagnetic calorimeter uses lead as passive and LAr as active layers build as an accordion-like structure. The accordion shape enables the construction without transition cracks and increases the effective thickness of the calorimeter as the particles enter under an angle with respect to the calorimeter front [10]. The barrel part of the electromagnetic calorimeter covers the range $|\eta| < 1.475$ while the two endcaps add coverage to this subsystem between $1.375 < |\eta| < 3.2$. All LAr calorimeters are cooled down to an operating temperature of $87\,\mathrm{K}$ [97]. Calorimeter cells are segmented into several layers with decreasing granularity for the outer layers. The finest segmentation is present in the first layers for $|\eta| < 2.5$ (e.g. $\Delta\eta \times \Delta\phi = 0.025/8 \times 0.1$ for the central barrel) to provide precision measurements in the region also covered by trackers. To provide adequate shower containment and energy resolution the electromagnetic calorimeter has a thickness of at least 22 (24) radiation lengths in the barrel (endcap). A presampler with LAr as active material is used in the range $|\eta| < 1.8$ to improve corrections for electrons and photons due to energy losses before the calorimeters e.g. in the cryostats.

Hadronic Calorimeter   Hadronic activity in the barrel region is measured by the tile calorimeter which uses steel plates as passive and scintillating tiles as active layers. The ultraviolet light produced by ionizing particles crossing the scintillator is collected by wave-length shifting fibres and transmitted to photomultipliers that produce the output signal. The tiles are
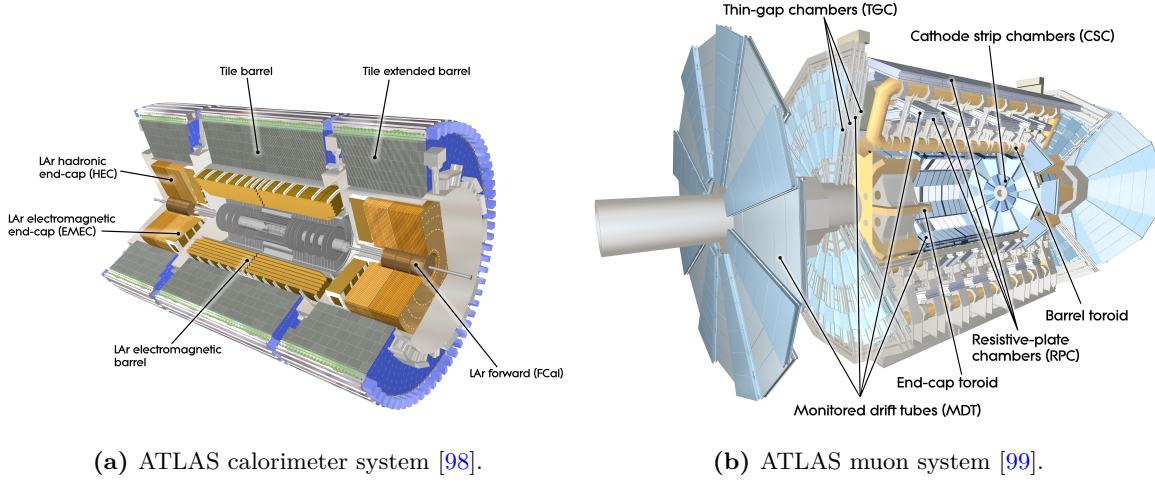
(a) ATLAS calorimeter system [98].

(b) ATLAS muon system [99].

Figure 3.4: Cut-away views of two subsystems of the ATLAS detector: calorimeters and muon spectrometer.

oriented radially and perpendicular to the beam axis with the readout at the edges to allow for a nearly seamless coverage in ϕ. Tile modules are grouped to form three layers of cells in radial depth with a total thickness of approximately 7.4 interaction lengths. The tile calorimeter extends up to $|\eta| < 1.7$ with a typical granularity of $\Delta\eta \times \Delta\phi = 0.1 \times 0.1$ except for the back part of the calorimeter which is segmented coarser in η. It consists of a central barrel part ($|\eta| < 1.0$) and two extended barrels ($1.0 < |\eta| < 1.7$).

Hadronic calorimetry is extended by a LAr endcap calorimeter in the range $1.5 < |\eta| < 3.2$, slightly overlapping with the tile and LAr forward calorimeter to reduce drops in material density in the transition regions. It consists of two cylindrical wheels per endcap, located directly behind the endcaps of the electromagnetic calorimeter. Each wheel is made out of copper plates as passive material separated by 8.5 mm gaps filled with LAr as active medium. The gaps are divided by three electrodes into four evenly-spaced drift zones serving as readout structure. In the precision measurement region ($|\eta| < 2.5$) the readout is segmented similarly as for the tile calorimeter ($\Delta\eta \times \Delta\phi = 0.1 \times 0.1$), while the granularity is coarser (0.2×0.2) at larger values of $|\eta|$.

LAr Forward Calorimeter Coverage from $|\eta| > 3.1$ up to $|\eta| < 4.9$ is provided by the LAr forward calorimeter. It is formed by two endcaps each split into a electromagnetic and two hadronic modules with a total depth of approximately 10 interaction lengths. To reduce reflection of neutrons into the ID the forward calorimeter is recessed with respect to the front of the electromagnetic calorimeter thus motivating the use of high-density material in its construction. The modules are built from a metal matrix as support for copper tubes oriented parallel to the beam axis that contain electrode rods. LAr in the gap between the rods and the tubes serves as active material. The electromagnetic modules utilize copper as material for the matrix and the rods to optimize resolution for electromagnetic induced showers. The other two modules are made dominantly from tungsten which ensures adequate containment of hadronic showers due to its high density.

3.2.6 Muon Spectrometer

The outer part of the ATLAS detector is formed by the muon system and is designed to provide tracking information and momentum measurements for charged particles that are able to pass through the inner detection layers. It is purely based on gaseous detectors that can cover the large area at a reasonable cost level [10]. The MS is located in the magnetic fields produced by the barrel and endcap toroid magnets. The subsystems of the MS are installed as three concentric rings in the barrel region and three wheels in each endcap, so that a particle traverses at least three layers of the MS. Monitored Drift Tubes (MDTs) are used in both the barrel and the endcaps to perform precision tracking up to $|\eta| < 2.7$. To cope with the higher rate, the first layer of the forward region utilizes Cathode Strip Chambers (CSCs) as precision chambers instead of MDTs. In the central region the precision chambers are installed on and between the barrel toroid, while in the forward regions they are placed before and after the endcap toroids. Thus they share the eight-fold symmetry of the magnet system and are ordered as octants. Each octant consists of a large and a small sector which differ slightly in size. The small and the large sectors overlap slightly in ϕ to avoid gaps in coverage. The precision chambers are complemented with trigger chambers: Resistive Plate Chambers (RPCs) and Thin Gap Chambers (TGCs) provide trigger capabilities on muons up to $|\eta| < 2.4$ in the barrel and endcaps, respectively. Figure 3.4b shows a schematic illustration of the MS. A gap in chamber coverage around $\eta \approx 0$ is left to allow for service supplies of the inner detector systems. The MS is designed to provide a stand-alone momentum resolution $\sigma_{p_\mathrm{T}}/p_\mathrm{T}$ below $3\,\%$ over a wide p_T range and up to $10\,\%$ at a p_T of 1 TeV [100]. The following paragraphs briefly summarize the subcomponents of the muon system.

Monitored Drift Tubes   Basic elements of MDTs are thin aluminum tubes with a diameter of approximately $30\,\mathrm{mm}$ filled with a $\mathrm{Ar/CO_2}$ gas mixture at $3\,\mathrm{bar}$ overpressure to increase resolution. A traversing charged particle ionizes the gas and the resulting electrons are collected in the center by a tungsten–rhenium wire anode with $50\,\mathrm{\mu m}$ diameter. The tubes are arranged as chambers that consist of two groups of 3–4 layers of MDTs with the tubes pointing along ϕ, forming tangents to circles arount the beam axis. Besides these regular chambers, sets of chambers with specific designs are installed to recover coverage at e.g. at the detector feet. MDTs determine the track coordinate in the bending plane η. The second coordinate is adopted from the measurement in the non-bending (ϕ) plane of the trigger chamber with matching hits to the MDT chamber.

Cathode Strip Chambers   Conceptually CSCs are multiwire proportional chambers. They consist of a layer of radially oriented anode wires enclosed between two planes forming the cathodes. The distribution of the induced charge on the cathodes created by the ions from the ionization process in the $\mathrm{Ar/CO_2}$ gas mixture is then used as output signal. The cathodes are segmented orthogonally to each other thus both coordinates are measured. A CSC chamber comprises four consecutive layers of CSC planes so there are four independent measurements of η and ϕ for each track. The CSCs are installed in the first layer of each endcap to cover the region $2.0 < |\eta| < 2.7$. Similarly to the MDTs they are arranged as wheels with small and large sectors.

Resistive Plate Chambers   In contrast to the other subsystems RPCs do not use wires as anodes. They operate via a 2 mm gas gap enclosed by two highly resistive plates made of plastic laminate. Movement of charge in the gas induces a signal via capacitive coupling on metallic strips mounted outside the plates. A RPC chamber consists of two units each with two gas volumes and two orthogonal sets of readout strips to provide track information in both coordinates. The RPCs are arranged as three concentric cylinders around the beam to cover the range $|\eta| < 1.05$ and provide six measurements of η and ϕ for triggering.

Thin Gap Chambers   To provide trigger capabilities in the forward region, TGCs have been selected for the range $1.05 < |\eta| < 2.4$. They are multiwire chambers build from a set of anode wires spaced by 1.8 mm enclosed by two sets of plates and filled with a high quenching gas mixture based on CO_2. Radial copper strips outside the plates measure the azimuthal coordinate ϕ while the bending coordinate η is measured by the signals from the wire groups. TGC chambers are arranged as doublets and triplets with two and three gas gaps respectively. These arrangements are installed as four wheels of TGCs in total, one in front of the first tracker layer of the MS and the others before and after the second wheel of MDTs.

3.2.7 Forward Detectors

ATLAS also hosts several forward detector systems [101] that are located tens to hundreds of meters away from the IP. Their primary purpose is to provide luminosity measurements for ATLAS and to study the physics of protons scattered at extremely small angles.

The luminosity determination for ATLAS in Run 2 was performed by LUCID-2 (LUminosity Cherenkov Integrating Detector) [102]. It comprises two modules of photomultiplier tubes around the beam pipe in each forward arm of the ATLAS detector, located about $z = \pm 17$ m away from the IP. Thin quartz windows in the photomultipliers function as Cherenkov medium and radioactive ^{207}Bi coating provides a calibration signal. Hit counts in the detectors are then converted into a visible interaction rate per bunch crossing which is proportional to the instantaneous luminosity.

3.2.8 ATLAS Trigger and Data Acquisition System

As the capabilities for permanent storage are limited, only a fraction of the collision events can be recorded. Main aim of the trigger system is to select those events containing interesting signatures for further study. Due to limited buffer sizes, this requires the decision whether an event should be kept or not, to be made at very short timescales. For that reason only the parts of the detector systems with a short response time can be read out and also only with reduced granularity. For Run 2, ATLAS adopted a two-level trigger system [103]: The level-1 (L1) trigger [104] is implemented on hardware and reduces the event rate from approximately 40 MHz defined by the 25 ns bunch-spacing interval to 100 kHz. Subsequently L1 decisions are refined by the high-level trigger (HLT) [105] using sophisticated software algorithms and reduces the rate to about 1 kHz on average to be written out for permanent storage. The data flow between the elements of the trigger system is handled by the data acquisition system (DAQ). A schematic illustration of the complete trigger system and its components is shown in Figure 3.5. At both trigger levels a large set of different selection logics are
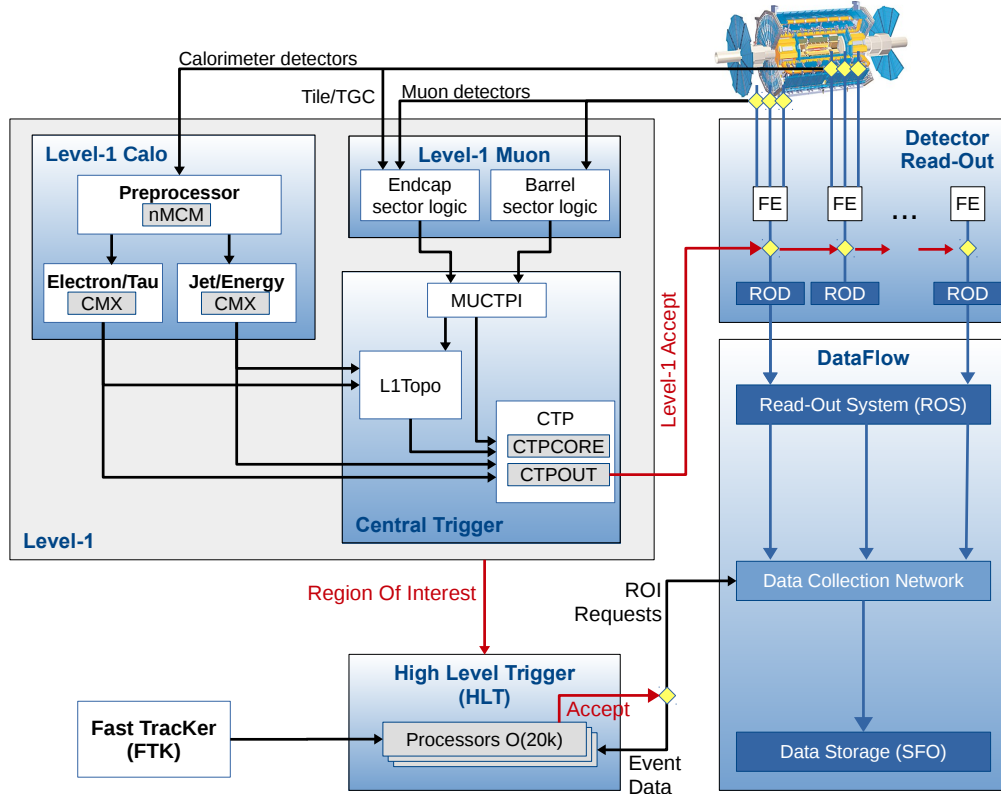
Figure 3.5: Illustration of the data flow from the detector to the data storage controlled by elements of the ATLAS trigger and DAQ system. Figure taken from [103].

implemented, e.g. look-ups for electron and muon signatures with different thresholds on the transverse momentum. The entire set of selection criteria is called trigger menu and is defined to distribute the available output rate so that the different signatures of physics objects are represented in a balanced way. Part of the bandwidth is also reserved for support and calibration triggers, whose events are e.g. used in efficiency measurements (see Chapter 4). In the following the components of the trigger system are described briefly.

Data Acquisition System   The DAQ handles the data flow from the detectors to the mass storage elements. Initially, event data are buffered by memory located in the front-end (FE) electronics of the detector systems until a decision from the L1 trigger is made [71]. On acceptance, the data is transferred from the readout drivers (ROD) via optical fibres to the read-out system and stored in the data collection network [106]. From there events are fed to the HLT to refine the trigger decision and eventually apply additional selection criteria. Events passing this final state are then written out for permanent storage.

Level-1 Trigger   In the L1 trigger system information from the calorimeters (L1 Calo) and the muon trigger chambers (L1 Muon) are processed to make a decision whether the event contains interesting physics signatures or not. The decision has to be made within 2.5 μs after

the associated bunch-crossing to account for the limited buffer sizes of the detector readout systems. The L1 trigger determines areas (in $\Delta\eta \times \Delta\phi$) with promising features called Regions of Interest (ROIs) which are subsequently processed by the HLT.

The L1 Calo scans the calorimeters at reduced granularity (for the most part the so-called trigger towers are of size 0.1×0.1 in $\Delta\eta \times \Delta\phi$) for energy deposits matching to electrons, photons, hadronically decaying τ-leptons and jets, and calculates from those the total and missing transverse energies contained in the events. A series of calibrations and corrections is applied to the energy deposits, e.g. to remove the average contribution from pile-up [107]. Muon candidates in the L1 Muon are built from hits in the RPCs and TGCs by requiring spatial and temporal coincidences between hits provided by the different layers. The transverse momentum of a muon candidate is then estimated by the degree of deviation of the hit pattern expected from a muon with infinite momentum [107]. During Run 2 a new topological trigger system (L1 Topo) was commissioned. It uses the objects defined by L1 Muon and L1 Calo as input to apply topological selections e.g. angular separation or requirements on the invariant mass of trigger objects.

The final L1 decision is made by the central trigger processor (CTP) and is based on the information received from the three L1 trigger systems described above. On acceptance, the L1-accept signal is sent, which triggers the subdetector readout of the whole event.

High Level Trigger The HLT is a computing farm that runs reconstruction algorithms similar to the ones used in the offline analysis to refine the trigger decisions of the L1 trigger. ROIs determined by the L1 triggers are taken as input so that only a subset of the event data has to be unpacked and reconstruction is performed in confined areas of the detector. As information from all detector components at full granularity are available, energy resolution and particle identification[†] are significantly improved at this trigger level. A decision is made within 200 ms and on selection the write-out to permanent storage is triggered.

3.2.9 Reconstruction

After selection by the DAQ the data enter a prompt calibration loop in which they are corrected for instance from detector misalignments to maximize detector and physics performance [108]. In the subsequent reconstruction steps the raw detector data are turned into physical objects to be used in the offline analysis and described by the coordinate system introduced in Section 3.2.2. Several different objects are built:

- Tracks are reconstructed both in the ID and MS. ID tracks are further fed into vertex fitting algorithms to reconstruct primary and secondary vertices.

- Electrons and photons are built from matching energy deposits in the electromagnetic calorimeter with the presence or absence of associated tracks, respectively.

- Jets represent hadronic showers in the calorimeter, which are built by grouping deposits in the calorimeter cells into topological clusters. Jets stemming from the hadronization of b quarks can be identified for instance by exploiting secondary vertex information.

[†] For example tracking information from the ID allows to discriminate electrons from photons.

- Taus that decay hadronically leave distinct signatures such as a narrow shower shape, which renders them distinguishable from jets originating from quarks and gluons.

- Muons are reconstructed by combining information from all subdetectors, but reconstruction algorithms that use only a subset of the detector systems are also available.

The object reconstruction algorithms are not perfect and can be wrong in two distinct ways. On the one hand, a real physical object might not be reconstructed at all, for instance because its signature is not pronounced enough in the detector. The probability to reconstruct an object with a particular algorithm is denoted as reconstruction efficiency and depends on the object's properties (e.g. its momentum) and on the detector region. On the other hand, an object can be falsely reconstructed from a signature in the detector that does not correspond to such an object. These misidentified objects are commonly referred to as *fakes*. In general, the reconstruction schemes are designed to balance the reconstruction efficiency and fake rate.

After the reconstruction step, the data is stored in the primary analysis format, and could in principle be used for analysis. But typically the output is first reduced in size by removing content not relevant for a particular analysis to keep file sizes at a level which allows processing with local computing resources.

3.3 Event Simulation

Besides recording and storing *real* collision data it is also a crucial task to generate simulated events. These are used to model how potential new signals would look in the recorded dataset and allow to design a selection that is sensitive to such signatures. Moreover, it is very common to base estimations of the contributions from SM processes on simulation that are then used for instance as background estimations in searches. Another application is the development of new or optimization of existing reconstruction schemes for physical objects such as muons and electrons. In all these use cases it is essential that the simulated events describe the real data reasonably well, i.e. model the underlying physics and the detector response adequately. The ATLAS simulation chain [109] can be divided into three, subsequent steps:

Event Generation generation of the hard-scattering process and immediate decays.

Detector Simulation interactions of the generated particles with the detector material.

Digitization conversion of energy deposits in the sensitive detector regions to currents and voltages in the readout systems.

The output format is provided in the same form as the output of the DAQ, so that the same trigger and reconstruction algorithms used for real data can be run over the simulated events. The subsequent steps of the data processing to the final input for analysis are then the same for real and simulated events. In addition to the reconstruction output, simulated samples include the history of the interactions between the incoming and outgoing particles in the event generation and simulation referred to as *truth* record. This truth information gives insights into the exact physics content of an event, which is not known in real data.
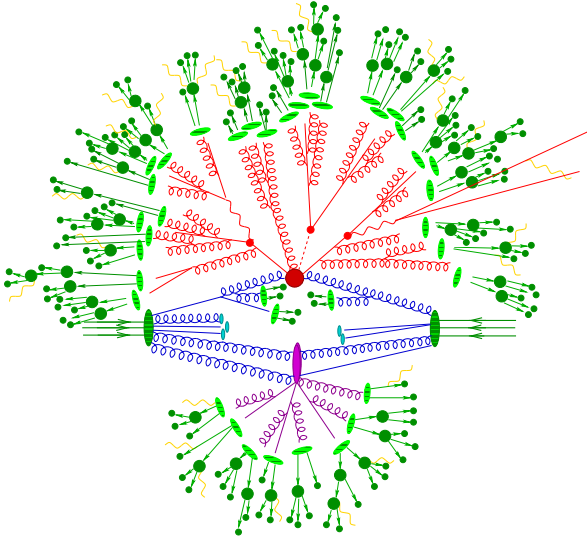
Figure 3.6: Pictorial representation of a $t\bar{t}H$ event. The hard interaction is represented by the dark red central blob. Red blobs indicate the immediate decays of particles produced in the hard-scatter process. Inital- and final state radiation are shown as curly blue and red lines, respectively. Contributions from the underlying event are depicted in purple. The hadronization of final-state partons is represented by the light green ellipses while dark green blobs symbolize hadron decays. QED radiation is shown as yellow lines. Figure adapted from [110].

3.3.1 Event Generation

Hadron–hadron collisions typically involve the production of hundreds of particles with their momenta ranging over many orders of magnitude. While interactions in the hard-scattering process can be calculated perturbatively, this ansatz breaks down at some points in the event evolution when the momentum scale becomes of the order $1\,\text{GeV}$ and the asymptotic freedom renders QCD non-perturbative [111]. Consequently the soft regime cannot be calculated from first principles but has to be modeled. It also has to be taken into account that pp collisions are in fact parton–parton collisions as protons are composite particles. This necessitates to consider the momentum distribution of the partons within the proton via parton distribution functions (PDFs) as well as the interplay of the other partons not participating in the hard interaction. The complications listed above make event generation a complex task which is executed in several steps. Figure 3.6 shows the layout of a complete event, indicating the different elements with a color code.

Most pp collisions are uninteresting in the sense that they contain only a few soft hadrons going out in beam direction. Events of interest usually involve hard scattering processes, i.e. processes with large momentum transfers. Thus the "heart" of an event is formed by two partons a, b hard-scattering into some state X, which can be calculated perturbatively and is shown as a dark red blob in the center of Figure 3.6. The general cross section $\sigma_{ab \to X}$ is a combination of short (parton interaction) and long (parton distribution within the proton) distance behavior and consequently not directly computable in QCD [112]. Instead cross sections use a collinear *factorization* [113] of the short- and long-distance contributions that has the schematic form

$$\sigma_{ab \to X} \sim \sum_{a,b} \int \underbrace{\mathrm{d}x_1 \mathrm{d}x_2 \mathrm{d}\Phi}_{\substack{\text{phase space} \\ \text{integral}}} \underbrace{f_a(x_1, \mu_F) f_b(x_2, \mu_F)}_{\substack{\text{parton distribution} \\ \text{functions}}} \underbrace{\mathrm{d}\hat{\sigma}_{ab \to X}(\mathrm{d}\Phi, \mu_F, \mu_R)}_{\substack{\text{differential parton-level} \\ \text{cross section}}}, \tag{3.4}$$

where $\mathrm{d}\Phi$ is the differential phase space element. The PDFs represent the probability to find a parton with moment fraction x with respect to the parent hadron and depend on

the factorization scale μ_F, which can be understood roughly as the threshold separating the long- and the short-distance behavior. The parton-level cross section depends on μ_F and the renormalization scale μ_R, and is governed by the matrix element (ME) squared $|\mathcal{M}_{ab\to X}|^2$, which can be computed from the Feynman diagrams for the process $ab \to X$. For that reason this step is also referred to as ME-level. The choice for values of μ_F and μ_R is to some extent arbitrary, although the logarithmic structure of QCD defines ranges for reasonable values [111]. Nevertheless, the freedom of choosing exact values for the factorization and renormalization scales represents a common source of systematic uncertainties on the generator predictions. Integrals over the phase space of the initial- and final-state particles are of high dimensionality due to the large number of particles involved. The numerical integration tools of choice are consequently Monte Carlo (MC) based methods as their accuracy scales inverse to the square root of the number of integration points $1/\sqrt{n}$ and is independent of the integral dimension [114]. Thus simulated events are also referred to as MC events†. Decays of short-lived particles such as top quarks and massive electroweak gauge bosons, shown as red blobs in Figure 3.6, are performed at ME level or in the next step, the parton shower.

The ME works very well to describe hard, well separated partons‡, but does not provide information about the structure of the jets that emerge from them. Similar to accelerated electric charges that radiate QED bremsstrahlung, colored partons will emit QCD radiation in the form of gluons. These can radiate further gluons or split into quark–antiquark pairs, leading to the formation of a parton shower. This shower describes the evolution of involved momenta from the scale defined by the hard-scatter interaction down to the infrared scale of order $1\,\text{GeV}$, at which QCD becomes non-perturbative and confinement of the partons into hadrons takes place. In principle the shower evolution corresponds to higher-order corrections to the ME level but a it would not be feasible to calculate a full shower exactly. Instead the evolution is approximated via an iterative procedure keeping only the dominant collinear terms. Two kinds of QCD radiation are added by the shower algorithm, initial state radiation (ISR) and final state radiation (FSR), shown as blue and red curly lines in Figure 3.6, respectively. The former describes radiation originating from the initial partons before their hard interaction and typically adds well-separated and high-energetic jets to the event. The latter originates from partons produced in the hard interaction and typically affect the resulting jet shapes.

There is some potential double-counting among partons added via the ME and by the parton shower. Both approaches are complementary as they have different benefits and drawbacks. Hard, well-resolved partons are described best by exact calculations in the ME while soft, collinear emissions are modeled well by parton showers even for many partons. Consequently partons from the ME and the parton shower have to be combined in a way that resolves the double counting and keeps the better-modeled partons among the two approaches. Several strategies exist that can be roughly separated into two distinct approaches. *Matching* refers to an integration of higher-order corrections to an inclusive process, into the parton shower, which correctly takes into account both real and virtual emissions. *Merging* involves the definition of a merging scale that can be understood as a jet resolution scale. Partons above that scale are generated by the ME and partons below are taken from the shower. Only

---

† MC methods are also used in some of the subsequent steps like the parton shower and hadronization modeling, which also motivates the naming. ‡ The term parton does not necessarily refer to an object within a hadron but is also used as a generic term for quarks and gluons.

real-emission contributions are correctly taken into account above the merging scale.

Additional contributions to the total event structure come from the *underlying event*, shown as purple blob and lines in Figure 3.6. This represents a component of the final state that does not originate from the original hard process and the associated ISR and FSR activity. As the incoming hadrons are complex bound states, more than one pair of partons may interact with each other. These multiple parton interactions are typically $2 \to 2$ scattering processes treatable with perturbative QCD, which produce additional back-to-back jet pairs [9]. Parton shower algorithms then handle the evolution down to the hadronization scale. Overall such contributions are rather soft and often do not lead to additional reconstructible jets. Instead, they increase the overall scattered energy in the event and increase the amounts of particles at hadronization level.

At some point in the parton shower evolution, the involved momenta decrease to the order of $1\,\mathrm{GeV}$, at which the perturbative treatment of QCD breaks down. The transition from the partonic to the actual hadronic final state, known as hadronization, cannot be derived from first principles and has to be described with phenomenological models. Two main hadronization models are currently in use. The *string* model assumes linear confinement as supported by lattice QCD calculations. This means increasing the distance between two color charges by one unit length requires always the same amount of energy [10], similar to stretching an elastic tube. The increasing energy in the strong color field between partons moving away from each other is then picked up by short-ranged $q\bar{q}$ fluctuations of the vacuum and puts the emerging quarks on their mass shell. This cuts the string between the original color charges into two smaller strings with lower total energy. Performing this in a probabilistic and iterative way only $q\bar{q}$ pairs with small relative momenta will be left, which form the final hadrons. *Cluster* models are based on the preconfinement property of parton showers [115]. After the shower evolution, partons group in colorless clusters with a mass distribution independent of the energy scale of the hard interaction. These clusters can be understood as prototypes for the final hadrons with heavy clusters split into lighter ones. If the clusters are light enough they are decayed into hadrons.

Many of the hadrons produced in the hadronization process are unstable resonances. These are decayed into lighter hadrons with a lifetime long enough to reach and interact with the detector material. These decays are represented by the light green ellipses in Figure 3.6.

Electromagnetic radiation, shown as yellow lines in Figure 3.6, can be present at all stages of the event generation where charged particles are involved. Commonly this is modeled by shower algorithms working similar as the parton shower.

Primarily the models to describe the parton shower, underlying event and hadronization introduce a large amount of free parameters that cannot be constrained from theoretical principles. Consequently these have to be derived (*tuned*) by parameter optimization against experimental data [116]. Several tuning approaches are available [117], and a variety of tunes have been derived from early LHC data.

3.3.2 Detector Simulation and Digitization

Generated events are subsequently read into the detector simulation. Particles with a proper lifetime $c\tau > 10\,\mathrm{mm}$ are assumed to propagate far enough to interact with the detector material. Event generators are agnostic to the detector geometry, consequently the decays

of these particles are not handled during the event generation. Instead, they are passed to GEANT4 [118, 119], a toolkit to simulate the passage of particles through matter. The simulation is aware of the detector layout and the involved materials, the presence of external electromagnetic fields and the physics processes that govern particle interactions. Energy deposits in the sensitive regions of the detector ("hits") are recorded in conjunction with their position and time during the simulation, and stored as output. Due to the complex detector geometry and the detailed physics description, a simulation of all detector components by GEANT4, referred to as *full simulation*, is computationally very expensive[†]. To reduce stress on the (limited) computing resources, fast simulation programs are available for applications that are not sensitive to a less accurate detector simulation. By far the most time-consuming step is the simulation of particles traversing the calorimeters. For that reason ATLFAST-II [120] uses GEANT4 only for simulating the ID and MS but FastCaloSim [121] for the calorimeters, which parametrizes electromagnetic and hadronic showers instead of simulating their development.

In the digitization step, the hits are converted into detector responses, i.e. voltages and currents in the readout channels. They are augmented with peculiarities such as detector noise and cross-talk among readout structures to make the detector response as realistic as possible. To account for contributions from in-time and out-of-time pile-up present in real *pp* collisions, the hits originating from the single hard scattering event are overlaid with hits from additional collisions to match the level of pile-up observed in data. These are also generated and passed through the standard simulation framework and include single-, double and non-diffractive components [88]. Other sources of pile-up such as cavern background, beam halo- and gas events are typically not included in the simulation because they can be removed at analysis level.

The detector description used in the simulation, digitization and also reconstruction steps is built from a conditions database that reflects the current status of the ATLAS detector. Therefore the detector simulation is capable to account for changes during data-taking such as changing alignment within a subdetector. In this manner, simulation can be adjusted to properly reflect detector effects present in different periods of data-taking.

[†] Full simulation of an event takes $\mathcal{O}(10^3\,\mathrm{s})$.

# 4 Efficiency Corrections for Low-Momentum Muons

Compressed mass spectra such as introduced in Section 2.3 are characterized by very soft particles in the final state. These are challenging to reconstruct as their signatures may not exceed detection thresholds or are shadowed by the activity of the vast amounts of other particles created in the LHC collisions. Muons leave a comparably clean and unique signature in the detector and can consequently be reconstructed also at low transverse momenta with a reasonable efficiency. Therefore, muons are one of the key ingredients to probe also very small mass splittings between the LSP and the heavier SUSY particles. Despite the very sophisticated generation of simulated events (see Section 3.3), which takes into account as many aspects of *pp* collisions and detector aspects as possible, the simulation is not perfect, i.e. the reconstruction efficiencies of physical objects in simulation will differ to some extent from those in data. For a reliable MC-based signal prediction and background estimation it is therefore essential to correct the reconstruction efficiency in simulation to match the one in data. This necessitates to measure the reconstruction efficiencies in both simulation and data to derive weights for correction, referred to as *scale factors*. After briefly reviewing the reconstruction and identification of muons, this chapter introduces the methodology of the efficiency measurements. In particular the extension towards even lower transverse momenta with respect to the early Run 2 status [122] is highlighted. This extension notably increases the signal acceptance in the analysis presented in Chapter 5 for small mass splittings.

4.1 Muon Reconstruction

As muons are the only directly detectable SM particles that are not stopped within the calorimeters, muon reconstruction [123] can be performed by using only information from the precision (MDTs and CSCs) and trigger (RPCs and TGCs) chambers of the MS, i.e. completely independent from the other subdetectors. Track-building in the MS starts by searching for hit patterns in each muon chamber that form short straight-line tracks, called *muon segments*. Matching hits from segments in different MS layers are then combined to MS track candidates. The hits associated with each candidate are fitted using a global χ^2 fit. In case the χ^2 of the fit fulfills the selection requirements, the track is accepted. By combining the MS measurement with information from the ID and calorimeters, the reconstruction performance can be enhanced. A variety of muon reconstruction algorithms are available, that differ in the subdetectors being used and how the information is combined. Muon candidates are then classified into several muon types that are described in detail in Ref. [122]. Most relevant for the following discussion are

- Combined (CB) muons: hits from both the ID and MS are refitted to form a combined

Figure 4.1: Illustration of the three muon types introduced in the text. The three concentric rings represent the ID, calorimeter and MS, respectively. CB muons are reconstructed by matching tracks in the ID and MS. SA muons rely only on a MS track that has to be loosely compatible with the IP when extrapolated inwards. CT muons are built from an ID track and trajectory in the calorimeter matching to minimal ionizing particle, without using information from the MS.
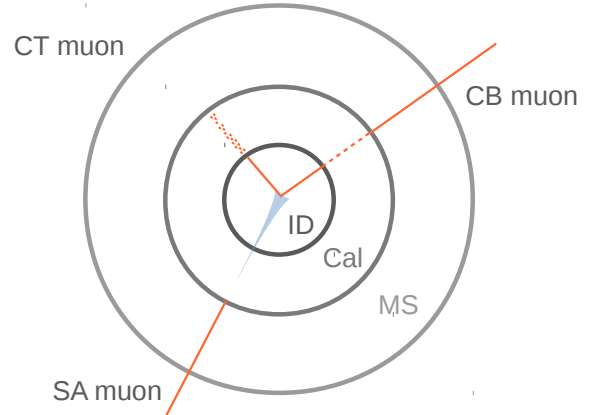
track. Muons are mainly reconstructed via an outside–in approach, that starts from MS tracks, extrapolates them inwards and matches them to an ID track. An inside–out reconstruction is used as a complementary approach. CB muons are the most widely used type in the region $|\eta| < 2.5$, which is covered by the ID.

- Standalone (SA) muons: muon candidates are built from information of the MS only. Tracks in the MS are extrapolated inwards and need to be loosely compatible with the IP (ME muons). This type is mainly used to provide muon reconstruction in the forward region $2.5 < |\eta| < 2.7$.

- Calorimeter-tagged (CT) muons: ID tracks can be identified as a muon if the energy deposits around their extrapolated trajectory in the calorimeters are compatible with a minimal ionizing particle. They are optimized to recover acceptance in detector regions that are only partially instrumented due to cabling and other services, as present in the so called muon *crack* region $|\eta| < 0.1$.

A schematic illustration of the three muon types is depicted in Figure 4.1. All muon types account for the energy loss in the calorimeters, which is either measured or estimated using a parametrization based on MC simulation. The four-vector of a reconstructed muon is given in terms of its coordinates at the IP and takes into account the energy losses.

4.2 Muon Identification

Objects defined as muons by one of the muon types are to a large extent not *prompt* muons, which would originate from the IP, but secondary, nonprompt muons from pion and kaon decays. This necessitates additional quality requirements to suppress background contamination and also ensure a robust momentum measurement. Muons from in-flight decays typically exhibit a distinct "kink"-like signature in their reconstructed track. Consequently, discrimination from fakes is based on variables sensitive to differences in the ID and MS track reconstruction, and on the χ^2 value of the combined track fit. Similarly, a well reconstructed ID track is ensured by requirements on the minimal amount of hits in each ID subsystem [122]. Several working points (WPs) are defined that represent a compromise between the reconstruction efficiency and purity for prompt muons:

- *Medium* muons represent the baseline identification quality and balance reconstruction efficiency and fake/non-prompt contributions. This WP is based on CB muons for $|\eta| < 2.5$ and SA muons for $|\eta| > 2.5$. Muons are required to have hits in at least two precision layers ("stations"), except for $|\eta| < 0.1$ where one-station tracks are allowed to recover acceptance. Loose cuts on the ID–MS momentum compatibility are applied to suppress misidentification from hadron decays.

- *Loose* muons are designed to maximize the reconstruction efficiency while keeping the fake and non-prompt contributions at a reasonable level. With respect to the *Medium* WP it allows one-station tracks up to $|\eta| < 1.3$ if the muon candidate is reconstructed in both approaches, outside–in and inside–out. To increase the reconstruction efficiency in the crack region, other muon types such as CT muons are used for $|\eta| < 0.1$.

- *Tight* muons aim to maximize the purity provided by the identification. With respect to *Medium* muons, tighter requirements on the ID–MS compatibility are applied, in particular at lower transverse momenta where the misidentification probability is higher.

- *Low-p_T* muons are specifically designed to provide a high reconstruction efficiency down to transverse momenta of $3\,\text{GeV}$. The WP is based on CB muons and allows, similarly to the *Loose* WP, one-station MS tracks for $|\eta| < 1.3$. In the range $1.3 < |\eta| < 1.55$ at least two MS stations are required while for $|\eta| > 1.55$ the same selection criteria as for the *Medium* WP are applied. Additional requirements on variables sensitive to in-flight hadron decays suppress the contributions from fake/non-prompt muons [124]. For $p_T > 18\,\text{GeV}$ the selection criteria of the *Medium* WP are applied. Consequently, this selection recovers low-p_T muons in particular in the barrel region with a reasonable increase of the misidentification rate. In the forward regions, *Low-p_T* muons are actually tighter than *Medium* muons, leading to slightly smaller reconstruction efficiencies for large $|\eta|$.

- *High-p_T* muons ensure good momentum resolution for transverse momenta up to $\mathcal{O}(\text{TeV})$ by requiring hits in three MS stations, while geometrical vetoes avoid detector regions that suffer from large alignment uncertainties. Naturally, this WP is not considered in the following discussion of measurements for low-p_T muons and is mentioned here only for completeness.

The *Loose*, *Medium* and *Tight* WPs are inclusive, i.e. a *Tight* muon automatically satisfies the identification criteria of the *Loose* and *Medium* WPs. Reconstruction efficiencies clearly depend on the p_T and η of the muons, but are typically well above $90\,\%^\dagger$ with a misidentification rate of hadrons at the per-mille level [122].

4.3 Muon Reconstruction Efficiency Measurements

The presented reconstruction efficiency measurements have been performed for the *Loose*, *Medium*, *Tight* and *Low-p_T* WPs in the region $|\eta| < 2.5$ and the transverse momentum range 3–$20\,\text{GeV}$. The measurement employs an established tag-and-probe method using $J/\Psi \to \mu\mu$

---

† Exceptions are the low-p_T range 3–$5\,\text{GeV}$ and for the *High-p_T* WP, where the reconstruction efficiencies are smaller.

decays [125], which is rich in muons carrying momentum in the range of interest. By requiring a well-reconstructed muon (tag) and an additional isolated track (probe) whose muon–track invariant mass is compatible with the J/Ψ mass, a sample very pure in $J/\Psi \to \mu\mu$ events can be selected. After the background contamination is taken into account, the reconstruction efficiency can then be derived from the number of probes that can be associated with a reconstructed muon. The efficiencies are measured using the full ATLAS Run 2 dataset (see Section 5.1.1) corresponding to $139\,\mathrm{fb}^{-1}$ of pp collision data, recorded during 2015–2018 at a center-of-mass energy of $\sqrt{s} = 13\,\mathrm{TeV}$ at the LHC. To compare the measured efficiencies with efficiencies in simulation, a $J/\Psi \to \mu\mu$ sample has been generated at leading order (LO) with PYTHIA 8.210 [126] using the A14 tune [127] and the CTEQ6L1 [128] PDF set, complemented with PHOTOS 3.52 [129] to simulate QED corrections of the final state. Requirements at generator level on the transverse momentum and on the pseudorapidity of one muon ($p_\mathrm{T} > 6\,\mathrm{GeV}, |\eta| < 2.5$) enhance the statistics of the sample in the relevant phase space. To simulate the effect of pile-up, additional pp collisions have been generated and overlaid on each hard-scatter event.

4.3.1 Measurement Strategy

The total reconstruction efficiency for muons reconstructed using information from both the ID and MS can be factorized into three parts: the reconstruction efficiency in the ID for the muon track, the reconstruction efficiency in the MS, and the matching efficiency between the ID and MS measurements. The tag-and-probe methodology outlined above is either sensitive to the ID reconstruction or to the combined MS and matching efficiency, depending on the probe type. As track reconstruction is performed independently in the ID and MS, the ID efficiency can be measured by *MS probes* formed by ME muons. The combined MS and matching efficiency is measured by *ID probes* formed by isolated ID tracks that fulfill the same requirements as used in the muon identification. ID probes suffer from a large combinatorial background contamination due to random tracks that satisfy the J/Ψ mass hypothesis with the tag muon. For that reason, this part of the efficiency measurements uses a second probe type labeled as *CT probes*, which is significantly purer in muons. CT probes are formed by CT muons and are thus a subset of ID probes. The calo-tagging algorithm [130] does not utilize information from the MS, which allows the usage of CT muons to measure the MS and matching efficiency. As calo-tagging is only implemented for transverse momenta above $5\,\mathrm{GeV}$, the measurements at very low p_T rely necessarily on ID probes.

In summary, the total reconstruction efficiency of a WP X, $\epsilon(\mathrm{X})$, can be written (using Bayes' theorem) as product of the efficiency that the muon is reconstructed in the ID, $\epsilon(\mathrm{ID})$, and the efficiency that the muon passes the selection criteria of X, given it was reconstructed in the ID $\epsilon(\mathrm{X|ID})$

$$\epsilon(\mathrm{X}) = \epsilon(\mathrm{X|ID}) \cdot \epsilon(\mathrm{ID})\,. \tag{4.1}$$

Assuming that the track reconstruction in the ID is independent from the presence (or absence) of a MS track, i.e. $\epsilon(\mathrm{ID}) = \epsilon(\mathrm{ID|MS})$, the total reconstruction efficiency is given by

$$\epsilon(\mathrm{X}) = \epsilon(\mathrm{X|ID}) \cdot \epsilon(\mathrm{ID|MS})\,. \tag{4.2}$$

Probe Type	Trigger Type	Identifiers
ID/CT Probes	Muon+Track	HLT_muX_bJpsi_Trkloose, X = 4,8,10,18
		HLT_muX_bJpsi_TrkPEB, X = 4,8,10,11,14,20
	Single-Muon	HLT_mu4, HLT_mu6, HLT_mu6_idperf
MS Probes	Di-Muon	HLT_mu4_mu4_idperf_bJpsimumu_noid

Table 4.1: Triggers used to select ID/CT and MS tag-and-probe pairs.

Under the assumption that calo-tagging does not influence the MS reconstruction and matching efficiency, for CT probes the total reconstruction efficiency becomes

$$\epsilon(\mathrm{X}) = \epsilon(\mathrm{X}|\mathrm{CT}) \cdot \epsilon(\mathrm{ID}|\mathrm{MS}) . \tag{4.3}$$

Consequently, the measurement is performed in two independent steps represented by the two factors in Equations (4.2) and (4.3): measuring the reconstruction efficiencies in the ID using MS probes and measuring the MS reconstruction and matching efficiency using ID/CT probes. The measurement for the *Loose* WP has to be split between the non-calo-tagged and the CT muon component, as the usage of CT probes for the latter would bias the measurement. Instead, the calo-tagging efficiency is measured with MS probes.

The deviation of the efficiencies measured in data $\epsilon^{\mathrm{Data}}(\mathrm{X})$ and MC simulation $\epsilon^{\mathrm{MC}}(\mathrm{X})$ is quantified by their ratio and denoted as efficiency scale factor

$$\mathrm{SF} = \frac{\epsilon^{\mathrm{Data}}(\mathrm{X})}{\epsilon^{\mathrm{MC}}(\mathrm{X})} . \tag{4.4}$$

The scale factors and their associated uncertainties are then used by physics analysis groups to correct the simulation to match the real detector behavior. To account for effects that may change during the course of data-taking, such as the degree of misalignment and pile-up conditions, the efficiencies (and scale factors) have been derived separately for each year of Run 2. Consequently there are four sets of measured efficiencies for each identification WP.

4.3.2 Selection Criteria

Events to measure the reconstruction efficiency with respect to an ID track or CT muon are mainly selected by dedicated combined muon+track triggers, that require the presence of an HLT muon and a track whose invariant mass lies within a window around the J/Ψ mass. The triggers share the same requirement on the track p_{T} of 3.5 GeV, but differ in the requirement on the trigger muon p_{T}, ranging from 4–18 GeV as shown in Table 4.1, to provide enough statistics also at larger muon momenta. During 2017 data-taking these triggers have been replaced with variants based on partial event building (PEB) [131]. With PEB, the detector is only read out within a cone of $\Delta R = 0.75$ around the HLT muon, which reduces the event size[†].

[†] The reconstruction efficiency measurement does not rely on any global variable such as the missing transverse momentum and is thus not affected by PEB.

Consequently, more events can be stored at the same data rate, which enhances the statistics available for the measurements. While the thresholds for the muon transverse momenta are mostly identical to the non-PEB triggers, the requirement on the track p_T increases with the muon p_T threshold. Due to an issue in the PEB algorithm (no information from the CSCs has been written out), which was fixed in early 2018, probes with $|\eta| > 2.0$ cannot be used in the affected period. This results in larger statistical uncertainties on the efficiencies for the forward region, in particular for the 2017 dataset. To maximize statistics, events selected by single-muon triggers are also added to the tag-and-probe sample. Tag-and-probe pairs to measure the ID efficiency relative to MS probes are built from events selected by a di-muon trigger with a 4 GeV threshold for each leg, that uses only information from the MS in order not to bias the measurement.

The tag muon must be of *Medium* quality and trigger the readout of the event. This is ensured by requiring a trigger object associated with the trigger around the tag within a cone of size $\Delta R = 0.005$. To match the cuts at MC generator level, only tags with $p_T > 6$ GeV and $|\eta| < 2.5$ are accepted.

Tag and probe are required to be oppositely charged and their invariant mass must be between 2.7 and 3.5 GeV. A cut on the difference of the longitudinal impact parameter z_0 between tag and probe $|z_0^{\text{tag}} - z_0^{\text{probe}}| < 5$ mm suppresses contributions from background tracks and non-prompt muons. To avoid low-momentum tracks sharing the same trigger ROI due to their strong curvature, the positions of the tag and probe tracks have to be at least $\Delta R = 0.2$ apart when extrapolated to the MS trigger surfaces.

4.3.3 Maximum-Likelihood Fit

To derive the reconstruction efficiency, the tag-and-probe pairs are divided into two statistically independent samples, labeled as *matched* and *unmatched*, depending on whether the probe can be matched to an object whose efficiency is being measured (either a muon satisfying a particular WP or an ID track) or not. A $\Delta R < 0.005$ requirement between the probe and the object serves as matching criterion. The distribution of the invariant mass of the tag-and-probe pair $m_{\text{t-p}}$, is then parametrized as the sum of a signal component S — corresponding to real $J/\Psi \rightarrow \mu\mu$ events — modeled with a Crystal Ball function (see Appendix A.1) and a background component B modeled with a first-order polynomial. The signal component in the distribution of the matched probes $f_M(m_{\text{t-p}})$ is proportional to the efficiency ϵ, while in the distribution of the unmatched probes $f_U(m_{\text{t-p}})$ it is proportional to $1 - \epsilon$. The efficiency is then derived by performing a simultaneous extended maximum-likelihood fit on both distributions using

$$
\begin{aligned}
f_M(m_{\text{t-p}}) &= \epsilon \, S(m_{\text{t-p}}, \boldsymbol{\theta_S}) + B(m_{\text{t-p}}, \boldsymbol{\theta_B}) \, , \\
f_U(m_{\text{t-p}}) &= (1 - \epsilon) \, S(m_{\text{t-p}}, \boldsymbol{\theta_S}) + B(m_{\text{t-p}}, \hat{\boldsymbol{\theta}}_B) \, ,
\end{aligned} \tag{4.5}
$$

to model the line shapes and Poisson terms to describe the number of matched and unmatched signal and background events. The set of signal parameters $\boldsymbol{\theta_S}$ (four parameters of the Crystal Ball function) is the same for the matched and unmatched parameterizations, as they are assumed to be strongly correlated in the two samples. This is not the case for the background, for which the composition may differ in the two samples, hence two distinct
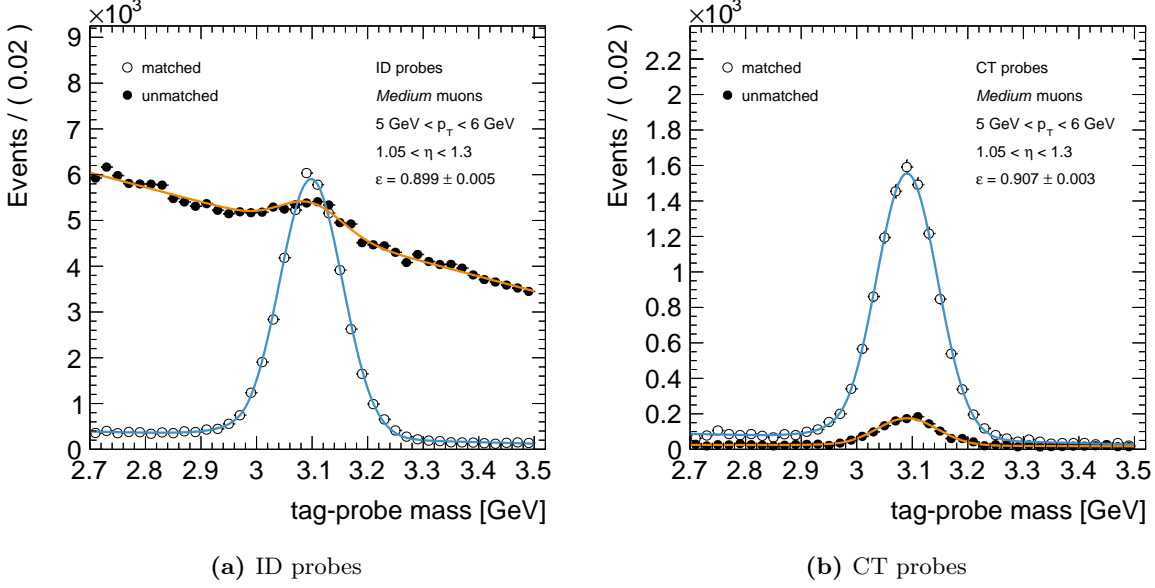
(a) ID probes   **(b)** CT probes

Figure 4.2: Example fit results for the matched (empty circles) and unmatched (full circles) tag-and-probe mass distributions to derive the reconstruction efficiency for the *Medium* WP using 2018 data. The plots show (a) ID probes and (b) CT probes with $5\,\text{GeV} < p_\text{T} < 6\,\text{GeV}$ in the region $1.05 < \eta < 1.3$. The measured efficiency ϵ is shown in the label of each plot.

background parameter sets $\boldsymbol{\theta_B}$ and $\boldsymbol{\hat{\theta}_B}$ are used. The uncertainty on the parameter ϵ after the fit is taken as statistical uncertainty on the efficiency.

The reconstruction efficiencies depend on the momentum of the muon and in which region of the detector it was reconstructed. To account for this, the tag-and-probe pairs are split into nine η bins that reflect the detector geometry

$$\eta : [-2.5, -2.0, -1.3, -1.05, -0.1, 0.1, 1.05, 1.3, 2.0.2.5]\,,$$

where the threshold $|\eta| = 0.1$ marks the crack region, while $|\eta| = 1.05$ and $|\eta| = 2.0$ represent the end of instrumentalization with RPCs and the start of the CSCs, respectively. As the calorimeter is thickest just before $|\eta| = 1.3$, this region is also a separate bin. In addition, there are 10 p_T bins

$$p_\text{T} : [3.0, 3.5, 4.0, 5, 6, 7, 8, 10, 12, 15, 20]\,\text{GeV}\,,$$

in which the efficiency is approximately constant. At low transverse momenta the efficiency varies strongly with p_T while it is more stable at larger momenta. For that reason the binning is not equidistant but finer at low and coarser at large p_T. In total, the measurement is performed in 90 η–p_T bins. As the reconstruction efficiency differs slightly between the large and the small sectors (see Appendix A.2), a parameterization also in ϕ would be desirable. However, the available tag-and-probe statistics does not allow for a more fine-grained measurement. The dependence on η and p_T is more pronounced than the dependence on ϕ, hence the efficiencies are parametrized in the former quantities. Furthermore, the modeling of the

(a) MS Probes Barrel
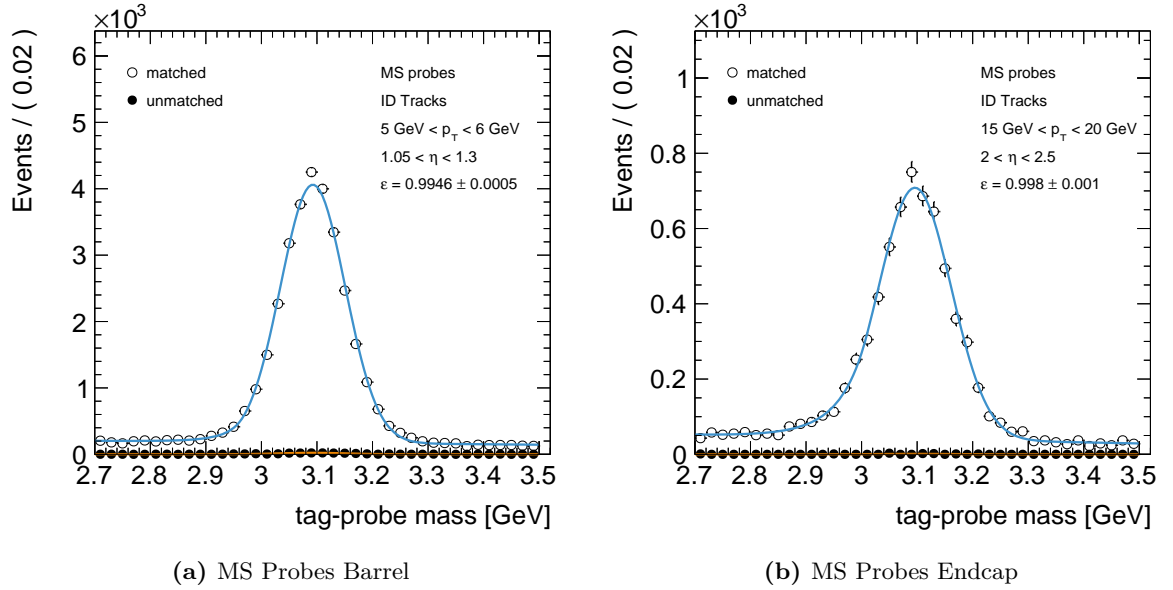
(b) MS Probes Endcap

Figure 4.3: Example fit results for the matched (empty circles) and unmatched (full circles) tag-and-probe mass distributions to derive the reconstruction efficiency for ID tracks using 2018 data. The plots show MS probes in the region (a) $1.05 < \eta < 1.3$ with $5\,\mathrm{GeV} < p_\mathrm{T} < 6\,\mathrm{GeV}$ and (b) $2 < \eta < 2.5$ with $15\,\mathrm{GeV} < p_\mathrm{T} < 20\,\mathrm{GeV}$. The measured efficiency ϵ is shown in the label of each plot.

efficiencies in simulation with respect to data in the large and small sectors is similar, so their ϕ-dependence is mitigated to a large extent in the scale factors.

Figure 4.2 shows representatives for the fits of matched and unmatched distributions of ID and CT probes with respect to *Medium* muons and the resulting efficiencies, which correspond to the $\epsilon(\mathrm{X|ID})$ and $\epsilon(\mathrm{X|CT})$ part in Equation (4.2) and Equation (4.3), respectively. While the measured efficiencies are compatible for both probe types, it is clearly visible that the level of background contamination is much larger for ID than for CT probes. Consequently, the efficiency measurements suffer from larger systematic uncertainties when ID probes are used, in particular due to the uncertainty on the background modeling. For that reason, the first part of the reconstruction efficiency measurement, $\epsilon(\mathrm{X|ID/CT})$, is performed with CT probes down to $5\,\mathrm{GeV}$, the reconstruction threshold of the calo-tagging algorithm, and with ID probes for lower transverse momenta.

Examples for the measurement of the second part of the total muon reconstruction efficiency, the ID efficiency $\epsilon(\mathrm{ID|MS})$, are shown in Figure 4.3. The efficiencies are shown for two representative η-p_T bins, with Figure 4.3a illustrating low-p_T MS probes in the central region while Figure 4.3b represents MS probes in the forward direction with larger p_T. In both cases MS probes are nearly background-free, enabling a very clean measurement. The track reconstruction efficiency is well above $99\,\%$ over the p_T spectrum covered by the measurement and hence represents only a small correction to the combined MS and matching efficiency.
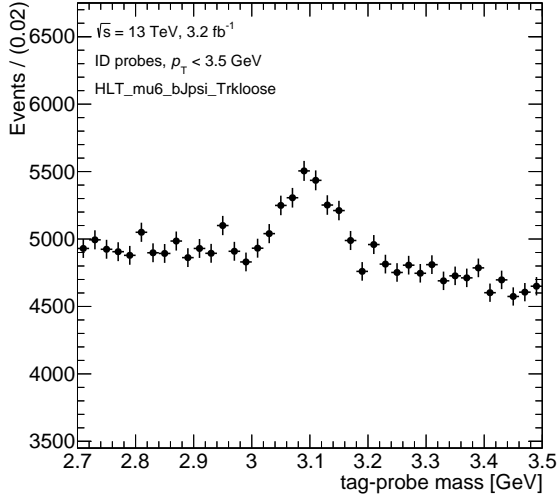
Figure 4.4: Distribution of the tag-and-probe mass using ID probes with $p_T < 3.5\,\text{GeV}$. The associated events have been selected by the trigger HLT_mu6_bJpsi_Trkloose during 2015 data-taking.

4.3.4 Extension Towards Very Low Transverse Momenta

To extend the efficiency measurements from 5 down to $3\,\text{GeV}$ with respect to the measurements performed in the early stages of Run 2, limitations set by the triggers to select the tag-and-probe pairs need to be taken into account. The muon+track triggers require a track p_T of at least $3.5\,\text{GeV}$ which indicates the absence of ID probes below that threshold. Likewise, the di-muon trigger requires the trigger muons to have transverse momenta above $4\,\text{GeV}$, which limits the measurement of the ID track reconstruction efficiency to that value.

Nevertheless, the muon+track triggers do also select tag-and-probe pairs with probe p_T below the track p_T threshold, given there is a random, "spectator" track that fulfills the J/Ψ mass hypotheses when matched with the tag muon. After the event was written out, the algorithm that builds the tag-and-probe pairs does not only consider the track that fired the trigger but can also build a pair with the correct track of the second J/Ψ muon. As illustration, Figure 4.4 shows the $m_{\text{t-p}}$ distribution of tag-and-probe pairs with probe $p_T < 3.5\,\text{GeV}$ selected by the trigger HLT_mu6_bJpsi_Trkloose in 2015 data. The peak originating from $J/\Psi \to \mu\mu$ events is clearly present, although the level of background is relatively large. Comparisons of the kinematic distributions of such indirectly triggered probes in data and simulation did not reveal any potential bias to be introduced in the measurement. Hence it was concluded that these ID probes are suitable to be used to extend the efficiency measurement to very low p_T.

The effect that tag-and-probe pairs can be triggered by spectator tracks is also present for MS probes but to a much lesser extent. As the MS is much less busy in terms of track multiplicity than the ID, the probability of a random track being compatible with the J/Ψ when matched to the tag is greatly reduced. Consequently, the available MS probe statistics below $4\,\text{GeV}$ does not allow to extend the measurement. As indicated in Figure 4.5, the efficiency of the ID track reconstruction is rather stable across the p_T range. This motivates the assumption that the efficiency between 3 and $4\,\text{GeV}$ should not differ too much from the efficiency in the higher p_T bins. The ID efficiencies are consequently extrapolated to

Figure 4.5: Efficiency of ID track reconstruction measured with MS probes in the region $1.3 < \eta < 2.0$. The efficiencies as measured in simulated $J/\Psi \to \mu\mu$ events are shown as red empty dots and are compared to the efficiency calculated with truth information. The pile-up distribution in the MC sample used was reweighted to match the distribution observed in 2017 data. The lowest three measured p_T bins in MC are identical, which represents the extrapolation of the ID efficiency as discussed in the text. The red error band represents only the statistical uncertainty.
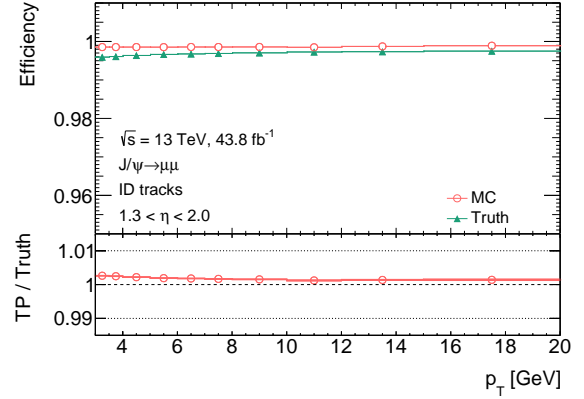
the bins below $4\,\mathrm{GeV}$ by taking the efficiencies from the 4–5 GeV bins, the lowest p_T bins in which the ID efficiency can be measured reliably. To validate this assumption, the measured and extrapolated efficiencies in simulation are compared to the truth efficiencies. These are derived by matching tracks on truth level to reconstructed tracks from simulation with a ΔR criterion. The truth efficiency is then simply calculated by dividing the number of matched by the number of all truth tracks. A comparison of the measured efficiencies in MC and the associated truth efficiencies is shown in Figure 4.5 for a representative η-bin. Even at very low p_T, the ID truth efficiency decreases only slightly and the value of the third lowest p_T bin represents an adequate proxy. To account for the small deviations, an uncertainty on the ID extrapolation is assigned as discussed in the next section.

In order to remove the limitations for the measurements set on trigger level, dedicated triggers have been requested for the trigger menu during 2017 and at the start of 2018 data-taking. These triggers have a requirement of $2\,\mathrm{GeV}$ for the track and the second muon, respectively, and thus provide ID and MS probes at very low p_T with adequate statistics. For the iteration of the measurement presented here, events selected by these triggers were however not yet available. Any further extension of the measurements to even lower p_T will be very challenging even with these triggers, as such muons will barely reach the MS. For a $10\,\mathrm{GeV}$ muon the most probable value for the energy loss in the calorimeters is around $3\,\mathrm{GeV}$ [132], which motivates to consider this value as a reasonable threshold for a reliable muon reconstruction.

4.3.5 Systematic Uncertainties

In addition to the statistical uncertainty which is taken from the maximum likelihood fit, the measurement procedure introduces several sources of systematic uncertainties on the measured efficiencies. For the final uncertainties on the scale factors, these are added in quadrature to the statistical uncertainty.

Signal and Background Modeling To estimate the uncertainty on the signal and background modeling, the functions that parametrize S and B in Equation (4.5) have been varied independently from each other. The fit is repeated with the alternative function choices, and the difference in the efficiency with respect to the nominal fit configuration is taken as
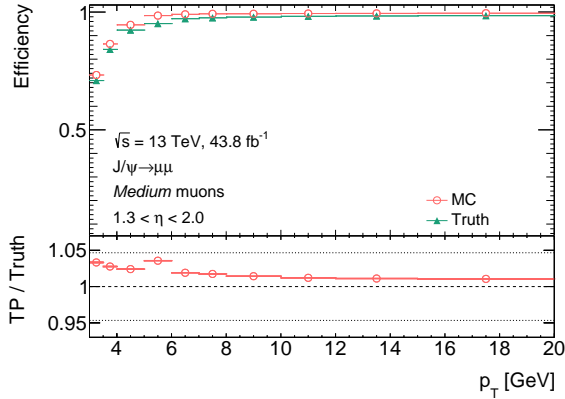
Figure 4.6: Comparison of the reconstruction efficiencies measured with simulated $J/\Psi \to \mu\mu$ events and the truth efficiencies for *Medium* muons in the range $1.3 < \eta < 2.0$. The pile-up distribution in the MC sample used was reweighted to match the distribution observed in 2017 data. The efficiency below $5\,\text{GeV}$ is measured using ID probes, above using CT probes. The red error band represents only the statistical uncertainty.

uncertainty. The impact of the signal modeling is estimated by replacing the Crystal Ball function with a convolution of Gaussian and exponential functions, while keeping the first-order polynomial to model the background. Likewise the first-order polynomial is replaced by an exponential function to estimate the impact of the background modeling. The signal modeling uncertainty from the choice of the fit function is found to be mostly negligible. The impact of the background modeling on the efficiencies is small for CT probes, while it is notably larger (see Figure 4.8) for ID probes as these suffer from a significant background contamination.

Truth Closure A comparison of the measured reconstruction efficiencies in simulation with the associated truth efficiencies enables to check if the measurement selection and procedure is unbiased. This is referred to as "truth closure". As shown in Figure 4.6, for $p_\text{T} > 5\,\text{GeV}$ a roughly constant offset of up to $2\,\%$ (up to $5\,\%$ in the muon crack region) with respect to the truth efficiencies is present. If ID probes instead of CT probes are used for the measurement in this momentum range ($p_\text{T} > 5\,\text{GeV}$), the offset nearly vanishes. Thus the calo-tagging introduces some slight bias in the measurement. The absence of this bias when ID probes are used indicates that the origin is a correlation between a successful match between the ID and MS measurements and the result of the calo-tagging algorithm: Assuming a large energy loss in the calorimeters of the muon, the compatibility of the ID and MS measurement will be reduced, as well as the probability of a reconstruction as CT muon. The discrepancies that appear below $5\,\text{GeV}$, where ID probes are used for the measurement, are not fully understood yet. These may be related to the strong p_T-dependence of the efficiencies at low momenta; a behavior that might not be ideally reflected in the current measurement, e.g. by the binning used. In both cases, a potential bias is present in both the data and MC efficiencies, consequently its impact will cancel out in the scale factors to some extend. To cover any potential difference in the bias between data and simulation, an uncertainty is added to the scale factors corresponding to half the difference between the measured MC efficiencies and truth efficiencies.

ID Efficiency Extrapolation As the efficiencies of the ID track reconstruction below $4\,\text{GeV}$ are not measured but extrapolated, an uncertainty of $0.5\,\%$ on this extrapolation is assigned

to the scale factors. This uncertainty covers well the observed differences of the truth ID efficiencies in the very low p_T regime as shown in Figure 4.5 and does not affect p_T-bins above 4 GeV.

4.4 Muon Reconstruction Efficiencies

The total reconstruction efficiencies are shown representatively for 2016 data in Figure 4.7 for the *Medium* and *Low-p_T* identification WPs. These illustrate a set of characteristics of the muon reconstruction at low transverse momenta:

- Already at moderately large p_T such as 6–7 GeV, the reconstruction efficiency is above 98 % in all detector regions except the muon crack region. The partial instrumentalization with MS chambers required to allow for cabling and other supply structures, results in a notable drop of the reconstruction efficiency.

- In the muon crack region, the reconstruction efficiency first increases with p_T as expected, but then decreases with p_T. This effect originates from the bending of the muon tracks. In case of low momenta, the track curvature is large so that if the muon was emitted originally into a non-instrumented region, its trajectory may bend into a region covered by MS chambers. With increasing p_T the track curvature gets more straight, so that this is less likely going to happen.

- For low transverse momenta, the reconstruction efficiencies are larger in the forward than in the central region. In contrast to central muons, muons in the forward direction can have a significant longitudinal contribution to the total momentum. Thus despite their low transverse momentum, those muons can leave a cleaner and easier to reconstruct signature in the detector.

- The efficiencies are lowest in the range $1.05 < |\eta| < 1.3$, where the calorimeter is thickest.

The efficiencies in data and simulation agree in most cases within 1 %, except at very low p_T, where discrepancies up to roughly 20 % arise, and in the crack region. As stated in Section 4.2, the *Low-p_T* WP recovers muon acceptance in the central region with respect to the *Medium* WP. The efficiencies for all years of data-taking as well as for the other identification WPs are presented in Appendix A.3.

A breakdown of the associated systematic uncertainties on the scale factors is shown in Figure 4.8. The total uncertainties range from approximately 10 % for $p_T < 5$ GeV to 1–2 % at larger transverse momenta. At low p_T, the dominating uncertainty is the limited statistics in the data sample, while at large p_T the total uncertainty is nearly exclusively driven by the truth closure. The large background contamination present in ID probes results in a notable uncertainty on the background modeling, whereas this uncertainty becomes negligible for $p_T > 5$ GeV, as CT probes are used in that regime. The uncertainties on the MC statistics, the extrapolation of the ID efficiency and the signal modeling are negligible almost everywhere.
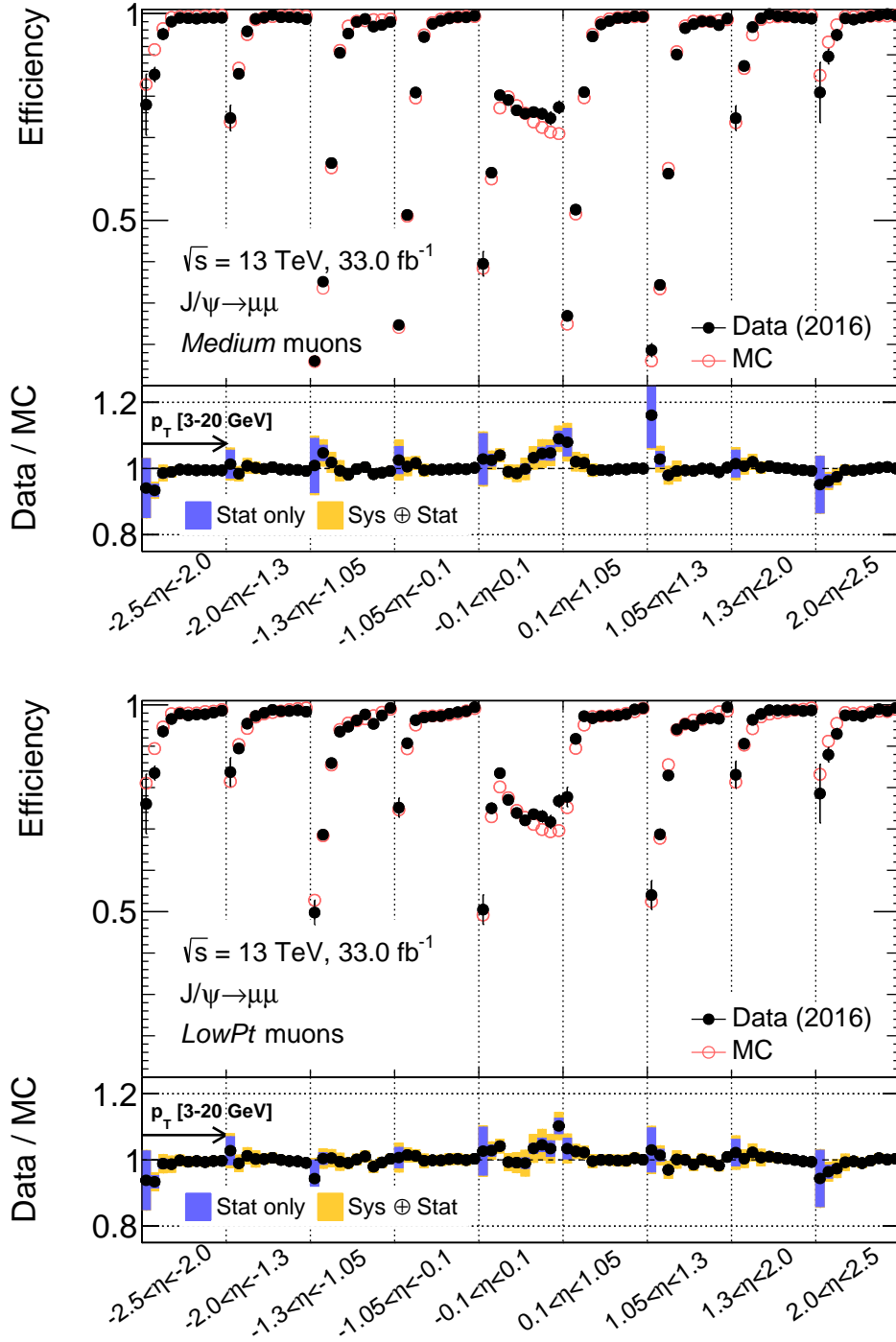
Figure 4.7: Muon reconstruction efficiencies for *Medium* (top) and *Low-p_T* (bottom) muons in 2016 data and simulation as a function of the muon pseudorapidity η and transverse momentum p_T. The nine segments represent the nine individual η-bins. The markers in a segment show the efficiencies in the associated p_T-bins. The bottom panel shows the efficiency scale factors with statistical uncertainties indicated as blue and the sum of statistical and systematic uncertainties as orange band.

4.5 Summary

In conjunction with reconstruction and isolation† efficiency measurements using $Z \to \mu\mu$ decays [133, 134], the derived corrections allow the use of muons in analyses over a wide p_T spectrum. The extension towards transverse momenta of $3\,\text{GeV}$ is beneficial in particular for analyses that expect soft leptons in the final state, as in the search for SUSY in compressed mass spectra presented in Chapter 5. In case the mass differences between the SUSY states become smaller, the lepton p_T spectrum becomes softer. Consequently, signal acceptance can be recovered when muons also with very low p_T can be used. Appendix A.4 contains a rough estimation of the sensitivity gain in the search for higgsinos. Mass splittings slightly below $2\,\text{GeV}$ can be probed, which represents an improvement of about half a GeV with respect to an analysis that can only rely on muons with transverse momenta above $5\,\text{GeV}$. This sensitivity gain originates in the increase in signal acceptance by roughly a factor 3 at preselection level of the analysis (see Section 5.3.5), when including muons with p_T between 3 and $5\,\text{GeV}$ for a signal point representing a higgsino mass splitting of $2\,\text{GeV}$.

---

† Analyses consider typically only muons that fulfill a set of isolation criteria, which necessitates to correct the isolation efficiency in simulation to match the one in data.
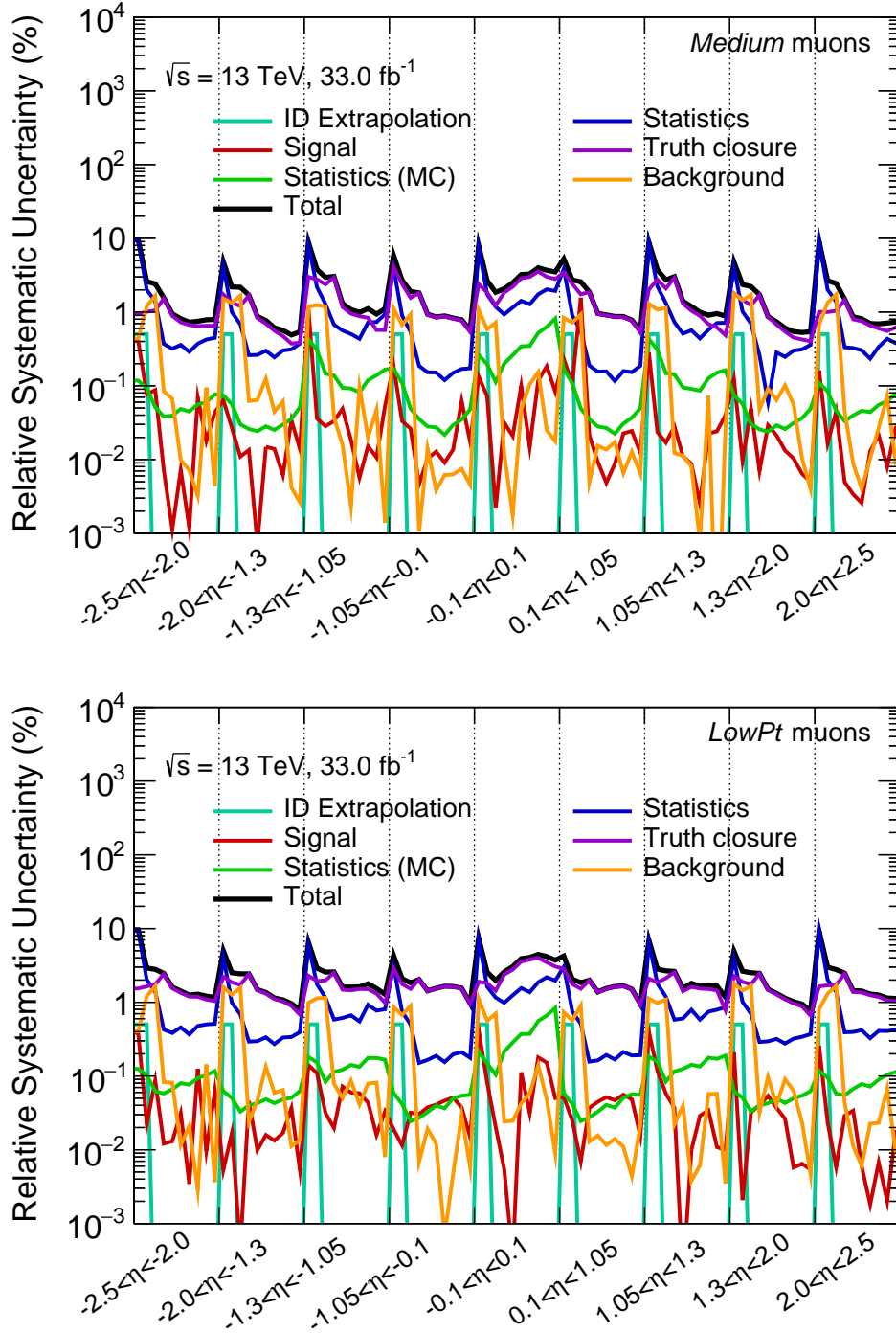
Figure 4.8: Breakdown of the systematic uncertainties on the scale factors for *Medium* (top) and *Low-p_T* (bottom) muons derived in 2016 data as function of the muon pseudorapidity η and transverse momentum p_T (within the η-bins). The nine segments represent the nine individual η-bins. The lines in a segment show the values of the uncertainties across the associated p_T-bins. The lines are only a guidance and do not indicate a interpolation between the individual p_T-bins.

5 Analysis

Despite new constraints from the ongoing effort of analyzing the LHC Run 2 datasets, compressed mass spectra remain promising scenarios in the search for physics beyond the SM. Their final states are characterized by low-energetic, "soft" objects that are challenging to reconstruct, which necessitates special treatments in e.g. the trigger and background estimation strategies. The analysis presented in this thesis considers final states with two soft leptons, hadronic activity from ISR and missing transverse momentum. Preliminary results of the search have already been published [135]. Some aspects of the analysis have been refined for the still to be published final results. These refinements are pointed out and their impact on the search is described in the corresponding sections.

5.1 Overview

The subsequent sections set the scene in which the analysis was performed. First, the Run 2 dataset and its characteristics are described, followed by an introduction to the benchmark models used to design and optimize the analysis, and the relevant background processes. Afterwards the existing constraints from previous searches on such compressed scenarios are summarized.

5.1.1 Run 2 Dataset

The data used in this thesis have been recorded during Run 2 of the LHC that took place between 2015 and 2018. In the four years of data-taking a total integrated luminosity of $148.5\,\mathrm{fb}^{-1}$ was recorded with an average data-taking efficiency[†] of $94.2\,\%$ [136]. The amount of data taken per year steadily increased during Run 2 as shown in Figure 5.1a. Beam conditions evolved notably over the years as can be seen from pile-up sensitive variables such as the mean number of inelastic pp interactions per bunch-crossing μ. Averaging μ over all colliding bunches is denoted as the average number of interactions per bunch-crossing $\langle\mu\rangle$ and is commonly used to quantify the level of pile-up. Over the years pile-up conditions became more challenging as shown by the individual distributions of $\langle\mu\rangle$ in Figure 5.1b. During 2015, the average over the year was $\langle\mu\rangle = 13.4$, while it was $\langle\mu\rangle = 34.2$ in 2018, meaning the pile-up conditions became more and more demanding in the course of data-taking.

The characteristic second peak in the $\langle\mu\rangle$ distribution present in 2017 data around 60 originates from the application of luminosity leveling during data-taking. Due to beam losses induced by problems in one of the LHC sectors [137] the default bunch filling scheme, utilizing a continuous train of up to 2544 colliding bunch pairs spaced by $25\,\mathrm{ns}$, was replaced by an alternative scheme named *8b4e* (train of eight bunches, separated by $25\,\mathrm{ns}$) [138]. To

---

[†] inefficiencies arise for example due to the ramp up of high voltage ("warm start") or dead time of subdetectors
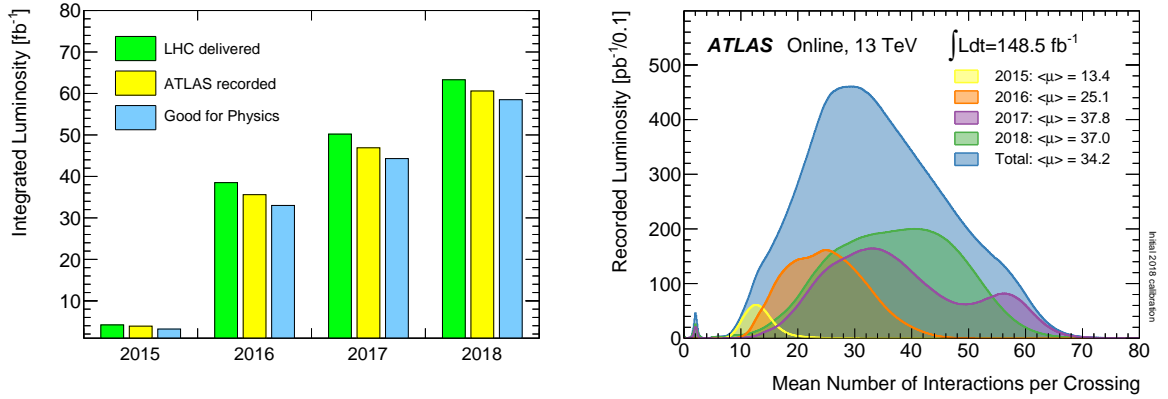
(a) Dataset of Run 2 split into each year of data-taking. The delivered and recorded luminosities are shown as well as the size of the dataset flagged as good for analyses.

(b) Mean number of interactions per bunch crossing weighted by the luminosity for all years of Run 2 [136].

Figure 5.1: Illustration of the ATLAS Run 2 dataset: integrated luminosities per year and pile-up conditions present in each year of data-taking.

compensate the reduced number of colliding bunches and the consequent loss in luminosity the beam intensity was increased. These adjustments resulted in an unprecedented level of pile-up and excessive demands on the CPU resources of the HLT [107]. To avoid higher thresholds in the trigger menu the instantaneous luminosity was controlled ("leveled") to not exceed $1.56 \times 10^{34} \, \text{cm}^{-1} \, \text{s}^{-2}$, implying $\langle \mu \rangle \approx 60$, until the beam intensities naturally drop below that level due to the ongoing collisions. The small peak around $\langle \mu \rangle \approx 2$ comes from dedicated low-μ runs of data-taking addressing special needs of some analyses, e.g. in the measurement of the W boson mass, but these data are not used in the analysis presented in this thesis.

Van der Meer scans [139] have been used to determine the absolute luminosity scale in dedicated low-luminosity fills of the LHC for every year of Run 2. These measure the size and shape of the beams by recording the interaction rate in x–y beam-separation scans. The calibrations are then extrapolated to the high-luminosity regime of the nominal data-taking similarly as in Run 1 [84]. The primary luminosity measurement was performed with the LUCID-2 Cherenkov detector (see Section 3.2.7) and complemented with measurements from other luminosity-sensitive detectors such as the ATLAS beam conditions monitor [140]. To ensure a good data quality, only those events are flagged as "good for physics" and used for analysis that have been recorded with all subdetectors fully in operation and good physics objects such as electrons and muons. After this selection step the size of the dataset analyzed in this thesis is $139 \, \text{fb}^{-1}$, corresponding to approximately 17.6 billion events, with an uncertainty of 1.7% derived in the luminosity measurements [141].

5.1.2 Signal Models

Two different scenarios with compressed mass spectra have been considered in this analysis: electroweakino ($\tilde{\chi}_2^0 \tilde{\chi}_1^\pm, \tilde{\chi}_2^0 \tilde{\chi}_1^0, \tilde{\chi}_1^\pm \tilde{\chi}_1^\mp$) and slepton ($\tilde{e}^- \tilde{e}^+, \tilde{\mu}^- \tilde{\mu}^+$) pair-production. Both scenar-
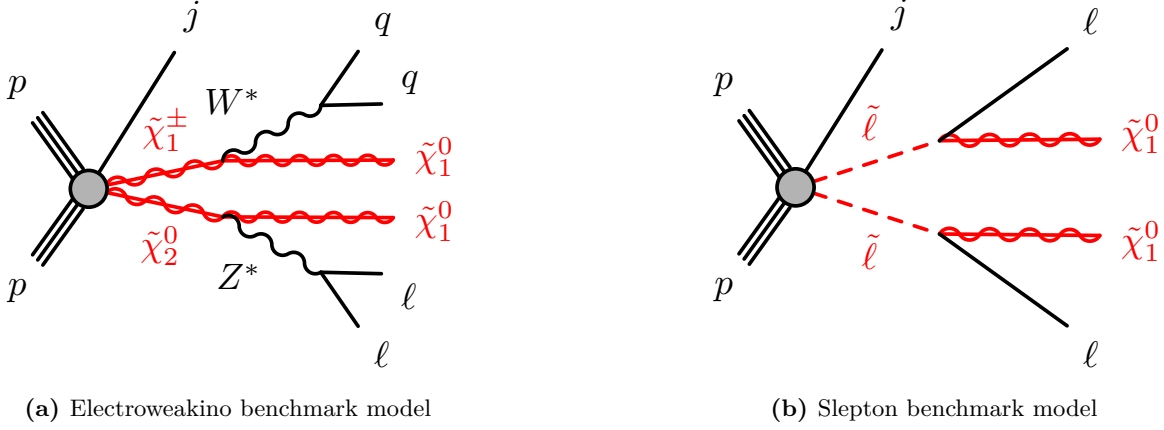
(a) Electroweakino benchmark model

(b) Slepton benchmark model

Figure 5.2: Feynman diagrams of the benchmark models under consideration. In the electroweakino model also $\tilde{\chi}_2^0 \tilde{\chi}_1^0$ and $\tilde{\chi}_1^\pm \tilde{\chi}_1^\mp$ production is considered. Figures taken from [135].

ios have been optimized and interpreted in terms of simplified models (see Section 2.3.3). Consequently, all SUSY particles not part of the decay chains are assumed to be decoupled with masses at the multiple TeV scale and can be neglected in the analysis.

The electroweakino search was optimized using the higgsino model described below. The analysis as presented in Ref. [135] considers also a reinterpretation of the search with an electroweakino scenario, in which the $\tilde{\chi}_2^0$ and $\tilde{\chi}_1^\pm$ states are wino-like and the LSP is bino-like. This scenario is not presented here, but naming schemes adapted in the analysis use the term electroweakinos to cover both interpretations. In the context of this thesis however, the terms higgsino and electroweakinos are used interchangeably.

Higgsino Model

The $\tilde{\chi}_2^0 \tilde{\chi}_1^\pm$ production mode of the first scenario is shown in Figure 5.2a. In this model, the $\tilde{\chi}_2^0$ and $\tilde{\chi}_1^\pm$ decay directly after production via off-shell Z and W bosons, respectively, into the $\tilde{\chi}_1^0$, which is assumed to be the LSP and stable. The search considers only leptonic Z decays into an ee or $\mu\mu$ pair, while the W is assumed to decay hadronically. The hadronic products of this decay are only soft and consequently do not play a significant role in the event kinematics. The distribution of the invariant mass of the lepton pair $m_{\ell\ell}$ from the $Z^* \to \ell\ell$ decay has an important characteristic which is exploited in the design of the analysis: the kinematic endpoint of $m_{\ell\ell}$ is governed by the mass splitting $\Delta m = m(\tilde{\chi}_2^0) - m(\tilde{\chi}_1^0)$ between the $\tilde{\chi}_2^0$ and the LSP as shown in Figure 5.3a. In case of $\tilde{\chi}_1^\pm \tilde{\chi}_1^\mp$ production, both emerging W bosons are assumed to decay leptonically. As the leptons originate from different legs, the $m_{\ell\ell}$ distribution misses a kinematic endpoint and thus this production mode contributes only minor to the sensitivity of the search.

Slepton Model

In the second scenario, shown in Figure 5.2b, a slepton pair is produced in the pp collisions. Each slepton then decays immediately into its SM counterpart and the LSP, which is again
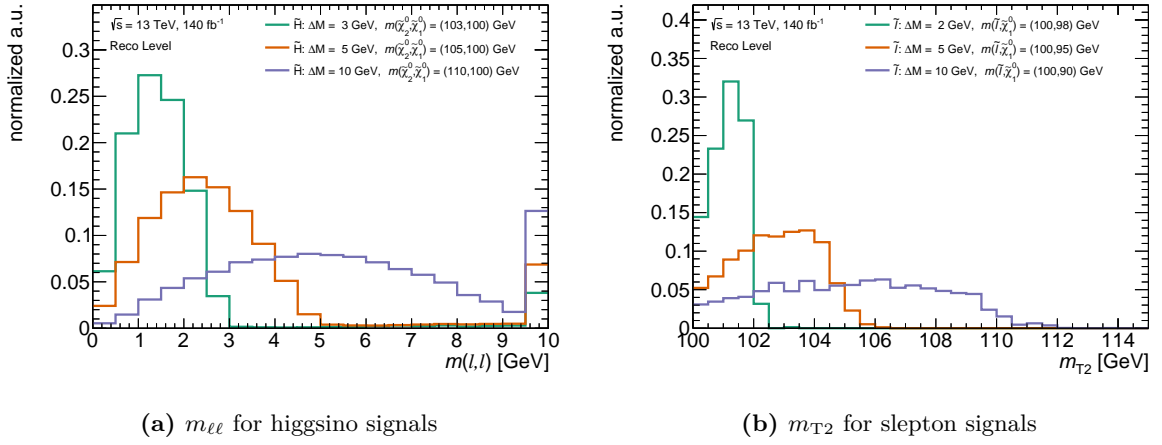
(a) $m_{\ell\ell}$ for higgsino signals

(b) m_{T2} for slepton signals

Figure 5.3: Distribution of $m_{\ell\ell}$ and m_{T2} for representative higgsino and slepton signal points, respectively. To improve the visualization of the respective signal shapes, all curves are normalized to 1. The plots are shown at reco level, i.e. the leptons are required to be reconstructed and need to pass the identification criteria given in Section 5.3.1. The first (last) bin contains the underflow (overflow).

the $\tilde{\chi}_1^0$. As the leptons originate from separate legs, there is no kinematic endpoint in the $m_{\ell\ell}$ distribution. Instead such an endpoint is present in the distribution of the stransverse mass m_{T2} [142, 143] (see Section 5.3.2) as shown in Figure 5.3b. To enhance the sensitivity of the search, in both scenarios the SUSY system is assumed to be boosted with respect to a jet from ISR.

Kinematics

In summary the final state covered by the analysis is characterized by a soft electron or muon pair with small invariant mass, hadronic activity from ISR and missing transverse momentum from the LSPs. Generally the kinematics in both scenarios are governed by the magnitude of the mass splitting Δm between the $\tilde{\chi}_1^0$ and the $\tilde{\chi}_2^0/\tilde{\ell}$. There is a tradeoff between the energy contained in the lepton and the invisible sector formed by the LSPs:

- In case of small mass splittings, most energy present in the decay will be required to create the mass of the LSPs. Consequently only little energy is left for the lepton pair, which will be very soft. Instead the amount of missing transverse momentum, defined in terms of its magnitude $E_{\mathrm{T}}^{\mathrm{miss}}$, originating from the massive LSPs will be large.

- If the mass splittings get larger, the intermediate Z boson can be less far apart from its rest mass, which results in harder leptons. On the contrary, the $E_{\mathrm{T}}^{\mathrm{miss}}$ distribution is getting softer compared to the previous case, because less energy is contained in the invisible sector of the decay chain.

To adequately capture the Δm-dependence of the signal kinematics, a set of simulated signal samples, referred to as *signal grid* has been generated for both simplified models.

Signal Monte Carlo Samples

MC samples for electroweakino pair production have been produced assuming pure higgsino $\tilde{\chi}_2^0$, $\tilde{\chi}_1^\pm$ and $\tilde{\chi}_1^0$ states, with the masses of the $\tilde{\chi}_2^0$ and $\tilde{\chi}_1^0$, as free parameters. The $\tilde{\chi}_1^\pm$ mass was set halfway in between, i.e. $m(\tilde{\chi}_1^\pm) = 0.5[m(\tilde{\chi}_2^0) + m(\tilde{\chi}_1^0)]$. The samples have been generated at LO with MG_aMC@NLO 2.6.1 [144] using the NNPDF23LO [145] PDF set with up to two additional partons at ME level. Contributions from *t*-channel diagrams including a colored SUSY particle are explicitly excluded from the generation. The decays of the electroweakinos were handled by MADSPIN [146]. To model the subsequent parton shower and hadronization processes as well as the underlying event, events were interfaced with PYTHIA 8.212 using the A14 tune. Matching between the ME and parton shower used the CKKW-L scheme [147] and a merging scale of 15 GeV. The branching ratios of the decays $\tilde{\chi}_2^0 \to Z^* \tilde{\chi}_1^0$ and $\tilde{\chi}_1^\pm \to W^* \tilde{\chi}_1^0$ have been set to one. The simulated signal grid covers $\tilde{\chi}_2^0$ masses from 81.5 to 290 GeV and mass splittings between 1.5 and 60 GeV.

Samples for the second scenario have been produced assuming the selectrons $\tilde{e}_{L,R}$ and smuons $\tilde{\mu}_{L,R}$ to be degenerate in mass. The sleptons are decayed with a 100 % branching fraction to the associated SM lepton and a pure bino $\tilde{\chi}_1^0$. The events were generated with MG_aMC@NLO 2.6.1 interfaced with PYTHIA 8.232, and the same PDF set and tune as used for the higgsino samples. Matching between the ME and the parton shower was also performed using the CKKW-L scheme, with the matching scale set to a quarter of the slepton mass. The slepton grid considers slepton masses from 70 to 300 GeV and mass splittings from 0.5 to 40 GeV.

To enforce an ISR topology, one jet with a $p_T > 50$ GeV is required at generation level. Further such requirements on the missing transverse momentum ($E_{T, gen}^{miss} > 75$ GeV) and on the number of leptons ($n_{lep, gen} \geq 2$) ensure adequate signal statistics.

The effect of pile-up was simulated by overlaying the signal events with additional *pp* collisions, which have been generated using PYTHIA 8.186 with the A3 tune [148] and the MSTW20008LO PDF set [149]. Simulated events are weighted such that the distribution of the interactions per bunch crossing μ matches the one observed in data, a procedure referred to as pile-up reweighting. In this procedure, the value of μ in data is divided by a empirically derived factor of 1.03 before calculating the weights, to improve the agreement in the number of primary vertices between data and simulation. To model the decay of bottom and charm quarks, all signal samples made use of EVTGEN [150] 1.2.0 . For all signal samples, the ATLFAST-II detector simulation was used, to model the detector response.

Cross Sections

Inclusive cross sections for higgsino and slepton pair production have been calculated using RESUMMINO 2.0.1 [151–153] at next-to-leading order (NLO) in the strong coupling constant and at next-to-leading-logarithm (NLL) accuracy for soft-gluon resummation. Following the recommendations from PDF4LHC [154], the signal cross sections and the associated uncertainties are obtained using the MSTW20008LO and CTQ6.6 [155] PDF sets. The final values are derived using the prescriptions from Ref. [156]. An envelope is constructed using the signal predictions of both PDF sets, in conjunction with variations of the factorization and renormalization scale by factors of 0.5 and 2 around their nominal values. The midpoint of
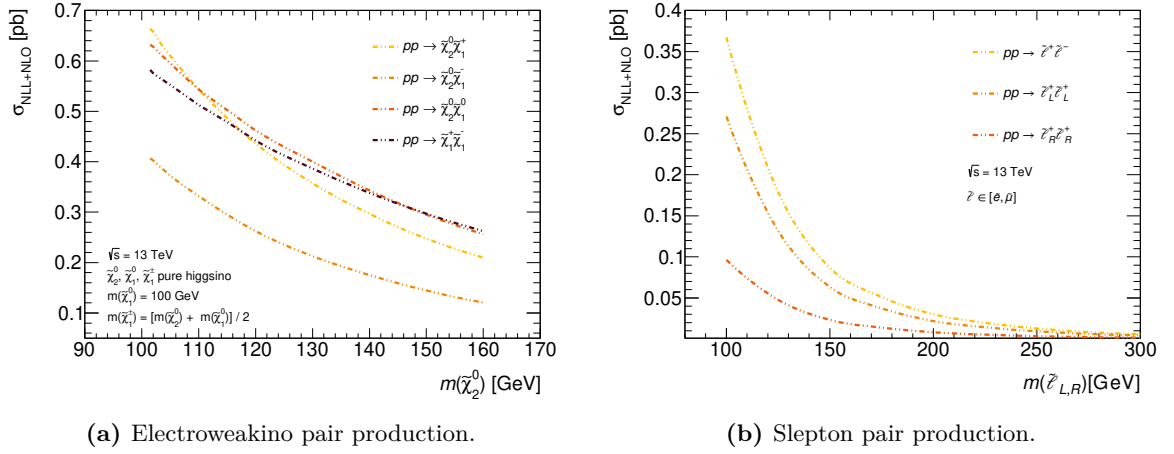
(a) Electroweakino pair production.

(b) Slepton pair production.

Figure 5.4: Cross sections calculated with RESUMMINO for the production of a (a) higgsino and (b) slepton pair, depending on the $\tilde{\chi}_2^0$ and slepton mass, respectively. The cross sections for the higgsinos assume a $\tilde{\chi}_1^0$ mass of 100 GeV. The corrections due to the jet requirement on generator level are included.

the envelope defines the nominal signal cross section and its half-width is taken as uncertainty on the cross section. To account for the jet requirement at generator level, the cross sections from RESUMMINO have been corrected by the ratio of the cross sections of the inclusive signal process and the process with at least one parton emission, both calculated with MG_aMC@NLO. Figure 5.4 shows the cross sections for higgsino and slepton pair production. In both scenarios, the cross sections are roughly of $\mathcal{O}(0.05$–$0.5\,\mathrm{pb})$, demonstrating the need of a large dataset in order to be sensitive to such processes. An additional correction arises for the higgsino scenario, as the branching ratios of the $Z^* \to \ell\ell$ and $W^{\pm *} \to \ell\nu$ decays have to be considered, which depend on the mass splitting (but not on the absolute scale of the $\tilde{\chi}_1^0$ mass). For instance, with decreasing mass splittings the decay modes $Z \to bb$ and $Z \to \tau\tau$ start to drop out at some point. Branching ratios have been calculated with SUSY-HIT 1.5a [157], taking into account the finite b-quark and τ masses. As shown in Figure 5.5, the leptonic branching ratios are stable for larger mass splittings, but increase slightly at low mass splittings due to the drop out of decay modes stated above.

5.1.3 Backgrounds

Several SM processes can yield final states similar to the ones present in the higgsino and slepton models, and are consequently considered as background in the analysis. As the selected leptons are predominantly soft, their misidentification rate is notably large, specifically at low lepton p_T. For that reason, contributions to the SM background stem also from events, in which one or even both of the leptons are either fake or nonprompt, i.e. do not originate from the primary vertex. This *fake/nonprompt* lepton background is estimated using a data-driven method, introduced in Section 5.5.2. The contribution from events containing two prompt leptons is instead estimated from MC simulation.

The production of vector bosons in association with jets, V+jets ($V = W, Z, \gamma^*$), that
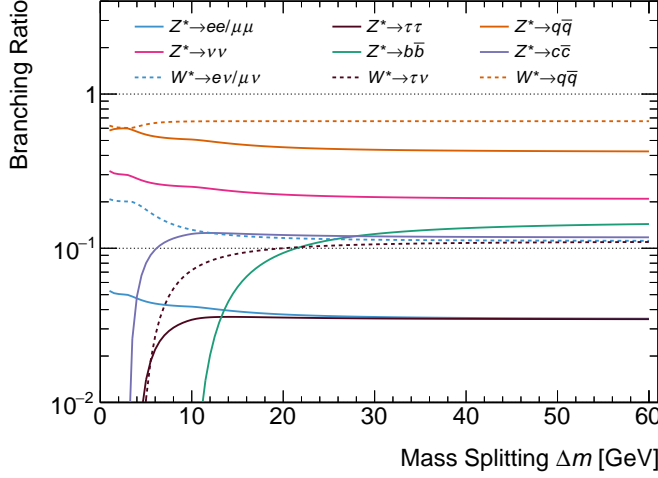
Figure 5.5: Branching ratios of the Z^* (solid lines) and W^* (dashed lines) decays with respect to the mass splitting Δm between the $\tilde{\chi}_1^0$ and $\tilde{\chi}_2^0$, calculated with `SUSY-HIT`.

involve leptonic decays of the vector bosons, was modeled using SHERPA 2.2.1 [110]. A significant background contribution for the analysis originates from $Z/\gamma^* \to \tau\tau$ events in which both taus decay leptonically. In that case, the final state comprises two prompt leptons and a source of true $E_{\mathrm{T}}^{\mathrm{miss}}$ from to the neutrinos in the tau decays, allowing such events to pass the analysis selection criteria. In the following, this background is referred to as $Z \to \tau\tau$. Due to the lack of sources for true $E_{\mathrm{T}}^{\mathrm{miss}}$, events from $Z/\gamma^* \to ee$ and $Z/\gamma^* \to \mu\mu$ decays contribute only in case of severe $E_{\mathrm{T}}^{\mathrm{miss}}$ mismeasurements, which was found to occur very rarely. Events from $W \to \ell\nu$ decays lack a second lepton and are thus contained in the fake estimate[†]. Pair production of vector bosons, (WW, ZZ and WZ), collectively referred to as *diboson* or VV, was simulated using SHERPA 2.2.1 and 2.2.2. Contributions from diboson events with three leptons in the final state arise, when the third lepton is below the reconstruction thresholds. Notable contributions originate also from dileptonic $t\bar{t}$ and single-top events, as well as from top-quark production in association with a W boson. These samples were generated using POWHEG-BOX [170] interfaced with PYTHIA 8.230 and are referred to as *top* in the following. Small contributions arise from Higgs-related processes, such as single-Higgs production via vector-boson fusion (VBF) and gluon–gluon fusion (ggF) as well as rarer top processes (see Table 5.1). Together with triboson and $Z/\gamma^* \to ee/\mu\mu$ events, these are considered in a sample labeled *others*. Table 5.1 presents a summary of the generator configurations, including the PDF sets used. Further information about the generated SM backgrounds can be found in Refs. [171–175].

To simulate the detector response, the full simulation in GEANT4 was used for the background samples. Except the samples generated with SHERPA, all background samples used EVTGEN 1.60 and 1.20 to model the decay of heavy flavor quarks. Similar to the generated signal samples, all background events were overlaid with additional simulated pp interactions and reweighted such that the distribution of pile-up matches the one observed in data.

Process	Matrix element	Parton shower	PDF set	Cross section
V+jets	Sherpa 2.2.1		NNPDF 3.0 NNLO [158]	NNLO [159]
VV	Sherpa 2.2.1/2.2.2		NNPDF 3.0 NNLO	Generator NLO
Triboson	Sherpa 2.2.1		NNPDF 3.0 NNLO	Generator LO, NLO
$h[ggF]$	Powheg-Box	Pythia 8.212	NLO CTEQ6L1 [128]	N^{3}LO [160]
$h[VBF]$	Powheg-Box	Pythia 8.186	NLO CTEQ6L1 [128]	NNLO + NLO [160]
$h + W/Z$	Pythia 8.186		NNPDF 2.3 LO [145]	NNLO + NLO [160]
$h + t\bar{t}$	MG5_aMC@NLO 2.2.3	Pythia 8.210	NNPDF 2.3 LO	NLO [160]
$t\bar{t}$	Powheg-Box	Pythia 8.230	NNPDF 2.3 LO	NNLO+NNLL [161–165]
t (s-channel)	Powheg-Box	Pythia 8.230	NNPDF 2.3 LO	NNLO+NNLL [166]
t (t-channel)	Powheg-Box	Pythia 8.230	NNPDF 2.3 LO	NNLO+NNLL [167, 168]
$t + W$	Powheg-Box	Pythia 8.230	NNPDF 2.3 LO	NNLO+NNLL [169]
$t + Z$	MG5_aMC@NLO 2.3.3	Pythia 8.212	NNPDF 2.3 LO	NLO [144]
$t\bar{t}WW$	MG5_aMC@NLO 2.2.2	Pythia 8.186	NNPDF 2.3 LO	NLO [144]
$t\bar{t} + Z/W/\gamma^*$	MG5_aMC@NLO 2.3.3	Pythia 8.210/8.212	NNPDF 2.3 LO	NLO [160]
$t + WZ$	MG5_aMC@NLO 2.3.3	Pythia 8.212	NNPDF 2.3 LO	NLO [144]
$t + t\bar{t}$	MG5_aMC@NLO 2.2.2	Pythia 8.186	NNPDF 2.3 LO	LO [144]
$tt\bar{t}$	MG5_aMC@NLO 2.2.2	Pythia 8.186	NNPDF 2.3 LO	NLO [144]

Table 5.1: Simulated SM background processes. The PDF set refers to that used in for the matrix element. Table adapted from [135].

5.1.4 Existing Constraints

First limits on these compressed scenarios have been established by the experiments at LEP [177–186] using electron–positron collisions. Gaugino masses are bound to $m(\tilde{\chi}_1^\pm) > 103.5\,\text{GeV}$ for $\Delta m(\tilde{\chi}_1^\pm, \tilde{\chi}_1^0) > 3\,\text{GeV}$ and $m(\tilde{\chi}_1^\pm) > 92.4\,\text{GeV}$ for smaller mass splittings. LEP contraints on sleptons are typically quoted conservatively, i.e. with respect to $\tilde{\ell}_R$, which has a weaker coupling to the Z boson than $\tilde{\ell}_L$. SUSY partners to the right-handed muon $\tilde{\mu}_R$ are excluded up to $m(\tilde{\mu}_R) \gtrsim 94.6\,\text{GeV}$ for mass differences $m(\tilde{\mu}_R, \tilde{\chi}_1^0) \gtrsim 2\,\text{GeV}$. Using the $\tilde{e}_L\tilde{e}_R$ production mode via t-channel neutralino exchange at LEP, a universal bound on the mass of the SUSY partner to the right-handed electron $m(\tilde{e}_R) \gtrsim 73\,\text{GeV}$ was established, independent of the $\tilde{\chi}_1^0$ mass [187]. The limits have been extended by recent results from CMS [188, 189] and ATLAS [176] for a range of mass splittings. The result from ATLAS represents an intermediate status of the search presented in this thesis, that used only the first $36.1\,\text{fb}^{-1}$ of the Run 2 dataset. The associated exclusion contours in conjunction with the LEP limits are shown in Figure 5.6. As the kinematics are governed by the mass splitting, the limits are presented in the $\Delta m(\tilde{\chi}_2^0, \tilde{\chi}_1^0)$–$m(\tilde{\chi}_2^0)$ and $\Delta m(\tilde{\ell}, \tilde{\chi}_1^0)$–$m(\tilde{\ell})$ plane, respectively. Higgsino-like $\tilde{\chi}_2^0$ masses are excluded up to $130\,\text{GeV}$ and mass splittings down to $3\,\text{GeV}$ are excluded. Constraints on sleptons were increased up to masses of $180\,\text{GeV}$ with mass splittings as small as $1\,\text{GeV}$. Further constraints for the higgsino scenario have been made by a reinterpretation of the disappearing-track search [190, 191]. In case the mass splittings between the LSP and the lightest chargino $\Delta m(\tilde{\chi}_1^\pm, \tilde{\chi}_1^0)$ are $\mathcal{O}(100\,\text{MeV})$, the lifetime of the chargino is $\mathcal{O}(0.05\,\text{ns})$ and it may reach the detector before decaying. In these scenarios, the chargino decays typically into the LSP via a soft pion, with a transverse momentum too low to be reconstructed. Since the LSP cannot be detected, the track of the chargino seems to disappear in the ID. Using

---

† the term fake is just an abbreviation and in the following meant to include also the nonprompt lepton contribution
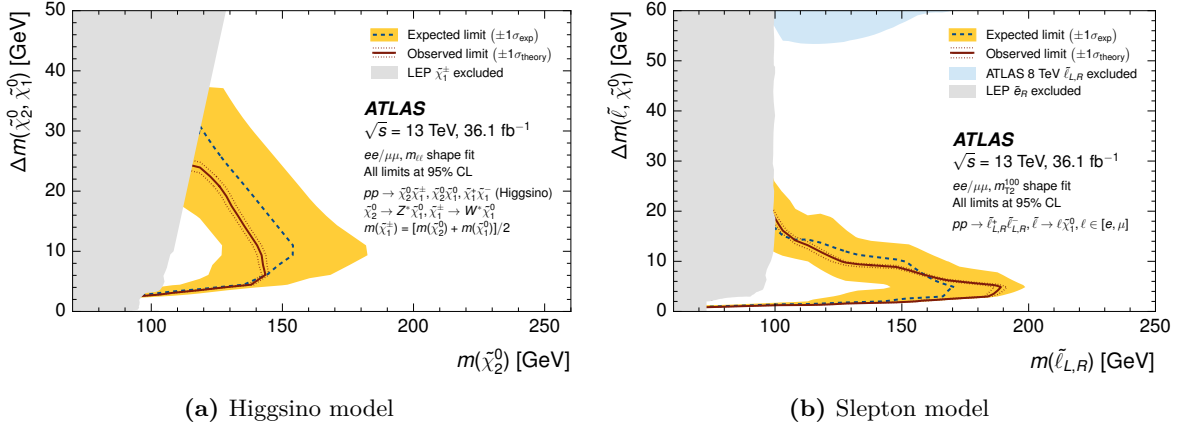
(a) Higgsino model   **(b)** Slepton model

Figure 5.6: Expected (dashed blue line) and observed (solid red line) exclusion contours at $95\,\%$ confidence level (CL) derived by the intermediate version of the analysis, using $36.1\,\mathrm{fb}^{-1}$ from the ATLAS Run 2 dataset [176]. The limits from LEP discussed in the text are shown as gray area.

these signatures, mass differences $\Delta m(\tilde{\chi}_1^\pm, \tilde{\chi}_1^0)$ up to $340\,\mathrm{MeV}$ have been excluded.

The aim of analysis presented in this thesis is to extend the sensitivity reach of the previous result by using the full integrated luminosity of Run 2, additional analysis channels and benefits from improved detector calibrations and reconstruction performance.

5.2 Analysis Strategy

To maximize the sensitivity for both electroweakino and slepton production, the analysis considers two independent sets of selections, which are optimized individually for each scenario. Both sets consist of several orthogonal analysis channels, which are optimized to provide sensitivity for a particular parameter space in the signal grid. For the final statistical evaluation, all channels are combined simultaneously to maximize the sensitivity across the signal grid. The backgrounds are estimated with a mix of data-driven and MC-based methods, depending on the needs of the individual channel. To account for potential mismodeling, important backgrounds estimated with MC simulation are normalized to data using a maximum likelihood fit.

5.2.1 Analysis Channels

To exploit the respective kinematic endpoints, the electroweakino and slepton selections are based on $m_{\ell\ell}$ and $m_{\mathrm{T}2}$, respectively. As the $E_\mathrm{T}^\mathrm{miss}$ distribution gets harder with decreasing mass splittings, it makes sense to split the searches into two channels, depending on the magnitude of $E_\mathrm{T}^\mathrm{miss}$. The low-$E_\mathrm{T}^\mathrm{miss}$ channels target primarily medium to large mass splittings, while the high-$E_\mathrm{T}^\mathrm{miss}$ channels are sensitive across the signal grid, notably also to very small mass splittings. As depicted in Figure 5.7 the high-$E_\mathrm{T}^\mathrm{miss}$ selections cover the phase space with $E_\mathrm{T}^\mathrm{miss} > 200\,\mathrm{GeV}$, while the low-$E_\mathrm{T}^\mathrm{miss}$ selections cover $120\,\mathrm{GeV} < E_\mathrm{T}^\mathrm{miss} < 200\,\mathrm{GeV}$. In case of tiny mass splittings, one of the leptons will most likely not pass the lepton reconstruction thresholds due to its very low p_T. To increase the signal acceptance in these scenarios,
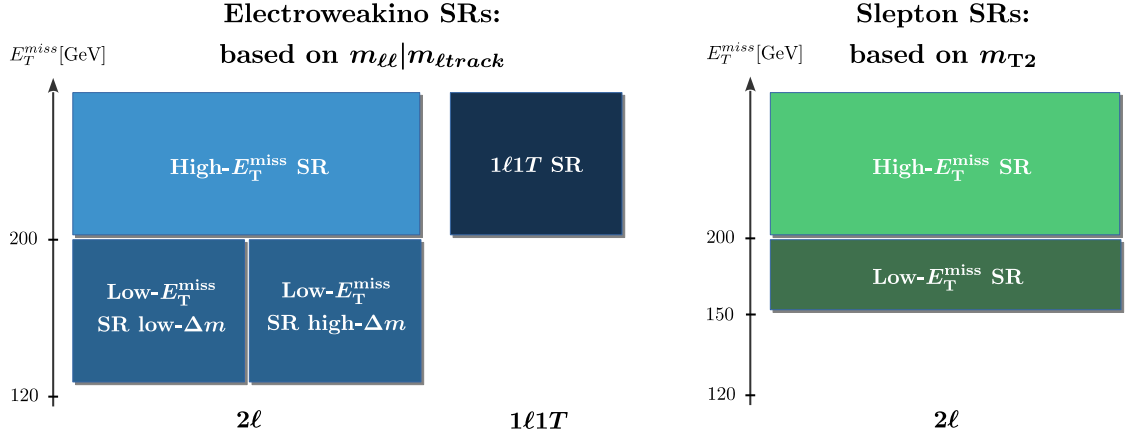
Figure 5.7: Schematic illustration of the analysis structure. Electroweakino channels, based on $m_{\ell\ell}$, are shown in blue and the slepton channels, based on m_{T2}, are shown in green.

a third channel is added to the higgsino search. This channel replaces the second lepton with an isolated track, which is reconstructed with much higher efficiency also at lower p_{T}. Consequently the higgsino search consists of three orthogonal channels: a one-lepton plus track ($1\ell1T$) and two two-lepton (2ℓ) channels. The $1\ell1T$ channel relies on collimated leptons and is therefore not present in the slepton search, which also comprises a high-$E_{\text{T}}^{\text{miss}}$ and low-$E_{\text{T}}^{\text{miss}}$ selection.

The analysis channels are defined by signal enriched regions, referred to as signal regions (SRs), and optimized independently from each other in terms of signal-to-background separation. All channels have one SR, except the low-$E_{\text{T}}^{\text{miss}}$ channel of the electroweakino search, which has two SRs to increase its sensitivity across the higgsino grid. To further enhance sensitivity, each SR is split into several $m_{\ell\ell}$ and m_{T2} SR bins, respectively. As the $m_{\ell\ell}$ and m_{T2} distributions change with the mass splitting, such a multi-bin approach enables to capture also the signal shape in the statistical analysis.

A dedicated background estimation strategy has been adapted for each of the SRs. While the strategies for the low-$E_{\text{T}}^{\text{miss}}$ and high-$E_{\text{T}}^{\text{miss}}$ selections are related and employ a mix of MC-based and data-driven methods, the $1\ell1T$ channel utilizes a purely data-driven background estimation.

Only the regions residing in the low-$E_{\text{T}}^{\text{miss}}$ regime have been developed and optimized by the author. Therefore the description of the analysis focuses on these. As the results have been produced using a statistical combination with the remaining channels, those are essential to understand the final outcome of the analysis. Hence, the $1\ell1T$ and high-$E_{\text{T}}^{\text{miss}}$ selections are briefly introduced in the associated sections with references to a more detailed description.

5.2.2 Statistical Model and Evaluation

To interpret the physics outcome of an experiment, a probabilistic model is required. The statistical evaluation involves then an assessment of the validity of the model in describing the
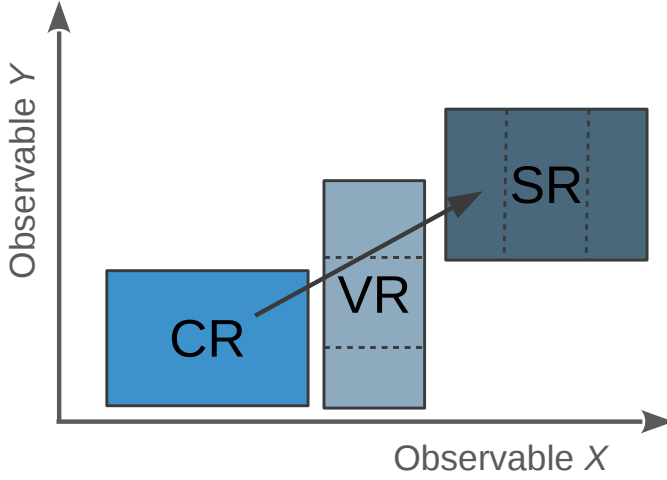
Figure 5.8: Schematic illustration of the concept of CRs, VRs and SRs. In the simple setup shown, background predictions are normalized to data in a CR, and extrapolated to the VR and SR as indicated by the arrow. The dashed lines illustrate that regions can consist of a single or multiple bins.

observations in data or to determine its parameters. A frequentist approach to statistics is employed, in which probability is interpreted as the frequency of the outcome of a repeatable experiment [9].

A hypothesis H describes the probability for the experimental outcome, which is typically characterized by a set of observed event counts ("yields") $\boldsymbol{x}$. The likelihood of H regards the probability $P(\boldsymbol{x}|H)$, i.e. to observe $\boldsymbol{x}$ under the assumption of H, as a function of the hypothesis. Usually H depends on a set of parameters $\boldsymbol{\theta}$, such that the likelihood is also a function of these parameters $L(\boldsymbol{\theta}) = P(\boldsymbol{x}|\boldsymbol{\theta})$, and forms a probability density function (p.d.f.). Maximizing the likelihood with respect to $\boldsymbol{x}$ yields estimators for the parameters $\boldsymbol{\theta}$. Input for constructing the likelihood are the observed event counts and the expected yields for the SM processes, typically taken from MC simulation or derived by data-driven methods, and their associated uncertainties.

The building of the statistical models, fitting and running hypothesis tests whether a particular model can be excluded or not, were performed using the HISTFITTER [192] package.

Concept of Control, Validation and Signal Regions

The search for BSM physics involves the definition of a region of phase space, in which the expected signature of the signal under study exceeds the predicted level of SM background. These signal-enriched selections are referred to as SRs. Backgrounds contaminating the SR(s) can be estimated in a semi data-driven way by the usage of control regions (CRs), in which SM predictions from MC simulation are normalized to data via *normalization factors*. CRs are designed to be very pure in one particular type of background and with negligible signal contamination. After the parameters of the model, such as the normalization factors and the ones parameterizing the systematic uncertainties, have been fitted in the CR(s), they can be extrapolated to the SR(s). To ensure the validity of the extrapolation, the background predictions are evaluated and compared to data beforehand in validation regions (VRs), typically placed between the CR(s) and SR(s). A statistically correct treatment requires the CR(s), VR(s) and SR(s) to be orthogonal, i.e. with no overlaps in phase space. As illustration, a

simple setup of one CR, VR and SR separated by requirements on two observables X and Y is depicted in Figure 5.8. The SM predictions are normalized in the CR, defined at low values of X and Y, and extrapolated to the SR, located at high values of X and Y, as indicated by the arrow.

In general such a configuration allows to constrain the contributions of important backgrounds in regions with large statistics, because the CRs requires usually looser selection criteria as the associated SRs. To minimize the uncertainties due to the extrapolation, CRs should be placed kinematically as close as possible to the SRs.

Model Building

To construct the likelihood, the HISTFACTORY [193] template is used. In each region, the expected event yield is the sum of the contributions from the individual physics processes (samples) considered. The sample rate may depend on a set of free parameters $\boldsymbol{\eta}$, such as the normalization factors, and constrained parameters $\boldsymbol{\chi}$, e.g. to include the effect of systematic variations. The p.d.f. of bin b in region r is modeled with a Poisson term $\text{Pois}(n_{rb}|\nu_{rb}(\boldsymbol{\eta}, \boldsymbol{\chi}))$, where n_{rb} is the number of observed events and $\nu_{rb}(\boldsymbol{\eta}, \boldsymbol{\chi})$ the expected event rate. The parameters representing the systematic uncertainties are constrained by additional terms to dictate the degree the variations can deviate from the nominal predictions. These constraint terms can be viewed as auxiliary regions with global observed data $\boldsymbol{a}$ from auxiliary measurements, such that the complete observation is written as $\boldsymbol{x} = (\boldsymbol{n}, \boldsymbol{a})$, where $\boldsymbol{n} = \{n_{rb}\}$. Schematically the overall structure of the likelihood is then formed by the Poisson terms of the individual regions and a set of constraint terms

$$L(\boldsymbol{x}|\boldsymbol{\eta}, \boldsymbol{\chi}) = \prod_{r \, \in \, \text{regions}} \prod_{b \, \in \, \text{bins}} \text{Pois}(n_{rb}|\nu_{rb}(\boldsymbol{\eta}, \boldsymbol{\chi})) \prod_{\chi \, \in \, \boldsymbol{\chi}} f_\chi(a_\chi|\chi), \qquad (5.1)$$

where the term $f_\chi(a_\chi|\chi)$, which constrains the nuisance parameter χ using auxiliary data a_χ, is modeled with a Gaussian. Consequently values of $\chi = \pm 1$ represent the $\pm 1\sigma$ variations for the event counts of the respective systematic variation. To derive the expected yields for any value of χ, polynomial interpolation and exponential extrapolation between the nominal and variational yields are used, as presented in Ref. [193]. The final likelihood contains further contributions, such as terms modeling the statistical uncertainties on the samples and the systematic uncertainties on the luminosity.

The parameters can then be fitted by finding their values that maximize the likelihood outlined in Equation (5.1). For instance, in a background-only fit, i.e. with no signal component, the values of the normalization and nuisance parameters are typically derived using only the CRs as constraining regions (not counting the auxiliary regions used to contrain the systematic uncertainties). These are then extrapolated to the VRs by evaluating the VR background yields with the parameters fixed to their fitted values from the background-only fit. In case the data agree with the post-fit VR predictions within their uncertainties, the background modeling is assumed to be reliable for the VRs and also the SRs.

The majority of parameters in the statistical model are not of main interest for the analysis, but are required to model the data. These are referred to as *nuisance* parameters, such as the parameters associated with the systematic uncertainties. Typically one of the free parameters is regarded as *parameter of interest*, for which the hypothesis tests are performed, such as

the signal strength μ. This parameter scales the expected signal yields, consequently $\mu = 1$ corresponds to the nominal signal model, while $\mu = 0$ corresponds to the background-only hypothesis.

Hypothesis Tests

The aim of hypothesis tests is to make a statement whether a hypothesis can be rejected or not. In the context of a search for new signal processes, a null hypothesis H_0 is defined, which represents the presence of only known processes, referred to as background-only hypothesis. H_0 is to be tested against an alternative hypothesis H_1, that includes a signal component and is denoted as signal-plus-background hypothesis. When setting limits on a particular signal model, the roles are reversed and the signal-plus-background model serves as null hypothesis.

To quantify the outcome of a search, the level of agreement between the observed data and a hypothesis H is quantified by a p-value, i.e. a probability of finding data of equal or greater incompatibility under the assumption of H [194]. A hypothesis can be regarded as excluded, if the observed p-value is below a specified threshold. Typically the p-value is converted into a significance Z, which is defined as

$$Z = \Phi^{-1}(1 - p) \,, \tag{5.2}$$

where Φ^{-1} is the quantile of the standard Gaussian. For exclusion of a signal model, a p-value of 0.05 is required, corresponding to a CL of 95 % and a significance $Z = 1.64$.

It is convenient to define a *test statistic* q that parameterizes the compatibility between the data and the hypothesis. Assuming that q is defined such that larger values indicate increasing incompatibility with the data, the p-value is then calculated as

$$p = \int_{q_{\text{obs}}}^{\infty} f(q|H) \mathrm{d}q \,, \tag{5.3}$$

where q_{obs} is the value of the test statistic observed in data and $f(q|H)$ is the p.d.f. of q under the assumption of H. The LHC collaborations use the *profile likelihood ratio* in the test statistic. For a hypothetical value of the signal strength μ it is defined as

$$\lambda(\mu) = \frac{L(\mu, \hat{\hat{\boldsymbol{\theta}}})}{L(\hat{\mu}, \hat{\boldsymbol{\theta}})} \,, \tag{5.4}$$

where $\hat{\hat{\boldsymbol{\theta}}}$ denotes the values of the nuisance parameters $\boldsymbol{\theta}$ that maximize L for a given μ. The symbols $\hat{\mu}$ and $\hat{\boldsymbol{\theta}}$ represent the estimators for the maximum of the unconditional likelihood function, so that by definition $0 \leq \lambda(\mu) \leq 1$. Usually, a signal process is assumed to contribute only non-negatively, e.g. $\mu \geq 0$. For convenience, an effective estimator $\hat{\mu}$, defined as value of μ maximizing the likelihood, is introduced, which can also take on negative values. The exact definition of the test statistics depends on the application. For the purpose of setting upper limits it is defined as [194]

$$q_\mu = \begin{cases} -2 \ln \lambda(\mu) & \hat{\mu} \leq \mu \,, \\ 0 & \hat{\mu} > \mu \,. \end{cases} \tag{5.5}$$

This definition ensures that data with $\hat{\mu} > \mu$ is not regarded to represent less compatibility between hypothesis and observation, as q_μ is set to 0 in such cases. To calculate the p-value according to Equation (5.3) the distribution of $f(q_\mu|\mu)$, i.e. the p.d.f. of q_μ assuming the signal-plus-background model at signal strength μ, is required. The distributions of $f(q_\mu|\mu)$ are approximated using the asymptotic formulas presented in Ref [194].

In order to avoid exclusion of a model to which the analysis has no sensitivity, i.e. when the predicted number of events in the SR of the background-only and signal-plus-background models are very close, the CL_s prescription [195] is used. The CL_s value is defined as

$$\mathrm{CL}_s = \frac{p_\mu}{1 - p_b}\,, \tag{5.6}$$

where p_b is the p-value of the background only hypothesis. At a CL of 95 %, a model can be regarded as excluded, if the associated CL_s value is below 0.05.

5.3 Event Selection

To define event selections, first appropriate object definitions reflecting the particular analysis needs are necessary. Selections are then built by requirements on these objects, such as the transverse momenta of the leptons in the event. Moreover, a set of triggers has to be chosen that selects the signal events in data with high efficiency. Typically also a loose basic selection, referred to as *preselection*, is introduced that selects those events that fall into the phase space considered. Further selections of the analysis are then based on this common preselection.

5.3.1 Object Definitions

The analysis uses signatures that have been reconstructed and identified either as electrons, photons, muons or jets. In general, the identification criteria on leptons have been chosen so that a reasonable reconstruction efficiency is maintained also at low p_T while keeping the fake/non-prompt contamination at an affordable level. Events containing jets that pass the selection criteria of a high-efficiency b-tagging WP are discarded in order to maximize rejection power with respect to backgrounds related to top quarks. Leptons and jets are first preselected by applying some rather loose *baseline* identification criteria and must fulfill tighter requirements to be flagged as *signal* objects. These are used to calculate the analysis variables defining the final selections, while baseline leptons are utilized in the data-driven estimate of the fake/nonprompt background, see Section 5.5.2. A summary of the requirements on each object type is given in Table 5.2.

Tracks and Vertices The reconstruction of tracks, i.e. the trajectories of charged particles, begins by assembling the raw measurements from the pixel and SCT detectors into clusters [196]. From these clusters, three-dimensional measurements called space-points are built, that represent the location where a charged particle traversed active ID material. Track candidates are then built using a combinatorial Kalman filter [197] that operates on track seeds formed by sets of three space points. After ambiguities among the track candidates are resolved by scoring the tracks with a reward/penalty scheme, tracks are extended into the TRT [198]. A complementary approach starts from segments in the TRT and extends them

Property	Signal	Baseline
Electrons		
Kinematic	$p_T > 4.5$ GeV, $|\eta| < 2.47$	$p_T > 4.5$ GeV, $|\eta| < 2.47$
Identification	*Medium*	*VeryLoose*
Isolation	*Gradient*	–
Impact parameter	$|d_0/\sigma(d_0)| < 5$, $|z_0 \sin\theta| < 0.5$ mm	$|z_0 \sin\theta| < 0.5$ mm
Muons		
Kinematic	$p_T > 3$ GeV, $|\eta| < 2.5$	$p_T > 3$ GeV, $|\eta| < 2.5$
Identification	*Low-p_T*	*Low-p_T*
Isolation	*FCTightTrackOnly*	–
Impact parameter	$|d_0/\sigma(d_0)| < 3$, $|z_0 \sin\theta| < 0.5$ mm	$|z_0 \sin\theta| < 0.5$ mm
Jets (anti-k_t with $R = 0.4$)		
Kinematic	$p_T > 30$ GeV, $|\eta| < 2.8$	$p_T > 20$ GeV, $|\eta| < 4.5$
Pileup mitigation	JVT *Medium* for $p_T < 120$ GeV, $|\eta| < 2.5$	–
b-Jets (anti-k_t with $R = 0.4$)		
Kinematic	$p_T > 20$ GeV, $|\eta| < 2.5$	$p_T > 20$ GeV, $|\eta| < 4.5$
Pileup mitigation	JVT *Medium* for $p_T < 120$ GeV, $|\eta| < 2.5$	–
b-tagging	*MV2c10* with 85 % Efficiency	–

Table 5.2: Definitions of signal and baseline objects used in the analysis.

inwards to the silicon detectors [199]. The final tracks are refitted taking into account the information from all three ID subdetectors. Reconstructed tracks are available for $p_T > 400$ MeV in the range $|\eta| < 2.5$. Their impact parameters are defined as the minimum transverse (d_0) and longitudinal (z_0) distance to a reference point (such as the primary vertex).

The reconstruction of primary vertices is performed in a iterative sequence of vertex finding and fitting algorithms [200]. Selected tracks from the track reconstruction passing a number of quality requirements [201] are used to define a first vertex. The best vertex position is found by an iterative χ^2 fit, in which less compatible tracks are down-weighted and eventually removed [202]. Rejected tracks can be used in subsequent sequences of vertex finding and fitting until no more vertices can be built. Vertices with at least two associated tracks are retained as primary vertex candidates and are described by their three dimensional position and covariance matrix. In events with multiple reconstructed interaction vertices, common in the high-luminosity environment of the LHC, the primary vertex is defined as the one with the highest $\sum p_T^2$ of associated tracks.

Electrons and Photons The input for electron and photon reconstruction are energy deposits, clustered into topological connected cells in the electromagnetic and hadronic calorime-

ter, referred to as topo-clusters [203]. Topo-clusters are derived from neighboring calorimeter cells that contain energies above a noise threshold. Energies of the calorimeter cells are measured at the electromagnetic scale, i.e. energy deposits are assumed to stem exclusively from electromagnetically interacting particles. ID tracks that are loosely matched to these clusters are refitted to account for energy losses, e.g. due to bremsstrahlung [204]. Furthermore photon conversion vertices are built and matched to the clusters [205]. Track-matched topo-clusters form the seeds to build variable-width superclusters [206]. Topo-clusters near the seed cluster can be added as satellite clusters in the algorithm, which may emerge for instance due to bremsstrahlung. Likewise, photon superclusters are built independently from conversion-matched and non-track-matched topo-clusters. The final superclusters then define the electron and photon objects for the analysis, whose energies are calibrated using $Z \to ee$ decays [207]. Selected electrons and photons have to fulfill a set of quality and identification requirements in order to improve their purities. The identification for prompt electrons relies on a likelihood discriminant, constructed from properties of the primary track, shape of the electromagnetic shower and the compatibility of the ID and calorimeter measurements [208]. Electrons are calibrated by measuring their energy scale and resolution in $Z \to ee$ decays.

Electrons in the analysis are required to have $p_{\mathrm{T}} > 4.5\,\mathrm{GeV}$ and are restricted to $|\eta| < 2.47$. Baseline electrons need to satisfy a very loose requirement on the likelihood discriminant, that keeps approximately $97\,\%$ of the signal electrons [206]. A requirement on the longitudinal impact parameter $|z_0 \sin\theta| < 0.5\,\mathrm{mm}$ reduces the contamination from objects emerging out of secondary interactions. Signal electrons need to fulfill the *Medium* likelihood identification [206], which yields reconstruction efficiencies of about $80\,\%$ at $E_{\mathrm{T}} = 4.5\,\mathrm{GeV}$ and increases up to $93\,\%$ for larger E_{T}. To ensure compatibility with the primary vertex, signal electrons further have to fulfill a requirement on the significance of the transverse impact parameter $|d_0|/\sigma(d_0) < 5$, which is defined with respect to the beam-spot position. The electron reconstruction efficiency is also measured using $Z \to ee$ decays [206], and small corrections are applied in simulation to match the efficiency in data. Photon identification utilizes a cut-based selection using shower shape variables. In the analysis, photons are required to have $p_{\mathrm{T}} > 13\,\mathrm{GeV}$, $|\eta| < 2.37$, and need to pass the *Tight* and *FixCutTight* identification and isolation WPs [206], respectively. Photons are only used in the calculation of the missing transverse momentum, otherwise the analysis is completely agnostic to this object type.

Muons Reconstruction and identification of muons relies on a combination of track measurements in the ID and MS, and is reviewed in Chapter 4. Muons are calibrated by applying corrections derived in $Z \to \mu\mu$ and $J/\Psi \to \mu\mu$ events to the transverse muon momenta in simulation, such that muon momentum scale and resolution agree with the ones measured in data.

The analysis considers muons with $p_{\mathrm{T}} > 3\,\mathrm{GeV}$ and restricts them to $|\eta| < 2.5$, as contamination of fakes would be unreasonably large at low p_{T} without assistance from the tracking systems. Baseline muons need to pass the *Low-p_T* identification WP, which was optimized in terms of signal efficiency and background rejection for muon candidates with $p_{\mathrm{T}} < 10\,\mathrm{GeV}$. Baseline muons also need to satisfy $|z_0 \sin\theta| < 0.5\,\mathrm{mm}$. To be considered as signal quality, muons need in addition to pass $|d_0|/\sigma(d_0) < 5$. The scale factors derived in Chapter 4 are are applied to match the reconstruction efficiencies between simulation and data.
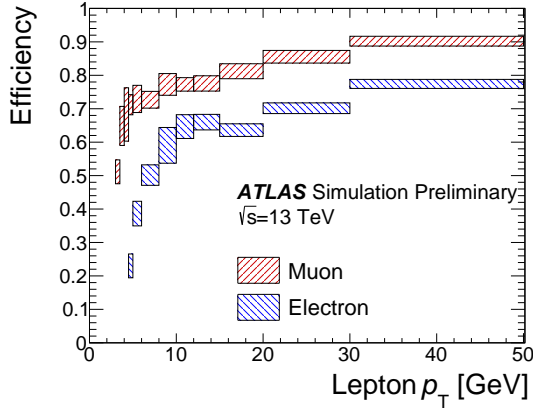
Figure 5.9: Signal-lepton efficiencies for electrons and muons in a mix of slepton and Higgsino samples. Combined reconstruction, identification, isolation and vertex association efficiencies are shown for leptons within detector acceptance, and with lepton p_T within a factor of 3 of $\Delta m(\tilde{\ell}, \tilde{\chi}_1^0)$ for sleptons or of $\Delta m(\tilde{\chi}_2^0, \tilde{\chi}_1^0)/2$ for Higgsinos. The average number of interactions per crossing in the MC samples is $\langle \mu \rangle = 33.7$. Uncertainty bands represent the range of efficiencies observed across all signal samples used for the given p_T bin. The η-dependence is consistent with values reported in ATLAS combined performance papers. Figure taken from [135].

Lepton Isolation   Prompt leptons (and photons) are typically isolated, i.e. without much activity around them, while non-prompt leptons often arise in the vicinity of jets, for instance in semi-leptonic decays of *b* and *c* quarks. Hence, restricting the maximum energy around the leptons is an effective approach to increase their purity in prompt leptons. Isolation energies are defined as the sum of activity within a cone around the lepton, which is calculated from the transverse momenta of track particles, transverse energies of calorimeter clusters or both. While tracking isolation is less affected by pile-up activity, calorimeter isolation can also account for the contribution from neutral hadrons.

In the isolation WPs used in this analysis, tracking isolation is calculated by summing the p_T of selected tracks within a cone of maximum size $\Delta R = 0.2$ around the lepton, excluding tracks associated with the lepton. The cone shrinks with increasing lepton p_T, as in boosted topologies other decay products can end up close to the lepton. Calorimeter-based isolation sums up the transverse energy of topo-clusters within a cone of size $\Delta R = 0.2$ around the lepton, which are corrected for contributions from pile-up and the underlying event [209]. Signal electrons need to pass the *Gradient* isolation WP [206], which combines both tracking and calorimeter-based isolation variables, and is approximately 80 % efficient at $E_T = 4.5$ GeV. To pass the signal criterion, muons have to pass the *FCTightTrackOnly* isolation WP, which is based on the one described in Ref. [122], with additions to better cope with the more demanding pile-up conditions during 2017 and 2018 data-taking [134]. Small corrections derived from measuring the isolation efficiencies in $Z \to ee/\mu\mu$ events are applied in simulation to match the efficiencies observed in data.

In the higgsino model, the lepton pair is likely to be collimated, i.e. the isolation cones of the leptons may overlap. This may result in one or both leptons failing the isolation criterion, and thus in a rejection of the signal event. To avoid this, the calculation of the isolation energies of each lepton has been adjusted to not take into account the contributions from the other lepton.

The lepton reconstruction efficiencies in a mix of higgsino and slepton samples after applying all identification, isolation and vertex association (impact parameter) requirements are shown in Figure 5.9. Signal electrons are reconstructed with an efficiency of about 20 % at $E_T = 4.5$ GeV which increases to about 75 % for $p_T > 30$ GeV. The muon reconstruction efficiency

ranges from approximately 50% at $p_\mathrm{T} = 3\,\mathrm{GeV}$ up to 90% for $p_\mathrm{T} > 30\,\mathrm{GeV}$.

Jets Jets are reconstructed at the electromagnetic scale from topo-clusters, using the anti-k_t algorithm [210, 211] with a radius parameter $R = 0.4$. Tracks with $p_\mathrm{T} > 500\,\mathrm{MeV}$ that are associated with the primary vertex are assigned to jets using ghost association [209, 212]. In this procedure, tracks are treated as infinitesimal soft, low-p_T particles in the jet finding algorithm, so they do not affect the calorimeter-jet reconstruction. Tracks are then assigned to the jet, they have been clustered with. Likewise, muon segments can be assigned to jets to account for hadronic leakage into the MS ("punch through"), if they can be ghost-associated during reconstruction.

In accord with Ref. [213], jets undergo a series of consecutive calibration steps for the jet energy scale (JES). First, the four-momenta of jets in data and simulation are corrected to point to the primary vertex without changing the jet energy. Next, contributions from pile-up are subtracted using a p_T density subtraction based on the jet area [209] and a residual pile-up correction derived from MC simulation. An absolute JES calibration corrects the jet energy and direction to the particle-level scale, which is derived by clustering stable final-state particle in simulation to truth jets. A global sequential calibration [214] reduces flavor dependence and energy-leakage effects to improve the JES resolution using calorimeter, track and muon-segment variables. To account for differences in jet responses between data and MC simulation, jets in data are calibrated using in-situ measurements. The differences are quantified by balancing the jet p_T against a well-measured reference object, such as photons and Z bosons. Similarly, the jet energy resolution (JER) is calibrated by measuring it in data and MC using p_T asymmetry in dijet events [215].

To suppress jets originating from pile-up activity, the tracks associated with a jet are used to construct variables sensitive to the fraction of the total p_T that can be associated with tracks originating from the primary vertex. These variables are combined into a multivariate discriminant by the jet vertex tagger (JVT) [216].

In the analysis, jets are required to have $p_\mathrm{T} > 20\,\mathrm{GeV}$ and $|\eta| < 4.5$. Jets with $p_\mathrm{T} < 120\,\mathrm{GeV}$ and $|\eta| < 2.5$ are required to pass the *Medium* WP of the JVT, that corresponds to an average efficiency of 92% for jets originating from a hard interaction. The hard-scatter jet efficiency of the JVT has been measured in $Z \to \mu\mu$ events recoiling against a jet, to derive corrections that match the efficiencies between data and simulation. Jet multiplicities and analysis variables are calculated with signal jets, which need to satisfy $p_\mathrm{T} > 30\,\mathrm{GeV}$ and $|\eta| < 2.8$.

Flavor Tagging In particular the comparable long lifetime ($\sim 1.5\,\mathrm{ps}, c\tau \sim 450\,\mu\mathrm{m}$), high mass and decay multiplicity of b hadrons allows to tag jets that contain such hadrons [217]. Their decays are characterized by displaced vertices and large impact parameter values of the charged particles from the b-hadron decays, thus central ingredients in b-tagging are the information from tracks. Several algorithms aim to tag such signatures, either based on the impact parameters or on explicit reconstruction of secondary vertices. To maximize b-tagging performance, the outputs of these taggers are combined via a multivariate classifier named *MV2*, which is based on a Boosted Decision Tree trained on $t\bar{t}$ and Z' samples [218].

In the analysis, the *MV2c10* discriminant is used as b-tagging algorithm. Baseline jets with $|\eta| < 2.5$ serve as input, maintaining the $p_\mathrm{T} > 20\,\mathrm{GeV}$ requirement of baseline jets

to maximize the rejection power against top-related backgrounds. For the same reason, a high-efficiency WP for the *MV2c10* tagger was chosen: b-jets from simulated $t\bar{t}$ events are identified with an 85 % efficiency, with a rejection factor of 3 for c-jets and 34 for light-quark and gluon jets. Corrections are applied to account for differences in the b-tagging efficiency between data and simulation, as well as differences in the misidentification rates.

Overlap Removal As the reconstruction schemes outlined above run independently from each other, ambiguities between the reconstructed leptons and jets may arise, i.e. a signature in the detector may have been identified as both an electron and a jet. To resolve these ambiguities, close-by objects are removed in several subsequent steps, following a scheme established in Run 1 [219]. It employs a distance measure $\Delta R_y = \sqrt{(\Delta y)^2 + (\Delta \phi)^2}$ that uses the rapidity y, which captures better where the jet's p_T is located than the pseudorapidity [220], as the latter neglects the mass of the jet's constituents. The steps are performed in the following order, with only surviving objects participating in subsequent steps:

- electrons are rejected that share an inner detector track with a muon candidate to remove muon bremsstrahlung followed by a photon conversion

- non-b-tagged jets separated from electrons by $\Delta R_y < 0.2$ are rejected

- electrons within $\Delta R_y < 0.4$ of a jet are rejected

- non-b-tagged jets having less than associated 3 tracks, separated from muons by $\Delta R_y < 0.2$ or being ghost-associated with a muon, are rejected

- muons within $\Delta R_y < 0.4$ of a jet are rejected

Missing Transverse Energy Momentum conservation in the transverse plane implies, that the transverse momenta of all final state particles should sum up to zero. Hence any momentum imbalance, referred to as missing transverse momentum $\mathbf{p}_\mathrm{T}^\mathrm{miss}$, infers the presence of invisible particles. It is constructed from all reconstructed particles and jets in the event. Tracks not associated with any of the reconstructed objects, but with the primary vertex are taken into account via an additional soft term. The missing transverse momentum, with its magnitude labeled as $E_\mathrm{T}^\mathrm{miss}$, is defined as the negative vector sum of the transverse momenta of all reconstructed objects[†] and the soft term [221]

$$-\mathbf{p}_\mathrm{T}^\mathrm{miss} = \sum \mathbf{p}_\mathrm{T}^e + \sum \mathbf{p}_\mathrm{T}^\gamma + \sum \mathbf{p}_\mathrm{T}^\mu + \sum \mathbf{p}_\mathrm{T}^\mathrm{jet} + \sum \mathbf{p}_\mathrm{T}^\mathrm{track}. \tag{5.7}$$

All reconstructed baseline objects as defined above are used in the calculation of $\mathbf{p}_\mathrm{T}^\mathrm{miss}$. To reduce dependence on pile-up, the *Tight* WP [222] (rejecting jets with $p_\mathrm{T} < 30\,\mathrm{GeV}$ and $|\eta| < 2.4$) was used for the calculation. Ambiguities between close-by objects are resolved by a dedicated overlap removal procedure [222] in the calculation, that runs independently from the one used in the analysis. The reconstructed $E_\mathrm{T}^\mathrm{miss}$ depends directly on the energy scale and resolution of the objects. As the reconstructed $E_\mathrm{T}^\mathrm{miss}$ is a global variable built from information of the whole detector, it is susceptible to many imperfections. The $E_\mathrm{T}^\mathrm{miss}$ depends

---

[†] in case hadronic taus are also reconstructed, an additional term $\sum \mathbf{p}_\mathrm{T}^\tau$ would arise, but in the analysis taus are treated as jets in the $E_\mathrm{T}^\mathrm{miss}$ calculation

strongly on the energy scale and resolution of the objects entering its calculation. Thus mismeasurements, contributions from pile-up activity or particles emitted in uninstrumented regions of the detector, can cause significant deviations from the "real" E_T^{miss} in the event. In particular, this allows events without invisible particles in the decay chain such as $Z \to ee/\mu\mu$, to pass selections with actual stringent E_T^{miss} requirements due to the presence of so-called fake E_T^{miss}.

5.3.2 Analysis Variables

From the objects defined above several variables are constructed for usage in the analysis. These variables are effective in separating signal from background events, but are also used to enrich a selection in a specific type of background. Most of these variables are already well established in experimental particle physics and have been adapted to optimize their performance for the analysis.

Transverse Mass   The transverse mass M_T is sensitive to the production of a massive particle with mass M, which decays into an invisible particle of mass m_1 and a visible particle with m_2. In case no other invisible states are produced in association with the parent particle, its mass can be constrained by

$$M_T^2 \equiv m_1^2 + m_2^2 + 2\left[E_T^1 E_T^2 - \mathbf{p}_T^1 \mathbf{p}_T^2\right], \text{ with } E_T^1 = E_T^{miss} \text{ and } \mathbf{p}_T^1 = \mathbf{p}_T^{miss}. \tag{5.8}$$

This variable has a kinematic endpoint given by the mass of the parent particle $M_T^2 \leq M^2$, where equality holds for cases, in which the decay is contained completely in the transverse plane. In the analysis, the transverse mass is in particular useful to tag events containing a W boson such as $W + \text{jets}$ and semi-leptonic $t\bar{t}$ events, as these tend to pile up just before the W boson mass M_W. For that purpose, the transverse mass in the analysis is calculated with the leading lepton ℓ_1 and assuming the second particle to be a neutrino. Consequently the masses of the daughter particles can be neglected and the formula for the transverse mass $m_T^{\ell_1}$ becomes

$$m_T^{\ell_1} = \sqrt{2\left(E_T^{miss} E_T^{\ell_1} - \mathbf{p}_T^{miss}\mathbf{p}_T^{\ell_1}\right)}. \tag{5.9}$$

Signal events do not have a kinematic endpoint and thus their distribution is rather flat in $m_T^{\ell_1}$, which is exploited to separate them from the backgrounds mentioned above.

Stransverse Mass   The Stransverse mass (m_{T2}) variable can be understood as a generalization of the transverse mass for final states with more than one invisible particle. The m_{T2} definition used in this analysis considers exactly the topology of the slepton model shown in Figure 5.2b: the pair production of a heavy particle $\tilde{\ell}$, which decays via $\tilde{\ell} \to \ell\chi$ into a detectable particle ℓ and an invisible particle χ. In case the invisible transverse momenta $\mathbf{p}_T^{\chi_1}, \mathbf{p}_T^{\chi_2}$ would be known, it follows from Equation (5.8) that

$$m_{\tilde{\ell}} \geq \max\left\{m_T(\mathbf{p}_T^{\ell_1}, \mathbf{p}_T^{\chi_1}), m_T(\mathbf{p}_T^{\ell_2}, \mathbf{p}_T^{\chi_2})\right\}. \tag{5.10}$$

However in the experiment it is unknown how the missing transverse momentum is distributed among the invisible particles, which spoils the direct application of the transverse mass.
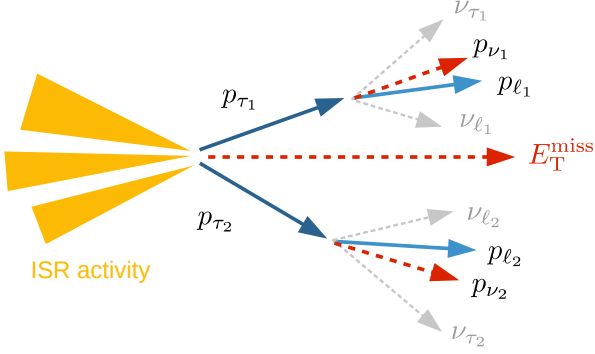
Figure 5.10: Schematic illustration of the target topology $m_{\tau\tau}$ is constructed for. The di-tau system is boosted by some hadronic ISR activity. Consequently, the tau leptons are not back-to-back, but are oriented in the same direction. The sum of the neutrino momenta p_{ν_i} in each decay leg is then approximately collinear to the visible lepton momenta p_{ℓ_i}.

To overcome this issue, the m_{T2} variable is constructed by iterating over all possible ways $\{\mathbf{q}_{\mathrm{T}}^1, \mathbf{q}_{\mathrm{T}}^2\}$ to distribute $\mathbf{p}_{\mathrm{T}}^{\mathrm{miss}}$ among the two invisible particles and is defined as

$$m_{\mathrm{T2}} \equiv \min_{\mathbf{q}_{\mathrm{T}}^1 + \mathbf{q}_{\mathrm{T}}^2 = \mathbf{p}_{\mathrm{T}}^{\mathrm{miss}}} \left[\max \left\{ m_{\mathrm{T}}(\mathbf{p}_{\mathrm{T}}^{\ell_1}, \mathbf{q}_{\mathrm{T}}^1), m_{\mathrm{T}}(\mathbf{p}_{\mathrm{T}}^{\ell_2}, \mathbf{q}_{\mathrm{T}}^2) \right\} \right] \leq m_{\tilde{\ell}}. \tag{5.11}$$

Similar to the transverse mass, m_{T2} is bounded from above by $m_{\tilde{\ell}}$, i.e. the kinematic endpoint in the slepton model is given by the slepton mass. From the definition of m_{T} it follows that the calculation of m_{T2} also depends on m_χ (with $m_\chi < m_{\mathrm{T2}}$). The m_{T2} calculation in the analysis assumed a mass of the invisible particles of $100\,\mathrm{GeV}$ and is hence denoted as m_{T2}^{100}. This value represents roughly the order of magnitude of the $\tilde{\chi}_1^0$ mass in the slepton grid. Only a slight dependence of the m_{T2} distribution on this parameter was observed, such that m_{T2}^{100} provides an approximate kinematic endpoint also in slepton signals with larger or smaller $\tilde{\chi}_1^0$ masses. In summary, m_{T2}^{100} is calculated with the transverse momenta $\mathbf{p}_{\mathrm{T}}^{\ell_1}, \mathbf{p}_{\mathrm{T}}^{\ell_2}$ of the two leptons and the missing transverse momentum $\mathbf{p}_{\mathrm{T}}^{\mathrm{miss}}$. The calculation of the variable is carried out using the implementation from Ref. [223], which utilizes a bisection-based algorithm to perform the minimization in Equation (5.11).

Di-Tau Invariant Mass   The di-tau invariant mass $m_{\tau\tau}$ [57, 224, 225] aims to reconstruct the tau momenta in fully leptonic $Z \to \tau\tau$ decays, in which the Z boson is sufficiently boosted such that the τ-leptons are not back-to-back. In this case, the neutrinos from each τ-decay are approximately collinear to the visible lepton momenta, as depicted in Figure 5.10. This allows to express the total invisible four-momentum of each decay leg $p_{\nu_i} = p_{\nu_{\tau_i}} + p_{\nu_{\ell_i}}$ as a rescaling of the visible lepton four-momentum $p_{\nu_i} \simeq \xi_i p_{\ell_i}$, where $i = 1, 2$ runs over both τ-decay chains. The four-momentum of each tau is then $p_{\tau_i} \simeq (1 + \xi_i) p_{\ell_i}$, so that the di-tau invariant mass squared becomes

$$m_{\tau\tau}^2 = (p_{\tau_1} + p_{\tau_2})^2 \simeq 2 p_{\ell_1} p_{\ell_2} (1 + \xi_1)(1 + \xi_2), \tag{5.12}$$

where the τ masses have been neglected, as the taus are assumed to be heavily boosted and thus ultra relativistic. The parameters ξ_1 and ξ_2 are determined by solving the equations

$$\mathbf{p}_{\mathrm{T}}^{\mathrm{miss}} = \xi_1 \mathbf{p}_{\mathrm{T}}^{\ell_1} + \xi_2 \mathbf{p}_{\mathrm{T}}^{\ell_2}. \tag{5.13}$$

From the above definitions it follows that $m_{\tau\tau}^2$ can become negative if exactly one of $\xi_i < -1$. As it can be seen from Equation (5.13) this can occur if the missing momentum points into

Figure 5.11: Decay tree used to calculate the RJR-related variables. Objects are grouped either into the ISR or the SUSY frame S. Their sum forms the center-of-mass frame CM, which moves within the laboratory frame Lab. The frame S consists of the frames for invisible particles I, the leptons L and for potential additional visible objects V.
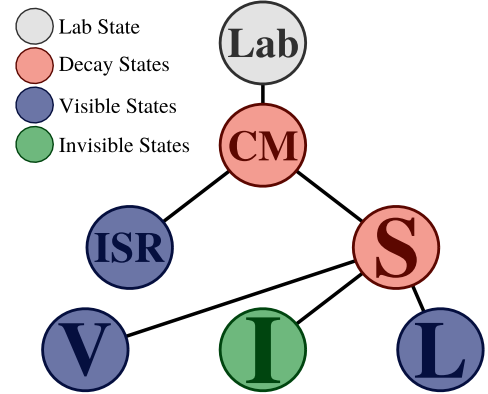
the opposite direction of a lepton, whose transverse momentum p_T is much smaller than the E_T^{miss}. Physically, this happens for instance in $t\bar{t}$ and WW events, in which a lepton and neutrino are back-to-back, presumably originating from different legs. Hence the $m_{\tau\tau}^2$ is heavily asymmetric and exhibits different features for positive and negative values[†]. To capture this behavior, the final $m_{\tau\tau}$ variable used in the analysis is defined as

$$m_{\tau\tau} = \begin{cases} \sqrt{m_{\tau\tau}^2}, & \text{for } m_{\tau\tau}^2 \geq 0 \,, \\ -\sqrt{|m_{\tau\tau}^2|}, & \text{for } m_{\tau\tau}^2 < 0 \,. \end{cases} \tag{5.14}$$

In the distribution of $m_{\tau\tau}$, $Z \to \tau\tau$ events exhibit then a clear peak around the Z boson mass (see e.g. Figure 5.27), which is exploited in the analysis to veto or enrich a selection with this background. Other backgrounds as well as signal events are mostly evenly distributed across $m_{\tau\tau}$.

Variables from Recursive Jigsaw Reconstruction   In order to directly exploit the ISR topology present in the signal models, two variables derived from Recursive Jigsaw Reconstruction (RJR) [226] are used in the analysis. RJR denotes a technique to analyze reconstructed particle interactions, in which the reconstructed objects are assigned to a set of decays and rest frames that represent the signal topology under consideration. Missing information due to invisible particles and combinatoric ambiguities due to indistinguishable particles are resolved by the application of so-called *jigsaw rules*. After the information reconstructed in the event was distributed across the superimposed decay tree, variables in the respective frames can be constructed.

For the analysis, the RJR approach designed for compressed mass spectra described in Ref. [227] was adapted. Figure 5.11 shows the decay tree used. Jets that are associated with ISR activity, are assigned to a frame labeled as ISR. In contrast, objects associated with the SUSY system are assigned to a system labeled S. The sum of the ISR and S frames defines their center-of-movement system CM, that moves within the laboratory frame Lab, in which all four-vectors are measured. The SUSY system S itself is built from a frame I containing invisible states, and the frames L and V, which contain lepton and potentially additional visible objects, respectively. Obviously, the lepton pair is assigned to the L frame, while the

---
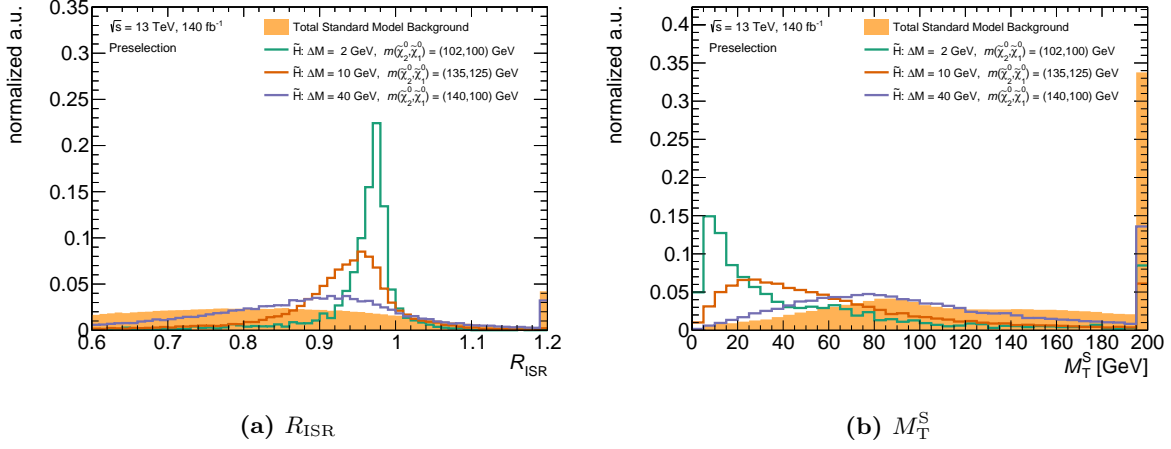[†] the most obvious one is the absence of a $Z \to \tau\tau$ peak for negative values

(a) R_{ISR} **(b)** $M_{\mathrm{T}}^{\mathrm{S}}$

Figure 5.12: Distributions of R_{ISR} and $M_{\mathrm{T}}^{\mathrm{S}}$ at preselection level for higgsino signal points corresponding to mass splittings of 2, 10 and 40 GeV. The distribution of the total SM background is shown in light orange. All curves are normalized to 1 in order to improve the visualization of the respective signal shapes. The first (last) bin contains the underflow (overflow).

measured missing transverse momentum $\mathbf{p}_{\mathrm{T}}^{\mathrm{miss}}$ is assigned to I. Jets can be assigned either to the ISR or V frame, an ambiguity that has to be resolved by an adequate jigsaw rule. No other ambiguities in the object assignment arise, as the analysis selection (see Section 5.3.5) vetoes events with any additional objects. Motivated by the topology of events containing a compressed SUSY system recoiling against hadronic ISR activity, the applied jigsaw rule aims to group objects together which are close-by in phase space. Effectively, this means to minimize the reconstructed masses of the ISR and S system, M_{ISR} and M_{S}, respectively. Following the strategy of Ref. [227], an exclusively transverse point of view is imposed by setting the longitudinal momenta of all objects to 0 in the RJR calculation. Moreover, the mass of the I system is chosen to be 0 for convenience[†]. The mass of the CM frame can be written as

$$M_{\mathrm{CM}} = \sqrt{M_{\mathrm{ISR}}^2 + \left|\mathbf{p}_{\mathrm{ISR}}^{\mathrm{CM}}\right|^2} + \sqrt{M_{\mathrm{S}}^2 + \left|\mathbf{p}_{\mathrm{S}}^{\mathrm{CM}}\right|^2}, \qquad (5.15)$$

where $\left|\mathbf{p}_{\mathrm{ISR}}^{\mathrm{CM}}\right|$ and $\left|\mathbf{p}_{\mathrm{S}}^{\mathrm{CM}}\right|$ are the magnitudes of the (transverse) momenta of the ISR and S system, respectively, evaluated in the CM frame. As M_{CM} is independent from the choice to assign an object either to the ISR or S system, a minimization of M_{ISR} and M_{S} is simultaneously a maximization of $|\mathbf{p}_{\mathrm{ISR}}^{\mathrm{CM}}|$ and $|\mathbf{p}_{\mathrm{S}}^{\mathrm{CM}}|$ (which are per definition of equal magnitude in the CM frame). Hence the applied jigsaw rule resolves ambiguities in the object assignment by maximizing the back-to-back p_{T} of the ISR and SUSY systems.

The decay tree and jigsaw rule described above have been set up using the `RestFrames` software package [228], to define two variables based on RJR that are used in the analysis.

R_{ISR}   This variable parametrizes the amount of ISR-assisted $E_{\mathrm{T}}^{\mathrm{miss}}$ in the event by projecting, in the CM frame, the momentum of the S system onto the axis defined by the momentum

---

[†] although this is not a necessarily correct assignment for signals with massive invisible particles, the derived quantities show the desired kinematic properties

of the ISR system and normalizing it by the magnitude of the latter, i.e.

$$R_{\text{ISR}} = \frac{\left| \mathbf{p}_{\text{I}}^{\text{CM}} \cdot \hat{\mathbf{P}}_{\text{ISR}}^{\text{CM}} \right|}{\left| \mathbf{p}_{\text{ISR}}^{\text{CM}} \right|} \, , \tag{5.16}$$

where all momenta are considered to be only transversal. R_{ISR} can be understood as an estimator of the quantity $E_{\text{T}}^{\text{miss}}/|\mathbf{p}_{\text{T}}^{\text{ISR}}|$ and scales as $m_{\tilde{\chi}}/m_{\tilde{P}}$ to zeroth order [227], where $\tilde{P}$ denotes the parent sparticle decaying into the LSP $\tilde{\chi}$. Hence, R_{ISR} is close to 1 for signal events, while it has a broader distribution for background. The resolution in R_{ISR} improves for smaller mass splittings as depicted in Figure 5.12a, which makes it very powerful to separate signal from background in the very compressed regime.

M_{T}^{S} The second RJR-based variable, M_{T}^{S}, is defined as the transverse mass of the S system (V+I+L). In particular for signal events that correspond to small mass splittings, M_{T}^{S} accumulates at lower values as shown in Figure 5.12b. For background events the M_{T}^{S} distribution is rather broad, rendering it a viable candidate to separate signal from background events.

5.3.3 Trigger Strategy

Triggers are required to select only those events for further processing during data-taking that contain promising signatures. Consequently each analysis needs to set up a trigger strategy, which defines how the events are selected at trigger level. This is typically a set of triggers that require the same or similar signatures as present in the signal models under consideration. After introducing the general terms to describe the performance of triggers, the trigger strategy for the analysis is presented.

General Trigger Characteristics

Although a trigger makes in principle only a yes–no decision, complexity in the analysis arises due to differences in the online and offline reconstruction, e.g. in the calculation of $E_{\text{T}}^{\text{miss}}$. The performance of a trigger shows several specific characteristics, and is typically described by its *turn-on curve*. A schematic example of such a turn-on curve for a simple trigger which fires only on one signature is depicted in Figure 5.13. Plotted with respect to the associated offline reference, the trigger efficiency is not a step function around the online threshold, but smeared out around that value[†]. First, the trigger efficiency rises dynamically in the so-called turn-on region before it reaches a constant maximum, referred to as plateau region. Triggers are not necessarily fully efficient even in their plateau, i.e. have a maximum efficiency of one, but their efficiency may be significant lower. Such inefficiencies may originate for example from a reduced coverage at trigger level as it is the case for muons, because trigger capabilities for them end at $|\eta| < 2.4$, but offline reconstruction extends up to $|\eta| < 2.7$ (see Section 3.2.6). A large width of the turn-on region typically indicates notable differences in the online and offline calculation of the signature that is triggered on. Triggers can be defined to have more than one trigger leg, i.e. require more than one distinct signature in the event. Such multi-leg

---

[†] mathematically, this can be thought of as a convolution of a step function with a Gaussian, which gives an error function representing the turn-on behavior
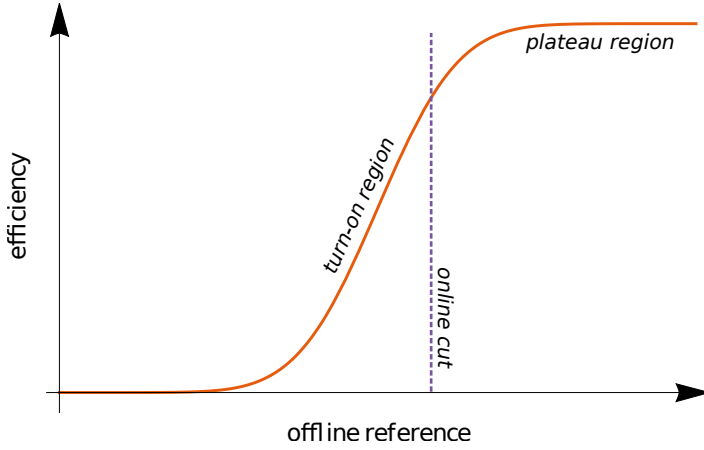
Figure 5.13: Schematic illustration of the turn-on curve for a trigger with one leg. The orange solid line represents the trigger efficiency with respect to some offline reference. The purple dashed line marks the online threshold for the trigger.

triggers have the advantage that the online thresholds of each leg are lower than the thresholds of the corresponding single-leg triggers with the same write-out rate. Combined triggers can consequently be tailored towards the needs of the individual analysis. On the other hand, the maximal efficiency is typically lower as the potential inefficiencies of each leg multiply with each other. Moreover, multi-leg triggers are much more complex because their turn-on curves are multi-dimensional and may be impacted by correlations among the individual trigger legs.

An important requirement on simulation is, that the trigger decisions are modeled well, i.e. the turn-on curves agree between data and MC. This is usually the case in the plateau region where the trigger efficiency is constant. In the turn-on region, systematic mismodeling of the offline–online differences can have a larger impact and change the slope of the turn-on curve notably. For that reason, triggers are typically used only in their plateau region by applying adequate offline cuts. Such cuts however reduce the signal acceptance and a significant signal loss may consequently motivate to select events also in the turn-on region of the triggers. In this case, scale factors have to be derived to correct the MC trigger efficiencies to match those in data.

Trigger Strategy for High-$E_{\mathrm{T}}^{\mathrm{miss}}$ Selection

Although the decay topology for higgsino production is quite rich as shown in Figure 5.2a, most of the final state objects are too soft for providing an adequate signature to trigger on. The LSPs are highly energetic, but escape undetected and are thus visible only indirectly via missing transverse momentum. At tree level, the LSPs are emitted roughly back-to-back, consequently the overall $E_{\mathrm{T}}^{\mathrm{miss}}$ is rather small and typically does not surpass the $E_{\mathrm{T}}^{\mathrm{miss}}$ trigger thresholds. In a similar fashion, this holds also for the slepton model. Consequently the analysis considers in both scenarios the SUSY system to be boosted with respect to an ISR jet, as depicted in Figure 5.14b. In this case, the LSPs are emitted in a similar direction and the magnitude of the missing transverse momentum is notably larger. This allows to select signal events that exhibit such an ISR topology using an $E_{\mathrm{T}}^{\mathrm{miss}}$ trigger. Due to evolving pile-up conditions during data taking in Run 2, the $E_{\mathrm{T}}^{\mathrm{miss}}$ trigger that gives the most data statistics varies from period to period. Hence, several $E_{\mathrm{T}}^{\mathrm{miss}}$ triggers with online thresholds between 70 in 2015 and 110 GeV in 2018 are used in the analysis, and are summarized in
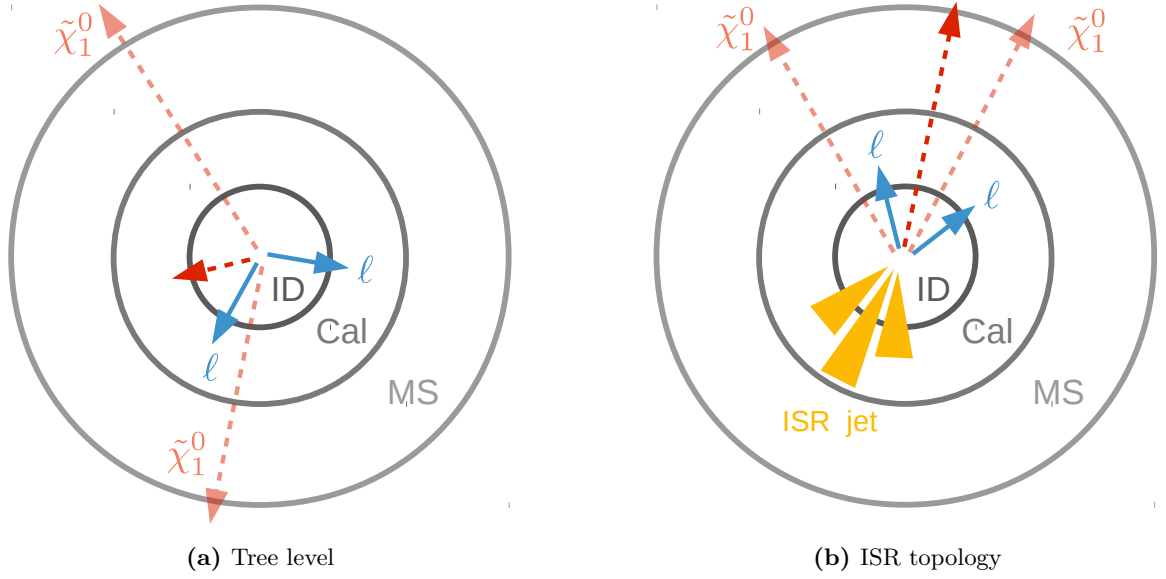
(a) Tree level

(b) ISR topology

Figure 5.14: Illustration of the trigger strategy used in the analysis. At tree level (a), the LSPs (pale red arrows) are approximately back-to-back, resulting in an overall small missing transverse momentum (red arrow). As the lepton pair (blue arrows) is very soft, no suitable signature for triggering is available. In case of ISR activity (b), the complete SUSY system is boosted with respect to one or multiple jets. The LSPs are emitted into the same direction, which increases the amount of missing transverse momentum in the event.

Appendix B.2.

All E_T^{miss} triggers were found to be fully efficient for E_T^{miss} above 200 GeV in the phase space covered by the analysis (see Appendix B), which consequently defines the lower threshold of the high-E_T^{miss} regime. An offline requirement of $E_T^{miss} > 200$ GeV ensures that these trigger are used in their plateau region and no trigger scale factors have to be applied.

Trigger Strategy for Low-E_T^{miss} Selection

The low-E_T^{miss} selection recovers signal events with E_T^{miss} below 200 GeV to enhance the sensitivity of the search. Triggering such events also with E_T^{miss} triggers as in the high-E_T^{miss} selection has some drawbacks. First, the E_T^{miss} triggers are for the most part not in the plateau region and consequently miss signal events, which would in principle pass the trigger threshold in terms of their offline E_T^{miss}. Second, the usage of the triggers in their turn-on regions necessitates the derivation of trigger scale factors in the phase space of the analysis. The specific decay topology of the higgsino model, motivates the usage of multi-object triggers that allow a lower online threshold for the E_T^{miss}-trigger leg. Four such "higgsino triggers", directly tailored towards the higgsino model have been added to the trigger menu for 2017 data-taking and onwards [107]. These do not trigger only on E_T^{miss} but have also some soft requirements on the presence of leptonic and hadronic activity. At HLT level, these triggers have the following requirements:

- two muons $p_T > 4$ GeV, one jet $p_T > 20$ GeV, $E_T^{miss} > 40$ GeV

- one muon $p_T > 4\,\text{GeV}$, one jet $p_T > 90\,\text{GeV}$, $E_T^{\text{miss}} > 90\,\text{GeV}$

- one electron $E_T > 5\,\text{GeV}$, one jet $p_T > 50\,\text{GeV}$, $E_T^{\text{miss}} > 70\,\text{GeV}$

- two electrons $E_T > 5\,\text{GeV}$, one jet $p_T > 40\,\text{GeV}$, $E_T^{\text{miss}} > 70\,\text{GeV}$

In addition, all higgsino triggers exploit the ISR topology by requiring a minimal angular distance between the E_T^{miss} and the two leading jets† at HLT of $\Delta\phi(j_{1,2}, E_T^{\text{miss}}) > 1.0$. The di-muon variant requires furthermore an invariant mass of the muon system above $1\,\text{GeV}$. All these triggers would allow for an offline cut on E_T^{miss} lower than $200\,\text{GeV}$ and hence could be promising additions to the regular E_T^{miss} triggers for the part of the dataset where they are available. Despite labeled as higgsino triggers, all trigger signatures used are present in the slepton model as well. Consequently they are potential additions also for that scenario.

Three different trigger configurations have been considered for the low-E_T^{miss} regime: using the same set of E_T^{miss} triggers as in the high-E_T^{miss} selection, a logical OR between the four higgsino triggers and a logical OR between the E_T^{miss} and the higgsino triggers. To compare the performance of each configuration, the trigger efficiencies have been evaluated in representative signal samples corresponding to mass splittings of 10 and $30\,\text{GeV}$. The performance was evaluated in a selection similar to the one used to preselect events for the main analysis (see Section 5.3.5). The selection requires exactly two signal leptons, the absence of any additional baseline leptons and at least one jet with $p_T > 100\,\text{GeV}$. The leptons need to be of same flavor (SF) and opposite sign (OS), and their invariant mass has to be above $1\,\text{GeV}$. To ensure the lepton legs of the higgsino triggers are in their respective plateau regions, muons (electrons) are required to have p_T above 5 (6) GeV, when the performance of the combined triggers is evaluated. Figure 5.15 shows the trigger efficiencies with respect to E_T^{miss} in the low-E_T^{miss} regime obtained from these three trigger configurations . For both mass splittings, the E_T^{miss} trigger reaches its maximal efficiency already at around 150–$160\,\text{GeV}$, which is roughly also the case for the higgsino triggers. However, due to inefficiencies originating from the individual trigger legs, these triggers are not fully efficient in their plateau. Between 100 and $130\,\text{GeV}$ the higgsino triggers pick up signal events that are missed by the E_T^{miss} trigger otherwise, so that the logical OR of both trigger types would be 80–$100\,\%$ efficient in signal across the considered E_T^{miss} spectrum.

As the E_T^{miss} trigger is already fully efficient around $150\,\text{GeV}$ in higgsino signal samples, which was found to be the case also for slepton signals, the gain in signal by including the higgsino triggers is not large enough to motivate their introduction to the analysis. Firstly, they are available only for parts of the total dataset, which limits their total contribution to the number of signal events even more. Further, the usage of combined triggers would require additional studies of the individual legs and their correlation. For these reasons — and to keep the complexity of the trigger strategy on a reasonable level — the low-E_T^{miss} selection uses the same E_T^{miss}-triggers as the high-E_T^{miss} selection. Dedicated scale factors are derived to take into account mismodeling of the efficiencies in simulation in the E_T^{miss} regime.

---

† leading is meant to be understood with respect to p_T, i.e. the leading jet in an event is the jet with the largest transverse momentum

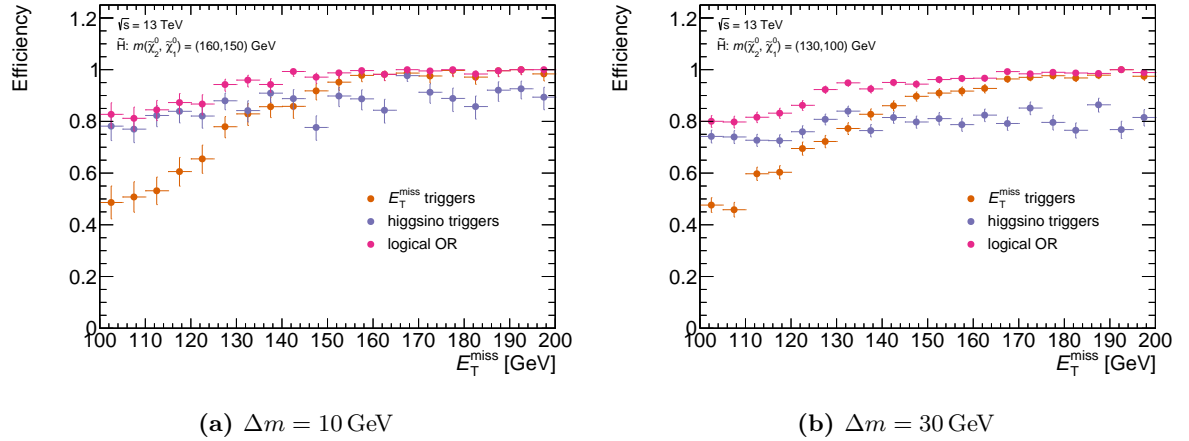**(a)** $\Delta m = 10\,\text{GeV}$ **(b)** $\Delta m = 30\,\text{GeV}$

Figure 5.15: Performance of the different trigger strategies in two representative higgsino signal, that correspond to mass splittings of 10 and 30 GeV, respectively. The trigger efficiencies for signal events obtained by requiring the E_T^miss and higgsino triggers are shown as orange and purple, respectively. The efficiency for the logical OR of both triggers types is shown in pink.

Trigger Scale Factors

The E_T^miss-trigger scale factors have been derived by measuring the trigger efficiencies in events selected by muon triggers, as described in Appendix B. The measurements were performed in a region close to the one used in the analysis, to account for the phase space dependence of E_T^miss-trigger scale factors. The efficiencies were measured separately for each E_T^miss trigger and with respect to a dedicated E_T^miss flavor, $E_{\text{T},\,\mu\,\text{invis}}^\text{miss}$, in which the muons are treated as invisible in the calculation. Scale factors are derived by fitting the ratio of the data and MC trigger efficiencies in terms of $E_{\text{T},\,\mu\,\text{invis}}^\text{miss}$, as shown exemplary in Figure 5.16. They have been found to provide meaningful corrections for values of the nominal E_T^miss flavor used in the main analysis down to 120 GeV, which defines the lower threshold of the low-E_T^miss regime. In the analysis, the values of the scale factors are typically in the range from approximately 0.8 to 1, with the vast majority being larger than 0.95. Consequently, the scale factors represent only a small correction to the MC predictions.

In the preliminary result, the scale factors have been applied only to signal events. As all important backgrounds, which are estimated with MC, are normalized to data in dedicated CRs, any mismodeling of trigger efficiencies in the background predictions is captured on a global scale in the normalization factors. This handling will be improved in the final analysis result, where the scale factors are also applied to the background samples, so that the corrections depend on E_T^miss. This has only a small impact on the normalization factors and the impact on the results of the analysis is negligible.

5.3.4 Event Cleaning

Before events are considered for analysis, they need to pass a series of cleaning cuts. The first set of cuts is applied in data only, and ensures a good event quality and a fully operational detector. Events are checked for error statuses of the tile and LAr calorimeters as well as the
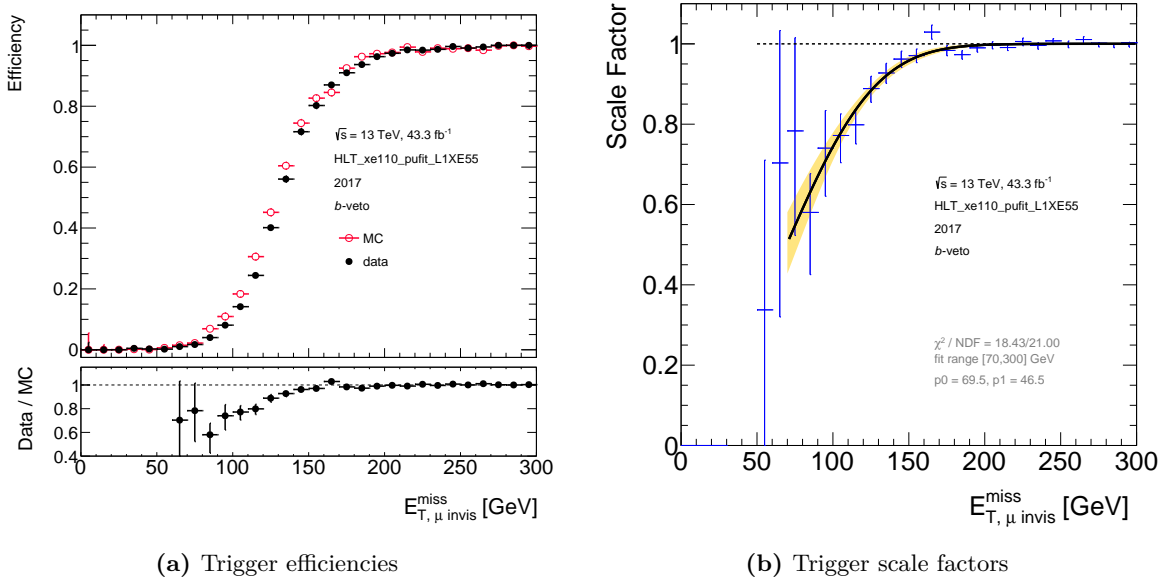
(a) Trigger efficiencies

(b) Trigger scale factors

Figure 5.16: Examples for E_T^{miss}-trigger efficiencies measured in data and MC simulation with respect to $E_{T,\,\mu\,\text{invis}}^{miss}$, as well as the associated scale factors. The plots show the results for the trigger HLT_xe110_pufit_L1XE55, in events with no b-tagged jet.

SCT detector, in order to reject events that are corrupted, e.g. by noise bursts. Furthermore, incomplete events, in which some detector information is missing, are removed. Data events are required to be contained in a luminosity block — a 1–2 minute period of approximately constant data-taking conditions — which was flagged to have all subdetectors working and provide physics objects of good quality [108]. A second set of cuts is applied in both data and simulation. Events need to have at least one reconstructed primary vertex, with a minimum of 2 assigned tracks satisfying $p_T > 500\,\text{MeV}$. Jets may not only originate from the hard-scattering interaction but also from non-collision background. To distinguish between them, a series of criteria is applied to each jet, referred to as jet cleaning [229]. As the presence of an "unclean" jet may affect many event quantities like the E_T^{miss}, events containing such jets are discarded.

5.3.5 Preselection

The 2ℓ signal selections are all based on a common preselection, which is summarized in Table 5.3. Events are required to have exactly two signal leptons of OS and of the SF. In the following, the leading and subleading leptons are labeled as ℓ_1 and ℓ_2, respectively. Events containing additional baseline leptons are vetoed.

The aim of the preselection requirements is to reduce background and to set up a basis for the SRs and CRs. The leptons are required to be at least $\Delta R_{\ell\ell} > 0.05$ far apart to reject extremely collimated leptons pairs from photon conversions, e.g. from $W\gamma \to \ell\nu\gamma$ events, where the lepton from the W boson is not reconstructed. Due to limitations of the data-driven fake estimation (see Section 5.5.2), this requirement is tighter for electron pairs

Variable	2ℓ Preselection Requirements
Number of leptons	$= 2$ leptons
Lepton charge and flavor	$e^{\pm}e^{\mp}$ or $\mu^{\pm}\mu^{\mp}$
$\Delta R_{\ell\ell}$	$\Delta R_{ee} > 0.3, \Delta R_{\mu\mu} > 0.05, \Delta R_{e\mu} > 0.2$
Lepton invariant mass	$m_{\ell\ell} \in [1, 60]\,\mathrm{GeV}$, excluding $[3, 3.2]\,\mathrm{GeV}$
Lepton p_T	$p_T(\ell_1) > 5\,\mathrm{GeV}$
$m_{\tau\tau}$	$< 0\,\mathrm{GeV}$ or $> 160\,\mathrm{GeV}$
E_T^{miss}	$> 120\,\mathrm{GeV}$
Number of jets	≥ 1
Number of b-tagged jets	$= 0$
Leading jet p_T	$> 100\,\mathrm{GeV}$
$\min(\Delta\phi(\text{any jets}, \mathbf{p}_T^{\mathrm{miss}}))$	> 0.4
$\Delta\phi(j_1, \mathbf{p}_T^{\mathrm{miss}})$	> 2.0

Table 5.3: Requirements that define the preselection applied on all events that enter the 2ℓ electroweakino and slepton SRs.

($\Delta R_{ee} > 0.3$) and for leptons of different flavor (DF) ($\Delta R_{e\mu} > 0.2$). The invariant mass of the lepton pair $m_{\ell\ell}$ is required to be $m_{\ell\ell} < 60\,\mathrm{GeV}$ in order to suppress contamination from on-shell $Z \to ee/\mu\mu$ decays. The restriction to $m_{\ell\ell} > 1\,\mathrm{GeV}$ accounts for requirements on the lepton invariant mass at generator level in some of the background MC samples. The necessary limitation of the minimal geometric distance for electron pairs ΔR_{ee} does not allow to access very low invariant masses, hence this regime is discarded by requiring $m_{ee} > 3\,\mathrm{GeV}$. The $m_{\ell\ell}$ range $[3, 3.2]\,\mathrm{GeV}$ is excluded to veto events originating from J/Ψ decays. No veto is placed around other resonances such as the Υ state, as these are expected to contribute much less to the SRs. A requirement on the leading lepton transverse momentum $p_T(\ell_1) > 5\,\mathrm{GeV}$ reduces contamination from fake/non-prompt leptons. A $m_{\tau\tau}$ veto defined as $m_{\tau\tau} \in\,]0, 160[\,\mathrm{GeV}$ suppresses contributions from fully leptonic $Z \to \tau\tau$ events. As top quarks decay most frequently into a W boson and a b quark [9], events containing a b-tagged jet are rejected to reduce top-related background processes. The E_T^{miss} is required to be $> 120\,\mathrm{GeV}$, with higher thresholds applied in some of the signal selections.

The signal models exhibit a back-to-back topology in which the SUSY system is recoiling against hadronic ISR activity. To enforce such a topology, at least one jet with $p_T > 100\,\mathrm{GeV}$ is required in the event, with the leading jet and the $\mathbf{p}_T^{\mathrm{miss}}$ being separated more than 2.0 radians in ϕ. Additional jets are also required to have an azimuthal separation larger than 0.4 radians to reduce the impact of jet energy mismeasurements on the E_T^{miss}.

5.3.6 Final Signal Selections

In the following the signal selections for the higgsino and slepton search in the individual channels are briefly summarized. Detailed information about the high-E_T^{miss} selections and the $1\ell1T$ channel can be found in Ref [135], while Section 5.4 gives an in-depth description of the SR design in the low-E_T^{miss} regime.

	Electroweakino SR Requirements			
	SR-ewk-low-E_T^{miss}			
Variable	low-Δm	high-Δm	SR-ewk-high-E_T^{miss}	SR $1\ell 1T$
E_T^{miss} [GeV]	$[120, 200]$	$[120, 200]$	> 200	> 200
E_T^{miss}/H_T^{lep}	> 10	< 10	$-$	> 30
$\Delta\phi(\text{lep}, \mathbf{p}_T^{miss})$	$-$	$-$	$-$	< 1.0
$p_T(\ell_2)/p_T^{track}$[GeV]	$-$	$> 5 + m_{\ell\ell}/4$	$> \min(10, 2 + m_{\ell\ell}/3)$	< 5
M_T^S [GeV]	< 50	$-$	$-$	$-$
$m_T^{\ell_1}$ [GeV]	$-$	$[10, 60]$	< 60	$-$
R_{ISR}	$-$	$[0.8, 1.0]$	$[\max(0.85, 0.98 - 0.02 \times m_{\ell\ell}), \ 1.0]$	$-$

Table 5.4: Requirements applied to all events entering into signal regions used for electroweakino searches. The preselection requirements from Table 5.3 are implied, except for the SR $1\ell 1T$ that uses the $1\ell 1T$ preselection given in Ref [135].

Electroweakino Signal Regions

The higgsino search utilizes a combination of three different channels, with in total four orthogonal, distinct SRs. The requirements of each SR are listed in Table 5.4. The 2ℓ SRs are further split into eight $m_{\ell\ell}$ bins ranging from 1 to 60 GeV, with coarser binning at larger $m_{\ell\ell}$ values

$$m_{\ell\ell} \ [\text{GeV}] : [1, 2], \ [2, 3], \ [3.2, 5], \ [5, 10], \ [10, 20], \ [20, 30], \ [30, 40], \ [40, 60] \,.$$

This allows to take into account the variation of the $m_{\ell\ell}$ shape across the signal grid. While the level of background is to a very rough approximation constant across $m_{\ell\ell}$, signal events are restricted to a kinematic endpoint defined by the mass splitting, as shown in Figure 5.3a. For example, in a higgsino signal representing a mass splitting of 3 GeV, the signal events accumulate at $m_{\ell\ell} < 3$ GeV, consequently the sensitivity originates exclusively from the first two $m_{\ell\ell}$ bins. The other bins contain little to no signal and do not contribute to the total sensitivity. However the background present in these bins is effectively cut away from the bins containing the majority of signal events and hence increases their sensitivity. Besides the binning in $m_{\ell\ell}$, the 2ℓ SRs are further split into ee and $\mu\mu$ to increase the sensitivity of the searches. As ee events are restricted to $m_{ee} > 3$ GeV the first two $m_{\ell\ell}$ bins are only present for $\mu\mu$ events. The $1\ell 1T$ channel uses a different binning due to the slightly different phase space it covers. In total, the results for the electroweakino search are derived by combining 44 SR bins in a simultaneous fit.

Low-E_T^{miss} The low-E_T^{miss} channel in the higgsino search covers the E_T^{miss} range $[120, 200]$ GeV. It comprises two different SRs, labeled as SR-ewk-low-E_T^{miss}-low-Δm and SR-ewk-low-E_T^{miss}-high-Δm, which target higgsino scenarios with low and high mass splittings, respectively. Those two SRs are kept orthogonal by a cut on the ratio of the missing transverse energy and the sum of the transverse momenta of the two leptons E_T^{miss}/H_T^{lep}. SR-ewk-low-E_T^{miss}-low-Δm covers the phase space $E_T^{miss}/H_T^{lep} > 10$ which is only sparely populated by background, so an upper requirement on M_T^S concludes this SR definition. As this region targets signals

with small mass splittings, $m_{\ell\ell}$ bins above 30 GeV are not populated with signal and are therefore not considered in the fit. SR-ewk-low-E_T^{miss}-high-Δm requires $E_T^{\text{miss}}/H_T^{\text{lep}} < 10$ and employs a $m_{\ell\ell}$-dependent cut on the transverse momentum of the subleading lepton $p_T(\ell_2)$ to veto fake/nonprompt leptons. Further requirements on $m_T^{\ell_1}$ and R_{ISR} improve the sensitivity of the SR. The background estimation utilizes three dedicated CRs to normalize important backgrounds to data (see Section 5.5). In total, the low-E_T^{miss} channel is present with 10 SR bins from SR-ewk-low-E_T^{miss}-low-Δm, 14 SR bins from SR-ewk-low-E_T^{miss}-high-Δm and 3 one-bin CRs in the statistical model of the combination.

High-E_T^{miss} The high-E_T^{miss} channel is defined to consider events with $E_T^{\text{miss}} > 200$ GeV. In the higgsino search it consists of one SR named SR-ewk-high-E_T^{miss}. To veto fakes, a $m_{\ell\ell}$-dependent requirement on $p_T(\ell_2)$ is applied, which increases from roughly 3 to 10 GeV for larger $m_{\ell\ell}$ values. The requirement $m_T^{\ell_1} < 60$ GeV rejects events with fakes and from top processes. For further background rejection, events are required to have a value of R_{ISR} above 0.85. The requirement on R_{ISR} gets tighter with decreasing $m_{\ell\ell}$, to exploit the $m(\tilde{\chi}_2^0)/m(\tilde{\chi}_1^0)$ scaling present in this RJR variable. Three dedicated CRs have been designed to normalize the contributions from top, diboson and $Z \to \tau\tau$ events. These are placed in the same regime of R_{ISR} and use the same requirement on $p_T(\ell_2)$ as the high-E_T^{miss} SR for electroweakinos. In summary, the high-E_T^{miss} channel adds 14 SR bins and 3 CRs to the combination.

1ℓ1T For very small mass splittings, the leptons are too soft and will to a large extent not pass the reconstruction thresholds. The lepton signatures may still be reconstructed as tracks, which are reconstructed with high efficiency also at low p_T. To increase the signal acceptance for these scenarios, the 1ℓ1T channel therefore replaces the second lepton with an isolated track of OS to form lepton–track pairs with an invariant mass $m_{\ell track}$. Signal tracks are required to be matched to a reconstructed muon or electron candidate, to enhance the efficiency of selecting a track stemming from a lepton. Muon (electron) candidates are available for p_T as low as 2 (3) GeV, but are required to fail the signal lepton definitions to remove overlap with the 2ℓ selections. The 1ℓ1T channel restricts to $E_T^{\text{miss}} > 200$ GeV and is based on a similar preselection as the 2ℓ channels, which also enforces an ISR topology of the event. The 1ℓ1T SR considers only signals with very soft momenta, and thus requires the identified lepton and track to have a p_T below 10 and 5 GeV, respectively. Requirements on the azimuthal distance between the lepton and $\mathbf{p}_T^{\text{miss}}$, and $E_T^{\text{miss}}/H_T^{\text{lep}}$ with H_T^{lep} being the scalar sum of lepton and track p_T, reduce the background contamination. The background estimation in the 1ℓ1T channel is purely data-driven and relies on the assumption that background events with OS and same sign (SS) are produced at equal rates. The background prediction is then given by the number of observed SS events in data. Uncertainties on the background prediction are estimated by evaluating the OS/SS ratio in phase spaces close to the SR. In summary, the 1ℓ1T channel contributes with 6 SR bins in the $m_{\ell track}$ range from 0.5 to 5 GeV.

Slepton Signal Regions

The slepton search comprises a low-E_T^{miss} and high-E_T^{miss} channel, with one SR each. The requirements for the individual SRs are given in Table 5.5. Similar to the electroweakino SRs,

	Slepton SR Requirements	
Variable	SR-slep-low-E_T^{miss}	SR-slep-high-E_T^{miss}
E_T^{miss} [GeV]	$[150, 200]$	> 200
m_{T2} [GeV]	< 140	< 140
$p_T(\ell_2)$ [GeV]	$> \min(15, 7.5 + 0.75 \times (m_{T2} - 100))$	$> \min(20, 2.5 + 2.5 \times (m_{T2} - 100))$
R_{ISR}	$[0.8, \ 1.0]$	$[\max(0.85, 0.98 - 0.02 \times (m_{T2} - 100)), \ 1.0]$

Table 5.5: Requirements applied to all events entering into signal regions used for slepton searches. The 2ℓ preselection requirements from Table 5.3 are implied.

the slepton SRs are binned in m_{T2}, exploiting the kinematic endpoint of the signals in this variable. The SRs are binned using 8 m_{T2} bins with increasing bin width at larger m_{T2} values

$$m_{T2} \text{ [GeV]} : [100, 100.5], [100.5, 101], [100, 102], [102, 105],$$
$$[105, 110], [110, 120], [120, 130], [130, 140].$$

As in the higgsino search, the SRs are further split into ee and $\mu\mu$ events to increase the sensitivity. Hence, the slepton results are derived using a simultaneous fit of 32 SRs bins.

Low-E_T^{miss}   The low-E_T^{miss} slepton SR requires $E_T^{miss} \in [150, 200]$ GeV and is denoted by SR-slep-low-E_T^{miss}. Discrimination from background is performed by requirements on R_{ISR} and a m_{T2}-dependent cut on $p_T(\ell_2)$. In total, the low-E_T^{miss} channel contributes with 16 SR bins to the fit.

High-E_T^{miss}   Events with $E_T^{miss} > 200$ GeV are considered by the region SR-slep-low-E_T^{miss}. Similar to the high-E_T^{miss} SR for electroweakinos, it employs m_{T2}-dependent cuts on $p_T(\ell_2)$ and R_{ISR} to separate background from signal events. Three dedicated slepton CRs have been designed to normalize the background of top, diboson and $Z \to \tau\tau$ events, which share the requirement on $p_T(\ell_2)$ with the SR and are placed in a similar regime of R_{ISR}. Thus, the high-E_T^{miss} channel is represented with three CRs and 16 SR bins in the fit to derive the results of the slepton search.

5.4 Low Missing Transverse Momentum Signal Selections

Aim of the low-E_T^{miss} channel is to increase the overall sensitivity reach of the analysis, in particular for moderate to large mass splittings, by including signal events with E_T^{miss} between 120 to 200 GeV. In these events, the SUSY system is less heavily boosted with respect to the high-E_T^{miss} regime, resulting in a less distinct signature. In conjunction with the overall higher level of background, this strongly motivates a dedicated optimization for this E_T^{miss} range.

5.4.1 Optimization Strategy

Each SR was optimized individually in terms of signal-to-background separation power. Several different methods exist to quantify this separation power or in other words make a

statement how significant a potential observation of an excess (or deficit) would be. For the analysis, the significance metric presented in Ref. [230] was adapted as sensitivity measure, which models the background prediction and its uncertainty in a similar way as it is done in the hypothesis tests carried out for the final results. This metric models the background prediction b as Poisson-counting term in the likelihood with the associated uncertainty σ constrained by an auxiliary Poisson measurement. The final value of the significance is estimated by approximating the profile likelihood test statistic with asymptotic formulas. This yields the following significance estimate Z for observing n events given a prediction of $b \pm \sigma$ background events

$$\text{Z} = \begin{cases} +F & n \geq b\,, \\ -F & n < b\,, \end{cases} \tag{5.17}$$

with

$$F = \sqrt{2 \left(n \ln \left[\frac{n(b + \sigma^2)}{b^2 + n\sigma^2} \right] - \frac{b^2}{\sigma^2} \ln \left[1 + \frac{\sigma^2(n - b)}{b(b + \sigma^2)} \right] \right)}\,. \tag{5.18}$$

The upper case of Equation (5.17) defines the scenario of an excess, which is used in the optimization with $n = s + b$, where s is the number of expected signal events. Likewise, the lower case represents observing a deficit. The uncertainty on the background prediction σ was taken to be the statistical uncertainty added in quadrature with a flat 30 % uncertainty as proxy for systematic uncertainties on b.

Typical landmarks for the significance are the values 1.64 and 3, which correspond to (one-sided) p-values of 0.05 and 0.0013. The former value marks the threshold that is typically required to exclude a signal model. However, the given formula for Z estimates the "discovery" significance (i.e. the search was optimized for discovery), in which the null hypothesis is the background-only model, while in an exclusion test the signal-plus-background hypothesis acts as null hypothesis. Consequently, Z is just an estimate whether there is enough sensitivity to a model that allows to potentially exclude it. The latter is the commonly accepted threshold for the required significance of an observation to claim evidence of a new particle.

To find the best performing set of selection criteria, the optimization procedure made use of N-1 plots, augmented with significance scans. In such N-1 plots, all current selection requirements are applied except the one on the variable being plotted. An additional panel evaluates then the significances yielded by upper and lower requirements on the variable across the spectrum shown. Careful iteration over the kinematic quantities that promise separation power leads then to an optimal set of cuts, defining the final signal selection.

A complication for the optimization arises through the fact that the final sensitivity of the searches is achieved by a multi-bin fit of the $m_{\ell\ell}$ and m_{T2} distribution, respectively. It is not trivial to extend the significance estimate above to multiple SR bins. To get an idea how a potential cut performs in the different $m_{\ell\ell}/m_{\text{T2}}$ bins, the N-1 plots have been evaluated also for all SR bins individually[†]. This allows to infer the position of the cut that performs best across the complete SR. For additional validation of the performance, requirements have also been compared with respect to their expected exclusion contour derived by a simplified fit configuration as introduced in Section 5.4.4.

[†] The bins have not been split into lepton flavor, as no different kinematics between ee and $\mu\mu$ events are expected.
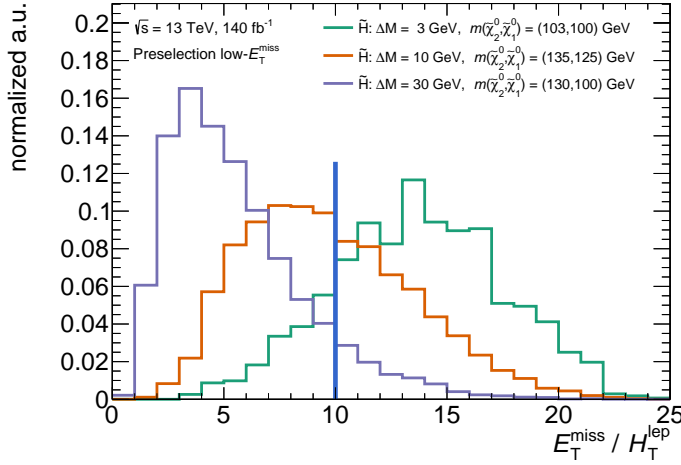
Figure 5.17: Distribution of E_T^{miss}/H_T^{lep} in the low-E_T^{miss} preselection for higgsino signals representing mass splittings of 3, 10 and 30 GeV. All curves are normalized to unity for illustration purposes. The vertical blue line at $E_T^{miss}/H_T^{lep} = 10$ indicates the separation threshold of the two low-E_T^{miss} electroweakino SRs.

At the time the SR optimization was performed, data-taking was still ongoing. Hence, the final size of the data set was unknown and an integrated luminosity of $140\,\mathrm{fb}^{-1}$ was used in the optimization as an estimate. This choice turned out to be close to the final value of $139\,\mathrm{fb}^{-1}$. The starting point of the optimization was at the preselection level introduced in Section 5.3.5. Furthermore, during optimization the analysis was blinded, i.e. performed without looking at data in the potential signal selections. This is a common approach in experimental particle physics to avoid introducing any potential bias by the experimentalist [231]. Only after the background estimation in the final SRs has been validated and proven to be reliable, the signal selections were unblinded to derive the results.

5.4.2 Electroweakino Signal Regions

In the development of a low-E_T^{miss} SR for higgsinos, it turned out to be beneficial to address the varying kinematics in the signal grid with two orthogonal SRs. Orthogonality ensures, that the regions can be fitted simultaneously. The first SR, labeled as SR-ewk-low-E_T^{miss}-low-Δm, is targeted at small to moderate mass splittings in the range from 3 to 10 GeV. Larger mass differences are covered by the second electroweakino SR named SR-ewk-low-E_T^{miss}-high-Δm. An appropriate quantity to split these is the ratio of the E_T^{miss} and the scalar sum of the lepton transverse momenta H_T^{lep}. The distribution of E_T^{miss}/H_T^{lep} is shown in Figure 5.17 at preselection level for three representative mass splittings. Events corresponding to small mass splittings have predominantly soft leptons, i.e. a low value of H_T^{lep} and thus an extended tails towards high E_T^{miss}/H_T^{lep}. Samples corresponding to larger mass splittings have harder leptons, hence their events accumulate at low values of E_T^{miss}/H_T^{lep}. Sensitivity for moderate mass splittings around 10 GeV will be provided by the combination of both SRs.

Signal Region for Small Mass Splittings

SR optimization was performed using signal samples, which represent mass splittings and neutralino masses slightly outside the exclusion range of the last iteration of the analysis (see

Figure 5.6a). The region SR-ewk-low-$E_\mathrm{T}^\mathrm{miss}$-low-$\Delta m$ was optimized considering signal samples with mass splittings of 3, 5 and 10 GeV:

- $\tilde{\mathrm{H}}: m(\tilde{\chi}_2^0, \tilde{\chi}_1^0) = (103, 100)$ GeV,

- $\tilde{\mathrm{H}}: m(\tilde{\chi}_2^0, \tilde{\chi}_1^0) = (155, 150)$ GeV,

- $\tilde{\mathrm{H}}: m(\tilde{\chi}_2^0, \tilde{\chi}_1^0) = (135, 125)$ GeV.

The phase space covered by SR-ewk-low-$E_\mathrm{T}^\mathrm{miss}$-low-$\Delta m$ is highly restricted, as the requirement $E_\mathrm{T}^\mathrm{miss}/H_\mathrm{T}^\mathrm{lep} > 10$ in combination with the constraint for low-$E_\mathrm{T}^\mathrm{miss}$, allows $H_\mathrm{T}^\mathrm{lep}$ to take on only small values (< 20 GeV). Thus only a requirement $M_\mathrm{T}^\mathrm{S} < 50$ GeV is applied as shown in Figure 5.18d. This requirement vetoes the Jacobian peak just before the W boson mass in M_T^S which arises dominantly from $W \to \ell\nu$ events in which the second lepton is faked. The transverse mass $m_\mathrm{T}^{\ell_1}$ is also capable of vetoing this peak, but performs worse than M_T^S, as summarized in Appendix D.1.1. It was verified that the placement of the cut at 50 GeV works well also in the individual $m_{\ell\ell}$ bins (see Figure D.4 in the appendix). These plots also illustrate that the background statistics is already quite limited, in particular for the low-$m_{\ell\ell}$ bins. To allow for a reliable background estimation in this SR that is not dominated by statistical uncertainties, no further requirements are applied. As visible in Figure 5.18, tighter requirements on $E_\mathrm{T}^\mathrm{miss}$ or $E_\mathrm{T}^\mathrm{miss}/H_\mathrm{T}^\mathrm{lep}$ would anyway result in only mild gains in sensitivity.

The final $m_{\ell\ell}$ distribution of SR-ewk-low-$E_\mathrm{T}^\mathrm{miss}$-low-$\Delta m$ is shown in Figure 5.18b, using the same binning as in the multi-bin fit. The background in this SR is formed dominantly by fake/nonprompt leptons, with further contribution originating from $Z \to \tau\tau$ and diboson events. No signal is present for $m_{\ell\ell} > 30$ GeV, so that this regime is discarded in the SR definition.

Signal Region for Large Mass Splittings

Larger mass splittings are covered by SR-ewk-low-$E_\mathrm{T}^\mathrm{miss}$-high-$\Delta m$, that requires $E_\mathrm{T}^\mathrm{miss}/H_\mathrm{T}^\mathrm{lep} < 10$ to ensure orthogonality to the other electroweakino SR in the low-$E_\mathrm{T}^\mathrm{miss}$ channel. This region was optimized using samples that correspond to mass differences of 10, 20 and 30 GeV

- $\tilde{\mathrm{H}}: m(\tilde{\chi}_2^0, \tilde{\chi}_1^0) = (135, 125)$ GeV,

- $\tilde{\mathrm{H}}: m(\tilde{\chi}_2^0, \tilde{\chi}_1^0) = (145, 125)$ GeV,

- $\tilde{\mathrm{H}}: m(\tilde{\chi}_2^0, \tilde{\chi}_1^0) = (130, 100)$ GeV.

In the low-$E_\mathrm{T}^\mathrm{miss}$ regime, the R_ISR variable does not exhibit a clear $m_{\tilde{\chi}_2^0}/m_{\tilde{\chi}_1^0}$ scaling as shown in Figure 5.19d. This may motivate to use a variable which is easier to access. In the phase space spanned by SR-ewk-low-$E_\mathrm{T}^\mathrm{miss}$-high-$\Delta m$, the distributions of R_ISR and the ratio of the $E_\mathrm{T}^\mathrm{miss}$ and the scalar sum of the signal-jet transverse momenta $E_\mathrm{T}^\mathrm{miss}/H_\mathrm{T}^{30}$ are related. Both can be understood as estimators for the fraction of $E_\mathrm{T}^\mathrm{miss}$ stemming from ISR. The two variables have similar distributions and background rejection performance, as presented in Appendix D.1.1. As R_ISR performs slightly better and is also used in the high-$E_\mathrm{T}^\mathrm{miss}$ channel, this variables is, besides its complexity, preferred for the SR definition. Instead of a $m_{\ell\ell}$-dependent cut as in the high-$E_\mathrm{T}^\mathrm{miss}$ channel, a flat requirement $R_\mathrm{ISR} > 0.8$ is employed.

(a) $E_{\mathrm{T}}^{\mathrm{miss}}$

(b) $m_{\ell\ell}$

(c) $E_{\mathrm{T}}^{\mathrm{miss}}/H_{\mathrm{T}}^{\mathrm{lep}}$

(d) $M_{\mathrm{T}}^{\mathrm{S}}$
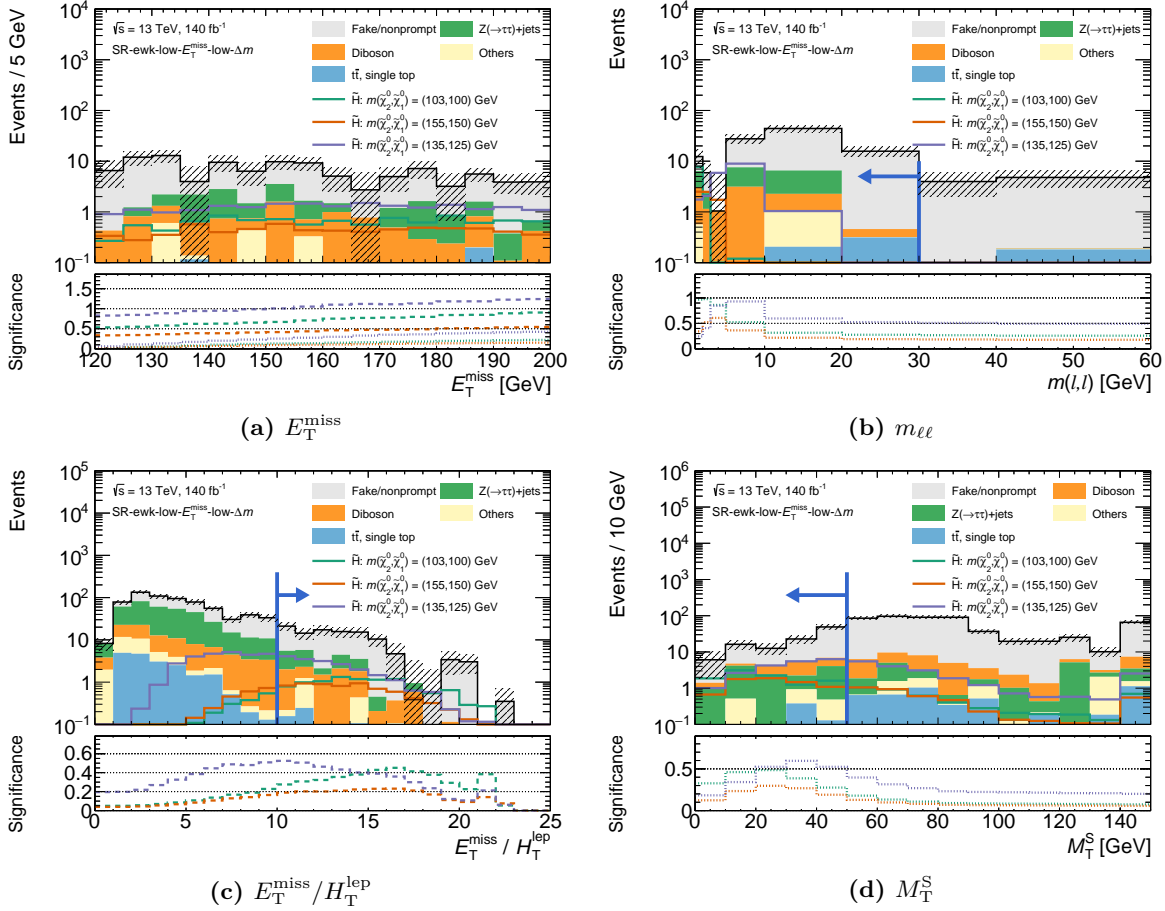
Figure 5.18: N-1 plots of SR-ewk-low-$E_{\mathrm{T}}^{\mathrm{miss}}$-low-$\Delta m$. The last bin contains the overflow. The blue arrows indicates the location and direction of the requirement on the variable shown. The bottom panel shows a significance scan with dashed (dotted) lines indicating the significance of a potential lower (upper) requirement at the shown position. Each significance curve corresponds to the signal with the same color.

Values of R_{ISR} above 1 are in principle unphysical for signal events and indicate some failure in the RJR calculation. Hence this regime is vetoed in the analysis. The signals considered in the optimization all peak within the selected R_{ISR} range $[0.8, 1]$ as depicted in Figure 5.19d, making this an efficient choice to pick up signal events.

As signals with larger mass splittings are accompanied by less soft leptons, this SR allows also to cut on lepton transverse momenta at an acceptable signal loss. The probability of a lepton being fake increases with decreasing p_{T}, so the fake/nonprompt contribution is best studied at the softer, i.e. the subleading lepton ℓ_2. Figure 5.19e shows the N-1 plot of $p_{\mathrm{T}}(\ell_2)$ in SR-ewk-low-$E_{\mathrm{T}}^{\mathrm{miss}}$-high-$\Delta m$. Fakes clearly pile up at low $p_{\mathrm{T}}(\ell_2)$, making this variable the predestinated candidate to reject this background. As samples with larger mass splittings have harder leptons they allow also a harder cut on $p_{\mathrm{T}}(\ell_2)$. To account for this relationship, an $m_{\ell\ell}$-dependent requirement on $p_{\mathrm{T}}(\ell_2)$ was introduced in order to veto fakes as efficiently

as possible: $p_T(\ell_2) > (5 + m_{\ell\ell}/4\text{ GeV})$. This expression was derived considering N-1 plots of the individual $m_{\ell\ell}$ bins (see Figure D.6) to find what cut on $p_T(\ell_2)$ performs best for each $m_{\ell\ell}$ range. The expression above was then derived as compromise between fake rejection and signal loss across the $m_{\ell\ell}$ spectrum.

To reject events from $Z \to \tau\tau$ decays that pile up at low values of $m_T^{\ell_1}$, in particular for the low-$m_{\ell\ell}$ bins (see Figure D.7), a requirement $m_T^{\ell_1} > 10\text{ GeV}$ is imposed. An upper bound on this variable $m_T^{\ell_1} < 60\text{ GeV}$ increases the sensitivity by vetoing events from top and diboson processes. Tighter requirements on other analysis variables such as E_T^{miss} do not result in a notable sensitivity gain, as shown in Figure 5.19.

The $m_{\ell\ell}$ distribution of the final signal selection is shown in Figure 5.19b. The background composition is formed by roughly equal parts of fake/nonprompt leptons, top, diboson and $Z \to \tau\tau$ events.

5.4.3 Slepton Signal Region

In the slepton scenario, the lepton pair does not originate from the same decay leg, but from separate ones. As a consequence, such signals have a kinematic endpoint in m_{T2} instead of in $m_{\ell\ell}$. Therefore, the $m_{\ell\ell} < 60\text{ GeV}$ requirement at preselection level has a significant impact on the signal acceptance across the signal grid. Figure 5.20 shows the $m_{\ell\ell}$ distribution for slepton signals representing mass splittings of 2, 10 and 30 GeV. Obviously, the $m_{\ell\ell}$ requirement has only a minor impact on small mass differences. On the contrary, samples with larger mass splittings, contain a significant fraction of events with $m_{\ell\ell} > 60\text{ GeV}$, which consequently drop out of the selection. This is precisely the signal parameter space where the low-E_T^{miss} channel would be sensitive the most. A simple extension towards larger $m_{\ell\ell}$ values is not trivial. In the $m_{\ell\ell}$ range around the Z boson mass from approximately 60 to 110 GeV, any signal would be covered by the several orders of magnitude larger $Z \to ee/\mu\mu$ background. Above 110 GeV, in the upper tail of the Z resonance, a potential high-$m_{\ell\ell}$ slepton SR could recover a notable amount of signal events. However such a region would require a dedicated background estimation, valid in the high-$m_{\ell\ell}$ regime. This was out of scope for the presented iteration of the analysis and this thesis. Consequently the low-E_T^{miss} channel is able to contribute only to a limited extend to the total sensitivity of the slepton search.

For the optimization of the low-E_T^{miss} slepton SR, labeled as SR-slep-low-E_T^{miss}, samples corresponding to mass splittings of 5, 10 and 30 GeV have been considered

- $\tilde{\ell} : m(\tilde{\ell}, \tilde{\chi}_1^0) = (200, 195)$ GeV,

- $\tilde{\ell} : m(\tilde{\ell}, \tilde{\chi}_1^0) = (175, 165)$ GeV,

- $\tilde{\ell} : m(\tilde{\ell}, \tilde{\chi}_1^0) = (100, 70)$ GeV.

During the slepton optimization studies, no adequate sensitivity could be achieved in the low-E_T^{miss} channel for mass splittings below 10 GeV. Consequently it is not practical to separate into two SR as in the electroweakino search. Instead, the optimization focused on the samples with larger mass splittings.

Also for slepton signals, the R_{ISR} distribution peaks in the interval $[0.8, 1]$, as depicted in Figure 5.21c. Hence the same requirement on R_{ISR} as for SR-ewk-low-E_T^{miss}-high-Δm is
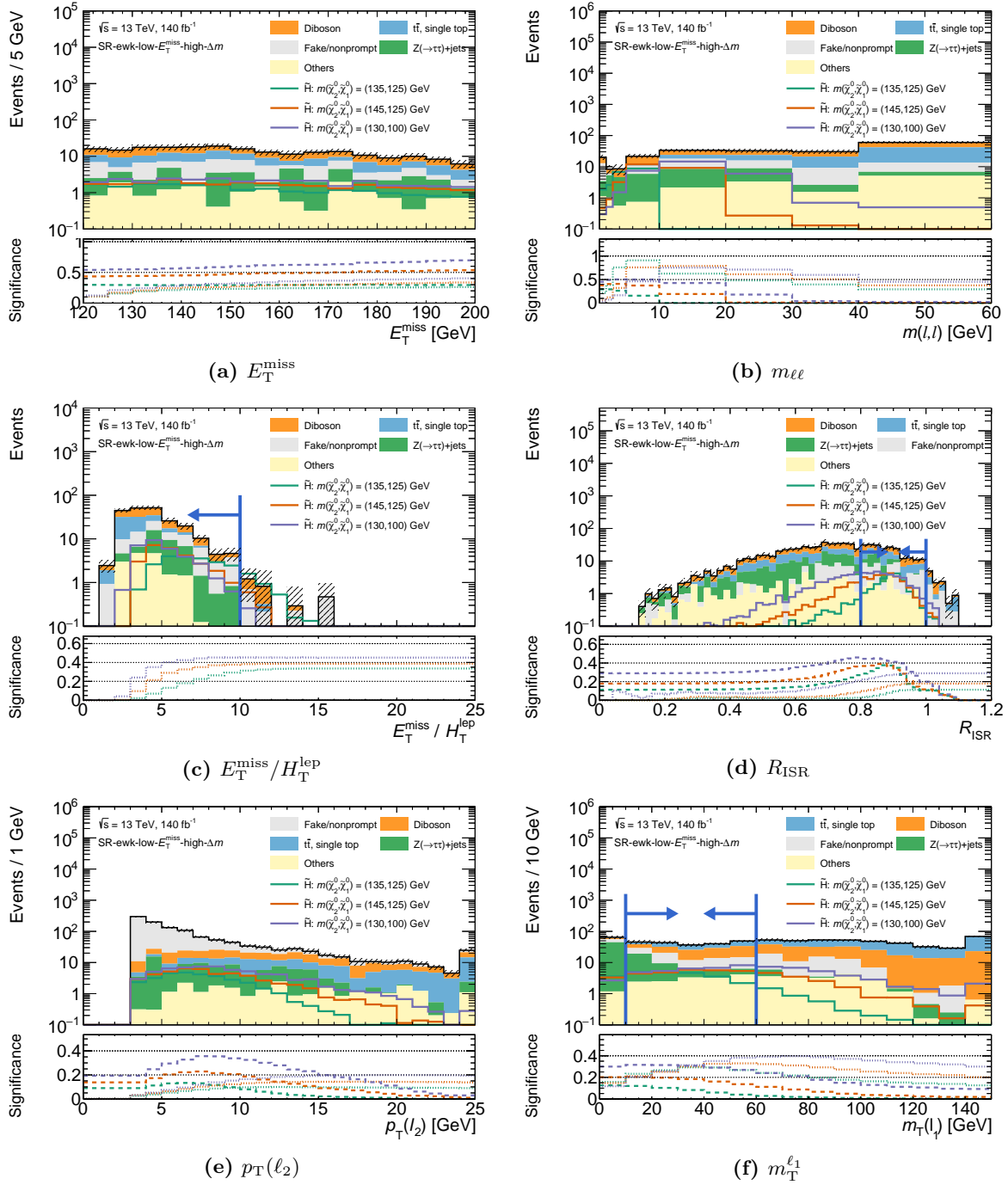
Figure 5.19: N-1 plots of SR-ewk-low-E_T^{miss}-high-Δm. The last bin contains the overflow. The blue arrows indicates the location and direction of the requirement on the variable shown. The bottom panel shows a significance scan with dashed (dotted) lines indicating the significance of a potential lower (upper) requirement at the shown position. Each significance curve corresponds to the signal with the same color.

Figure 5.20: Distribution of $m_{\ell\ell}$ at preselection level for slepton signals representing mass splittings of 2, 10 and 30 GeV. All curves are normalized to unity for illustration purposes. The blue arrow indicates the requirement on $m_{\ell\ell}$ of the preselection.
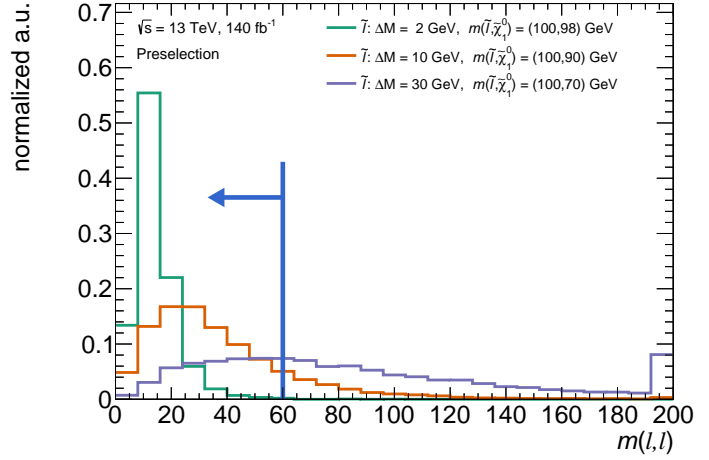
imposed. Likewise, the contribution of fakes is also reduced by a m_{T2}-dependent cut on $p_{T}(\ell_2)$. As the leptons in the slepton grid arise from separate decay legs, they are harder than in the higgsino scenario. Hence the requirement on ℓ_2 is also tighter:

$$p_{T}(\ell_2) > \min(15, 7.5 + 0.75 \times (m_{T2} - 100)) \text{ GeV}.$$

This expression was also derived by considering the $p_{T}(\ell_2)$ distributions in the individual m_{T2} bins shown in Figure D.10, which suggest a minimum requirement around 7.5 GeV and a maximum requirement around 15 GeV. Raising the minimum requirement on E_{T}^{miss} to 150 GeV increases the sensitivity in the low m_{T2} bins, as shown in Figure D.8.

The final distribution in m_{T2} of SR-slep-low-E_{T}^{miss} is shown in Figure 5.21b, with top and diboson processes being the most dominant backgrounds. As events above $m_{T2} = 140$ GeV have no sensitivity to the slepton signals under consideration, this regime is excluded from the slepton search.

5.4.4 Expected Sensitivity

To evaluate the sensitivity from the SRs defined above, expected exclusion limits have been derived using a simplified configuration of the simultaneous fit. In this configuration, the hypothesis tests are carried out using blinded SRs, i.e. taking the pre-fit background estimation as the number of observed events in each SR bin. As the observation is set to the background prediction, signal grid points to which the analysis is sensitive will be excluded, i.e. their CL_s values are below 0.05. The results of the hypothesis tests are interpolated[†] between the grid points to estimate the contour where $\text{CL}_s = 0.05$. This exclusion contour marks the area of the signal grid up to which points can be excluded at 95 % CL and hence serves as a visualization where the searches are sensitive and where they start to loose sensitivity. For these sensitivity estimates, only a simplified handling of the systematics uncertainties was employed. Besides the statistical uncertainty on the background, defined by the MC

[†] Before the interpolation, the CL_s values are transformed into significances, which were found to behave more linearly and thus better suited for this purpose.
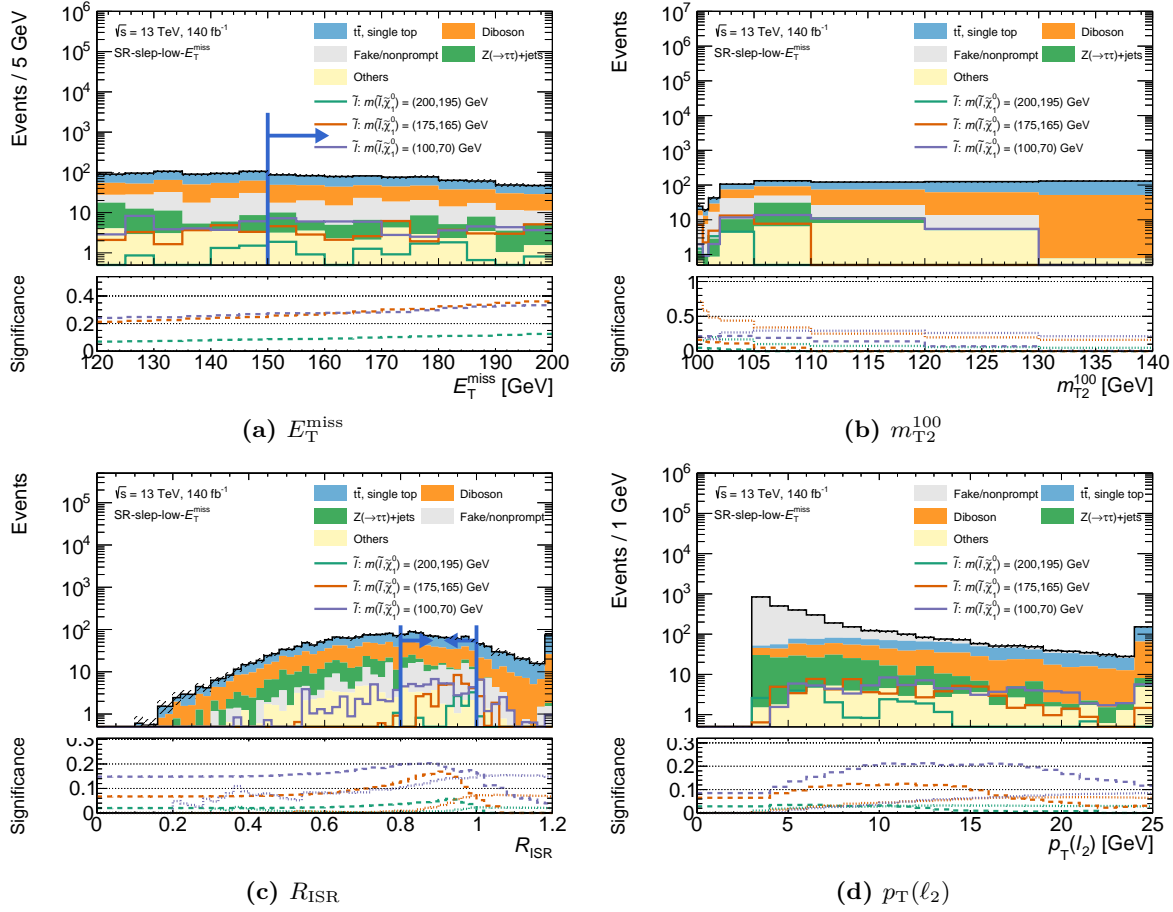
Figure 5.21: N-1 plots of SR-slep-low-E_T^{miss}. The last bin contains the overflow. The blue arrows indicates the location and direction of the requirement on the variable shown. The bottom panel shows a significance scan with dashed (dotted) lines indicating the significance of a potential lower (upper) requirement at the shown position. Each significance curve corresponds to the signal with the same color.
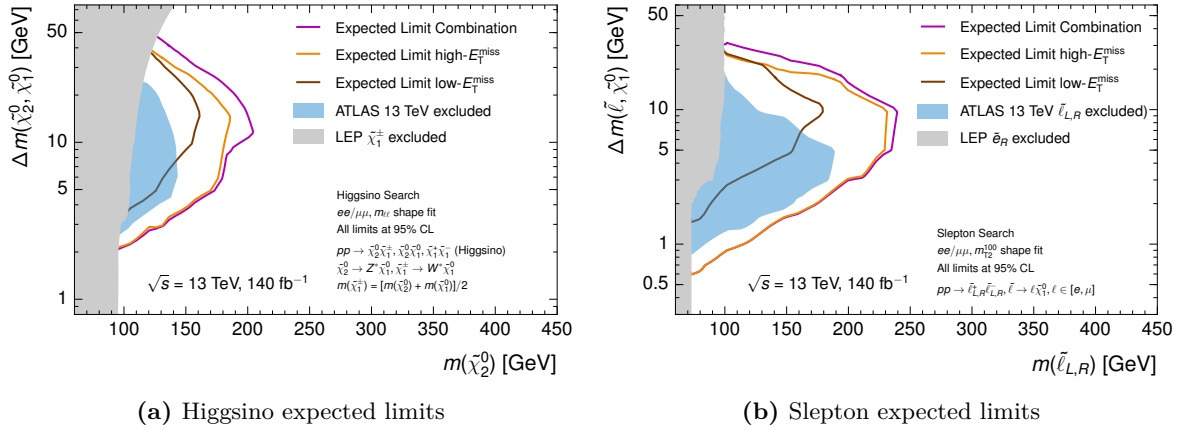
(a) Higgsino expected limits **(b)** Slepton expected limits

Figure 5.22: Expected exclusion limits at $95\,\%$ CL for the higgsino and the slepton search using a simplified fit configuration as explained in the text. The results for the combination and the individual high-$E_{\mathrm{T}}^{\mathrm{miss}}$ and low-$E_{\mathrm{T}}^{\mathrm{miss}}$ channels are shown. The gray area marks the associated exclusion limits from the LEP experiments. The blue regions indicate the limits from the previous iteration of the analysis.

statistics and the statistical uncertainty of the fake estimate, a flat, uncorrelated uncertainty of magnitude $20\,\%$ was assigned to each SR bin. This flat uncertainty serves as proxy for the systematic uncertainties and its size is motivated from the size of the total systematic uncertainties observed in the previous iteration of the analysis.

The expected exclusion contours for the low-$E_{\mathrm{T}}^{\mathrm{miss}}$ channel, the high-$E_{\mathrm{T}}^{\mathrm{miss}}$ channel and their combination in the higgsino grid are shown in Figure 5.22a. As expected, the low-$E_{\mathrm{T}}^{\mathrm{miss}}$ channel is mostly sensitive to larger mass splittings $\Delta m > 10\,\mathrm{GeV}$, where its sensitivity notable exceeds the existing constraints. For lower mass splittings, the sensitivity of the low-$E_{\mathrm{T}}^{\mathrm{miss}}$ channel is not able to surpass these. The combination of both channels adds only marginal sensitivity at low mass splittings with respect to the high-$E_{\mathrm{T}}^{\mathrm{miss}}$ channel alone. However, at large mass splittings, where both channels show comparable exclusion power, a notable gain in sensitivity can be observed. In summary, the combination is able to exclude $\tilde\chi_2^0$ masses up to $200\,\mathrm{GeV}$, and mass splittings down to $2\,\mathrm{GeV}$ and up to $50\,\mathrm{GeV}$. The performance of the individual low-$E_{\mathrm{T}}^{\mathrm{miss}}$ electroweakino SRs is presented in Appendix D.1.2.

Likewise, the expected exclusion contours for the slepton grid are depicted in Figure 5.22b. A very similar picture as for the higgsino scenario is present. The sensitivity of the low-$E_{\mathrm{T}}^{\mathrm{miss}}$ channel is able to surpass existing constraints only for large mass splittings, where its performance is comparable with the one of the high-$E_{\mathrm{T}}^{\mathrm{miss}}$ channel. Consequently, the combination of both channels shows mild gains in sensitivity at moderate to large mass splittings with respect to the high-$E_{\mathrm{T}}^{\mathrm{miss}}$-only configuration. To summarize, the expected exclusion reach of the slepton search extends up to $\tilde\ell$ masses of $230\,\mathrm{GeV}$, and mass splittings down to $0.6\,\mathrm{GeV}$ and up to $30\,\mathrm{GeV}$.
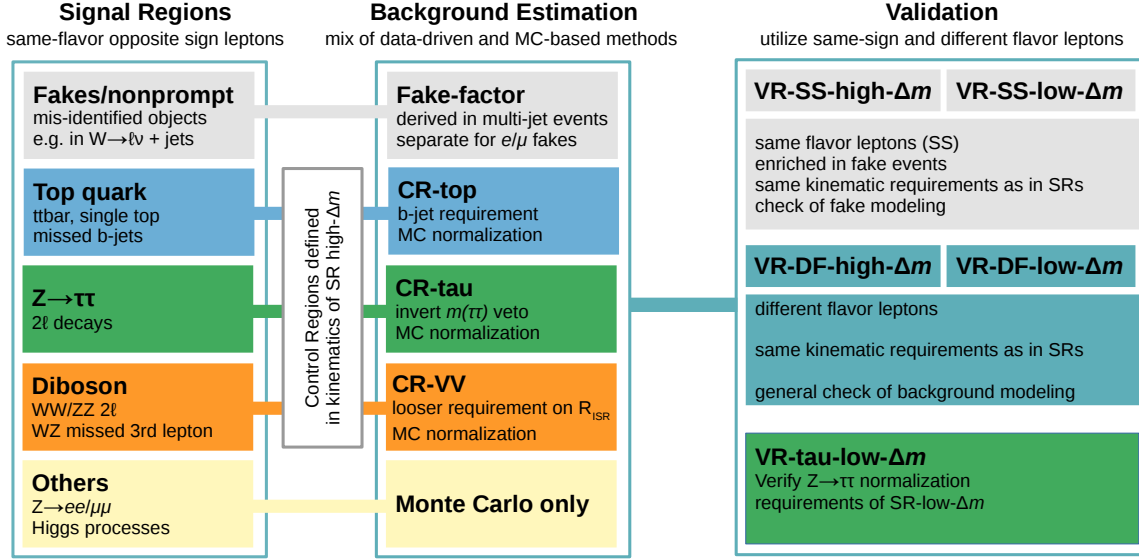
Figure 5.23: Schematic illustration of the background estimation in the low-$E_{\mathrm{T}}^{\mathrm{miss}}$ channel for the electroweakino search.

5.5 Background Estimation

To allow conclusive statements about the significance of a potential excess in the signal selection, a reliable prediction of the SM background in the corresponding phase space is required. Typically, two types of backgrounds are distinguished. This analysis defines reducible background as events in which one or both leptons are either fake or nonprompt. Hence, this background could be removed completely with a perfect detector and identification algorithms. Irreducible background stems from events that contain two prompt leptons, as for instance present in dileptonic $t\bar{t}$ and $Z \to \tau\tau$ decays. In the following, the estimation techniques for both background types are presented.

5.5.1 Estimation Strategy

A mix of MC-based and data-driven methods is employed in the analysis and has been adapted to the low-$E_{\mathrm{T}}^{\mathrm{miss}}$ regime to ensure an adequate background modeling. Central ingredient of the background estimation is to take advantage of the two-lepton topology present in the analysis. The SRs require a SF lepton pair of OS. These flavor and charge requirements on the leptons can be individually flipped and released, which allows for a background estimation with large statistics and a validation in essentially the same kinematic regime as the SRs.

Figure 5.23 shows a schematic illustration of the background estimation strategy for the low-$E_{\mathrm{T}}^{\mathrm{miss}}$ electroweakino SRs. The contributions from top, $Z \to \tau\tau$ and diboson related processes are estimated from MC simulation and normalized to data in three dedicated CRs. These CRs are located in a similar phase space as covered by SR-ewk-low-$E_{\mathrm{T}}^{\mathrm{miss}}$-high-$\Delta m$, i.e. contain less soft leptons. In particular, the CRs share the same sliding requirement on $p_{\mathrm{T}}(\ell_2)$. The kinematic region spanned by SR-ewk-low-$E_{\mathrm{T}}^{\mathrm{miss}}$-low-$\Delta m$ is too sparsely populated to allow

Region	SR orthogonality	Lepton Flavor	Additional requirements
CR-top-ewk-low-$E_{\mathrm{T}}^{\mathrm{miss}}$	$N_{b\text{-jet}}^{20} \geq 1$	$ee + \mu\mu + e\mu + \mu e$	$E_{\mathrm{T}}^{\mathrm{miss}}/H_{\mathrm{T}}^{\mathrm{lep}}$ and $m_{\mathrm{T}}^{\ell_1}$ removed
CR-top-slep-low-$E_{\mathrm{T}}^{\mathrm{miss}}$			$E_{\mathrm{T}}^{\mathrm{miss}} \in [120, 200]$
CR-tau-ewk-low-$E_{\mathrm{T}}^{\mathrm{miss}}$			$R_{\mathrm{ISR}} \in [0.6, 1.0]$, $m_{\mathrm{T}}^{\ell_1}$ removed
CR-tau-slep-low-$E_{\mathrm{T}}^{\mathrm{miss}}$	$m_{\tau\tau} \in [60, 120]$ GeV	$ee + \mu\mu + e\mu + \mu e$	$R_{\mathrm{ISR}} \in [0.6, 1.0]$, $E_{\mathrm{T}}^{\mathrm{miss}} \in [120, 200]$
VR-tau-ewk-low-$E_{\mathrm{T}}^{\mathrm{miss}}$-low-$\Delta m$			–
CR-VV-ewk-low-$E_{\mathrm{T}}^{\mathrm{miss}}$	$R_{\mathrm{ISR}} \in [0.6, 0.8]$	$ee + \mu\mu + e\mu + \mu e$	$m_{\mathrm{T}}^{\ell_1} > 30$ GeV, $N_{\mathrm{jet}}^{30} < 3$, $E_{\mathrm{T}}^{\mathrm{miss}}/H_{\mathrm{T}}^{\mathrm{lep}}$ removed
CR-VV-slep-low-$E_{\mathrm{T}}^{\mathrm{miss}}$			$m_{\mathrm{T}}^{\ell_1} > 30$ GeV, $N_{\mathrm{jet}}^{30} < 3$
VR-SS-ewk-low-$E_{\mathrm{T}}^{\mathrm{miss}}$-high-$\Delta m$	Same sign $\ell^{\pm}\ell^{\pm}$	$ee + \mu e$, $\mu\mu + e\mu$	$E_{\mathrm{T}}^{\mathrm{miss}}/H_{\mathrm{T}}^{\mathrm{lep}}$, $m_{\mathrm{T}}^{\ell_1}$ and $p_{\mathrm{T}}^{\ell_2}$ removed
VR-SS-ewk-low-$E_{\mathrm{T}}^{\mathrm{miss}}$-low-$\Delta m$			–
VR-DF-ewk-low-$E_{\mathrm{T}}^{\mathrm{miss}}$-low-$\Delta m$			–
VR-DF-ewk-low-$E_{\mathrm{T}}^{\mathrm{miss}}$-high-$\Delta m$	$e\mu + \mu e$	$e\mu + \mu e$	–
VR-DF-slep-low-$E_{\mathrm{T}}^{\mathrm{miss}}$			–

Table 5.6: Definition of control and validation regions used for background estimation in the low-$E_{\mathrm{T}}^{\mathrm{miss}}$ channel. The preselection criteria from Table 5.2 and selection criteria from the associated SR (Table 5.4 and Table 5.5, respectively) are implied unless specified. Additional or modified requirements are provided with respect to the selection of the signal region indicated in the suffix of the CR or VR. Table adapted from Ref. [135].

for the construction of CRs. Fake/nonprompt leptons are in principle also contained in MC simulation but this contribution is not expected to be well modeled. One reason for that is that the applied corrections, e.g. for the lepton reconstruction efficiency, have been derived and thus are only valid for real, prompt leptons. Therefore these contributions are estimated using a data-driven approach referred to as Fake Factor method. Other backgrounds that contribute only marginally to the total background are estimated with their plain prediction from MC simulation. Before being extrapolated to the SRs, the background predictions have been compared to data in dedicated VRs. For this a background-only fit is employed, in which only the CRs are used to constrain the fit parameters, such as the normalization factors. The reliability of the fake estimation was verified in VRs selecting SS events, which naturally enriches the samples in fakes. As fakes are the most dominant background in SR-ewk-low-$E_{\mathrm{T}}^{\mathrm{miss}}$-low-$\Delta m$, a dedicated VR was designed to validate the fake estimate in this particular phase space. Likewise, a VR enriched in $Z \to \tau\tau$ events is used to verify that the derived normalization for this process is also applicable in this kinematic regime. A general validation of the background estimation is performed in VRs based on DF events sharing the same kinematic requirements with the SRs.

Background estimation for the low-$E_{\mathrm{T}}^{\mathrm{miss}}$ slepton SR is performed in a similar fashion. Three dedicated slepton CRs for top, $Z \to \tau\tau$ an diboson events, which share the sliding cut on $p_{\mathrm{T}}(\ell_2)$ with SR-slep-low-$E_{\mathrm{T}}^{\mathrm{miss}}$, allow for a potential different normalization of these processes in the slepton search. In accord with the higgsino search, VRs using DF leptons enable a validation of the background estimation in the phase space of the SR.

Table 5.6 contains the definitions of all CRs and VRs used in the background estimation for the low-$E_{\mathrm{T}}^{\mathrm{miss}}$ channel.

5.5.2 Fake Factor Method

The Fake Factor method is a well established approach to model the contribution of fakes and was employed in a wide range of analyses, see e.g. Refs. [232, 233]. Its implementation for the analysis presented here is described in detail in Ref. [135] and hence only briefly reviewed in the following.

Common sources of fake/nonprompt leptons are misidentified jets, photon conversions and semileptonic decays of heavy-flavor hadrons, with the latter being the dominant component in the SRs as indicated by MC studies. The essential idea of the Fake Factor method is to estimate the contribution from fake/nonprompt leptons that fulfill the tight signal criteria (T) with leptons that fulfill only looser, less restrictive lepton requirements (L) via

$$N^{\text{fake}} = \sum_i N_L^i \times F \,, \tag{5.19}$$

where $F = N_T/N_L$ is the transfer factor (Fake Factor) relating the number of tight and loose leptons, measured in a dedicated sample. As the analysis considers final states with two leptons, both can be of tight and loose quality, hence the expression above becomes schematically

$$N^{\text{fake}} = N_{TL} \times F_2 + N_{LT} \times F_1 - N_{LL} \times F_1 \cdot F_2 \,, \tag{5.20}$$

where the minus sign for the last term accounts for double counting. The factors F_1 and F_2 denote the Fake Factors for the leading and subleading lepton, respectively. This method assumes that the Fake Factors depend only on the properties of the physics object such as its p_{T} and the origin of the fake lepton. Hence it is essential that the fake composition, i.e. the contributions from the various fake/nonprompt lepton sources, are similar between the region where the Fake Factors are measured and where they are applied.

The selection criteria for loose leptons are based on the definitions of baseline electrons and muons shown in Table 5.2, but they are required to explicitly fail the signal definition. Muons are considered as loose if they fail the isolation or d_0 requirement but not both. Likewise, loose electrons are allowed to fail either the *Medium* identification, isolation or d_0 requirement but not simultaneously the identification and isolation criteria. The restrictions to fail multiple signal-lepton requirements were found to improve the fake estimate. The presence of collimated lepton pairs, in which the individual lepton isolation cones overlap, necessitates a special handling in the calculation of the isolation energies for the analysis. In the first place, the isolation energy of a lepton has to be corrected for the contribution of the partner lepton. Second, the energies of "stray" objects not associated with either one of the leptons, such as a track originating from pile-up activity, that lie in the overlapping area of the isolation cones need to be distributed to the isolation energy of only one lepton. Otherwise these stray objects may make both leptons to fail their isolation criteria, leading to the N_{LL}-term in Equation (5.20) becoming too large. Due to technical limitations in the isolation calculation algorithms, only the track-based isolation variable can be corrected but not the calorimeter-based one. This is not an issue for muons, whose isolation WP uses only track isolation. However the *Gradient* isolation WP employed for electrons uses calorimeter-isolation with a radius parameter $\Delta R = 0.2$ (see Section 5.3.1). Hence, the analysis requires a minimal distance $\Delta R_{e\mu} > 0.2$ for electron–muon events (see Table 5.3). Moreover due to limitations to correct for electron calorimeter deposits in their "core" ($\Delta R < 0.1$), the fake
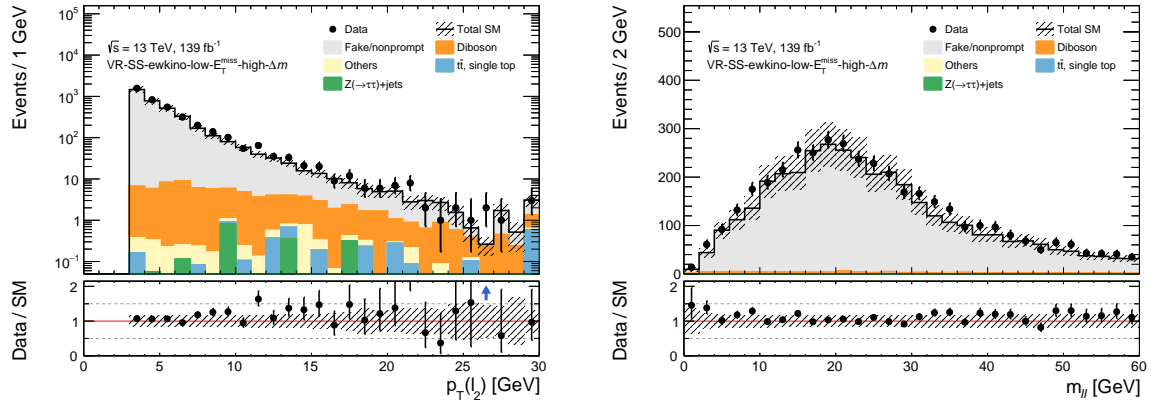
Figure 5.24: Kinematic distribution of $p_T(\ell_2)$ (left) and $m_{\ell\ell}$ (right) in VR-SS-ewk-low-E_T^{miss}-high-Δm after the background-only fit, showing the data as well as the expected background. The uncertainty bands include the statistical and systematic uncertainties.

estimation performance degrades for $\Delta R_{ee} < 0.3$ in electron–electron events. Therefore, such events are also vetoed in the analysis.

The Fake Factors have been measured in a data sample selected by prescaled single-lepton triggers with low p_T thresholds, which is dominated by fake/nonprompt leptons from multijet events. They are calculated as the ratio of the number of tight to loose leptons in this sample, measured separately for electrons and muons, and binned in lepton p_T. Some dependence of the fake factors on the presence or absence of a b-tagged jet was observed, consequently they are calculated separately for events with 0 or at least 1 b-tagged jet. For the first category, the p_T-averaged electron (muon) Fake Factor was found to be approximately 0.35 (0.45) and for the second category 0.5 (0.35).

To account for the contribution of prompt leptons in the loose lepton samples, the contribution is estimated with MC simulation and subtracted in the measurement and application of the Fake Factors. This prompt subtraction has only a minor impact on the final fake estimate.

To avoid double-counting of the fake/nonprompt background, fake/nonprompt leptons are removed from the MC samples by discarding simulated events in which one or both of the leptons cannot be matched to a truth prompt lepton using a ΔR-based criterion. This means, i.e. semileptonic $t\bar{t}$ events, in which the second lepton is faked, are not contained in sample labeled as top, but are accounted for in the fake estimation.

Validation of the fake estimate was performed in regions selecting lepton pairs of SS. As barely any SM process yields a pair of leptons with the same electric charge in the final state, at least one of the leptons is most likely fake in such events. Consequently the SS requirement naturally enriches a selection in fake/nonprompt leptons. These VR-SS are constructed to have the same requirements as the associated SR, in order to select similar fake/nonprompt processes in both regions. Requirements to veto fakes, such as the sliding $p_T(\ell_2)$ cuts are dropped to ensure a high purity in this background. The region VR-SS-ewk-low-E_T^{miss}-high-Δm shares the R_{ISR} requirements applied in SR-ewk-low-E_T^{miss}-high-Δm and SR-slep-low-E_T^{miss}, which allows to validate the fake modeling for both SRs in this VR. This
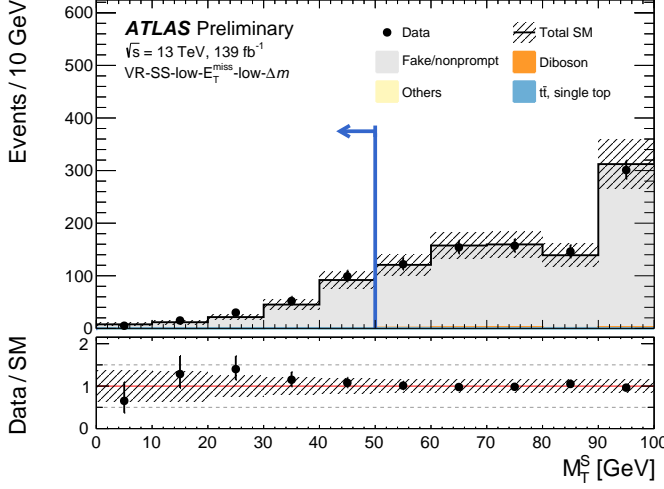
Figure 5.25: Kinematic distribution of M_T^S after the background-only fit in VR-SS-ewk-low-E_T^{miss}-low-Δm, showing the data as well as the expected background. The uncertainty bands include the statistical and systematic uncertainties. The full region definition is applied, except for the requirement imposed on M_T^S. The blue arrow indicates the requirement. Figure taken from Ref [135].

selection is more than 93 % pure in fake/nonprompt leptons, with some minor contributions from VV processes, in which the leptons do not originate from the same vector boson and hence can have the same electric charge. To validate the derived electron and muon Fake Factors, the VR-SS have been split into two samples using the flavor of the subleading lepton. As this lepton is more likely to be be faked, $\mu\mu + e + \mu$ ($ee + \mu e$) events have been used to verify the modeling of fake muons (electrons). For both lepton flavours adequate modeling of the fake/nonprompt leptons was observed.

Figure 5.24 shows the $p_T(\ell_2)$ and $m_{\ell\ell}$ distribution for VR-SS-ewk-low-E_T^{miss}-high-Δm inclusively in lepton flavor. The shape of $p_T(\ell_2)$ is modeled well over the complete spectrum. A similar conclusion can be drawn for the $m_{\ell\ell}$ spectrum. Even in the challenging case of very low $m_{\ell\ell}$, where the leptons are close-by, the data is well within the prediction and its uncertainty. As fakes are by far the most important background in SR-ewk-low-E_T^{miss}-low-Δm, the region VR-SS-ewk-low-E_T^{miss}-low-Δm shares the exact same requirements as the SR, but selects SS lepton pairs. This allows to validate the fake estimate in precisely the same kinematic regime as spanned by the SR. Figure 5.25 shows the distribution of M_T^S in a N-1 fashion for this region. Good modeling of this variable is observed, also at very low values, where potential signals are assumed to accumulate in an OS selection. The signal contamination is calculated as the ratio of the number of signal to the number of total expected background events. Due to the SS requirement, it is negligible ($< 1\%$) for not yet excluded signal points in both VR-SS regions.

5.5.3 Control Regions

In both the higgsino and slepton search, contributions from top, $Z \to \tau\tau$ and diboson processes are normalized to data in three dedicated low-E_T^{miss} CRs. These are based on the preselection summarized in Table 5.3 but typically invert some requirements to enrich the selection in a particular background instead of rejecting it. In addition, the CRs allow lepton pairs of any flavor (AF) to enter the selection instead of only SF as for the SRs. This exploits the lepton flavor symmetry of top, diboson (WW, WZ) and $Z \to \tau\tau$ events, which

| Control Region | | Normalization Parameters | |
		electroweakino	slepton
CR-top	high-$E_\mathrm{T}^\mathrm{miss}$	1.08 ± 0.20	1.05 ± 0.20
	low-$E_\mathrm{T}^\mathrm{miss}$	1.02 ± 0.18	1.01 ± 0.17
CR-tau	high-$E_\mathrm{T}^\mathrm{miss}$	0.96 ± 0.14	0.80 ± 0.17
	low-$E_\mathrm{T}^\mathrm{miss}$	1.01 ± 0.14	1.04 ± 0.15
CR-VV	high-$E_\mathrm{T}^\mathrm{miss}$	0.90 ± 0.27	0.84 ± 0.29
	low-$E_\mathrm{T}^\mathrm{miss}$	0.71 ± 0.23	0.67 ± 0.24

Table 5.7: Normalization factors obtained from a background-only fit of the control regions defined for electroweakino and slepton searches. The uncertainties include statistical and systematic contributions combined. Table adapted from Ref. [135].

yield SF (*ee* and $\mu\mu$) and DF (*e*μ and μe) at approximately equal rates, to increase the CR statistics. The CRs were designed to be kinematically as close as possible to their associated SRs, in order to ensure that the derived normalizations are also valid for the SRs. In particular they employ the same $m_{\ell\ell}/m_\mathrm{T2}$-dependent requirement on $p_\mathrm{T}(\ell_2)$, to guarantee similar lepton kinematics as in the SRs. CRs for the electroweakino search are placed in the phase space of SR-ewk-low-$E_\mathrm{T}^\mathrm{miss}$-high-$\Delta m$. Similarly, their slepton counterparts are placed in the phase space of SR-slep-low-$E_\mathrm{T}^\mathrm{miss}$. The separation into two sets of CRs allows to account for potentially different normalizations in the electroweakino and slepton searches via two sets of normalization factors. Table 5.7 shows the normalization factors derived in a background-only fit. Only small differences arise between the normalizations of the low- and high-$E_\mathrm{T}^\mathrm{miss}$ regime. The normalization factors between the electronweakino and slepton regions are also mainly compatible with each other. Only the normalization for $Z \to \tau\tau$ in the high-$E_\mathrm{T}^\mathrm{miss}$ channel differs to some extend, confirming the decision to introduce two separate sets of normalization factors. Pre- and post-fit event yields for the low-$E_\mathrm{T}^\mathrm{miss}$ CRs are shown in Tables D.1 and D.2.

In the preliminary results presented here, the $E_\mathrm{T}^\mathrm{miss} > 150\,\mathrm{GeV}$ requirement of the low-$E_\mathrm{T}^\mathrm{miss}$ slepton SR was not applied in the slepton CRs. This was adjusted for the final results to move the CRs even closer to the SR. The change has only a minor impact on the low-$E_\mathrm{T}^\mathrm{miss}$ normalization factors and does not change the final outcome of the slepton search in any notable way.

Control Regions for Top

The top CRs constrain the contribution from top processes and are based on the requirements of the preselection but instead of vetoing, they require the presence of at least one *b*-tagged jet. This naturally enriches the selection in events containing a top quark. Further the window cut $R_\mathrm{ISR} \in [0.8, 1.0]$ ensures to select the same event kinematics as present in the associated SRs. The same sliding cuts on $p_\mathrm{T}(\ell_2)$ as applied in the signal selections veto also fakes efficiently, such that the regions are more than $94\,\%$ pure in top events. Only small contaminations, mainly from fake/nonprompt leptons and to a smaller extent diboson events, remain in this
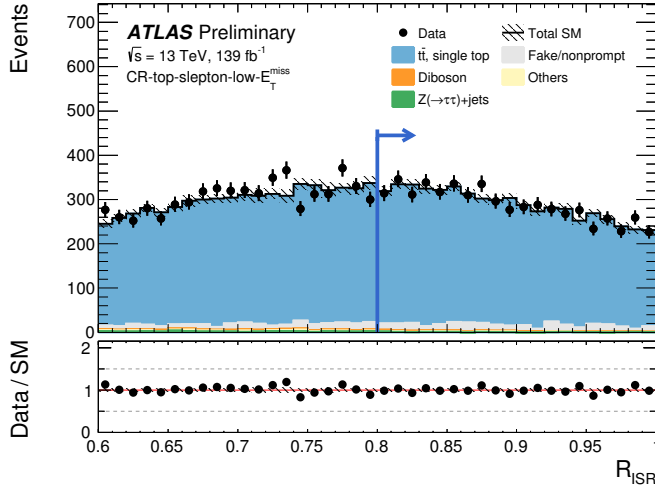
Figure 5.26: Kinematic distribution of R_{ISR} after the background-only fit in CR-top-slep-low-$E_{\mathrm{T}}^{\mathrm{miss}}$, showing the data as well as the expected background. The uncertainty bands include the statistical and systematic uncertainties. The full region definition is applied, except for the requirement imposed on R_{ISR}. The blue arrow indicates the requirement. Figure taken from Ref [135].
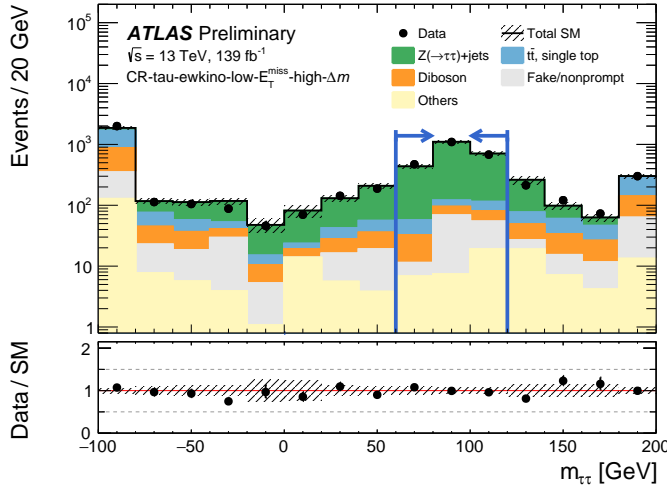

Figure 5.27: Kinematic distribution of $m_{\tau\tau}$ after the background-only fit in CR-tau-ewk-low-$E_{\mathrm{T}}^{\mathrm{miss}}$, showing the data as well as the expected background. The uncertainties bands include the statistical and systematic uncertainties. The full region definition is applied, except for the requirement imposed on $m_{\tau\tau}$. The blue arrows indicate the requirement. The first (last) bin contains the underflow (overflow). Figure taken from Ref [135].

selection. In conjunction with the large statistics of approximately 6000 events in both CR variants, the high purity allows to constrain the top normalization very effectively in the electroweakino and slepton search. Figure 5.26 shows the kinematic distribution of R_{ISR} for the slepton variant, labeled as CR-top-slep-low-$E_{\mathrm{T}}^{\mathrm{miss}}$. An excellent modeling over the complete range used in the SR of this RJR-based variable is observed. Additional plots for the CRs can be found in Appendix D.2.2. For both CRs, the signal contamination is below 0.5 % across the respective signal grid and hence negligible.

Control Regions for $Z \to \tau\tau$

To construct the tau CRs, the $m_{\tau\tau}$ veto is inverted and narrowed to a 60 GeV broad window centered around the Z boson mass, i.e. $m_{\tau\tau} \in [60, 120]$ GeV, to maximize the purity in $Z \to \tau\tau$ events. The selected R_{ISR} range is extended to $[0.6, 1.0]$ in order to increase the statistics of the regions. The $m_{\ell\ell}/m_{\mathrm{T2}}$ dependent requirements on $p_{\mathrm{T}}(\ell_2)$ of the respective SR reduces

Figure 5.28: Kinematic distribution of E_T^{miss}/H_T^{lep} after the background-only fit in VR-tau-ewk-low-E_T^{miss}-low-Δm, showing the data as well as the expected background. The uncertainties bands include the statistical and systematic uncertainties. The full region definition is applied, except for the requirement imposed on the variable being plotted. The blue arrow indicates the requirement. Figure taken from Ref [135].
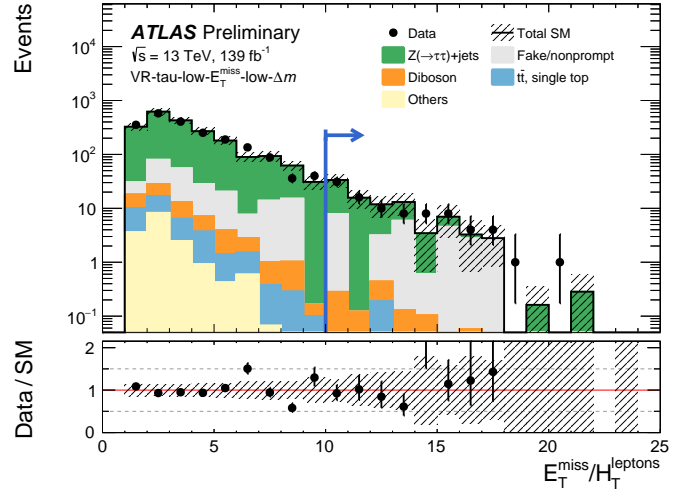
the contamination from fakes. Both tau CRs are approximately 87% pure in $Z \to \tau\tau$ events and are populated by a sufficient number of data events (~ 2200 for the electroweakino and ~ 1600 for the slepton CR) to constrain this background efficiently. The remaining events originate roughly to equal parts from fake/nonprompt leptons, top and diboson-related processes. Figure 5.27 shows the $m_{\tau\tau}$ distribution in the electronweakino variant of the CRs, labeled CR-tau-ewk-low-E_T^{miss}. The $Z \to \tau\tau$ resonance is clearly visible around $m_{\tau\tau} = 90\,\text{GeV}$, but a notable smearing of $Z \to \tau\tau$ events outside the selected mass window is present. The background prediction describes the data well, also for $m_{\tau\tau} \in\,]0, 160[\,\text{GeV}$, which confirms the derived normalization for $Z \to \tau\tau$ events is also valid for the kinematic regime of the SR. For both signal grids, the signal contamination is below 1% in the associated CR.

As the CR in the electroweakino search employs the requirement $E_T^{miss}/H_T^{lep} < 10$ from the respective SR, it has to be verified that the derived $Z \to \tau\tau$ normalization is also valid in the phase space of SR-ewk-low-E_T^{miss}-low-Δm ($E_T^{miss}/H_T^{lep} > 10$). For this purpose, VR-tau-ewk-low-E_T^{miss}-low-Δm inverts the $m_{\tau\tau}$ veto of this SR to select the same mass window as described above and applies the same requirement on E_T^{miss}/H_T^{lep} as the associated SR. This selection is over 70% pure in $Z \to \tau\tau$ events, with the remaining contribution stemming nearly exclusively from fake/nonprompt leptons, which are confirmed to be adequately modeled in this phase space. This allows to make reliable statements about the $Z \to \tau\tau$ modeling despite the limited statistics in this region (~ 90 events). The signal contamination in this region is slightly larger, but below 4% across the non-excluded part of the signal grid and hence on a tolerable level. The distribution of E_T^{miss}/H_T^{lep} is shown in Figure 5.28 and found to be adequately modeled across the spectrum.

Control Regions for Diboson

The CRs to constrain the contribution from diboson events are placed adjacent to the SR by requiring $R_{ISR} \in [0.6, 0.8]$ and thus remain orthogonal but kinematically as close as possible to the SRs. As for the other CRs, the sliding $p_T(\ell_2)$ requirements veto fakes and ensure to select events with the same lepton kinematics as the associated SRs. To suppress top
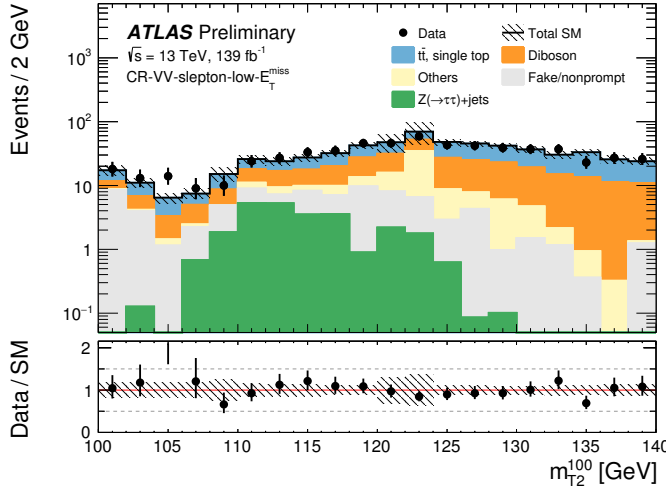
Figure 5.29: Kinematic distribution of m_{T2}^{100} after the background-only fit in CR-VV-slep-low-E_T^{miss}, showing the data as well as the expected background. The uncertainties bands include the statistical and systematic uncertainties. Figure taken from Ref [135].

events, the CRs are restricted to events with less than three jets. Likewise, the requirements on $m_T^{\ell_1} > 30\,\text{GeV}$ reduce the contamination from $Z \to \tau\tau$ events. Despite these additional requirements, the purity of the dibons CRs does not exceed 45 % in simulation. In particular the top background is challenging to discriminate against and contributes roughly as much as the diboson events. However, as the top processes are constrained in their own, dedicated CRs of high purity, the regions will nevertheless be sensitive to any mismodeling of the diboson background. The available statistics in the electroweakino (~ 700 events) and slepton (~ 600 events) CR-VV are sufficient to verify that also the kinematic shapes are adequately modeled. The distribution of m_{T2}^{100} is shown exemplarily in Figure 5.29 for the slepton variant of the CRs, labeled accordingly as CR-VV-slep-low-E_T^{miss}. The m_{T2} mass spectrum is excellently modeled, except for the third bin, where some deviation is found. As no general mismodeling is present, this is interpreted as a statistical fluctuation. In both CR variants, the signal contamination is at most 5 % across the associated signal grid and hence on a tolerable level.

5.5.4 Different-Flavor Validation Regions

A powerful validation of the overall goodness of the background estimate can be achieved by replacing the SF requirement on the leptons in the SR with a DF ($e\mu$, μe) requirement. This allows to probe the background modeling in an orthogonal but kinematically identical region. For this purpose, one VR-DF is defined for each SR of the analysis, in which the accuracy of the background modeling is verified. Figure 5.30 shows the comparison of the background predictions obtained from the background-only fit with data for all electronweakino and slepton DF VRs, including the ones corresponding to the high-E_T^{miss} SRs introduced in Section 5.3.6. The same binning in $m_{\ell\ell}$ and m_{T2} as in the associated SRs is used to validate the modeling separately in the respective kinematic regimes. Good agreement is found across the selected mass spectra, with deviations below 2σ using the significance measure defined in Equation (5.17). No notable over- or underestimation of the data is present neither in the $m_{\ell\ell}$ nor in the m_{T2} based regions, which would indicate a general misconception in the background estimation. Two, slightly more pronounced deviations are present in the first bin
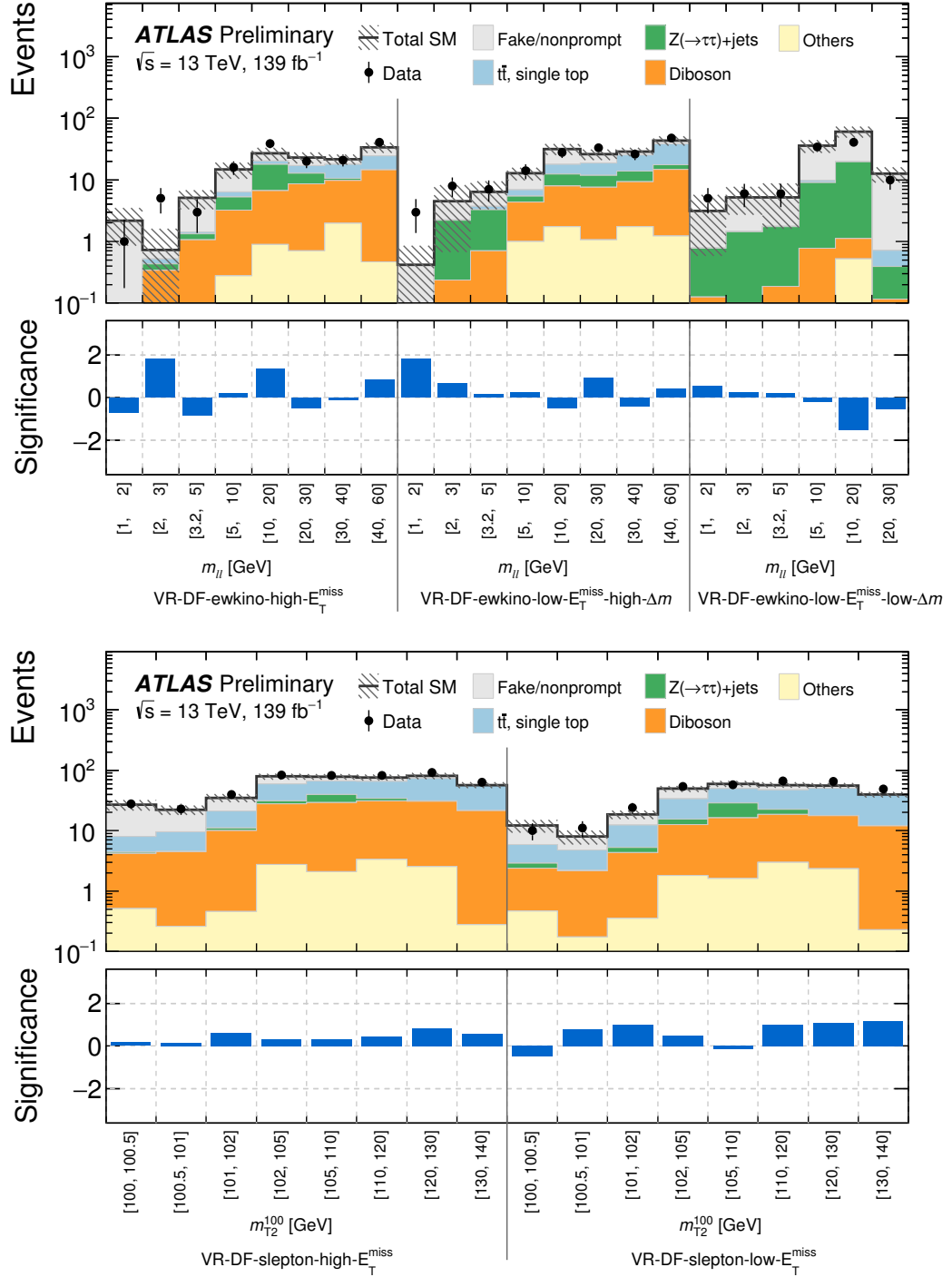
Figure 5.30: Comparison of observed and expected event yields in the high-E_T^{miss} and low-E_T^{miss} VR-DF after a background-only fit of the CRs. The three electronweakino DF VRs are shown at the top, separated by the black vertical lines. Each VR is binned in $m_{\ell\ell}$ as the associated SR. The two slepton DF VRs are shown in the bottom plot, binned in m_{T2}^{100} as the corresponding SRs. Uncertainties on the background prediction include both the statistical and systematic uncertainties. The bottom panel shows the significance of the difference between the observed and expected yields, calculated with Equation (5.17). Figures taken from Ref. [135]

of the high-$E_\mathrm{T}^\mathrm{miss}$ electroweakino VR-DF labeled as VR-DF-ewk-low-$E_\mathrm{T}^\mathrm{miss}$-high-$\Delta m$ and the second bin of VR-DF-ewk-low-$E_\mathrm{T}^\mathrm{miss}$-high-$\Delta m$. As these deviations happen in different $m_{\ell\ell}$ bins for high-$E_\mathrm{T}^\mathrm{miss}$ and low-$E_\mathrm{T}^\mathrm{miss}$, and good modeling is observed for the neighboring $m_{\ell\ell}$ bins, they are interpreted as statistical fluctuations.

5.6 Systematic Uncertainties

Besides statistical uncertainties originating from limited data and MC sample sizes, the background and signal predictions are subjected to systematic uncertainties as well. Typically, an uncertainty yields an upwards and a downwards variation of the predicted event count. These are parametrized and included as nuisance parameters in the statistical model, which is then fitted to data. The large number of systematic uncertainties considered, leads, in conjunction with the high number of regions present in a combination of all analysis channels, to a rather complex statistical model. To decrease the complexity and increase fit stability, *pruning* was introduced in the building of the statistical model. Uncertainties on a sample in a particular region are only added to the likelihood if the upwards or downwards variation differs by more than 3 % from the nominal yield in that region. This level of pruning was found to give a good compromise between the residual complexity of the fit configuration and the impact on the analysis. To study the impact of this pruning approach the CL_s values from a pruned and unpruned setup for a couple of signal points have been compared. As the CL_s values of both configurations were found to be compatible with each other, the pruning applied is assumed to have a negligible impact on the final results.

Systematic uncertainties are categorized into two groups: experimental and theoretical uncertainties.

5.6.1 Experimental Uncertainties

Uncertainties falling into this category arise from the experimental methods used to derive the nominal yield predictions, such as calibration and efficiency measurements. These are evaluated using variational samples (i.e. produced with varied calibration inputs) or variational weights in replacements of the nominal ones. The various sources of experimental uncertainties are discussed below.

Luminosity and Pile-Up Reweighting

Several uncertainties have been considered in the measurements of the integrated luminosity as discussed in Ref. [141]. The total uncertainties for each individual year vary between 2 and 2.4 %, with the largest contributions originating from the uncertainties on the calibration transfer and the long-term stability. Due to inter-year correlations between the individual uncertainty components, the final uncertainty on the integrated luminosity of the combined Run 2 dataset is 1.7 %. This uncertainty is not assigned on backgrounds whose contributions are normalized to data, i.e. on top, $Z \to \tau\tau$ and diboson background samples.

An additional source of uncertainty arises from the employed procedure for pile-up reweighting. To estimate the magnitude of this uncertainty, the pile-up weights have been re-evaluated after varying the data rescaling factor with ±0.04 around its nominal value at 1.03.

Trigger Scale Factors

The E_T^{miss} triggers used in the analysis are not in their efficiency plateaus for $E_T^{miss} < 200\,\text{GeV}$. Hence scale factors have been derived to correct for mismodeling of the trigger efficiencies in simulation. Several sources of systematic uncertainties on these scale factors have been evaluated, as presented in Appendix B.7. In the preliminary analysis results presented here, trigger scale factors and consequently their uncertainties have been assigned only on the signal samples. Uncertainties cover the dependence of the scale factors on analysis variables such as $m_{\ell\ell}$ and R_{ISR}, as well as differences between the trigger efficiencies measured in background and signal samples.

The final analysis results use trigger scale factors also for the background samples. An additional uncertainty is assigned on these samples to cover differences in the measured trigger efficiencies between the individual background processes.

Fake Estimate

Uncertainties in the Fake Factor method originate from the finite sample sizes in the region where the Fake Factors are derived, and differences in the event kinematics between that region and the application region, such as the SRs. The latter uncertainty has been estimated by evaluating the dependence of the Fake Factors on variables such as the lepton $|\eta|$, R_{ISR} and the number of jets. The Fake Factors were binned in these variables instead of the lepton p_T and the difference to the average nominal Fake Factors allows to estimate their variable dependence. Flat uncertainties of 40 % for electrons and 20 % for muons were found to cover these differences. Variations of the MC estimates used in the prompt subtraction were found to have a negligible impact on the fake estimate. To account for the mismodeling of the fake/nonprompt background not yet covered by the uncertainties above, additional uncertainties were computed based on the background predictions and the observed data in regions enriched in fakes such as the SS VRs. Discrepancies in the $p_T(\ell_2)$ spectrum not within the envelope of the other fake uncertainties, are covered with a residual uncertainty, such that the disagreement observed in the SS VRs is covered by the total uncertainty on the fake estimate.

Leptons

Uncertainties associated with electrons arise from calibrations of the electron energy scale and resolution [206, 207]. A simplified scheme is used in this analysis in which all physical effects are summed in quadrature and the individual components are treated as fully correlated in η, resulting in one nuisance parameter for the energy scale and one for the resolution. Likewise, muon uncertainties arise from the calibrations of the muon momentum scale and resolution [122]. These are defined by variations in the p_T smearing of the ID and MS track, and variations in the scale of the muon momentum. Additional lepton uncertainties originate from the measurements of reconstruction, identification, isolation and track-to-vertex-association (muons only) efficiencies.

Jets

Uncertainties on jets arise from the calibration of the JES and JER. The former considers predominantly uncertainties in the in-situ calibrations using $Z/\gamma+$jets and multijet events, as well as pile-up uncertainties and uncertainties to account for differences in the jet response and flavor composition of the MC sample used [213]. Uncertainties on the JER arise from observed differences between the data and MC resolution, noise from pile-up and electronics as well as from the measurement of the JER in dijet events [215]. For both the JES and JER the number of nuisance parameters is reduced by an eigenvector decomposition of the uncertainties [234], in which components of smaller magnitude are combined into single nuisance parameters at the price of correlation losses. The preliminary results used a stronger reduced set of JES and JER uncertainties with additional correlation losses. The final analysis results will be based on the less-reduced sets of uncertainties. The jet uncertainties of the differently reduced sets have been found to be compatible with each other.

The calibration of the JVT constitutes an additional source of uncertainty, and consists of a statistical component and a flat uncertainty on the estimation of pile-up [235].

Uncertainties on the *b*-tagging efficiency arise, e.g. , from uncertainties on the background modeling and the *b*-tagging performance on charm and light-flavor jets, as well as on the extrapolation to high-p_T jets [236]. The analysis uses a reduced set of flavor tagging-uncertainties, which is constructed by summing the covariance matrices of each uncertainty source [237].

Missing Transverse Energy

Being a global event variable, the uncertainty on the $E_\mathrm{T}^\mathrm{miss}$ is computed using the systematics assigned to the individual objects entering the $E_\mathrm{T}^\mathrm{miss}$ calculation. Additional uncertainties arise in the computation of the track soft term from detector resolution effects. Uncertainties are evaluated by comparing the agreement between data and simulation in the parallel and perpendicular components of the track soft term (with respect to the hard term in the $E_\mathrm{T}^\mathrm{miss}$ calculation) in events with zero true $E_\mathrm{T}^\mathrm{miss}$ [222].

Low Background Statistics Uncertainty

Due to the large number of $m_{\ell\ell}/m_\mathrm{T2}$ SR bins present in the analysis, in few cases some of the bins are not populated by either top, $Z \to \tau\tau$ or diboson events due to the limited MC statistics. Similarly, in rare cases also the fake estimate vanishes, when no data events with loose leptons fall into the particular region of phase space. In such cases, no contribution of the respective background would appear in the term modeling the associated region in the likelihood. To improve the handling of vanishing backgrounds due to limited MC/fake statistics, their expectation is set to a small value instead of zero in such cases. A dedicated uncertainty is assigned which magnitude is defined by the average event weight in the top, $Z \to \tau\tau$ and diboson sample, respectively. In case of a vanishing fake estimate, the uncertainty is defined by the average electron (muon) Fake Factor for *ee* ($\mu\mu$) bins. The idea of this "upper limits on zeroes" approach is to improve the fit stability in cases of a deviation between the observed and predicted yields in SR bins that are statistically-wise only sparsely populated. Instead of pulling the nuisance parameters of other systematics, the fit can pull these parameters.

5.6.2 Theoretical Uncertainties

Theoretical uncertainties cover uncertainties on modeling parameters in the simulation of background and signal events.

Background

Uncertainties on the background modeling of top, $Z \to \tau\tau$ and diboson events in the CRs and all SR bins were evaluated using internal weights, and propagated as variations of the nominal background predictions to the statical model. The uncertainties are assumed to be independent of the lepton flavor and have thus been evaluated inclusively in $ee, \mu\mu, e\mu$ and μe events. Consequently, the DF VRs share the same background modeling uncertainties as the associated SRs. Several sources of modeling uncertainties have been considered for these backgrounds, while a flat 50% uncertainty is assigned to the backgrounds contained in the "others" sample.

Renormalization and Factorization Scale Uncertainties on the QCD renormalization scale μ_R and factorization scale μ_F (see Section 3.3) have been evaluated by variations of the corresponding generator parameters with a factor of 2 around their nominal values. The envelope of the variations is taken as uncertainty on the scale variations.

Strong Coupling Parameter The uncertainty on the choice of the value for the strong coupling parameter α_S was derived by variations from its nominal value $\alpha_S = 0.18$ to 0.17 and 0.19. The differences to the nominal background expectation are taken as up- and down variations of this systematic uncertainties.

PDF Uncertainties on the choice of the PDF set have been evaluated by symmetrizing the variations in the predictions with respect to the NNPDF3.0 [158], CT14 [238] and MMHT14 [239] PDF sets, in accord with Ref. [154].

Signal

Uncertainties on the expected yields for SUSY signals have — except for the uncertainty on the signal cross section — been taken from the last iteration of the analysis [176], as the generator configurations used in the simulation step have been very similar. Some of the sources for uncertainties listed below such as the choice of PDF set may also have an impact on the $m_{\ell\ell}/m_{\mathrm{T2}}$ shapes of the SUSY signals. These were found to be small and are consequently neglected.

Cross Section Uncertainties on the signal cross sections have been calculated with Re-summino as presented in Section 5.1.2. Following an ATLAS convention, the uncertainty on the signal cross section is not taken into account in the nominal observed model-dependent exclusion limits. Instead, two additional sets of CL_s values are computed in which this uncertainty is fixed manually at its $\pm 1\sigma$ values. The exclusion contours defined by these two sets of CL_s values, represent the dependence of the analysis result on the signal cross-section uncertainty.
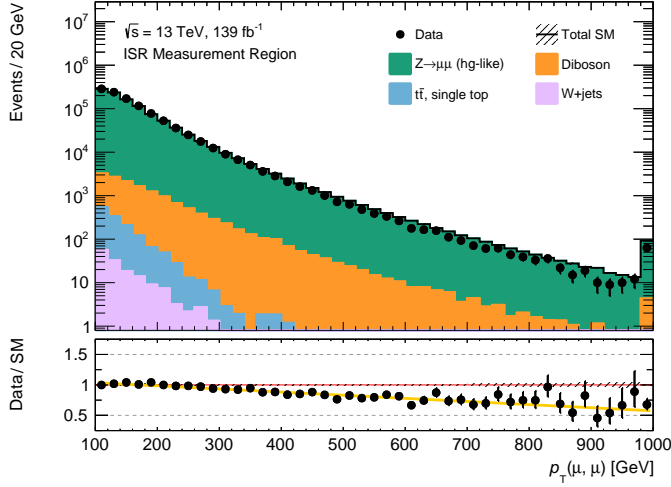
Figure 5.31: Kinematic distribution of $p_T(\mu, \mu)$ showing the data as well as the expected background in the region defined to estimate the uncertainty on ISR. The higgsino-like $Z \to \mu\mu$ MC sample (see text) was normalized to data and is scaled by a factor of 0.794. The last bin contains the overflow. The uncertainty bands show only the statistical uncertainty. A linear fit of the ratio of the data and the MC prediction, indicated as yellow line in the bottom panel, is used to estimate the uncertainty on ISR.

PDF   PDF uncertainties were evaluated at truth level using higgsino and slepton events passing the signal selections. The contributions were reweighted with the 100 eigen-variations of the PDF4LHC15 PDF set [154] to derive the final uncertainty estimate. The uncertainties were found to increase with $\tilde{\chi}_2^0/\tilde{\ell}$ mass but are in general below 15 %. Hence, a conservative uncertainty of 15 % is assigned to all higgsino and slepton samples.

ISR, FSR and Underlying Event   Uncertainties on the modeling of ISR, FSR and the underlying event were estimated by variations of the renormalization and factorization scales, the parameters defining the merging scale in PYTHIA and the PYTHIA shower tunes. In general the uncertainties were found to be below 20 % for the higgsino models and 25–50 % for the slepton models, increasing with decreasing mass splittings. In the preliminary analysis results, a flat 20 % uncertainty is assigned on the higgsino signals, while the uncertainty is 50 % for $\Delta m < 1$ GeV, 40 % for $\Delta m < 2$ GeV, 30 % for $\Delta m < 4$ GeV and 25 % on slepton samples with larger mass splittings.

Due to the signal topology, the uncertainty estimate is assumed to be predominantly driven by the uncertainty on ISR. The final analysis results will use a data-driven estimate of the ISR uncertainty, using $Z \to \mu\mu$ as proxy for signal events, see Appendix C. In a sample enriched in $Z \to \mu\mu$ events, the transverse momentum of the dimuon system $p_T(\mu, \mu)$ is sensitive to the modeling of ISR, as shown in Figure 5.31. A dedicated $Z \to \mu\mu$ MC sample was generated, using a generator configuration as close as possible to the one used in the signal generation. This allows to estimate the uncertainty on ISR modeling in the signal samples with the discrepancy observed in the (fitted) $p_T(\mu, \mu)$ distribution. The final ISR uncertainties are estimated on a event-by-event basis, individually for each SR. They are found to be 7–20 % in the high-E_T^{miss} channel and 2–3 % in the low-E_T^{miss} channel. The resulting decrease in signal uncertainty notably improves the higgsino and slepton limits with respect to the preliminary analysis results.
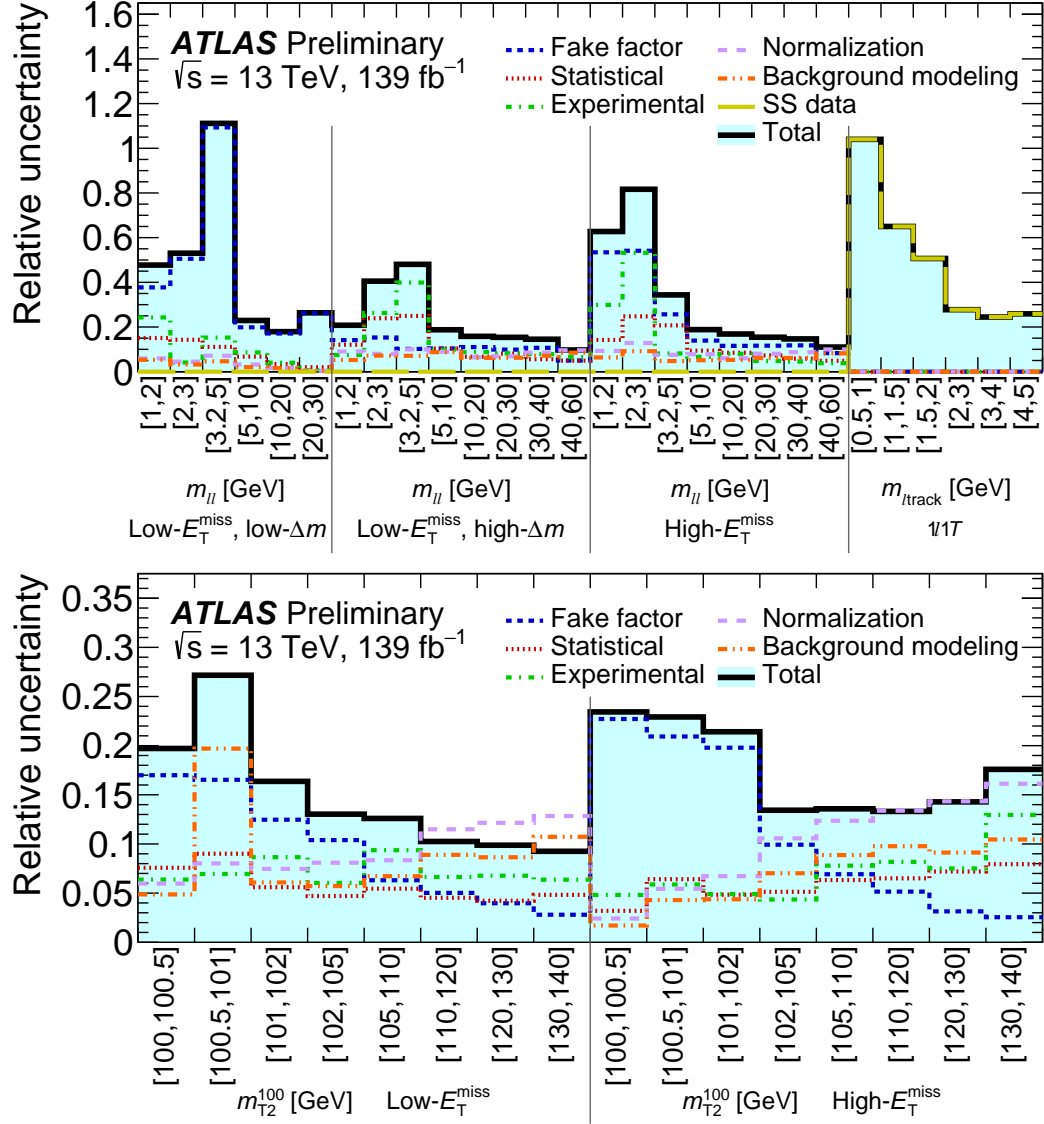
Figure 5.32: The relative systematic uncertainties in the background prediction as obtained from background-only fits extrapolated to the electroweakino SRs (top) and to the slepton SRs (bottom). The *Statistical* uncertainty originates from the limited size of the MC samples used to model the irreducible background contributions. The *Normalization* uncertainty arises from the use of CRs to normalize the contributions of top, $Z \rightarrow \tau\tau$ and diboson backgrounds. The individual uncertainties can be correlated and do not necessarily add up in quadrature to the total uncertainty. Figures taken from Ref. [135].

5.6.3 Impact on Signal Regions

Figure 5.32 shows the breakdown of the systematic uncertainties on the background predictions into categories after a background-only fit and the extrapolation of the nuisance parameters to the SRs. In general, the total uncertainty on the background prediction is about 50–70 % in low-$m_{\ell\ell}$ bins and decreases to 10–20 % in the higher $m_{\ell\ell}$ bins. In the slepton SRs, the total uncertainty is about 20–30 % in the low- and 10–20 % in the high-$m_{\mathrm{T}2}$ bins. At low $m_{\ell\ell}/m_{\mathrm{T}2}$, the total uncertainty is mainly dominated by the uncertainty on the fake estimate, as there the fake/nonprompt lepton background contributes the most to the total background. A significant contribution originates also from the experimental uncertainties (excluding the uncertainties from the Fake Factor method). These are dominated by the JES and JER uncertainties, while the other sources of experimental uncertainties contribute only minor to the total background uncertainty. The theoretical uncertainties on the background modeling are roughly 10 % across the $m_{\ell\ell}$ and $m_{\mathrm{T}2}$ bins. The associated nuisance parameters are strongly correlated with the normalization factors, which results in the total uncertainty actually being smaller than some of its components as present in some of the high $m_{\mathrm{T}2}$ bins.

5.7 Results

After the validity of the background estimation in the kinematic phase space of the SRs has been verified, the predictions were compared to data. The interpretations in terms of the higgsino and slepton models are derived using a combination of the respective analysis channels. Consequently, the results of all channels are reviewed briefly, with the main focus on the low-$E_{\mathrm{T}}^{\mathrm{miss}}$ SRs.

5.7.1 Channel Combination

As the low-$E_{\mathrm{T}}^{\mathrm{miss}}$ and high-$E_{\mathrm{T}}^{\mathrm{miss}}$ channels, and in case of the electroweakino analysis the $1\ell 1T$ channel, are orthogonal to each other by construction, they are combined via a simultaneous fit to maximize the sensitivity in the higgsino and slepton interpretations. This means, the signal-strength parameter is constrained using all available SR bins. Normalization of the top, diboson and $Z \to \tau\tau$ backgrounds is performed individually in the associated CRs, using separate normalization parameters for the low-$E_{\mathrm{T}}^{\mathrm{miss}}$ and high-$E_{\mathrm{T}}^{\mathrm{miss}}$ channel. The effects of the experimental systematic uncertainties are assumed to impact the low-$E_{\mathrm{T}}^{\mathrm{miss}}$ and high-$E_{\mathrm{T}}^{\mathrm{miss}}$ regions in a similar way and are thus implemented as correlated across the regions. This is not necessarily true for systematic uncertainties on the background modeling. Hence, these are implemented as uncorrelated between the low-$E_{\mathrm{T}}^{\mathrm{miss}}$ and high-$E_{\mathrm{T}}^{\mathrm{miss}}$ channel, i.e. with separate nuisance parameters. As the $1\ell 1T$ channel has a separate, purely data-driven background estimate with dedicated uncertainties, it is rather loosely connected to the 2ℓ channels. Correlation occurs only via the signal-strength parameter and the experimental uncertainties on the signal predictions.

5.7.2 Signal Regions

Figure 5.33 shows the observed and expected event yields in all $m_{\ell\ell}$ and $m_{\mathrm{T}2}$ bins of the electroweakino and slepton search, respectively. The yields have been derived in a background-
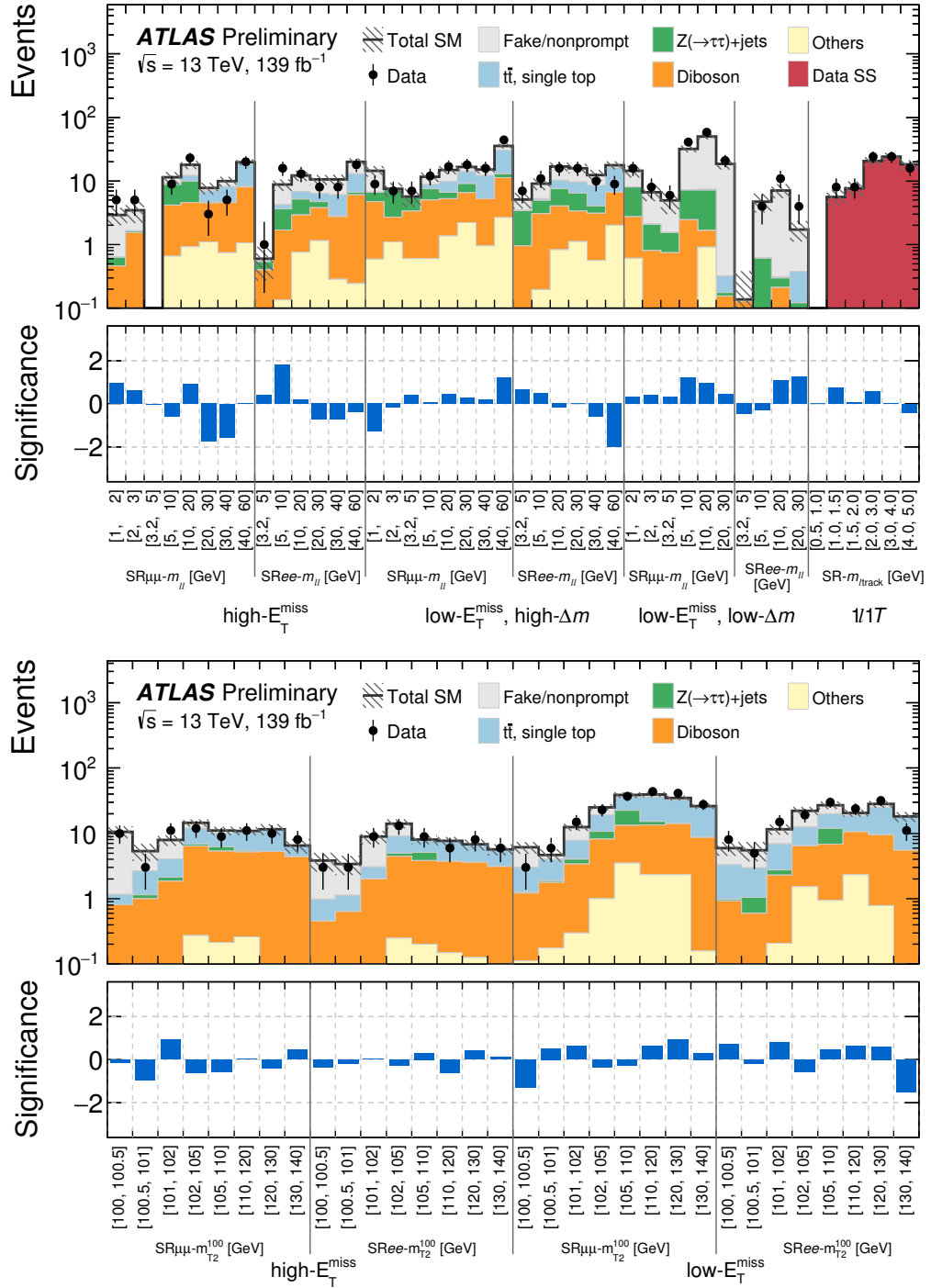
Figure 5.33: Comparison of observed and expected event yields in the SRs after the SR-constrained background-only fits. The SRs used for electroweakino searches recoiling against ISR are shown at the top, binned in $m_{\ell\ell}$. The SRs used for slepton searches recoiling agains ISR are shown at the bottom, binned in m_{T2}^{100}. The bottom panel in each plot shows the significance of the difference between the observed and expected yields, calculated with Equation (5.17). Figures taken from Ref. [135].

only fit in which the SRs bins were added in addition to the CRs as constraining regions. Such a configuration is better suited to test how well the background model can describe the observation than a fit in which the nuisance parameters are only constrained in the control regions. Furthermore it is similar to the setup used in the hypothesis tests for model exclusion and thus aids to understand the shape of the excluded signal parameter space in the higgsino and slepton interpretations. The associated observed and expected event yields using this fit configuration are listed in Appendix D.3.

The top plot in Figure 5.33 depicts the 44 $m_{\ell\ell}$ bins of the electroweakino search. No significant deviations from the SM predictions have been observed, as illustrated by the bottom panel which illustrates the significance of an excess or deficit in the single bins. A notable excess of slightly below 2σ is present in the second $m_{\ell\ell}$ bin for electron pairs in the high-$E_{\mathrm{T}}^{\mathrm{miss}}$ SR. Due to the absence of significant deviations in the low-$E_{\mathrm{T}}^{\mathrm{miss}}$ and $1\ell 1T$ channels, it is interpreted as a statistical fluctuation. While the SM predictions show a mostly excellent agreement in SR-ewk-low-$E_{\mathrm{T}}^{\mathrm{miss}}$-high-$\Delta m$, a small tendency to underestimate the data is present in SR-ewk-low-$E_{\mathrm{T}}^{\mathrm{miss}}$-low-$\Delta m$. As the main background in these regions originates from fake/nonprompt leptons, it indicates a small underestimation of this contribution by the Fake Factor method. However, the deviations are covered by the uncertainties in most of the bins. In SR bins with no observed event, the background expectation nearly vanished after the fit. The reason for this behavior, is that the nuisance parameters associated with the statistical uncertainty are getting pulled to zero in the fit, rendering tiny post-fit background yields in the affected SR bins. This is improved for the final results, where the statistical uncertainties are modeled with Poisson instead of Gaussian constraint terms in the likelihood, which do not exhibit such a behavior. The continuous $m_{\ell\ell}$ spectrum and the kinematic distributions of $M_{\mathrm{T}}^{\mathrm{S}}$ and $p_{\mathrm{T}}(\ell_2)$, respectively, are shown in the top and middle row of Figure 5.34. Except for the slight underestimation of the fake/nonprompt lepton background in SR-ewk-low-$E_{\mathrm{T}}^{\mathrm{miss}}$-low-$\Delta m$, the kinematic shape of the data is overall reproduced well by the SM prediction. The dashed lines indicate the shape and location of potential higgsino signals at nominal signal strength.

The 32 m_{T2} bins of the slepton search are shown in the bottom plot of Figure 5.33. Excellent agreement between the SM prediction and the data is found, with no tendency of under- or overestimation of the background in any region of phase space. The modeling of the m_{T2} and $p_{\mathrm{T}}(\ell_2)$ distributions in SR-slep-low-$E_{\mathrm{T}}^{\mathrm{miss}}$ are shown exemplary in the bottom row of Figure 5.34. Similarly to the electroweakino SRs, the kinematics of the data are well reproduced by the predictions and do not indicate any presence of BSM physics.

5.7.3 Higgsino and Slepton Interpretations

The absence of significant deviations from the SM predictions motivates to set exclusion limits on the signal models considered. To decide whether a signal point can be excluded or not, the CL_s prescription introduced in Section 5.2.2 is used. Figure 5.35 shows the observed and expected exclusion contours for the higgsino and slepton model at 95 % CL, i.e. points with $\mathrm{CL}_s < 0.05$ are excluded.

In the higgsino model, the observed exclusion limit is notably weaker than the expected one due to the several small to moderate excesses in the electroweakino SRs. Significant improvements of the limits derived by the previous iteration of the analysis are observed for
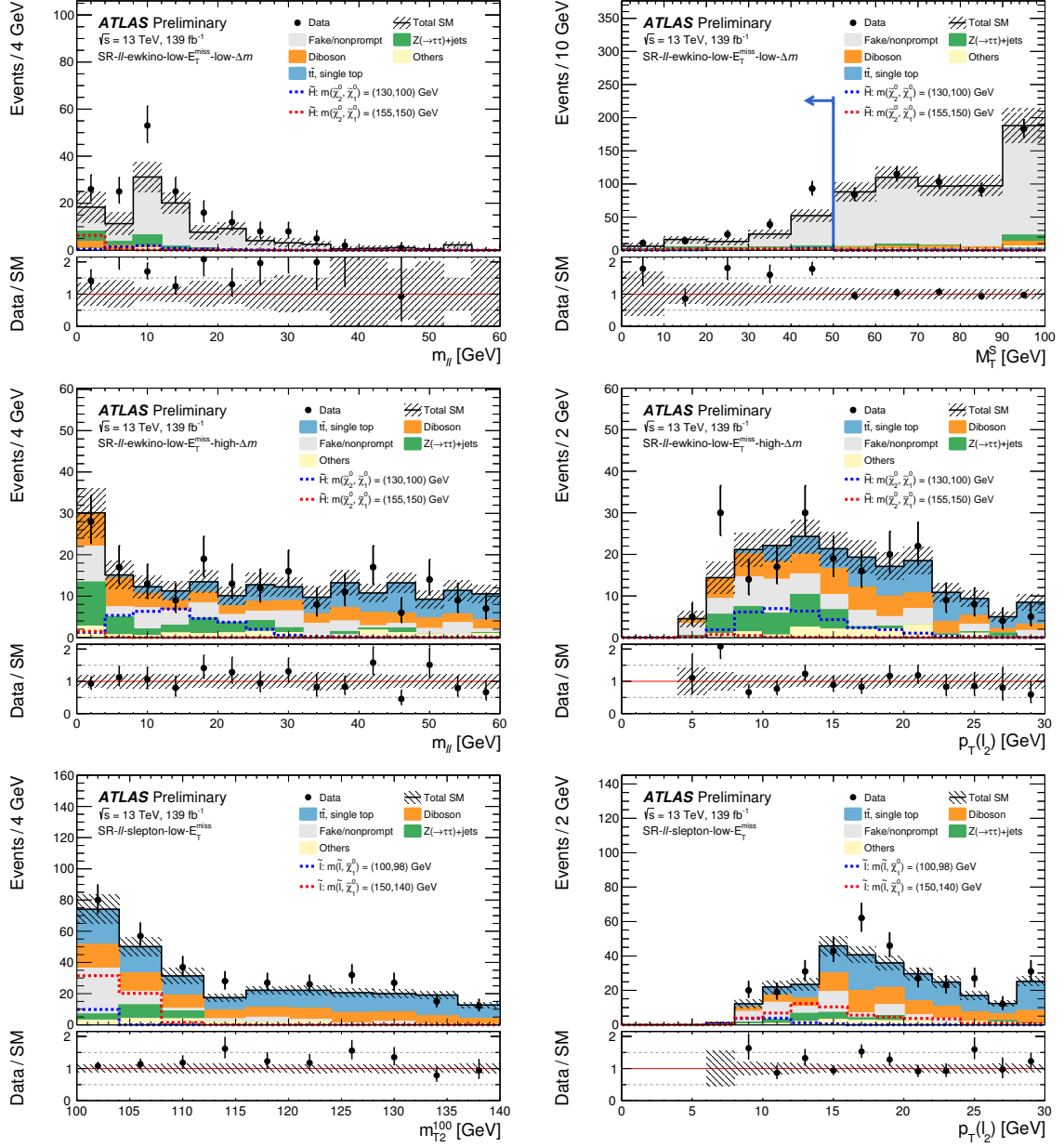
Figure 5.34: Examples of kinematic distributions after the background-only fits showing the data as well as the expected background in the low-E_T^{miss} signal regions sensitive to electroweakinos (top, middle) and sleptons (bottom). The full event selection of the corresponding regions is applied, except for the requirement that is imposed on the variable being plotted. This requirement is indicated by blue arrows in the distributions. The first (last) bin includes underflow (overflow). The uncertainty bands plotted include all statistical and systematic uncertainties. Figures takes from Ref. [135].
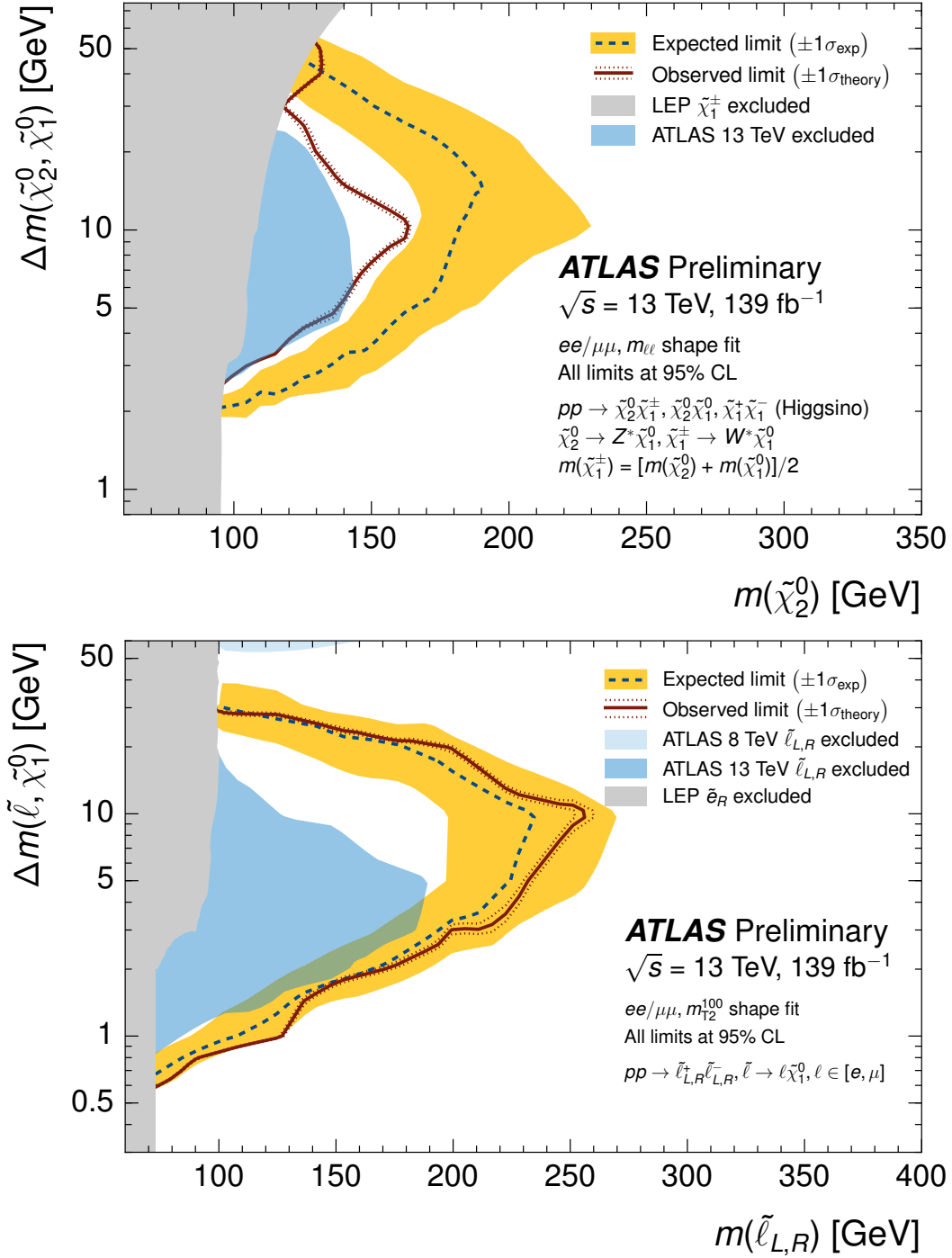
Figure 5.35: Expected 95% CL exclusion sensitivity (blue dashed line) with $\pm 1\sigma_{\mathrm{exp}}$ experimental systematic uncertainties (yellow band) and observed limits (red solid line) with $\pm 1\sigma_{\mathrm{theory}}$ from signal-cross section uncertainties (dotted red line) for simplified models of direct higgsino (top) and slepton (bottom) production. The limits are projected into the $\Delta m(\tilde{\chi}_2^0, \tilde{\chi}_1^0)$–$m(\tilde{\chi}_2^0)$ and $\Delta m(\tilde{\ell}, \tilde{\chi}_1^0)$–$m(\tilde{\ell})$ plane, respectively. The gray regions denote mass limits from the LEP experiments, while the blue regions indicates the limits from the previous iteration of the analysis [176]. The slepton exclusion plot also includes the limit on slepton masses from ATLAS in Run 1 [240]. Figures taken from Ref. [135].

mass splittings $\Delta m(\tilde{\chi}_2^0, \tilde{\chi}_1^0)$ above 5 GeV. $\tilde{\chi}_2^0$ masses up to 162 GeV are excluded at mass splittings of approximately 10 GeV. At the bounds from the LEP experiments, mass differences from 2.6 GeV to 53 GeV are excluded. The behavior of the observed contour can be understood from the pulls between the data and the SM predictions shown in Figure 5.33. In low-$m_{\ell\ell}$ bins, both the high-E_T^{miss} and $1\ell1T$ SRs show small excesses, resulting in the reduced observed exclusion strength at small mass splittings with respect to the expected exclusion limit. The drop in the observed exclusion contour around a mass splitting of 30 GeV originates dominantly from the excesses in the $\mu\mu$-$m_{\ell\ell}$ [10, 20] GeV and ee-$m_{\ell\ell}$ [5, 10] GeV bins of SR-ewk-high-E_T^{miss}. A large fraction of events from signals with mass splittings between 10 and 30 GeV enters these $m_{\ell\ell}$ bins, such that the signal-strength parameter is less constrained by the fit and the exclusion power is reduced. Finally, the stronger observed exclusion contour at large mass splittings around 50 GeV with respect to the expected contour, is a consequence from the series of deficits observed in the large $m_{\ell\ell}$ bins of the electroweakino SRs.

Due to the overall excellent agreement between data and SM prediction in the m_{T2} bins of the slepton SRs, the expected and observed exclusion contours are close to each other across the signal grid. A significant improvement with respect to the limits from LEP and to the previous iteration of the analysis is present. Slepton masses $m(\tilde{\ell})$ up to 256 GeV for mass splittings of 10 GeV are excluded. Slepton signals can also be excluded over a wide range of mass splittings, down from 590 MeV up to 29 GeV.

6 Conclusions

This thesis presented searches for the electroweak production of higgsinos and sleptons in compressed mass spectra with the ATLAS detector, using the full LHC Run 2 dataset. To increase the signal acceptance, the system of supersymmetric particles is assumed to be boosted with respect to one or multiple hadronic jets from ISR. The final state under consideration is characterized by missing transverse momentum, two soft leptons of the same flavor and opposite electric charge, as well as hadronic activity pointing in the opposite direction of the missing transverse momentum.

The phase space covered by the analysis was extended towards lower missing transverse momenta to enhance the sensitivity reach of the searches by including less heavily boosted higgsino and slepton events. For this purpose, dedicated SRs targeting this less boosted regime have been constructed that increase the sensitivity of the searches specifically for moderate to large mass splittings between the supersymmetric particles. These have been designed and optimized to capture the kinematic features present in the hypothetical signals events. In particular, the signal selections account for the dependence of the signal kinematics on the mass splitting, to maximize their performance across the signal grids. To correct for mismodeling in the simulation of the E_T^miss trigger for such events, dedicated scale factors applicable in the phase space of the analysis have been derived. A strategy for background estimation in the regime of low missing transverse momentum was developed and validated as part of this work. The three dominant contributions from irreducible backgrounds are estimated with MC simulation and normalized to data in CRs. The validity of the contribution from reducible fake/nonprompt lepton background, derived from transfer factors measured in data, is verified in validation regions.

Research and developments in the performance measurements of muons with low transverse momenta were presented, which increase the acceptance of the analysis for signals with very soft muons. Specifically the extension down to transverse momenta of $3\,\text{GeV}$ allowed "to expand this search to the lowest-yet measured muon momenta for ATLAS" [241]. This increased notably the sensitivity reach for signals with small mass splittings.

In conjunction with the large Run 2 dataset, the extension of the phase space covered by the analysis, new analysis techniques and revised reconstruction schemes and performance measurements, enabled "to look for higgsinos in areas that were previously inaccessible" [242]. However, no significant deviations from the SM predictions were found in the selections sensitive to higgsino and slepton production. This allowed to set exclusion limits for the higgsino and slepton scenarios, surpassing the current constraints on those models. For higgsino production, $\tilde{\chi}_2^0$ masses up to $162\,\text{GeV}$ can be excluded. At the chargino mass limits of the LEP experiments, higgsino mass splittings down to $2.6\,\text{GeV}$ and up to $53\,\text{GeV}$ can be excluded. Scalar superpartners of the electron and muon are excluded up to $256\,\text{GeV}$, with the contraints in terms of mass splittings extending down to $590\,\text{MeV}$ and up to $29\,\text{GeV}$ at the limits from LEP.

The absence of physics beyond the Standard Model in the full Run 2 dataset of the LHC in the searches presented here is in line with the observations of other analyses [243]. Hence, it may be tempting to discard the presence of new phenomena at LHC energies and to question the sense of any further searches for physics beyond the Standard Model at the LHC. However, such conclusions are drawn far too early. On the one hand, the derived exclusion limits are valid only in the simplified models they have been calculated with. These models contain significant simplifications, such as assuming 100 % branching ratios in the decay chains of interest. Consequently, the signal contribution to the SRs is most-likely overestimated with respect to a "real world" model, in which the presence of other SUSY particles may lead to additional final states to the one covered by the analysis. Scans over a reduced parameter space of the MSSM using the analysis results of Run 1 at ATLAS [244], found that mass constraints for such models can be notably weaker than the constraints derived for the simplified models. On the other hand, only a fraction of the full dataset that is expected to be recorded at the LHC and its upgrade, the HL-LHC, was analyzed so far. With the high-luminosity upgrade, about $3000\,\mathrm{fb}^{-1}$ of data are planned to be collected during the total lifetime of the HL-LHC. Recent projections expect sensitivity for higgsinos up to $350\,\mathrm{GeV}$ at the HL-LHC [245]. Thus there is still plenty of room for surprises and tantalizing hints for new phenomena may arise only with the support from a larger fraction of the ultimate LHC luminosity.

Regardless of the current absence of signs for new physics at the LHC, the motivations to search for them, such as the unknown nature of DM, remain strong as ever. For this reason, the preparations for a post-LHC experiment, the Future Circular Collider (FCC) [246–248] are in full swing. By scaling the parameters of the LHC up by roughly one order of magnitude, the FCC is planned to collide particles at center-of-mass energies up to $\sqrt{s} = 100\,\mathrm{TeV}$ and collect $30\,\mathrm{ab}^{-1}$ of data. Although targets of searches for new phenomena are less obvious than in the pre-LHC era, higgsinos stay a promising DM candidate. Consequently these particles are considered as an essential part of the potential FCC search program, which expects sensitivity for discovery of higgsinos with masses well beyond $1\,\mathrm{TeV}$ [246].

The FCC is just in its concept phase and potential operations at its full capability will take place decades into the future. Until then, the quest for a refined, more in-depth understanding of nature will continue at the currently accessible energies. New and improved experimental methods, as developed for the presented searches, allow to illuminate the last dark corners where new physics could be hidden already now.

Appendices

A Muon Reconstruction Efficiencies

This appendix contains additional material for the reconstruction efficiency measurements of low-p_{T} muons.

A.1 Crystal Ball Function

The Crystal Ball function [249] can be understood as an overlay of a Gaussian and a power-law at the low-end tail, and is defined as

$$f(x; \alpha, n, \mu, \sigma) = N \cdot \begin{cases} \exp\left(-\dfrac{(x-\mu)^2}{2\sigma^2}\right), & \dfrac{x-\mu}{\sigma} > -\alpha \\ A \cdot \left(B - \dfrac{x-\mu}{\sigma}\right)^{-n}, & \dfrac{x-\mu}{\sigma} \leq -\alpha \end{cases} \tag{A.1}$$

where

$$A = \left(\frac{n}{|\alpha|}\right)^n \cdot \exp\left(-\frac{|\alpha|^2}{2}\right),$$
$$B = \frac{n}{|\alpha|} - |\alpha|,$$

and N is a normalization parameter. A typical use case of the Crystal Ball function is to fit measurements of resonances such as $J/\Psi \to \mu\mu$. The elongated tail at the lower end (see Figure A.1) with respect to a plain Gaussian accounts for energy losses e.g. due to FSR.
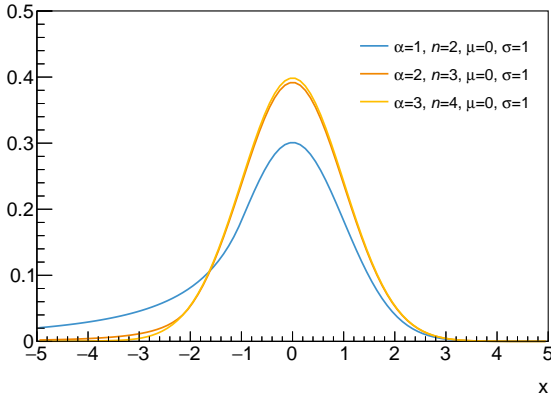
Figure A.1: Example shapes for the Crystal Ball function. Each function has the same mean μ and width σ while the parameters α and n are varied.

(a) Efficiencies vs ϕ
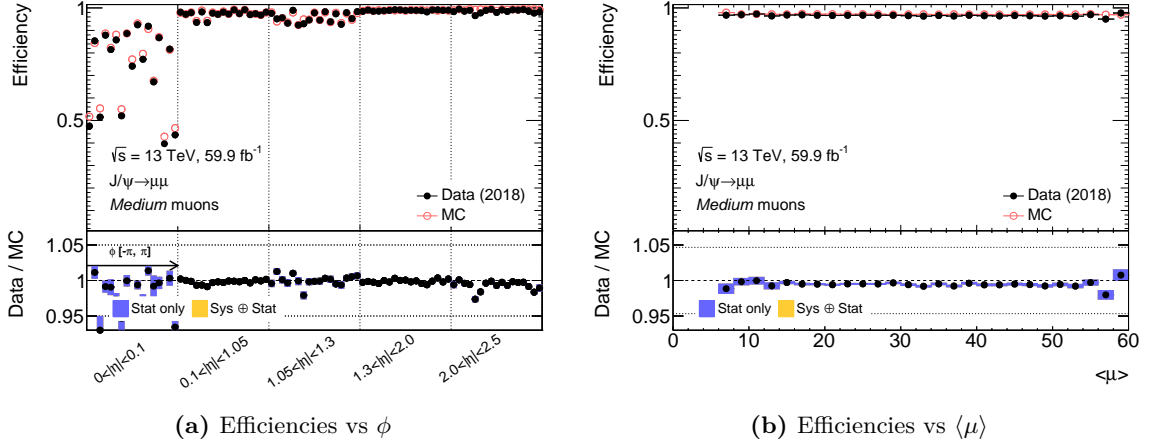
(b) Efficiencies vs $\langle\mu\rangle$

Figure A.2: Azimuthal (a) and pile-up dependence (b) of the muon reconstruction efficiencies in 2018 data using CT probes.

A.2 Pile-up and Azimuthal Dependence

The muon reconstruction efficiencies do not only depend on the p_T and η of the muon, but to some extent also on other variables. The available tag-and-probe statistics does not allow to split the measurements further but it is necessary to check if these dependencies would introduce a significant impact on the scale factors. This means the p_T binning in the measurements has to be replaced by an appropriate binning of the variable of interest. To mitigate the p_T-dependence, the checks are restricted to CT probes with p_T above $5\,\text{GeV}$ as the efficiencies are approximately constant in this regime.

Figure A.2a shows the efficiencies in bins of $|\eta|$ and the following binning in ϕ

$$\phi : [-3.142, -2.960, -2.535, -2.175, -1.750, -1.390, -0.965, -0.605, -0.180,$$
$$0.180, 0.605, 0.965, 1.390, 1.750, 2.175, 2.535, 2.960, 3.142],$$

which represents the segmentation into small (width: 0.360 radians) and large sectors (width: 0.425 radians) in the barrel. Except for the muon crack region, the efficiencies in the small sectors tend to by slightly higher than in the large sectors. For the most part, the scale factors across ϕ are compatible with each other.

The pile-up dependence is studied by considering the number of average bunch crossings $\langle\mu\rangle$ as shown in Figure A.2b. Across the whole $\langle\mu\rangle$ range, the efficiencies are rather stable, which indicates that muon reconstruction is pile-up robust also at low muon transverse momentum.

A.3 Muon Reconstruction Efficiencies in Run 2

The muon reconstruction efficiencies measured for each year of Run 2 data-taking are presented in Figures A.3 to A.6 for the *Medium*, *Low-p_T*, *Tight*, and the non–calotagged component of the *Loose* WP, respectively. Reconstruction efficiencies for calo-tagged muons are shown in Figure A.7. The measurements are performed for $|\eta| < 2.5$ and in the p_T-range $[3, 20]$ GeV, except for *Tight* muons where reconstruction efficiencies become very small below $4\,\mathrm{GeV}$ and consequently the measurements are only performed down to that threshold. Calo-tagged muons are only available for $p_\mathrm{T} > 5\,\mathrm{GeV}$, so the measurements start at $5\,\mathrm{GeV}$.

The offset in the muon crack region $|\eta| < 0.1$ between the efficiencies in 2015 data and simulation, which can be seen for example in Figure A.3, is under study. As the agreement in the crack region is much better for the other years, a potential source could be an incorrect pile-up reweighting to 2015 data. A common MC sample is used for the 2015 and 2016 measurements, in which the overlaid pile-up is distributed according to the conditions in the joint 2015 and 2016 dataset. Hence, a broken pile-up reweighting would roughly set the pile-up conditions in the simulation for 2015 to the harscher ones in 2016, explaining the drop of the efficiencies in MC with respect to the efficiencies in data for 2015.

(a) 2015

(b) 2016

(c) 2017

(d) 2018
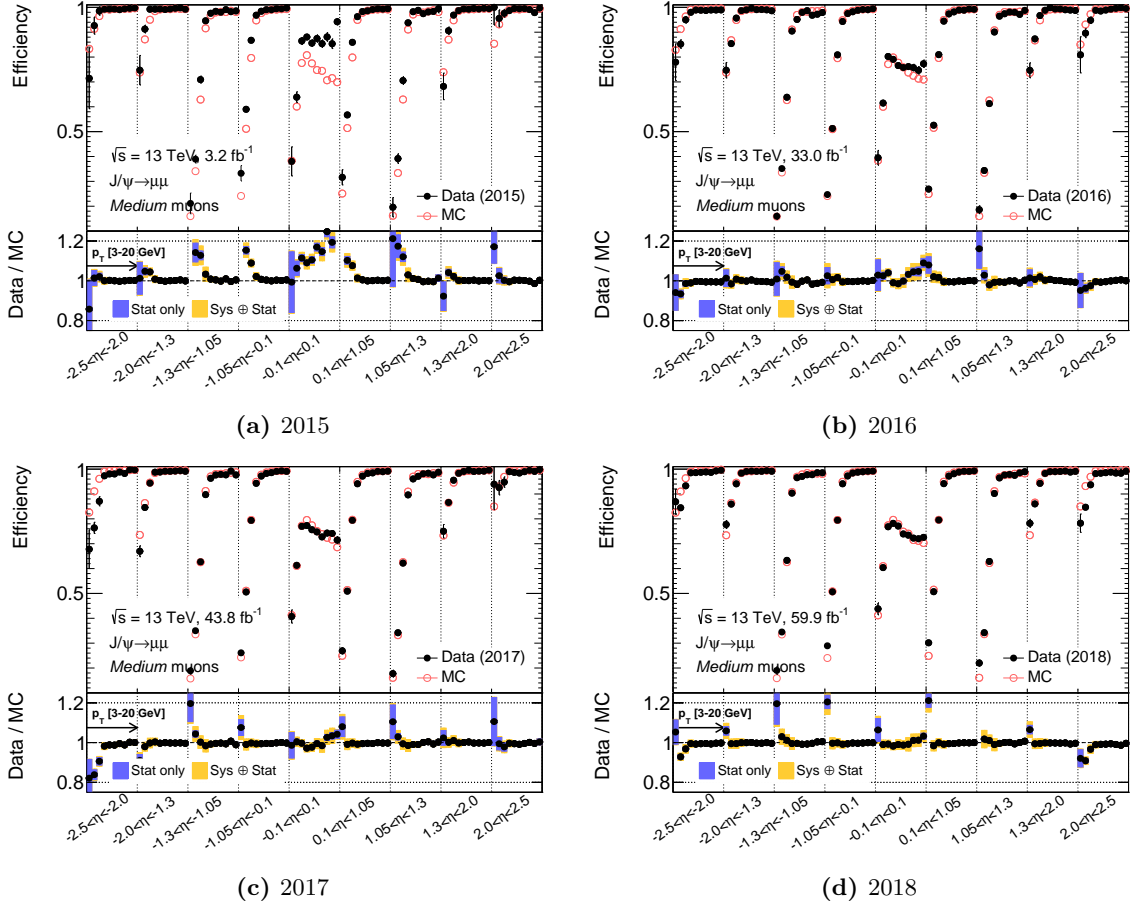
Figure A.3: Muon reconstruction efficiencies for *Medium* muons in 2015–2018 data-taking as a function of the muon pseudorapidity η and transverse momentum p_T. The bottom panel shows the efficiency scale factors with statistical uncertainties indicated as blue and the sum of statistical and systematic uncertainties as orange band.
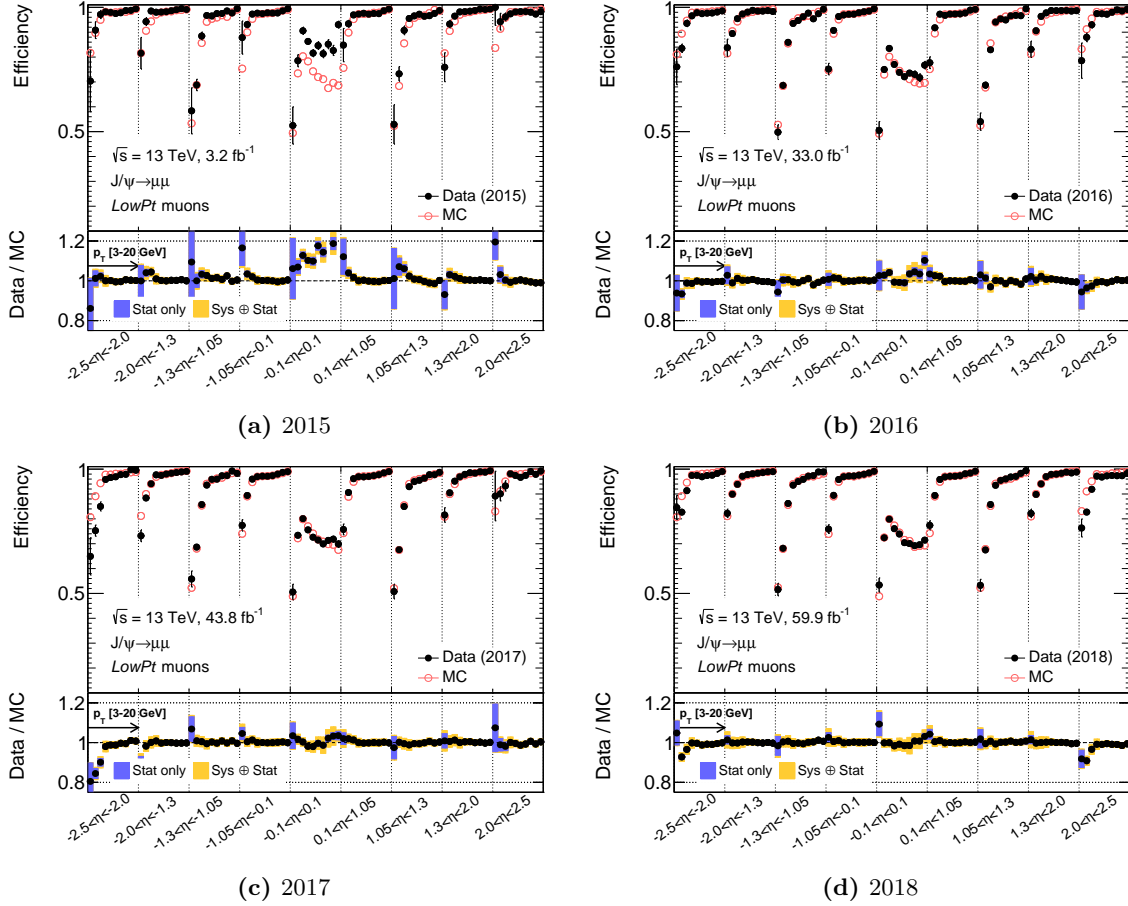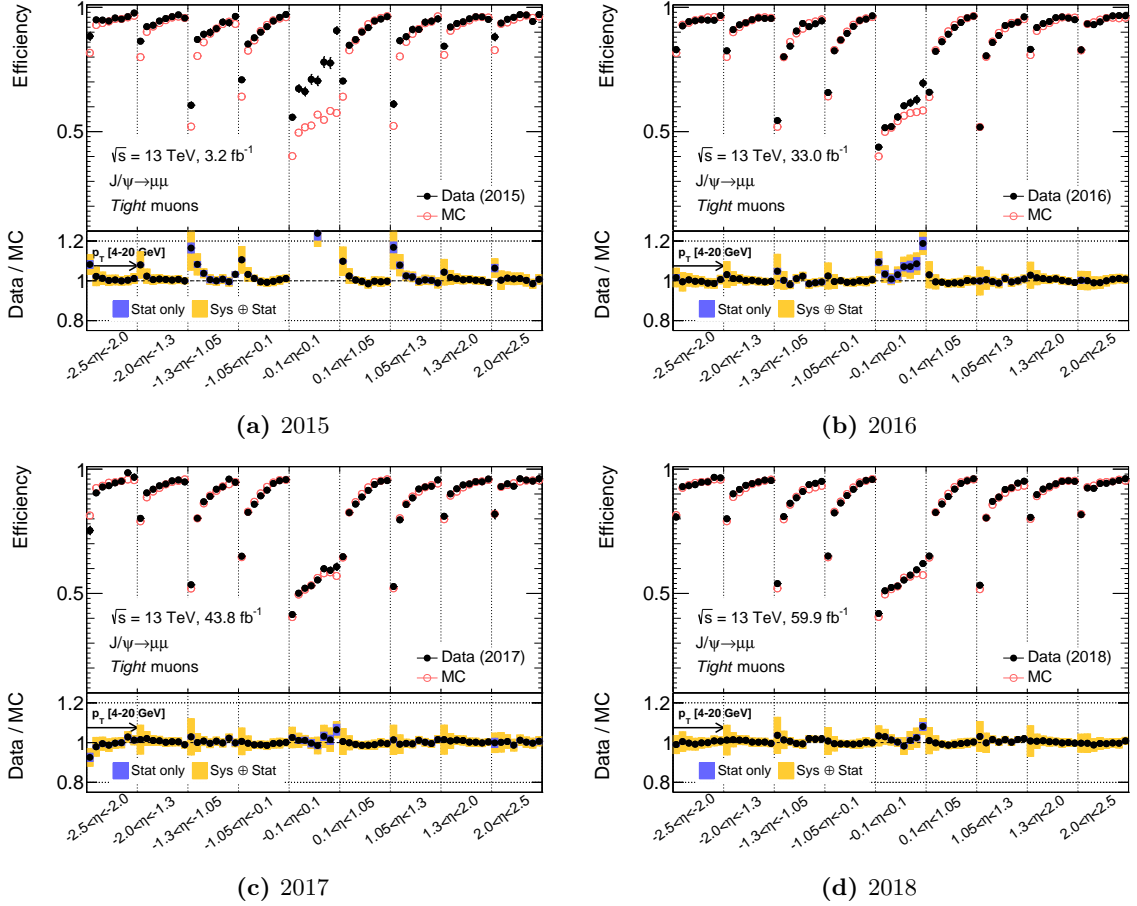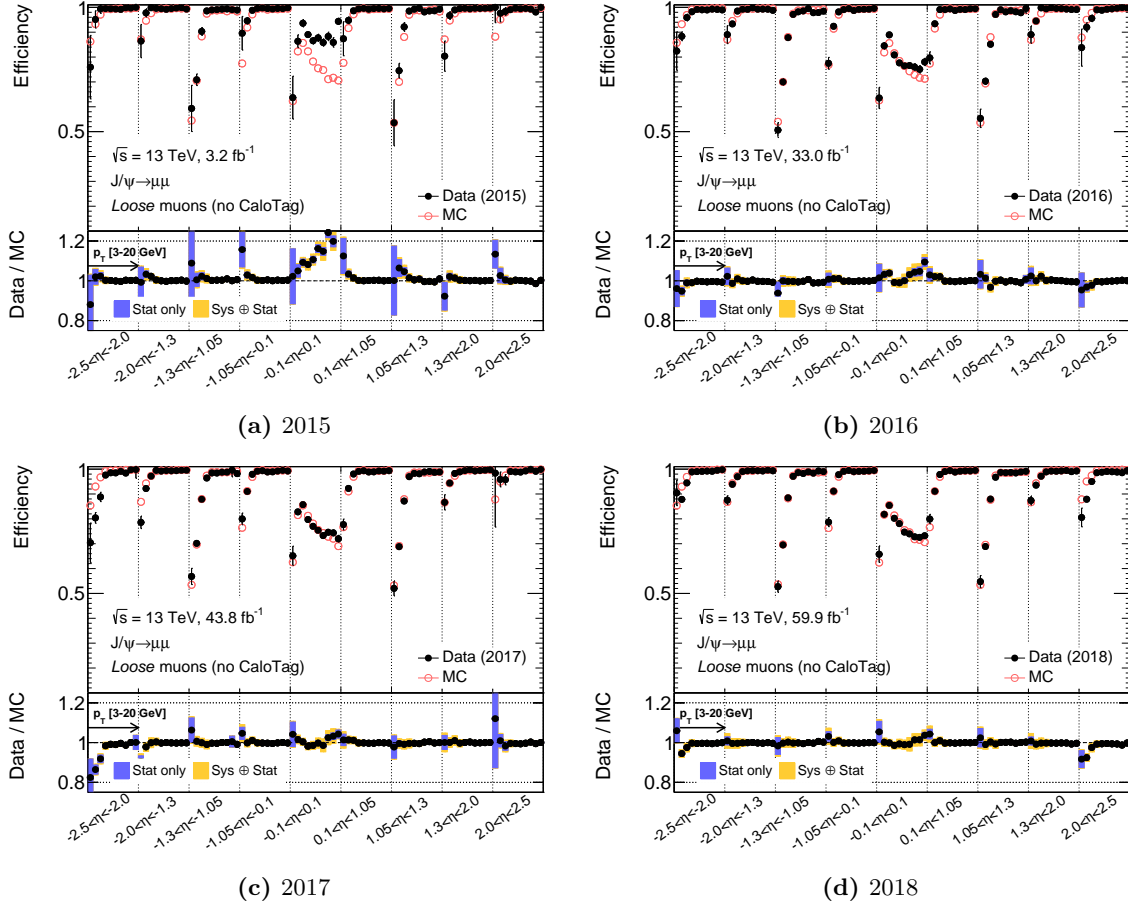
(a) 2015

(b) 2016

(c) 2017

(d) 2018

Figure A.4: Muon reconstruction efficiencies for *Low-p_T* muons in 2015–2018 data-taking as a function of the muon pseudorapidity η and transverse momentum p_T. The bottom panel shows the efficiency scale factors with statistical uncertainties indicated as blue and the sum of statistical and systematic uncertainties as orange band.
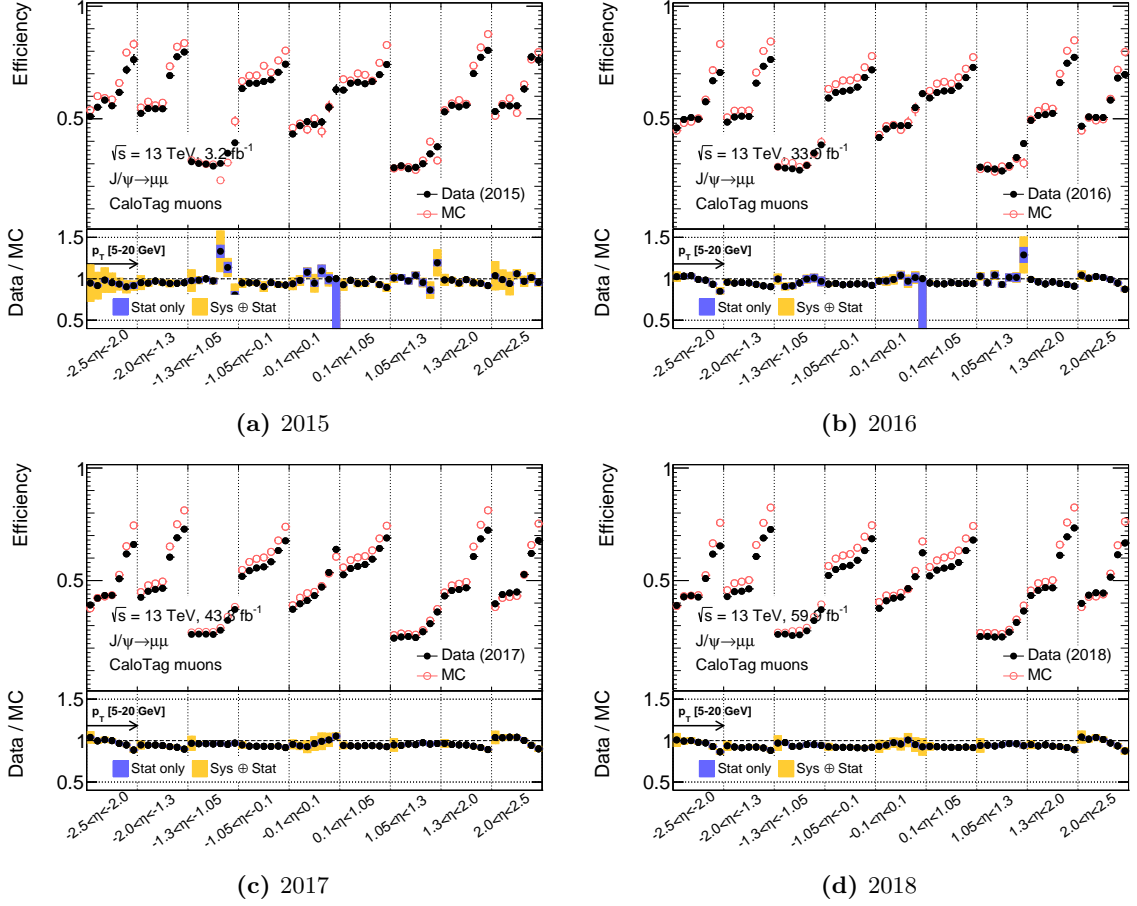
(a) 2015

(b) 2016

(c) 2017

(d) 2018

Figure A.5: Muon reconstruction efficiencies for *Tight* muons in 2015–2018 data-taking as a function of the muon pseudorapidity η and transverse momentum p_{T}. The bottom panel shows the efficiency scale factors with statistical uncertainties indicated as blue and the sum of statistical and systematic uncertainties as orange band.

(a) 2015

(b) 2016

(c) 2017

(d) 2018

Figure A.6: Muon reconstruction efficiencies for the non–calo-tagged component of *Loose* muons in 2015–2018 data-taking as a function of the muon pseudorapidity η and transverse momentum p_{T}. The bottom panel shows the efficiency scale factors with statistical uncertainties indicated as blue and the sum of statistical and systematic uncertainties as orange band.

(a) 2015

(b) 2016

(c) 2017

(d) 2018

Figure A.7: Muon reconstruction efficiencies for calo-tagged muons in 2015–2018 data-taking as a function of the muon pseudorapidity η and transverse momentum p_{T}. The bottom panel shows the efficiency scale factors with statistical uncertainties indicated as blue and the sum of statistical and systematic uncertainties as orange band.

A.4 Sensitivity Gain in Searches for Compressed Mass Spectra

To estimate the gain in sensitivity by the extension of the muon reconstruction measurements, that allows the use of muons down to $3\,\mathrm{GeV}$ in analyses, the expected exclusion reaches of the searches presented in Chapter 5 are derived in two different configurations. The first configuration restricts the use of muons to transverse momenta above $5\,\mathrm{GeV}$, while the second allows muons down to $3\,\mathrm{GeV}$. For this study, only the high-$E_\mathrm{T}^\mathrm{miss}$ selections of the higgsino and slepton analyses are considered as these drive the sensitivity towards small mass splittings (see Figure 5.22). Further, the simplified fit setup introduced in Section 5.4.4 has been used, i.e. flat $20\,\%$ systematic uncertainties are used for the background and signal expectations in every SR bin. Only blinded data is used in the hypothesis tests, taking the pre-fit background expectation as observation.

The results are shown in Figure A.8. Going down in muon p_T to $3\,\mathrm{GeV}$ allows to probe higgsino mass splittings slightly below $2\,\mathrm{GeV}$ which represents a gain of about half a GeV with respect to an analysis that is restricted to muons with p_T above $5\,\mathrm{GeV}$. In the slepton grid the gain is only minimal, as the m_T2-dependent cut on the subleading lepton p_T in the slepton analysis imposes stringent requirements on the lepton momenta to veto fakes efficiently. This study has to be taken with a grain of salt, as the exclusion power of optimized selections ($p_\mathrm{T} > 3\,\mathrm{GeV}$) are compared with the sensitivity of non-optimized selections. Nevertheless, it illustrates roughly the magnitude of the sensitivity gain.
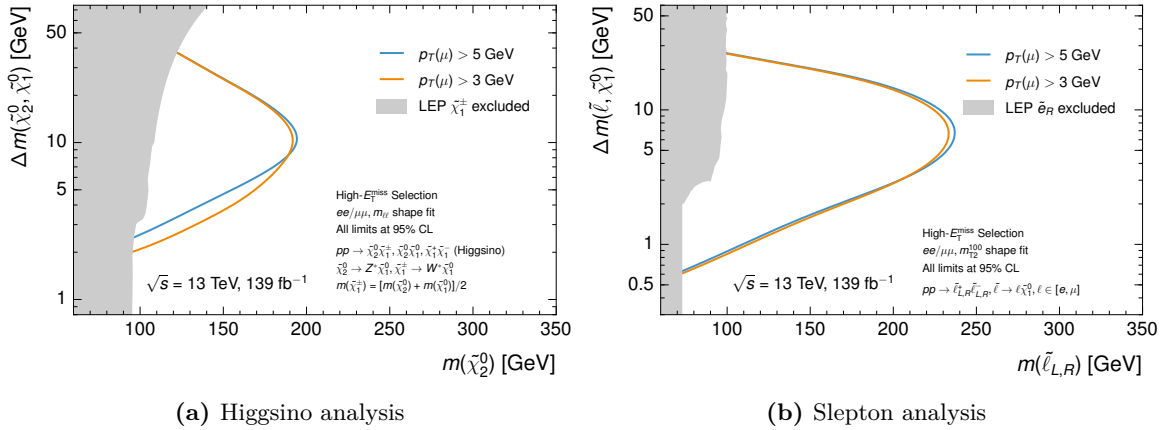

(a) Higgsino analysis

(b) Slepton analysis

Figure A.8: Expected exclusion reaches for the higgsino and slepton searches using muons with $p_\mathrm{T} > 5\,\mathrm{GeV}$ (light blue) and $p_\mathrm{T} > 3\,\mathrm{GeV}$ (orange). The exclusion limits are derived using a simplified fit configuration.

B Scale Factors for Triggers on Missing Transverse Momentum

The low-$E_\mathrm{T}^\mathrm{miss}$ selections of the analysis use $E_\mathrm{T}^\mathrm{miss}$ triggers in their turn-on regions, where the triggers are not fully efficient. Therefore, it is essential to account for any potential mismodeling of the turn-on regions in simulation. In order to derive scale factors, measurements of the $E_\mathrm{T}^\mathrm{miss}$-trigger efficiencies in both data and simulation are required. In contrast to muon reconstruction efficiencies, these cannot be measured generically as the trigger efficiencies are to a large degree phase space dependent. Generally, the turn-on region is thought to get broader with increasing hadronic activity, as this leaves more room for differences between the $E_\mathrm{T}^\mathrm{miss}$ calculation at trigger and at offline level. This necessitates to derive the $E_\mathrm{T}^\mathrm{miss}$-trigger scale factors in a selection as close as possible to the phase space considered by the analysis.

B.1 Measurement Concept

To measure $E_\mathrm{T}^\mathrm{miss}$-trigger efficiencies an unbiased data sample is required. Such a sample is not trivial to derive as the events have to be selected by some trigger themselves. As many of the signatures a trigger can fire on, such as jets and electrons, enter the $E_\mathrm{T}^\mathrm{miss}$ calculation, the usage of such triggers may bias the measurement of the $E_\mathrm{T}^\mathrm{miss}$-trigger efficiencies. An established strategy is to use events selected by muon triggers for these efficiency measurements [250]. As information from the MS is not used at L1 and HLT trigger level (see Section 3.2.8), these triggers can be used to select an unbiased sample. The efficiency ϵ of a particular $E_\mathrm{T}^\mathrm{miss}$ trigger can be derived by dividing the number of events that fired the muon trigger and simultaneously the $E_\mathrm{T}^\mathrm{miss}$ trigger by the number of all events selected by the muon trigger

$$\epsilon = \frac{N(\text{muon trigger \&\& } E_\mathrm{T}^\mathrm{miss} \text{ trigger})}{N(\text{muon trigger})} \,. \tag{B.1}$$

As reconstructed muons are considered in the offline $E_\mathrm{T}^\mathrm{miss}$ calculation, these events have an intrinsic large difference between the trigger and offline $E_\mathrm{T}^\mathrm{miss}$. To account for this feature, the trigger efficiencies are not measured with respect to the nominal $E_\mathrm{T}^\mathrm{miss}$ flavor used in the baseline analysis, but with respect to a dedicated $E_\mathrm{T}^\mathrm{miss}$ flavor in which the muons are treated as invisible particles, denoted as $E_{\mathrm{T},\,\mu\,\mathrm{invis}}^\mathrm{miss}$. This approach brings the online and offline $E_\mathrm{T}^\mathrm{miss}$ used to measure the trigger efficiencies conceptually closer together, while the offline $E_\mathrm{T}^\mathrm{miss}$ still shares the object definitions and calibrations with the baseline analysis. Multiple versions of $E_\mathrm{T}^\mathrm{miss}$ triggers have been used during Run 2 data-taking, that differ in particular in their online threshold. This necessitates to measure the efficiencies (and derive the scale factors) separately for each single $E_\mathrm{T}^\mathrm{miss}$ trigger.

Trigger	Period	Luminosity [fb^{-1}]
HLT_xe70_mht	2015	3.2
HLT_xe90_mht_L1XE50	2016, Period A-D3	6.1
HLT_xe100_mht_L1XE50	2016, Period D4-E3	3.9
HLT_xe110_mht_L1XE50	2016, Period F1-L	23.2
HLT_xe110_pufit_L1XE55	2017	43.3
HLT_xe110_pufit_xe70_L1XE50	2018, Period B-C5	6.4
HLT_xe110_pufit_xe65_L1XE50	2018, Period C5-Q	52.0

Table B.1: List of E_T^{miss} triggers used in the analysis. The second column states the period in which the triggers are used to select events, while the third column lists the integrated luminosity this period corresponds to.

B.2 Missing Transverse Momentum Triggers in Run 2

The E_T^{miss} triggers use primarily information from the calorimeters to calculate the amount of momentum imbalance present in an event. Consequently these triggers are sensitive to the level of pile-up in the *pp* collisions. As the overall instantaneous luminosity increased notably during Run 2, the E_T^{miss} trigger with the lowest online threshold evolved in the course of data-taking to cope with the resulting larger data rates. To maximize the event statistics for the analysis, it is common to use the trigger with the lowest online threshold for each period of data-taking. Table B.1 lists the E_T^{miss} triggers used in the analysis, that differ not only in the trigger thresholds but also in the HLT algorithms used to determine the missing transverse momentum at trigger level:

- Jet based algorithm (mht): the E_T^{miss} is calculated from the negative transverse momentum sum of all jets reconstructed at HLT level using the anti-k$_t$ algorithm with a radius parameter of $\Delta R = 0.4$. The jets are build from locally calibrated topo-clusters [203] and calibrated in a procedure similar to the one used for offline jets to correct for contributions from pile-up.

- Pile-up fit algorithm (pufit): the transverse energy deposits in the calorimeters are grouped into coarse towers. In case the energy sum E_T within one of the towers exceeds a given threshold, it is assumed to originate from a hard *pp* interaction and the event is kept for further consideration. The contribution from pile-up is estimated with a fit based on the deposits in low-E_T towers. The E_T^{miss} is then given by the sum of all high-E_T towers after subtracting the fitted pile-up contribution.

- Cell algorithm: the E_T^{miss} is determined by summing over the full set of calorimeter cells. To reduce effects from noise fluctuation effects and pile-up, cells are only considered in case their cell energy exceeds a given threshold. In 2018, triggers using the pufit algorithm have been complemented with this algorithm to increase the robustness with respect to pile-up.

Several other algorithms to determine the E_T^{miss} at HLT level exist, but are not part of the triggers used in the analysis and hence not reviewed here.

Trigger	2015 HLT_mu20_iloose_L1MU15 HLT_mu40		2016–2018 HLT_mu26_ivarmedium HLT_mu50	
Jets	$p_T(j_1)$ [GeV] > 100	$\Delta\phi(j_1, \mathbf{p}_T^{\mathrm{miss}})$ > 2.0	$\min(\Delta\phi(\text{any jets}, \mathbf{p}_T^{\mathrm{miss}}))$ > 0.4	
Leptons	n_{lep} $= 2$	$q_{\ell_1} \cdot q_{\ell_2}$ -1	$\Delta R_{\ell\ell}$ > 0.05	$m_{\ell\ell}$ [GeV] $[10, 60]$

Table B.2: Trigger selection and kinematic requirements on the region used to measure the E_T^{miss}-trigger efficiencies. Additionally, the samples used for the presented studies have an intrinsic requirement on the p_T of the leptons ($> 9\,\mathrm{GeV}$) as discussed in the text.

B.3 Event Selection

Events used in the measurements are selected by a set of single-muon triggers, listed in Table B.2. Single-muon triggers require the presence of a muon-like signature on trigger level (trigger muon) carrying a p_T larger than a particular threshold (e.g. $20\,\mathrm{GeV}$ for the trigger HLT_mu20_iloose_L1MU15). In addition to the p_T requirement on the trigger muon, these triggers either apply an additional isolation requirement or alternatively a stricter p_T threshold. The event has to contain a reconstructed muon that can be associated with the trigger that caused the write-out of the event using a ΔR matching criterion. Muon trigger efficiencies in simulation are corrected to match those in data by the application of muon trigger scale factors, that have been derived by a method similar to the one described in Ref. [251]. The further event selection is based on the preselection introduced in Section 5.3.5, to assure the measurements are performed in a phase space close to the one considered in the analysis. In particular, events need to fulfill the same jet and angular requirements as in the preselection, to ensure an ISR-like topology. Moreover exactly two signal leptons need to be contained in the event (with one of them being a muon due to the trigger matching requirement), that are oppositely charged and at least $\Delta R_{\ell\ell} > 0.05$ far apart. To improve the capture of any phase space dependence, the efficiencies are split into two categories, *b*-tag and *b*-veto, depending on the presence of at least one *b*-tagged jet. As shown in Figure B.1, these selections are dominated by $t\bar{t}$ and $Z + \text{jets}$ (mainly $Z(\to \mu\mu) + \text{jets}$) events, respectively. Further contributions originate from diboson and $W + \text{jets}$ processes. In contrast to the baseline analysis, the contribution from fake/nonprompt leptons is not estimated separately with the Fake Factor method, but taken from MC simulation instead. Good agreement between data and prediction can be observed down to $m_{\ell\ell} \approx 10\,\mathrm{GeV}$. At lower $m_{\ell\ell}$, events from the J/Ψ and Υ resonances enter the selection, which are not contained in the simulation. As such events do not have any special kinematics, these can be in principle used for the measurements. A global offset is present for $m_{\ell\ell}$ below $10\,\mathrm{GeV}$ in the *b*-tag category, which indicates some general problem of the MC prediction in this particular phase space. As the final scale factors show only a small dependence on $m_{\ell\ell}$, t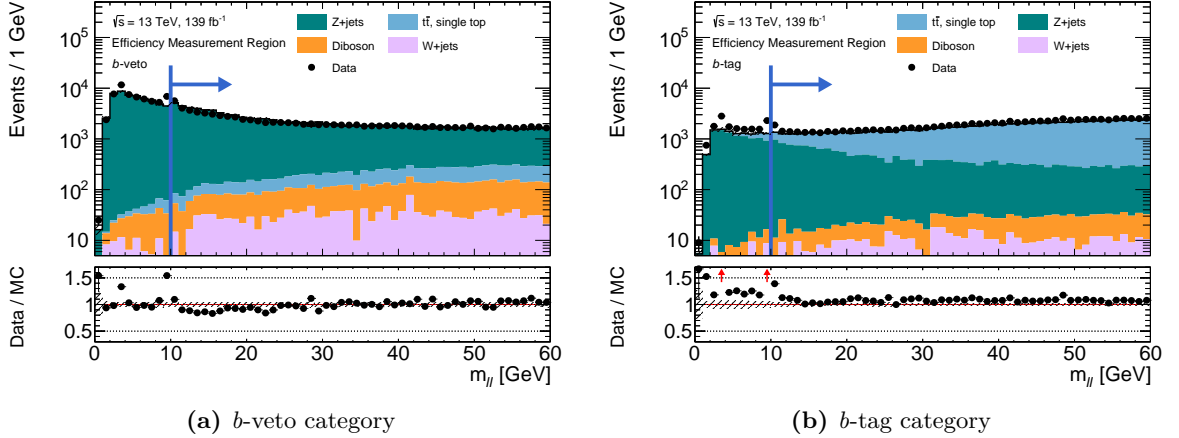he measurement region is restricted to $10\,\mathrm{GeV} < m_{\ell\ell} < 60\,\mathrm{GeV}$. An additional requirement on the leptons ($p_T > 9\,\mathrm{GeV}$) arises

(a) *b*-veto category **(b)** *b*-tag category

Figure B.1: Kinematic distribution of $m_{\ell\ell}$ for the full Run 2 dataset in the *b*-veto and *b*-tag selections to measure $E_{\mathrm{T}}^{\mathrm{miss}}$-trigger efficiencies. The MC predictions also include the fake/nonprompt contribution. The hatched band in the bottom panel indicates the statistical uncertainty.

from an intrinsic cut applied on the samples used for these studies, that ensures to keep the total data size on a level suitable for analysis purposes. As there is at least one hard muon in the event due to the trigger requirement, this affects only events with a soft second lepton. These events will potentially have a low invariant mass of the lepton pair $m_{\ell\ell}$, which are anyway neglected in the measurement. Hence, the impact of this requirement is assumed to be only minor.

B.4 Efficiency Measurement

Efficiencies have been measured according to Equation (B.1) in 30 equidistant $E_{\mathrm{T},\,\mu\,\mathrm{invis}}^{\mathrm{miss}}$-bins from 0 to 300 GeV, with the last bin including the overflow. To derive the trigger efficiencies in MC simulation, the contributions from the four SM backgrounds are summed up and the efficiency is calculated using this common sample. The results are shown exemplary for the trigger HLT_xe110_pufit_L1XE55 in Figure B.2 for both categories. The efficiencies measured in data and MC simulation for all triggers can be found in Appendix B.8. All efficiency curves show clearly a characteristic turn-on behavior, with the start of the plateau region depends on the online threshold of the trigger. It was verified by considering the efficiencies with respect to the nominal $E_{\mathrm{T}}^{\mathrm{miss}}$ flavor, that all triggers are fully efficient around 200 GeV, which confirms that no trigger scale factors are needed for the high-$E_{\mathrm{T}}^{\mathrm{miss}}$ selections. In principle, the ratio of the data a MC efficiency shown in each plot corresponds to the scale factors. However, triggers that correspond to a small fraction of the total integrated luminosity suffer from limited statistics in the measurement, which is manifested in the large uncertainty bars. Therefore — and to be in general less sensitive to statistical fluctuations — the scale factors are not taken directly from the ratios, but derived by a fit of these ratios.
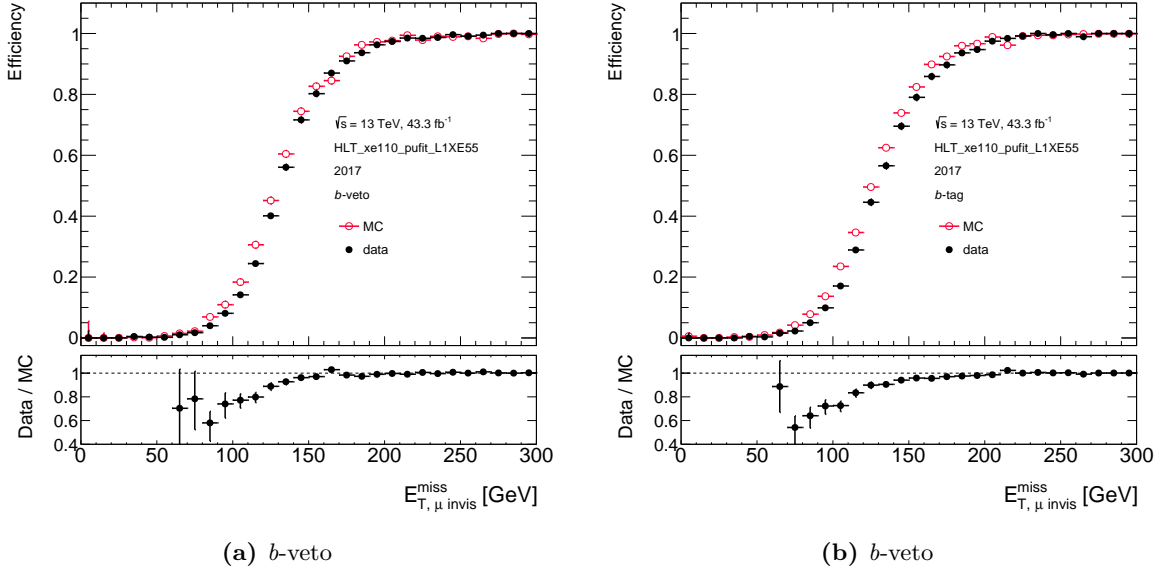
(a) *b*-veto

(b) *b*-veto

Figure B.2: Measured $E_{\mathrm{T}}^{\mathrm{miss}}$-trigger efficiencies in data (black full dots) and MC simulation (red empty circles) with respect to $E_{\mathrm{T},\,\mu\,\mathrm{invis}}^{\mathrm{miss}}$ in the *b*-veto and *b*-tag categories for the trigger HLT_xe110_pufit_L1XE55.

(a) *b*-veto

(b) *b*-tag
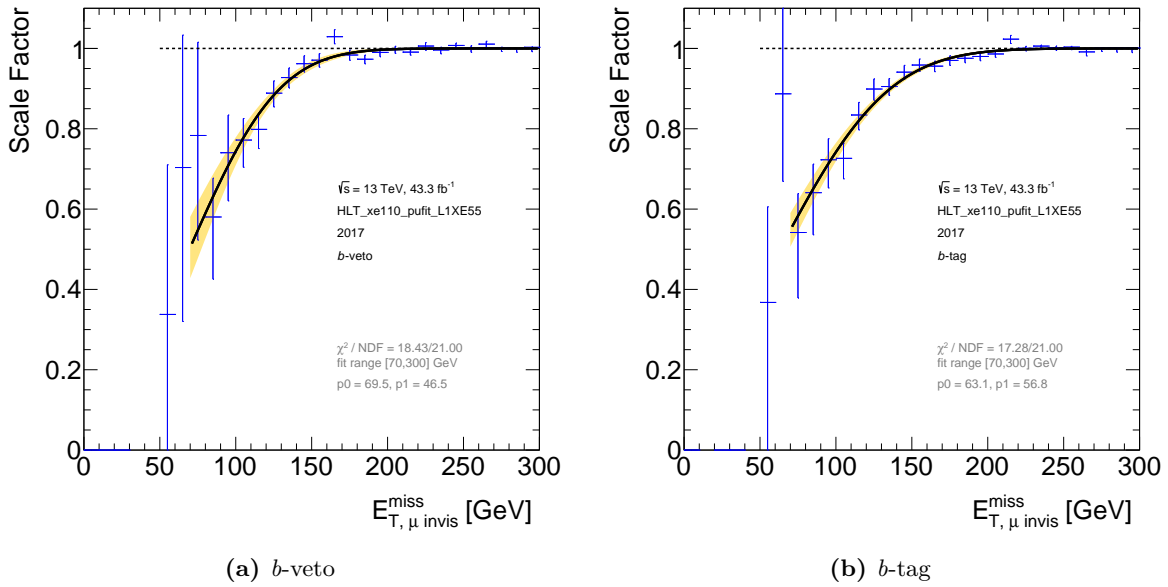
Figure B.3: Fitted $E_{\mathrm{T}}^{\mathrm{miss}}$-trigger scale factors for the trigger HLT_xe110_pufit_L1XE55. The yellow band indicates the statistical uncertainty of the fit.

145

Figure B.4: Correlation between E_T^{miss} and $E_{T,\mu\text{ invis}}^{miss}$ at preselection level. The z-axis shows the number of unweighted ("raw") background MC events. The rectangular spanned by the red lines indicate the region not covered by the derived scale factors.
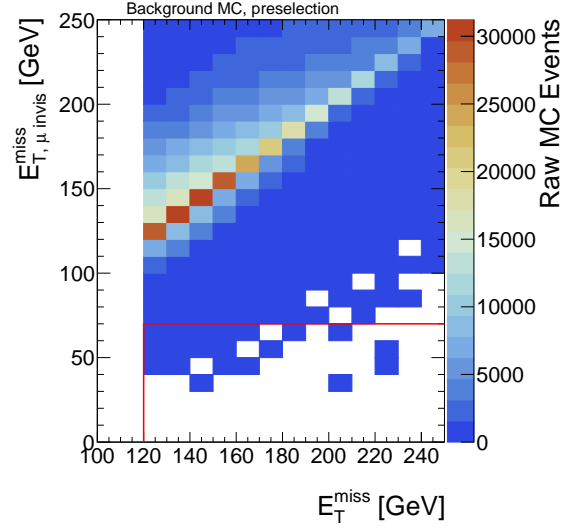
B.5 Derivation of Scale Factors

The scale factors are derived by fitting the ratios of the data and MC efficiencies with a function $F(x)$ based on the error function

$$F(x) = 0.5 \cdot \left[1 + Erf\left(\frac{x - p_0}{\sqrt{2p_1^2}}\right)\right], \tag{B.2}$$

with two free parameters p_0 and p_1, which roughly represent the location and the width of the turn-on region with respect to the offline reference. The error function captures the shape of the scale factors, that rise continuously until they reach unity and stay constant. Other parameterizations of the scale factors have also been tested and yielded compatible results. The function presented above showed the most stable results in terms of fit convergence and consequently was preferred over the other variants. A χ^2 fit using the MINUIT2 [252] package in the $E_{T,\mu\text{ invis}}^{miss}$ range from 70 to 300 GeV is used to derive the efficiencies. Fitted scale factors for the trigger HLT_xe110_pufit_L1XE55 are shown representatively in Figure B.3. The results for all triggers are presented in Appendix B.8. The statistical uncertainties on the scale factors are calculated using the errors of the fit parameters p_0, p_1 and their correlation, and are shown as yellow band in the plots. For the triggers that suffer from low statistics in the efficiency measurement, the statistical uncertainties can get comparable large at low $E_{T,\mu\text{ invis}}^{miss}$ values. Relevant for the analysis is roughly the range $E_{T,\mu\text{ invis}}^{miss} > 120$ GeV, where the scale factors are typically above 0.85 with an statistical uncertainty at the percentage level.

B.6 Application in Analysis

The derived E_T^{miss}-trigger scale factors are derived and also applied with respect to $E_{T,\mu\text{ invis}}^{miss}$. As the scale factors are valid only for $E_{T,\mu\text{ invis}}^{miss} > 70$ GeV, but the baseline analysis considers

(a) without E_T^{miss}-trigger scale factor   **(b)** E_T^{miss}-trigger scale factor applied
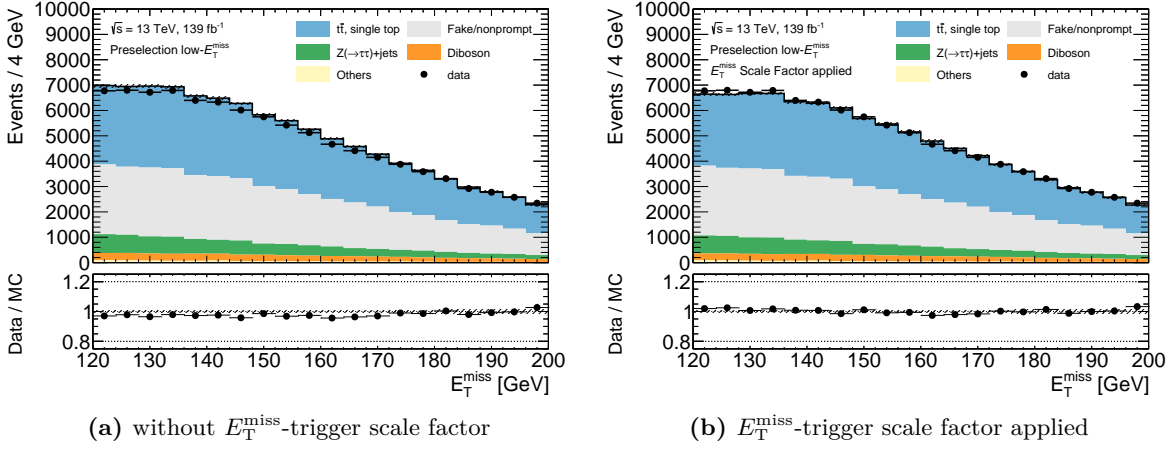
Figure B.5: Distribution of E_T^{miss} at low-E_T^{miss} preselection level without and with applied trigger scale factors. The hatched band in the bottom panel shows only the statistical uncertainty. As the estimate for the fake/nonprompt component is data-driven, no scale factors are applied for this sample.

a different E_T^{miss} flavor, there might be events with $E_T^{miss} > 120\,\text{GeV}$ but $E_{T,\,\mu\text{ invis}}^{miss} < 70\,\text{GeV}$, which spoils the usage of the scale factors. In general, $E_{T,\,\mu\text{ invis}}^{miss}$ is correlated linearly with the nominal E_T^{miss}, being smeared more towards higher values than to lower values, as depicted in Figure B.4. The issue outline above affects only a tiny fraction of the total number of MC events and thus has an negligible impact on the overall correction. For these events, the scale factor evaluated at $E_{T,\,\mu\text{ invis}}^{miss} = 70\,\text{GeV}$ is taken as approximate value. The impact of the scale factors on the analysis is presented in Figure B.5, which compares the data/MC agreement in the E_T^{miss} distribution at preselection level with and without trigger efficiency scale factors. After applying the scale factors, the mismodeling in simulation is clearly improved, with larger corrections at low- and smaller corrections at higher E_T^{miss} values, as expected.

B.7 Systematic Uncertainties

Several sources of systematic uncertainties have been considered in the derivation of the trigger scale factors. Their impact on the scale factors has been evaluated to give a set of alternative, variational scale factors that are supplied to the analysis and are used to parametrize and assess the uncertainties for the final results. When calculating the alternative scale factors, it is enforced that they do not exceed unity, their maximum value allowed in the fit (see Equation (B.2)).

Variable Dependence

The scale factors have been derived only with respect to $E_{T,\,\mu\text{ invis}}^{miss}$ and parametrized in the presence or absence of a b-tagged jet. To evaluate their dependence on kinematic variables relevant for the analysis, such as $m_{\ell\ell}$, m_{T2} and R_{ISR}, the scale factors are plotted with respect to these three variables in Figure B.6. The vast majority of MC events contributes with a scale factor above 0.95 and they are mostly evenly distributed across the three kinematic variables.
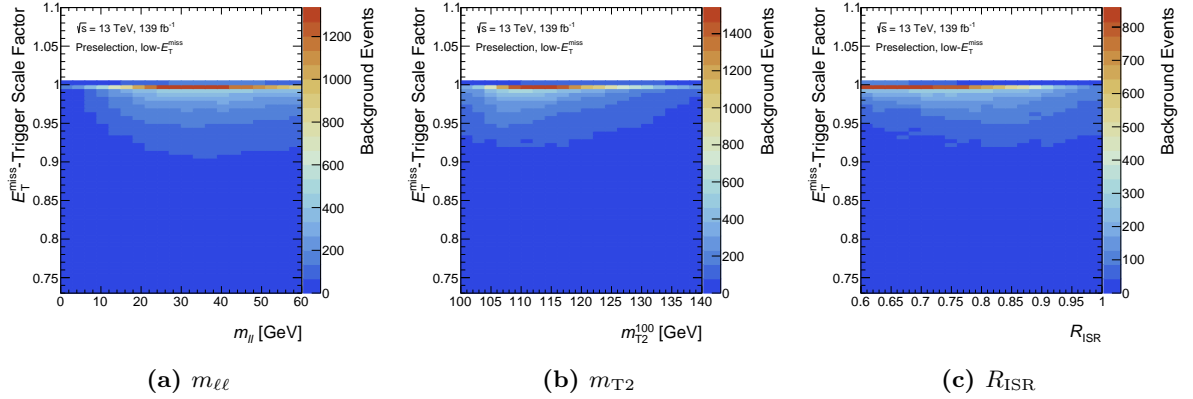
(a) $m_{\ell\ell}$ **(b)** m_{T2} **(c)** R_{ISR}

Figure B.6: Correlation between the trigger scale factors and $m_{\ell\ell}$, m_{T2} and R_{ISR} at low-$E_{\mathrm{T}}^{\mathrm{miss}}$ preselection level. The z-axis shows the number of weighted background MC events.

To cover the small variable dependency that is observed, a conservative flat uncertainty of $5\,\%$ is assigned on the scale factors.

Background Process Dependence

Although the efficiencies are measured in the same phase space, they differ between the individual background processes. Figure B.7 shows the efficiencies measured in the total SM background, as well as for the $Z + \mathrm{jets}$, top and diboson components. In general, the trigger efficiency in $Z + \mathrm{jets}$ events rises slower as for top and diboson events. This is present in both categories, b-veto and b-tag. This observation might indicate that the parameterization in the number of b-tagged jets does not capture the phase space dependence of the efficiencies sufficiently. Parameterizations using the number of jets and the total hadronic activity given by H_{T}, the sum of all jet transverse momenta, showed the same discrepancies between the background trigger efficiencies. The origin of these discrepancies have not been completely understood, but the efficiencies seem to depend also on the scale of the hard interaction process, which is higher for diboson and top processes than for $Z + \mathrm{jets}$. In particular for the b-veto category the background composition in the efficiency measurement region (mostly $Z \to \mu\mu$) and the baseline analysis (approximately an even mix of $Z \to \tau\tau$, top and diboson) differ. Consequently a dedicated uncertainty was assigned, based on the discrepancies among the efficiencies. In the b-veto category, the top and diboson efficiencies are roughly $10\,\mathrm{GeV}$ "in advance" with respect to $Z + \mathrm{jets}$ in terms of $E_{\mathrm{T},\,\mu\,\mathrm{invis}}^{\mathrm{miss}}$, so the uncertainty is derived by calculating the scale factors at $\pm 10\,\mathrm{GeV}$ around the nominal $E_{\mathrm{T},\,\mu\,\mathrm{invis}}^{\mathrm{miss}}$ value in each event. In the same way the uncertainty is evaluated in the b-tag category, but with an offset of $\pm 15\,\mathrm{GeV}$ as the discrepancies are found to be slightly larger.

Trigger Efficiency in Signal

Similar as in top and diboson events, the trigger efficiencies in signal have been found to be significantly larger than the measured efficiency for the total SM background. For a representative higgsino signal point, the trigger efficiency is shown as blue dashed line in
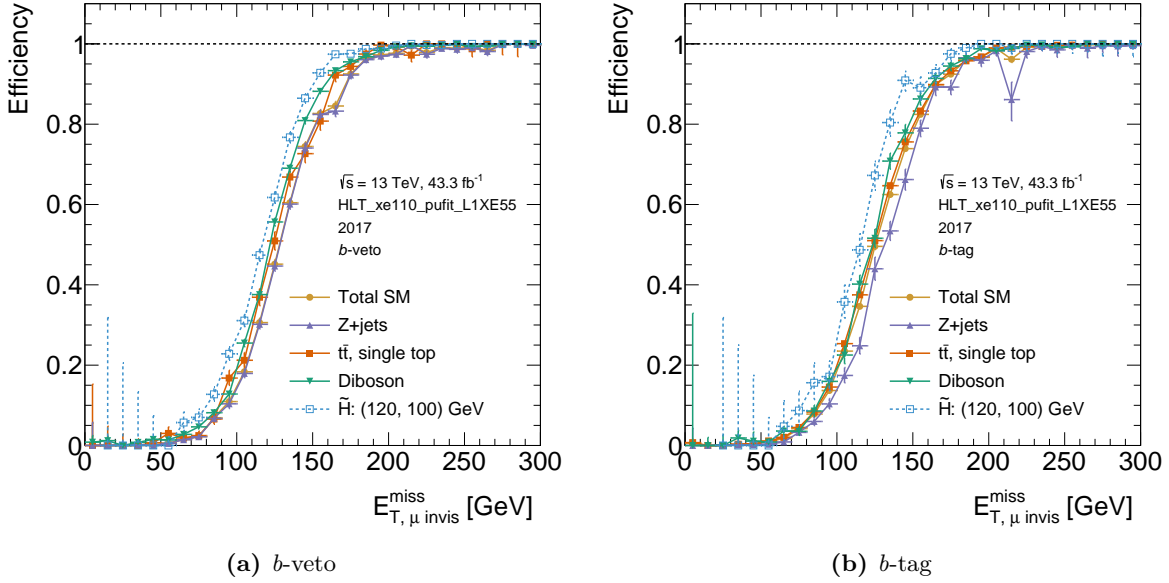
(a) *b*-veto

(b) *b*-tag

Figure B.7: Trigger efficiencies of HLT_xe110_pufit_L1XE55 measured for the total SM background and for its individual components, the $Z + $ jets, top and diboson related processes. The blue dashed line shows the trigger efficiency calculated in a higgsino signal sample corresponding to $m(\tilde{\chi}_2^0, \tilde{\chi}_1^0) = (120, 100)$ GeV.

Figure B.7. The trigger efficiencies in signal cannot be measured with the method described above, as there are barely any muons produced in compressed scenarios, that would surpass the single-muon trigger thresholds. Instead the trigger efficiencies shown in the plot are directly calculated which is possible in simulation: the trigger efficiency is given by dividing the number of events that have passed the E_T^{miss} trigger by the number of all signal events. The trigger efficiencies do not vary notably across the grid and are very similar among the higgsino and slepton signals. One potential origin of the different trigger efficiencies observed might be that the signals are produced with ATLFAST-II, while the background samples have been generated using the full simulation. The effect of the detector simulation on the efficiencies has been evaluated by comparing the efficiencies of top and $Z + $ jets samples in ATLFAST-II and full simulation with each other. In all cases the efficiencies are compatible with each other. Consequently, the origin of the deviation may also reside in the higher scale of the hard interaction than present in $Z +$jets events. To account for the observed deviation, a dedicated uncertainty for the signal samples was derived by evaluated the scale factors with an offset of ± 15 GeV in $E_{T, \mu \text{ invis}}^{miss}$.

B.8 Trigger Efficiencies and Scale Factors for 2015–2018

The efficiencies measured in data and MC simulation for the *b*-veto and *b*-tag categories are shown in Figures B.8 to B.11. The associated fits to derive the scale factors are shown in in Figures B.12 to B.15.
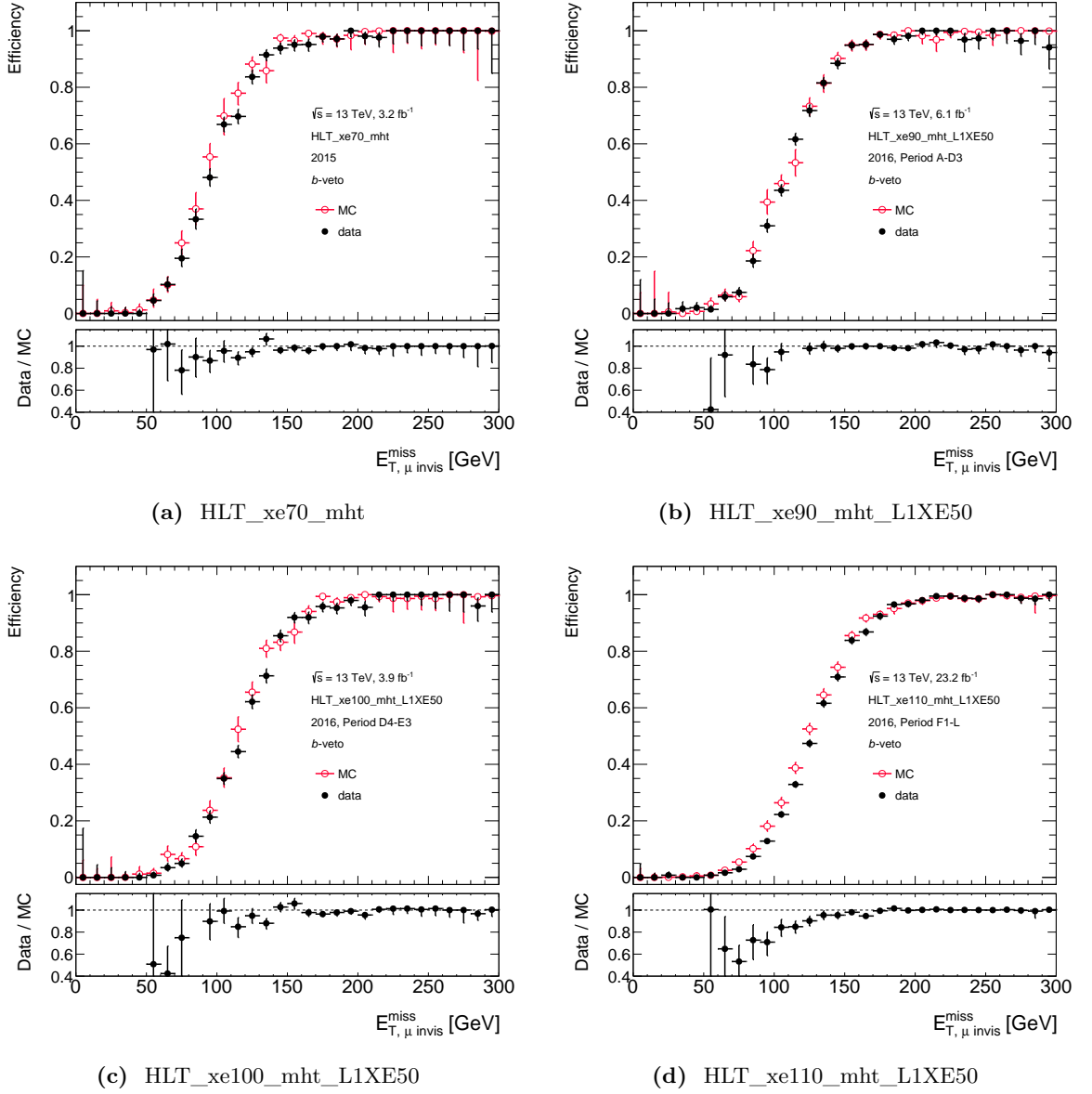
(a) HLT_xe70_mht

(b) HLT_xe90_mht_L1XE50

(c) HLT_xe100_mht_L1XE50

(d) HLT_xe110_mht_L1XE50

Figure B.8: Measured $E_{\mathrm{T}}^{\mathrm{miss}}$-trigger efficiencies in data (black full dots) and MC simulation (red empty circles) in the *b*-veto category for triggers used in 2015 and 2016 data.
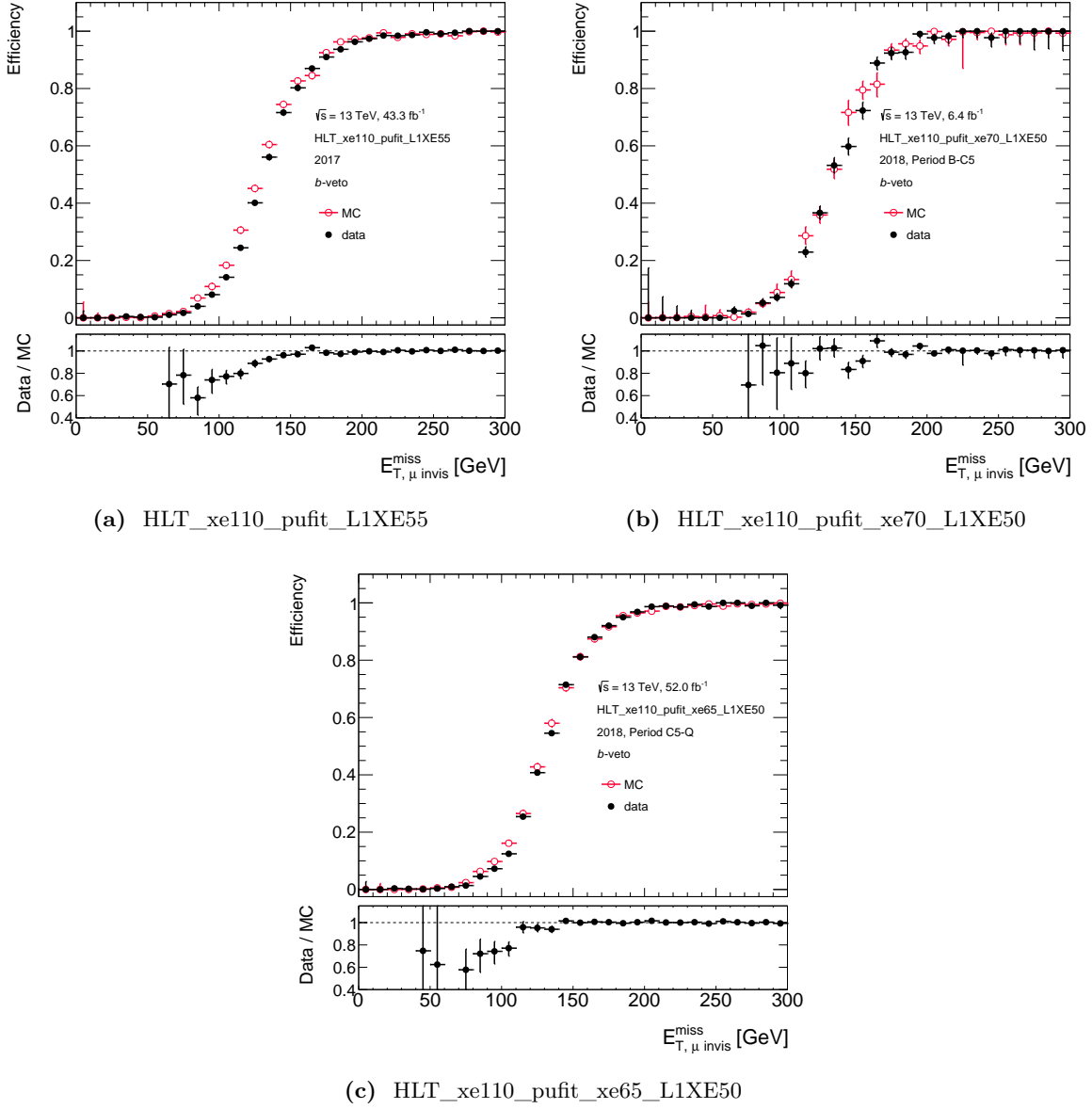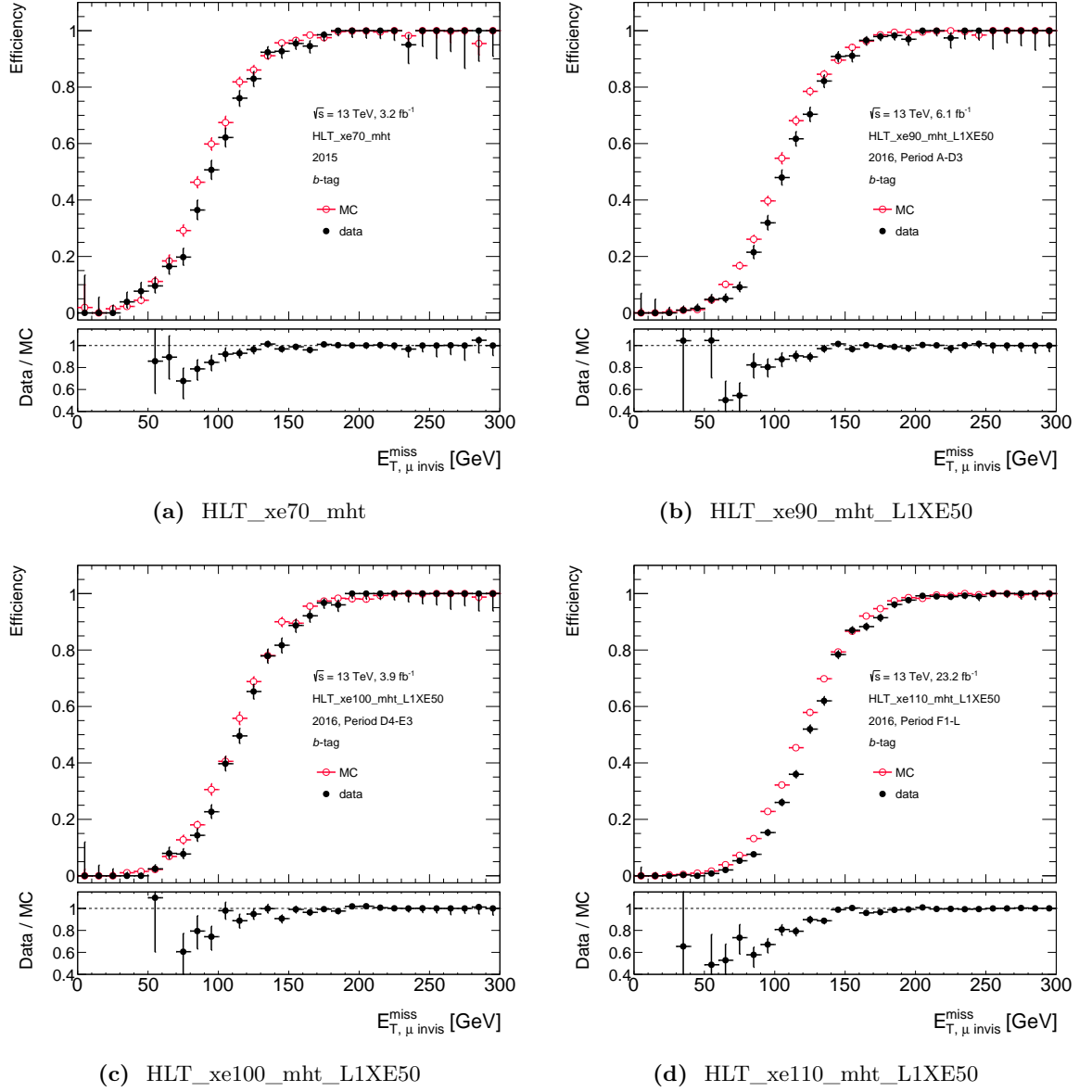
(a) HLT_xe110_pufit_L1XE55

(b) HLT_xe110_pufit_xe70_L1XE50

(c) HLT_xe110_pufit_xe65_L1XE50

Figure B.9: Measured $E_{\mathrm{T}}^{\mathrm{miss}}$-trigger efficiencies in data (black full dots) and MC simulation (red empty circles) with respect to $E_{\mathrm{T},\,\mu\,\mathrm{invis}}^{\mathrm{miss}}$ in the *b*-veto category for triggers used in 2017 and 2018 data.

(a) HLT_xe70_mht

(b) HLT_xe90_mht_L1XE50

(c) HLT_xe100_mht_L1XE50

(d) HLT_xe110_mht_L1XE50

Figure B.10: Measured $E_{\mathrm{T}}^{\mathrm{miss}}$-trigger efficiencies in data (black full dots) and MC simulation (red empty circles) in the *b*-tag category for triggers used in 2015 and 2016 data.

(a) HLT_xe110_pufit_L1XE55

(b) HLT_xe110_pufit_xe70_L1XE50

(c) HLT_xe110_pufit_xe65_L1XE50
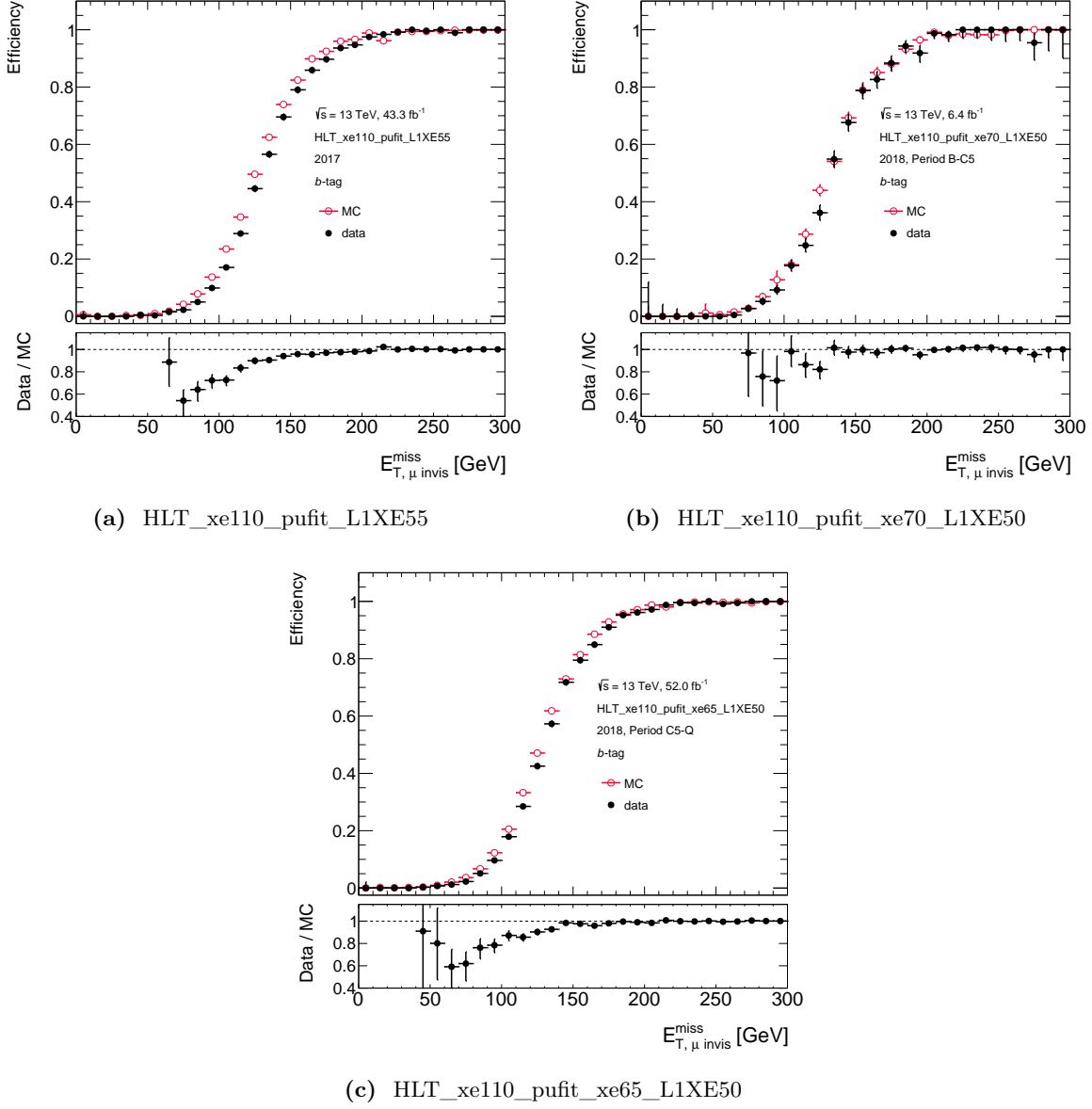
Figure B.11: Measured $E_{\mathrm{T}}^{\mathrm{miss}}$-trigger efficiencies in data (black full dots) and MC simulation (red empty circles) with respect to $E_{\mathrm{T},\,\mu\,\mathrm{invis}}^{\mathrm{miss}}$ in the *b*-tag category for triggers used in 2017 and 2018 data.

(a) HLT_xe70_mht

(b) HLT_xe90_mht_L1XE50

(c) HLT_xe100_mht_L1XE50

(d) HLT_xe110_mht_L1XE50
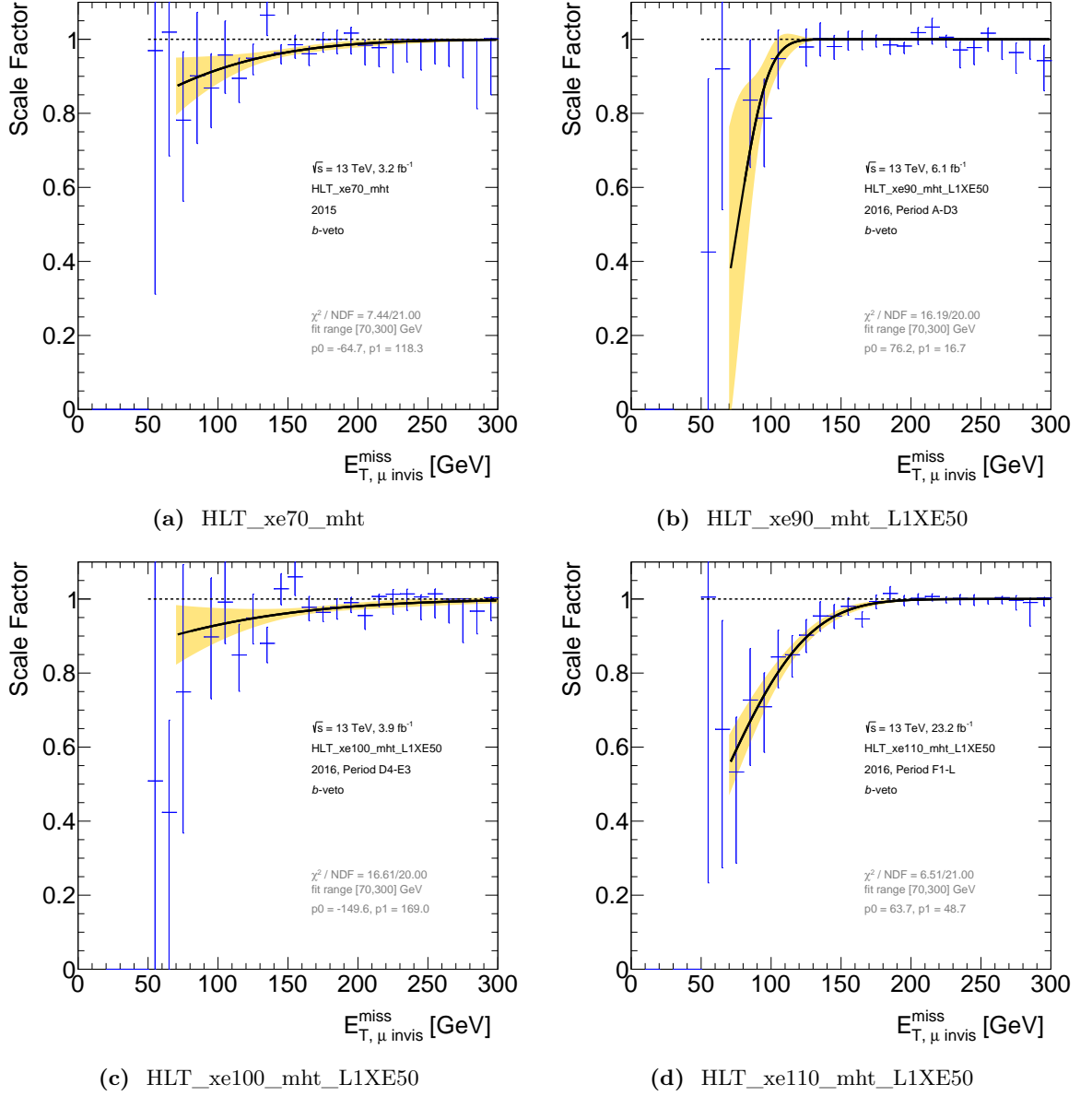
Figure B.12: Fitted E_T^{miss}-trigger scale factors in the *b*-veto category for triggers used in 2015 and 2016 data. The yellow band indicates the statistical uncertainty of the fit.

(a) HLT_xe110_pufit_L1XE55

(b) HLT_xe110_pufit_xe70_L1XE50

(c) HLT_xe110_pufit_xe65_L1XE50
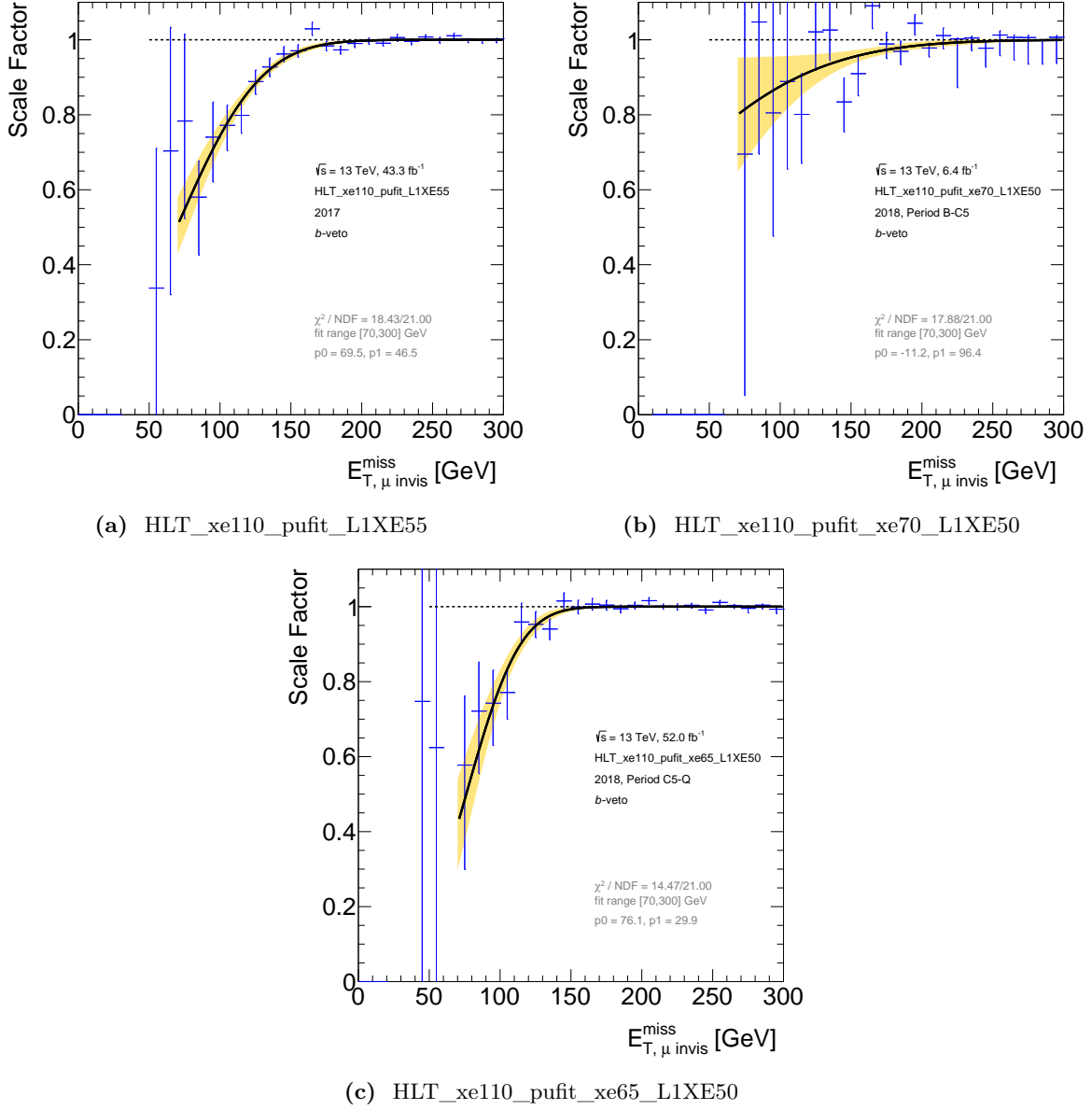
Figure B.13: Fitted E_T^{miss}-trigger scale factors in the b-veto category for triggers used in 2017 and 2018 data. The yellow band indicates the statistical uncertainty of the fit.

(a) HLT_xe70_mht

(b) HLT_xe90_mht_L1XE50

(c) HLT_xe100_mht_L1XE50

(d) HLT_xe110_mht_L1XE50
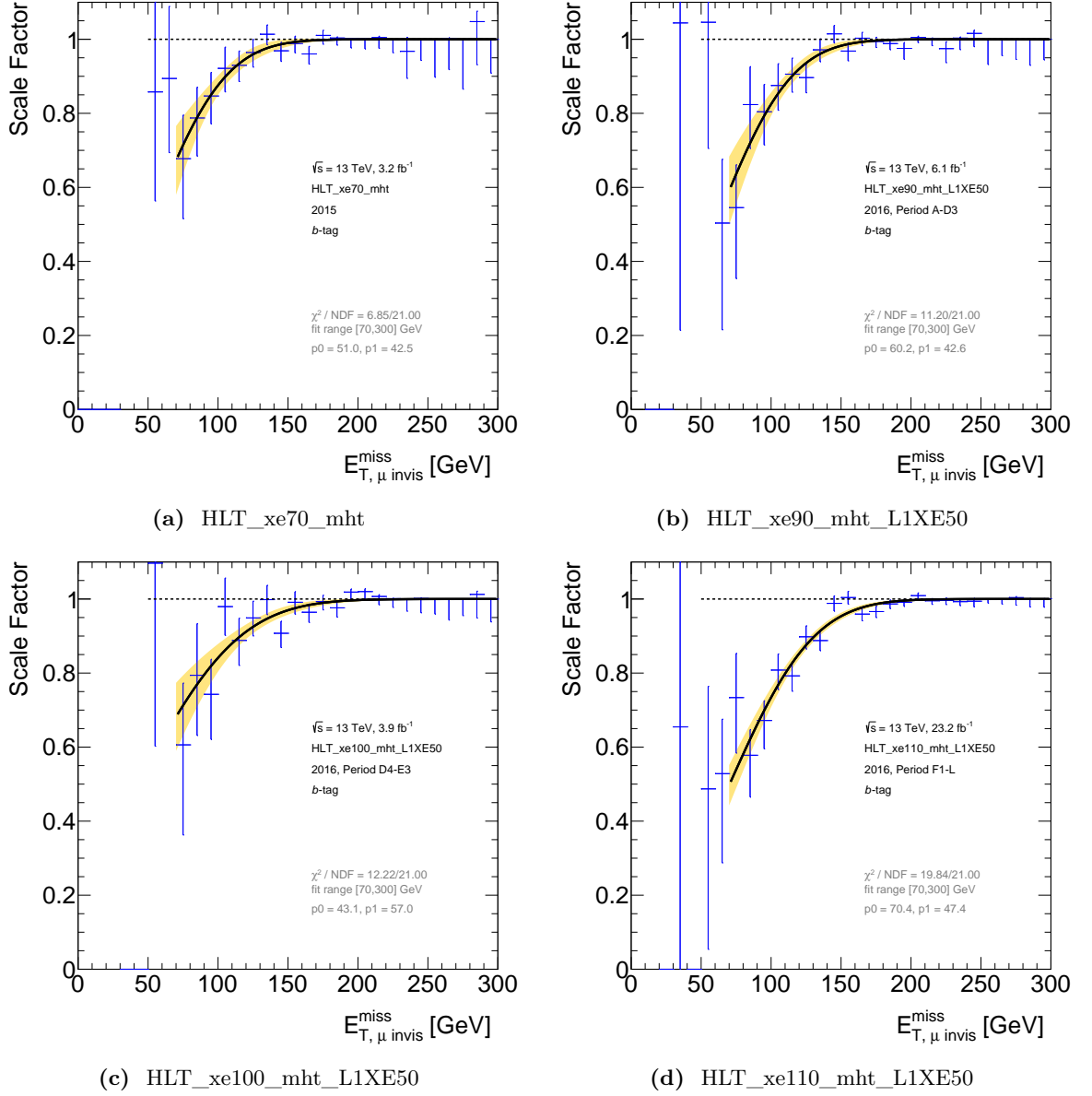
Figure B.14: Fitted $E_{\mathrm{T}}^{\mathrm{miss}}$-trigger scale factors in the *b*-tag category for triggers used in 2015 and 2016 data. The yellow band indicates the statistical uncertainty of the fit.

(a) HLT_xe110_pufit_L1XE55

(b) HLT_xe110_pufit_xe70_L1XE50

(c) HLT_xe110_pufit_xe65_L1XE50
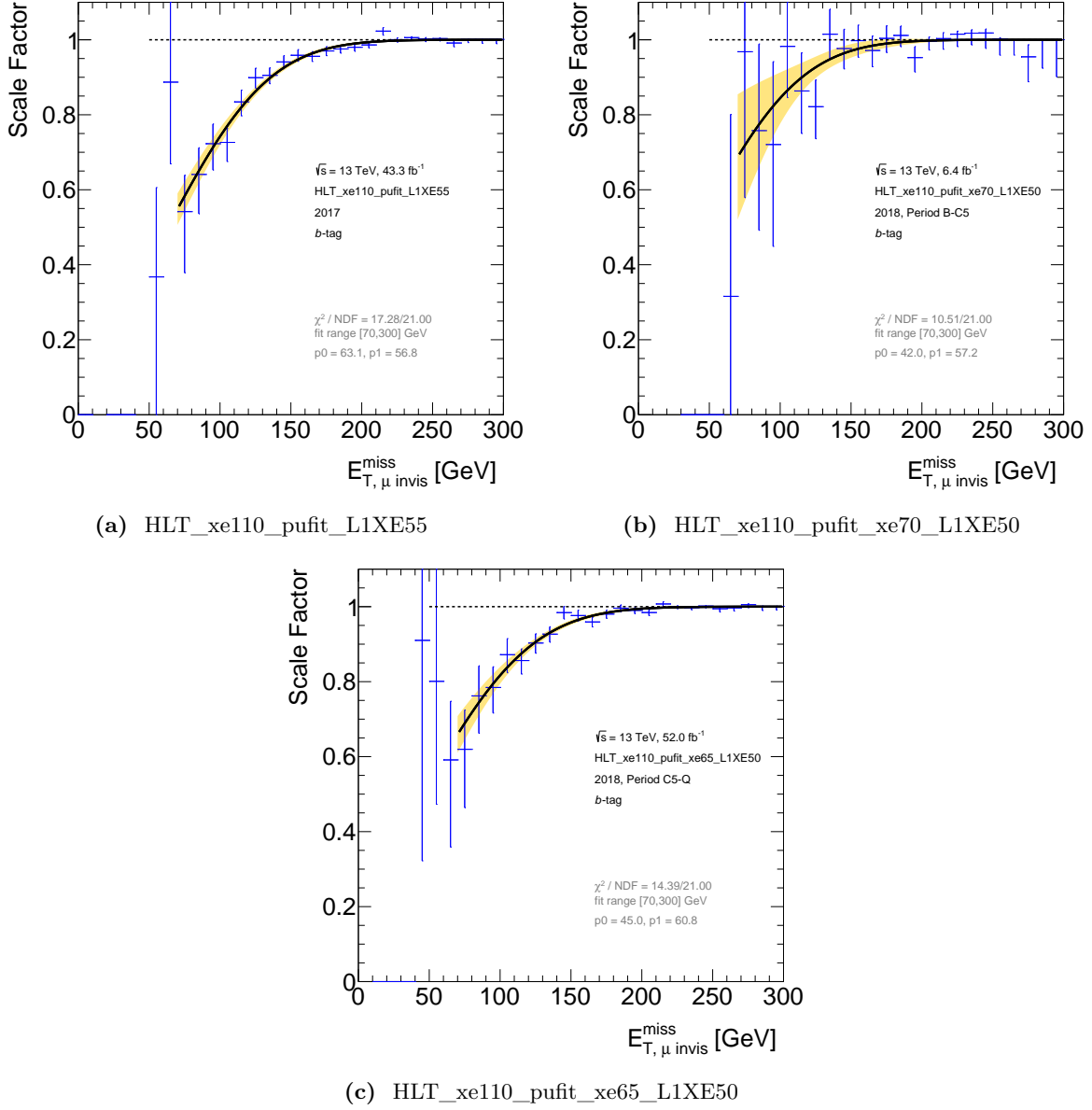
Figure B.15: Fitted $E_{\mathrm{T}}^{\mathrm{miss}}$-trigger scale factors in the *b*-tag category for triggers used in 2017 and 2018 data. The yellow band indicates the statistical uncertainty of the fit.

C ISR Modeling Uncertainty

The most striking signature of the signal models is the boost the SUSY system receives by hadronic ISR activity, that increases the amount of missing transverse energy contained in the event. Consequently, the uncertainty on the modeling of ISR dominates to a large extent also the uncertainties on the signal modeling. Typically, this uncertainty is estimated by variations of the renormalization, factorization and merging scales in the signal generation around their nominal values by a factor of 2. The uncertainty is then derived by the impact of these variations on the signal acceptance in the SRs. The preliminary result of the analysis uses uncertainties on ISR derived by this MC-based method, that have been estimated to be 20 % for the higgsino grid and 20–40 % for the slepton grid, which increase for smaller mass splittings. ISR uncertainties for the final results will be derived via a data-driven way, adapting an approach established by CMS [253], which promises smaller uncertainties.

C.1 Methodology

To estimate the uncertainty on ISR, $Z \to \mu\mu$ events are used as proxy. Such events can be easily selected with a high purity and large statistics. In case the Z boson is boosted with respect to ISR activity, the emerging di-muon system will have a large transverse momentum $p_T(\mu, \mu)$, i.e. up to several hundreds of GeV. The data-to-MC agreement in the $p_T(\mu, \mu)$ distribution can then be taken to assess how well ISR is modeled in MC simulation and to derive an uncertainty estimate. This approach is based on the assumption that the source and consequently the modeling of ISR is similar in signal and $Z \to \mu\mu$ events. As the production of electroweakino and slepton pairs in the considered SUSY models occurs dominantly via intermediate (offshell) W and Z bosons (see Section 2.3.2), the initial parton states are mostly $q\bar{q}$ for both event types. Consequently the form of ISR should also be comparable, which supports the assumption above. This means any mismodeling present in the $p_T(\mu, \mu)$ distribution of $Z \to \mu\mu$ events is likely present in a similar fashion also in the distribution of the transverse momentum of the SUSY system $p_T(\text{SUSY})$.

Foremost it has to be ensured that ISR is modeled equivalently in simulation, i.e. signal and $Z \to \mu\mu$ samples need to be generated using the same configuration. For this purpose a dedicated, "higgsino-like" $Z \to \mu\mu$ MC sample has been generated that uses a generator setup as close as possible to the one used in the higgsino signal generation. It was generated using MG_aMC@NLO 2.6.1, with up to 2 additional partons at ME level. Events are interfaced with PYTHIA 8.232 using the NNPDF23LO PDF set and the A14 tune. As in the signal samples, the requirement of at least one jet with $p_T > 50$ GeV at generator level enforces an ISR topology. To provide enough statistics in the relevant phase space, the sample is split into several slices in $p_T(\mu, \mu)$. The detector response was modeled using the ATLFAST-II simulation. The cross section for each slice was taken from the MG_aMC@NLO prediction

Figure C.1: Distribution of $p_T(\mu, \mu)$ split into the individual slices of the generated higgsino-like $Z \to \mu\mu$ sample. The distribution is shown at truth level, i.e. the muons are not reconstructed but are taken from the event truth record.
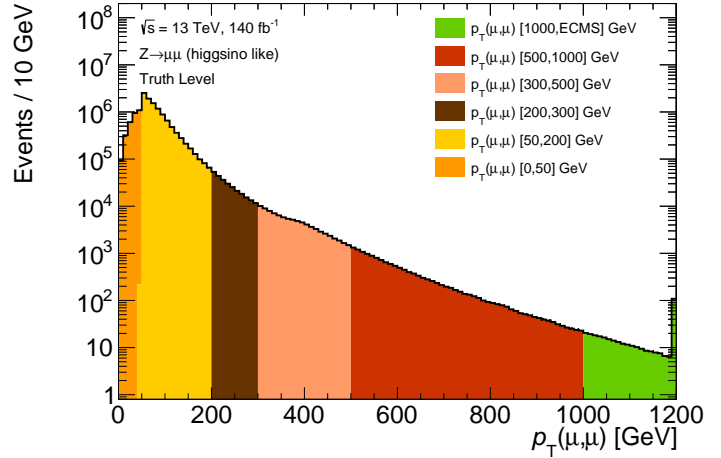
during generation, but the complete $Z \to \mu\mu$ sample is normalized to data before the ISR uncertainty is evaluated.

The $p_T(\mu, \mu)$ distribution of the generated sample split into the individual slices is shown in Figure C.1. The plot uses truth level information, i.e. particles have not been reconstructed but are taken from the generator record. Except for the first two, the transition between the slices is smooth, which validates that the slicing is working correctly. The contribution of the first slice ($p_T(\mu, \mu) < 50\,\text{GeV}$) is sculpted by the jet requirement ($p_T(j_1) > 50\,\text{GeV}$) and therefore the transition to the second slice is not smooth. The slice was just generated for completeness and is not relevant for the study presented, because the covered phase space is cut away as discussed below. However, the $p_T(\mu, \mu)$ distribution is not falling off continuously towards the tail as expected, but interrupted by an unphysical bump emerging around 350 GeV. This bump results in a significant overestimation of the $Z \to \mu\mu$ contributions for large $p_T(\mu, \mu)$. Studies showed that this feature is connected with the particular version of PYTHIA used in the event generation. Figure C.2 shows the $p_T(\mu, \mu)$ distribution of the 300–500 GeV slice before and after the events have been interfaced with PYTHIA. Before PYTHIA is applied, the distribution is falling off exponentially as expected, i.e. the unphysical bump is introduced by PYTHIA 8.232. It was verified that this bug is not present when a generator configuration with an older version of PYTHIA (8.212) is used.

To avoid the re-generation of the MC sample, which would have required a lot of computing resources for the detector simulation, a reweighting at truth level with respect to $p_T(\mu, \mu)$ is performed. First the event generation for all slices has been run again using PYTHIA 8.212. Afterwards a bin-by-bin re-weighting is introduced so that the $p_T(\mu, \mu)$ distribution in the PYTHIA 8.232 sample matches the distribution in the PYTHIA 8.212 sample. No unphysical behavior was found in other kinematic distributions such as the pseudorapidity of the di-muon system, consequently a one-dimensional reweighting in $p_T(\mu, \mu)$ should be sufficient to overcome the issue. The validity of the procedure was confirmed in a private discussion with one of the PYTHIA authors. The weight of each event derived in the reweighting procedure is propagated to the reconstruction level of the higgsino-like MC samples to eliminate the unphysical behavior also there.
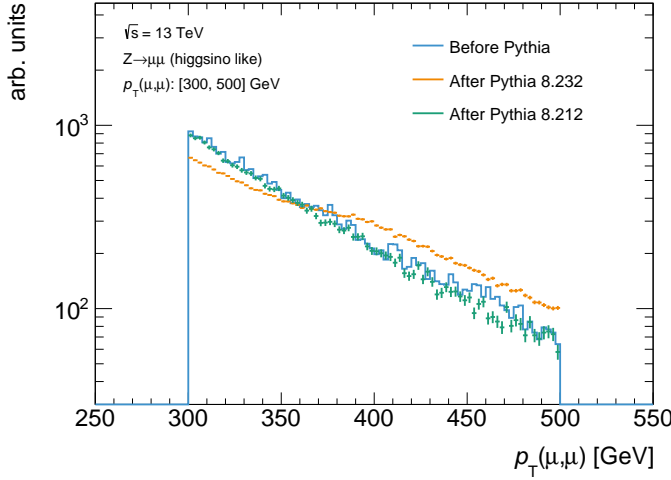
Figure C.2: Distribution of $p_{\mathrm{T}}(\mu, \mu)$ for the 300–500 GeV slice of the higgsino-like $Z \to \mu\mu$ sample, before and after the events have been interfaced with Pythia 8.232 and Pythia 8.212, respectively. All three distributions have been scaled to the same arbitrary number, to simplify the comparison.

C.2 Event Selection

To collect a sample pure in $Z \to \mu\mu$, events are selected by single-muon triggers in data an MC simulation. The same triggers as in the measurement of $E_{\mathrm{T}}^{\mathrm{miss}}$-trigger efficiencies are used, and listed in Table B.2. Further, exactly two muons of OS are required, with one of them having triggered the write-out of the event. Only muon pairs with an invariant mass around the Z resonance $70\,\mathrm{GeV} < m_{\mu\mu} < 110\,\mathrm{GeV}$ are considered. To suppress contamination from top-related events as $t\bar{t}$, events with at least one b-tagged jet are vetoed. Requirements on $p_{\mathrm{T}}(j_1) > 100\,\mathrm{GeV}$ and $p_{\mathrm{T}}(\mu, \mu) > 100\,\mathrm{GeV}$ enforce that the Z boson is boosted with respect to an ISR jet. This results in a selection more than $98\,\%$ pure in $Z \to \mu\mu$ events according to simulation. To account for a global offset in the MC prediction, the higgsino-like $Z \to \mu\mu$ sample is normalized to data in this region. A normalization factor of approximately 0.8 was derived and results in a good data-to-MC agreement across the $m_{\mu\mu}$ spectrum, as depicted in Figure C.3. On the contrary, Figure C.4a shows a clear, linear slope in the $p_{\mathrm{T}}(\mu, \mu)$ distribution. As $p_{\mathrm{T}}(\mu, \mu)$ is directly related to the transverse momentum of the Z boson, this variable is sensitive to the presence of ISR. Hence the mismodeling observed in $p_{\mathrm{T}}(\mu, \mu)$ can be related to a mismodeling of ISR. Finally, because $p_{\mathrm{T}}(\mu, \mu)$ is considered as a proxy for $p_{\mathrm{T}}(\mathrm{SUSY})$, the estimate of the uncertainty on ISR modeling at a certain value of $p_{\mathrm{T}}(\mathrm{SUSY})$ is given by the degree of mismodeling observed at the associated value in the $p_{\mathrm{T}}(\mu, \mu)$ distribution.

## C.3 Uncertainty Estimate in the Signal Regions

The slope in the data-to-MC agreement visible in the bottom panel of Figure C.4a is fitted with a χ^2 fit using a first-order polynomial in the range from 100–1000 GeV. The value of the fitted line is approximately 1 around 200 GeV and decreases to about 0.6 at 1000 GeV. The fitted line is shown in yellow in the bottom panel of Figure C.4a. As a cross-check, the data-to-MC agreement has been additional evaluated in a second variable sensitive to ISR. Assuming all jets in the event originate from ISR activity, the four vectors of all baseline jets

Figure C.3: Distributions of $m_{\mu\mu}$ in the region defined to estimate the ISR uncertainty. A normalization factor of 0.794 is applied to the higgsino-like $Z \to \mu\mu$ sample as discussed in the text. The hatched bands indicate the statistical uncertainty.
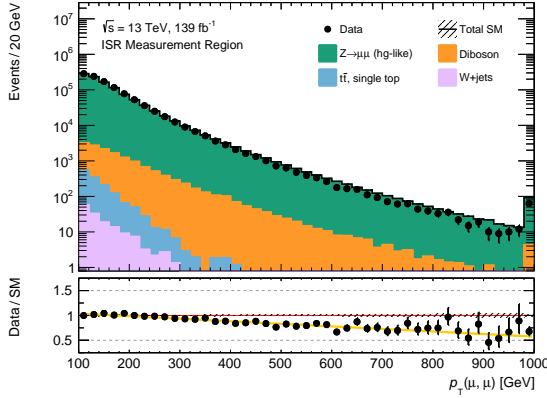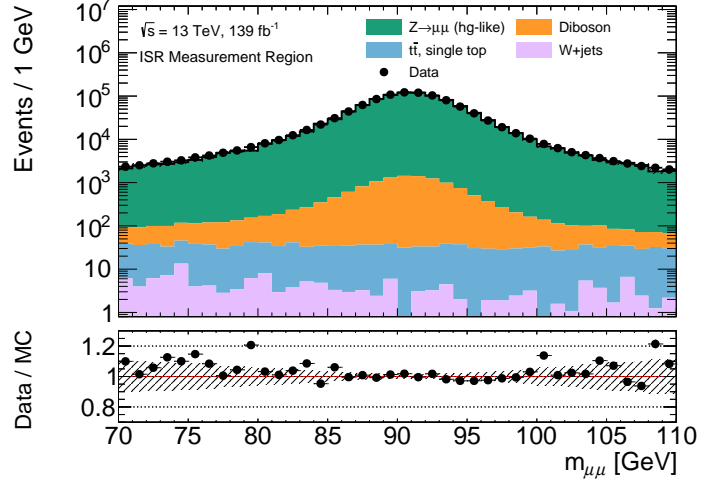
(a) $p_T(\mu, \mu)$
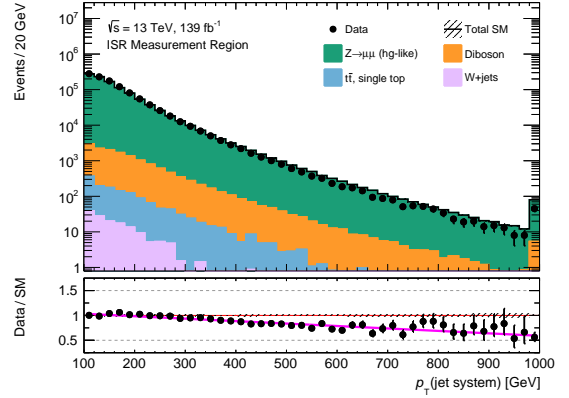
(b) p_T of the jet system

Figure C.4: Distributions of $p_T(\mu, \mu)$ and the p_T of the jet system in the region defined to estimate the ISR uncertainty. A normalization factor of 0.794 is applied to the higgsino-like $Z \to \mu\mu$ sample as discussed in the text. The last bin contains the overflow. The colored line in the respective bottom panel shows the result of the linear fit of the data/MC ratio. The hatched bands indicate the statistical uncertainty.
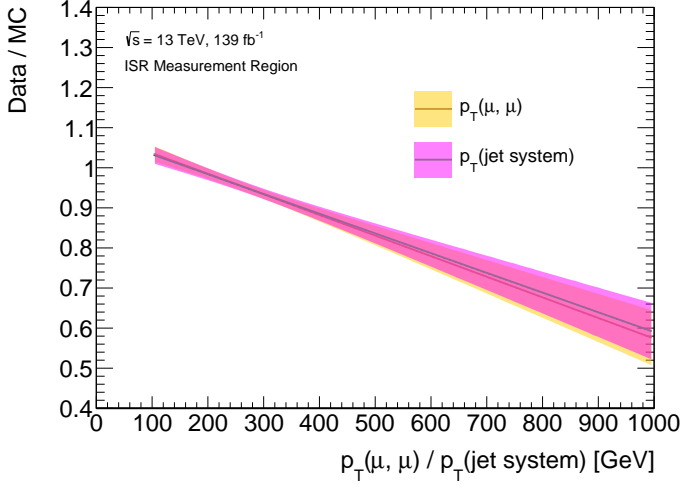
Figure C.5: Fits of the slopes present in the distributions of $p_{\mathrm{T}}(\mu, \mu)$ (yellow) and the p_{T} of the jet system (purple). The bands represent the 95 % CL interval of the fit parameters.

are added to calculate the p_{T} of the jet system. The distribution of this variable and the fit of the data/MC ratio is depicted in Figure C.4b. As shown in Figure C.5, both slope fits are compatible with each other within their uncertainties.

To derive the final estimates for the ISR uncertainty in the SRs, essentially the deviation from one of the slope is used. Technically, a signal yield representing the systematic variation is introduced by reweighting the signal sample on an event-by-event basis. The relative uncertainty is given by the difference of the variational yield $N_{\mathrm{syst}}(\mathrm{SR})$ that uses the "ISR weights" described above and the nominal signal yield $N_{\mathrm{nom}}(\mathrm{SR})$

$$\frac{\Delta\sigma_{\mathrm{ISR}}}{\sigma_{\mathrm{ISR}}} = \frac{|N_{\mathrm{nom}}(\mathrm{SR}) - N_{\mathrm{syst}}(\mathrm{SR})|}{N_{\mathrm{nom}}(\mathrm{SR})} \,. \tag{C.1}$$

To derive the yield for the systematic uncertainty, each signal event is weighted with the value of the fitted slope of $p_{\mathrm{T}}(\mu, \mu)$, evaluated at the value of $p_{\mathrm{T}}(\mathrm{SUSY})$. For instance, if the the the p_{T} of the SUSY system is found to be $300\,\mathrm{GeV}$, the weight for this event would be approximately 0.9, corresponding to an uncertainty of $10\,\%$. Thus, the magnitude of the total uncertainty depends on the distribution of $p_{\mathrm{T}}(\mathrm{SUSY})$. As an illustration, Figure C.6 shows $p_{\mathrm{T}}(\mathrm{SUSY})$, calculated with information from the truth record of the $\tilde{\chi}_2^0\tilde{\chi}_1^\pm$, $\tilde{\chi}_2^0\tilde{\chi}_1^0$ and $\tilde{\chi}_1^+\tilde{\chi}_1^-$ pair, respectively, in two of the electroweakino SRs, SR-ewk-low-$E_{\mathrm{T}}^{\mathrm{miss}}$-high-$\Delta m$ and SR-ewk-high-$E_{\mathrm{T}}^{\mathrm{miss}}$. In the low-$E_{\mathrm{T}}^{\mathrm{miss}}$ regime, the vast majority of signal events have $p_{\mathrm{T}}(\mathrm{SUSY})$ between 150 and $250\,\mathrm{GeV}$, hence the uncertainty is expected to be rather small as the fitted slope is close to 1 in this range. At high-$E_{\mathrm{T}}^{\mathrm{miss}}$, the distribution of $p_{\mathrm{T}}(\mathrm{SUSY})$ is notably harder, with tails going up to $1000\,\mathrm{GeV}$. In general, the $p_{\mathrm{T}}(\mathrm{SUSY})$ distribution was found to become harder with decreasing mass splittings, resulting in larger uncertainties for the low-Δm signal points. For the slepton grid, $p_{\mathrm{T}}(\mathrm{SUSY})$ is calculated with truth information of the $\tilde{\ell}^+\tilde{\ell}^-$ pair and shows the same characteristics as in the higgsino grid. As the fit of the slope is performed in the range from 100 to $1000\,\mathrm{GeV}$, $p_{\mathrm{T}}(\mathrm{SUSY})$ is only evaluated in that range. In case $p_{\mathrm{T}}(\mathrm{SUSY})$ should be outside of this range, the values are calculated with the lower and upper thresholds of the range, respectively. This is required only for a tiny fraction of the signal events as shown in Figure C.6, and consequently has a completely negligible
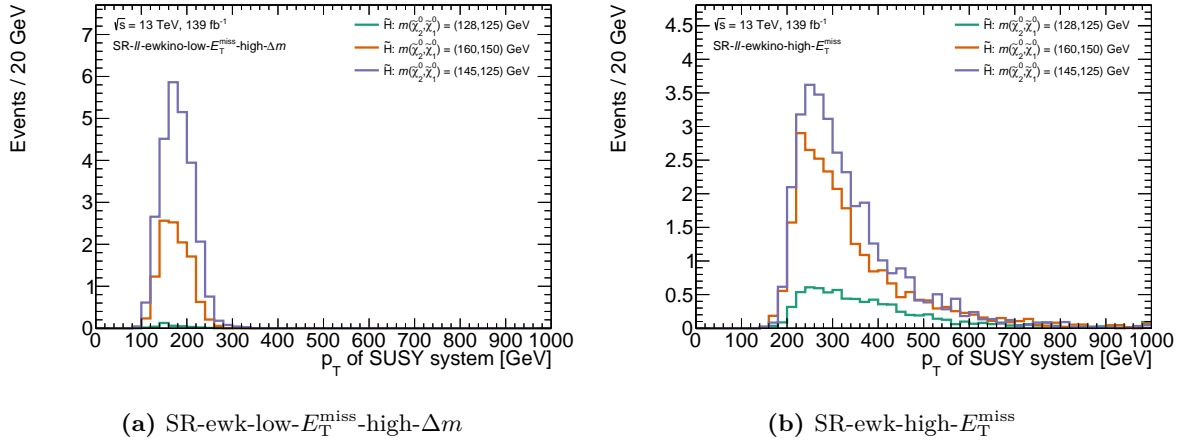
(a) SR-ewk-low-$E_\mathrm{T}^\mathrm{miss}$-high-$\Delta m$

(b) SR-ewk-high-$E_\mathrm{T}^\mathrm{miss}$

Figure C.6: Distribution of the p_T of the SUSY system in the low-$E_\mathrm{T}^\mathrm{miss}$ high-Δm and the high-$E_\mathrm{T}^\mathrm{miss}$ electroweakino SRs for three signal points, which represent mass splittings of 3 (green), 10 (orange) and 20 GeV (purple).

impact on the final uncertainties. Small signal MC statistics require to loosen the high-$E_\mathrm{T}^\mathrm{miss}$ slepton SR slightly, to be less sensitive to statistical fluctuations in the uncertainty estimation. The m_T2-dependent cut on R_ISR was replaced by a flat requirement $R_\mathrm{ISR} > 0.85$, while the m_T2-dependent requirement on $p_\mathrm{T}(\ell_2)$ is neglected.

The final uncertainties estimates for the electroweakino and slepton SRs are shown in Figures C.7 and C.8. For low-$E_\mathrm{T}^\mathrm{miss}$, these are roughly flat across both signal grids with a magnitude of 2–3 %. At high-$E_\mathrm{T}^\mathrm{miss}$, the uncertainties get larger with increasing $\tilde{\chi}_2^0/\tilde{\ell}^\pm$ mass and smaller mass splitting, ranging from 7 to 20 %. This represents a clear improvement on the ISR modeling uncertainties with respect to the approach using scale variations at truth level. In particular small mass splittings in the slepton grid, where the uncertainties have been up to 40 %, will benefit from the presented data-driven approach to estimate ISR uncertainties. Consequently, the final results will have an enlarged exclusion reach compared to the preliminary results, due to smaller signal uncertainties.
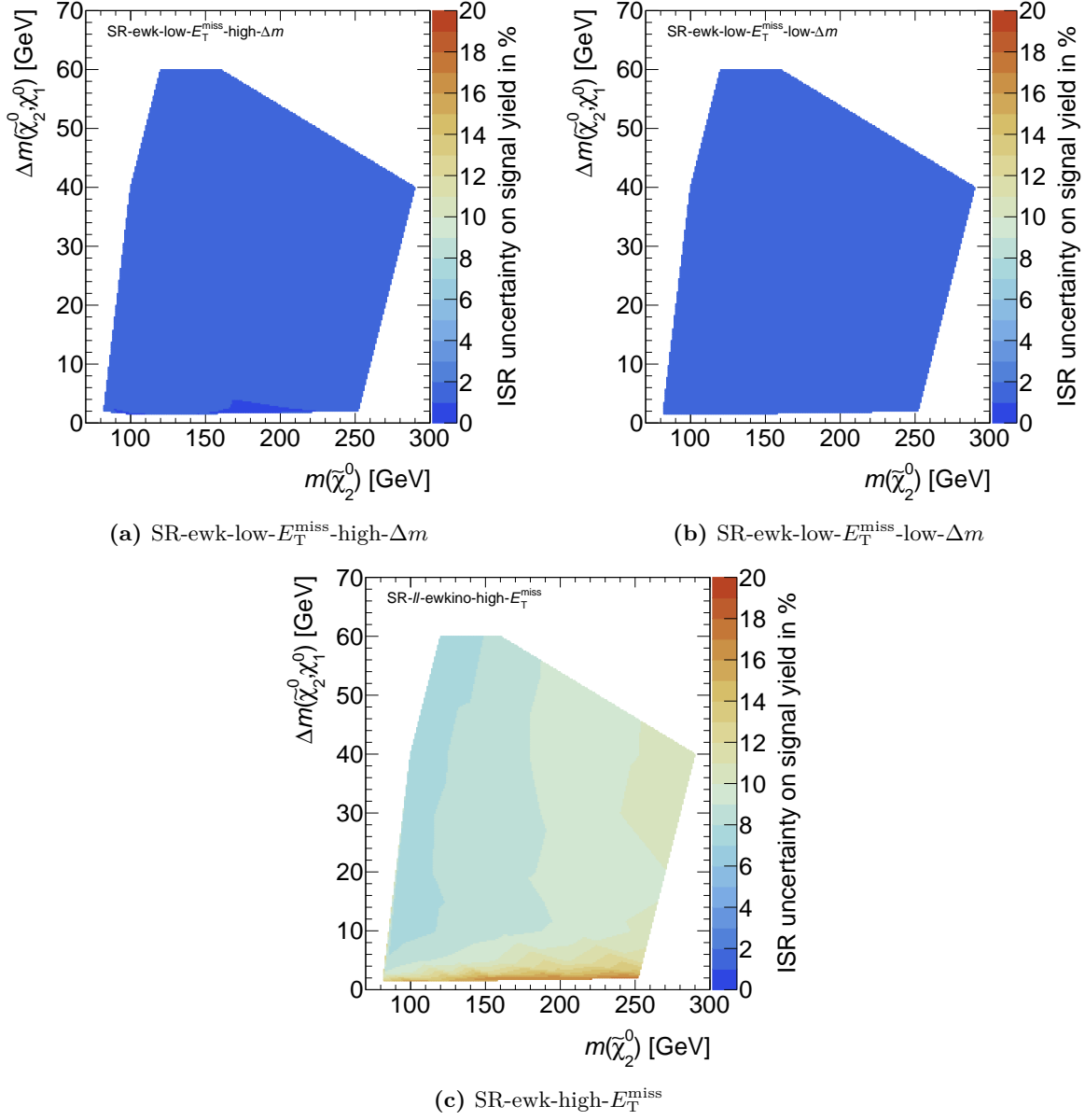
(a) SR-ewk-low-$E_{\mathrm{T}}^{\mathrm{miss}}$-high-$\Delta m$

(b) SR-ewk-low-$E_{\mathrm{T}}^{\mathrm{miss}}$-low-$\Delta m$

(c) SR-ewk-high-$E_{\mathrm{T}}^{\mathrm{miss}}$

Figure C.7: Data-driven ISR uncertainty estimates for the electroweakino SRs.

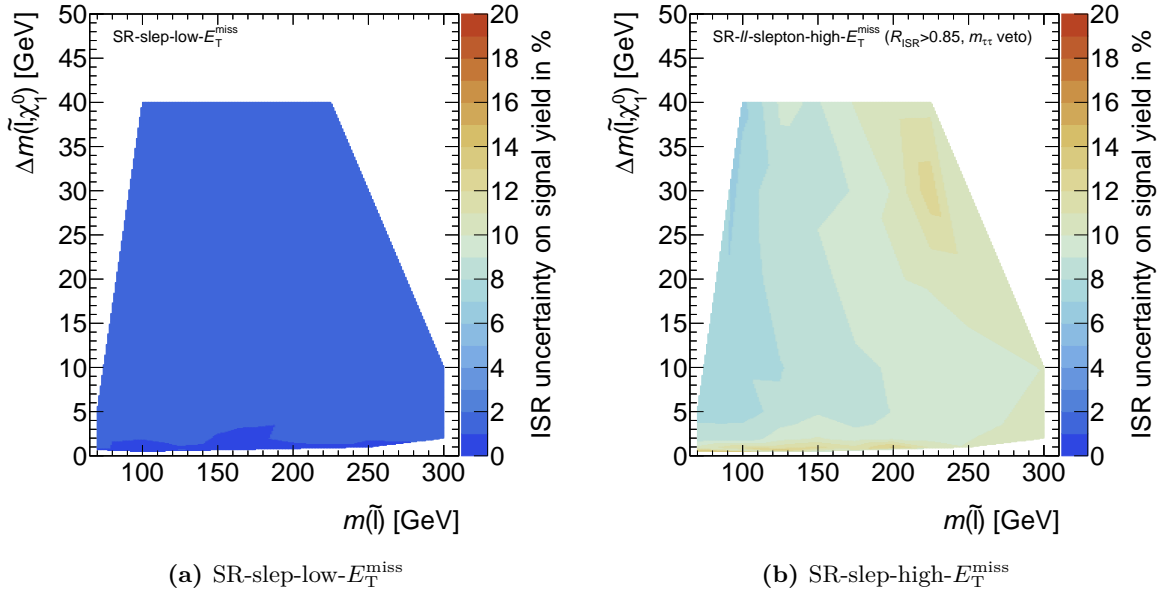**(a)** SR-slep-low-E_T^{miss}

(b) SR-slep-high-E_T^{miss}

Figure C.8: Data-driven ISR uncertainty estimates for the slepton SRs.

D Additional Analysis Material

This appendix contains additional studies performed for the analysis and provides further plots for the sections of Chapter 5.

D.1 Signal Region Optimization

The following sections summarize studies performed during the optimization of the SRs and contain N-1 plots for the variables used in the SR definitions split into the individual $m_{\ell\ell}/m_{\mathrm{T2}}$ bins.

D.1.1 Performance of RJR Variables

The intrinsic complexity of RJR motivates to compare the performance of variables derived by this algorithm with more common kinematic quantities, which are also simpler to understand.

The obvious counterpart of $M_{\mathrm{T}}^{\mathrm{S}}$ is the transverse mass calculated with the leading lepton $m_{\mathrm{T}}^{\ell_1}$. Figure D.1 shows N-1 plots of the two variables in SR-ewk-low-$E_{\mathrm{T}}^{\mathrm{miss}}$-low-$\Delta m$, before applying the associated requirement on $M_{\mathrm{T}}^{\mathrm{S}}$ in the SR definition. Both distributions exhibit a distinct Jacobian peak just before the W boson mass, that arises from $W \to \ell\nu$ events in which the second lepton is faked. However in $M_{\mathrm{T}}^{\mathrm{S}}$, notably less background accumulates at low values than in the $m_{\mathrm{T}}^{\ell_1}$ distribution. This renders $M_{\mathrm{T}}^{\mathrm{S}}$ more powerful in rejecting background with an upper requirement, as it visible in the significance scan.

The distribution of R_{ISR} behaves very similar to the ratio of the $E_{\mathrm{T}}^{\mathrm{miss}}$ and the scalar sum of all signal jet transverse momenta. $E_{\mathrm{T}}^{\mathrm{miss}}/H_{\mathrm{T}}^{30}$ can, similar to R_{ISR}, be understood as an es-
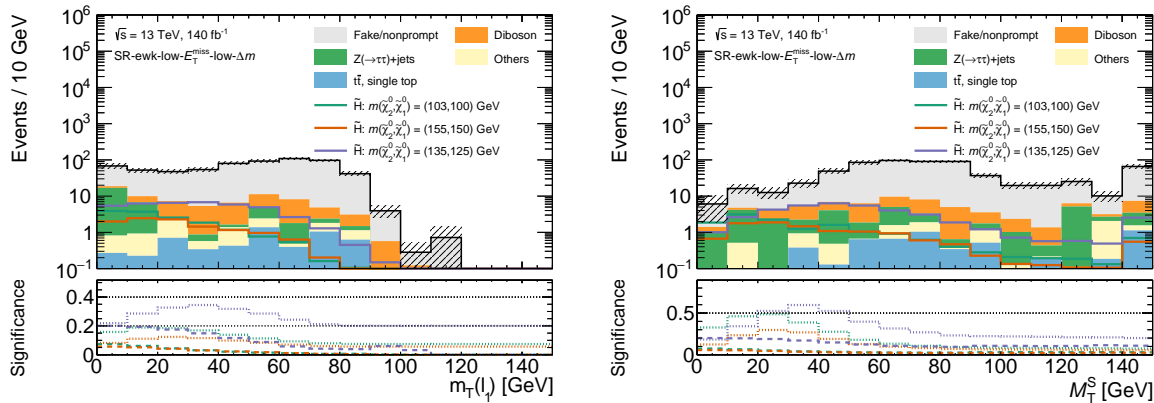
Figure D.1: N-1 plots of $m_{\mathrm{T}}^{\ell_1}$ (left) and $M_{\mathrm{T}}^{\mathrm{S}}$ (right) in the region SR-ewk-low-$E_{\mathrm{T}}^{\mathrm{miss}}$-low-$\Delta m$ before applying requirement on $M_{\mathrm{T}}^{\mathrm{S}}$ in the SR definition.
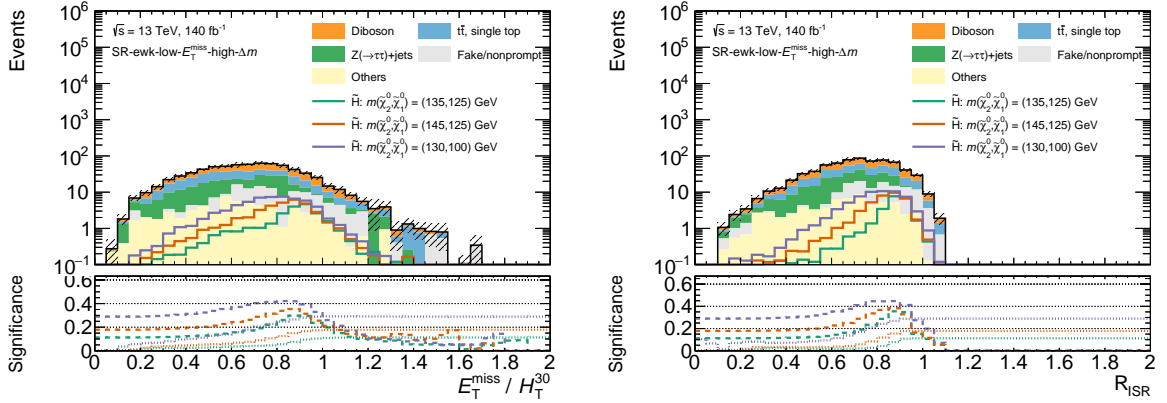
Figure D.2: N-1 plots of E_T^{miss}/H_T^{30} (left) and R_{ISR} (right) in the region SR-ewk-low-E_T^{miss}-high-Δm before applying requirement on R_{ISR} in the SR definition.

Figure D.3: Expected exclusion reach of the two electroweakino low-E_T^{miss} SRs and their combination (see Figure 5.22a). The gray area marks the associated exclusion limits from the LEP experiments. The blue regions indicate the limits from the previous iteration of the analysis.
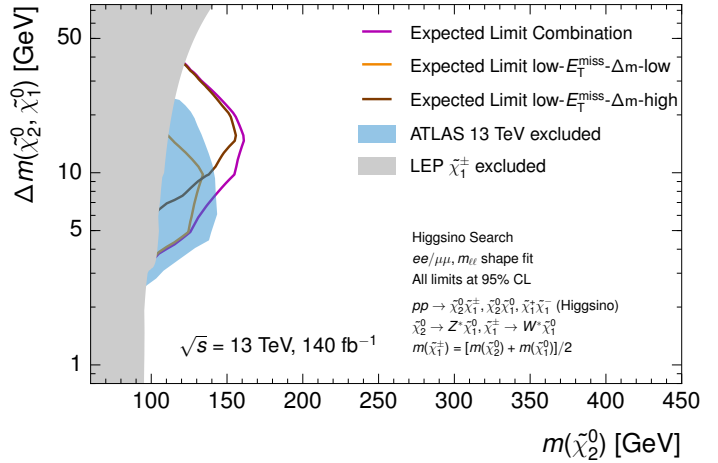
timator how much of the E_T^{miss} originates from ISR. The comparison of both distributions for SR-ewk-low-E_T^{miss}-high-Δm is shown in Figure D.2, without applying the R_{ISR} requirement from the SR definition. Signals peak in both distributions between 0.8 and 1, and the significance scan suggests both variables have comparable signal-to-background discrimination power, with R_{ISR} performing slightly better. For that reason the RJR variable was preferred in defining the signal selection.

D.1.2 Performance of Individual Electroweakino Signal Regions

During optimization studies for the low-E_T^{miss} electroweakino SRs, it turned out to be beneficial to derive two separate SRs, optimizing for small and large splittings individually. The performance of both SRs and their combination is shown in Figure D.3, using the simplified fit configuration described in Section 5.4.4. Although the sensitivity of SR-ewk-low-E_T^{miss}-low-Δm is completely within already excluded signal parameter space, it improves the sensitivity for mass splittings between 7 and 15 GeV in a combination with SR-ewk-low-E_T^{miss}-high-Δm. The expected exclusion contour of the combination exceeds then notably the

existing constraints.

D.1.3 N-1 Plots for SR Bins

This section contains N-1 plots with significance scans for the variables in the individual SR definitions split into each $m_{\ell\ell}/m_{\mathrm{T2}}$ bins. The split into the single SR bins better shows the motivation for the placements of the requirements that the significance scans of the inclusive SR. All plots show the sum of ee and $\mu\mu$ events.

Figure D.4 shows the N-1 plots for $M_{\mathrm{T}}^{\mathrm{S}}$ in SR-ewk-low-$E_{\mathrm{T}}^{\mathrm{miss}}$-low-$\Delta m$ for all $m_{\ell\ell}$ bins used in this SR. The distributions of R_{ISR}, $p_{\mathrm{T}}(\ell_2)$ and $m_{\mathrm{T}}^{\ell_1}$ in the single $m_{\ell\ell}$ bins of SR-ewk-low-$E_{\mathrm{T}}^{\mathrm{miss}}$-low-$\Delta m$ are shown in Figures D.5 to D.7. Likewise, the $E_{\mathrm{T}}^{\mathrm{miss}}$, R_{ISR} and $p_{\mathrm{T}}(\ell_2)$ distributions for SR-slep-low-$E_{\mathrm{T}}^{\mathrm{miss}}$ are shown in Figures D.8 to D.10.
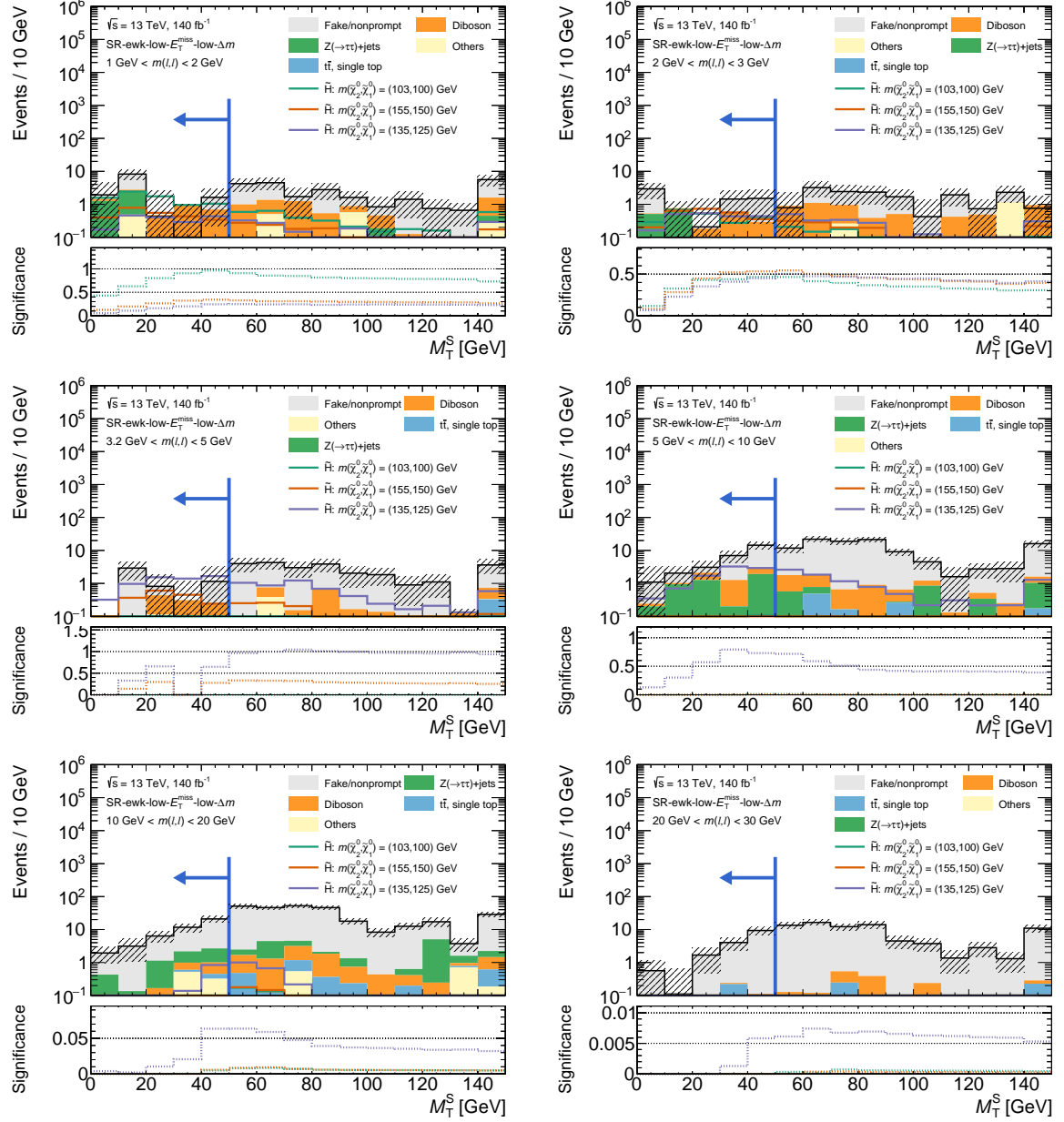
Figure D.4: N-1 plots of $M_{\mathrm{T}}^{\mathrm{S}}$ in SR-ewk-low-$E_{\mathrm{T}}^{\mathrm{miss}}$-low-$\Delta m$ for the individual $m_{\ell\ell}$ bins. The blue arrow indicates the location and direction of the requirement on the variable shown. The bottom panel shows a significance scan with dotted lines indicating the significance of a potential upper requirement at the shown position.
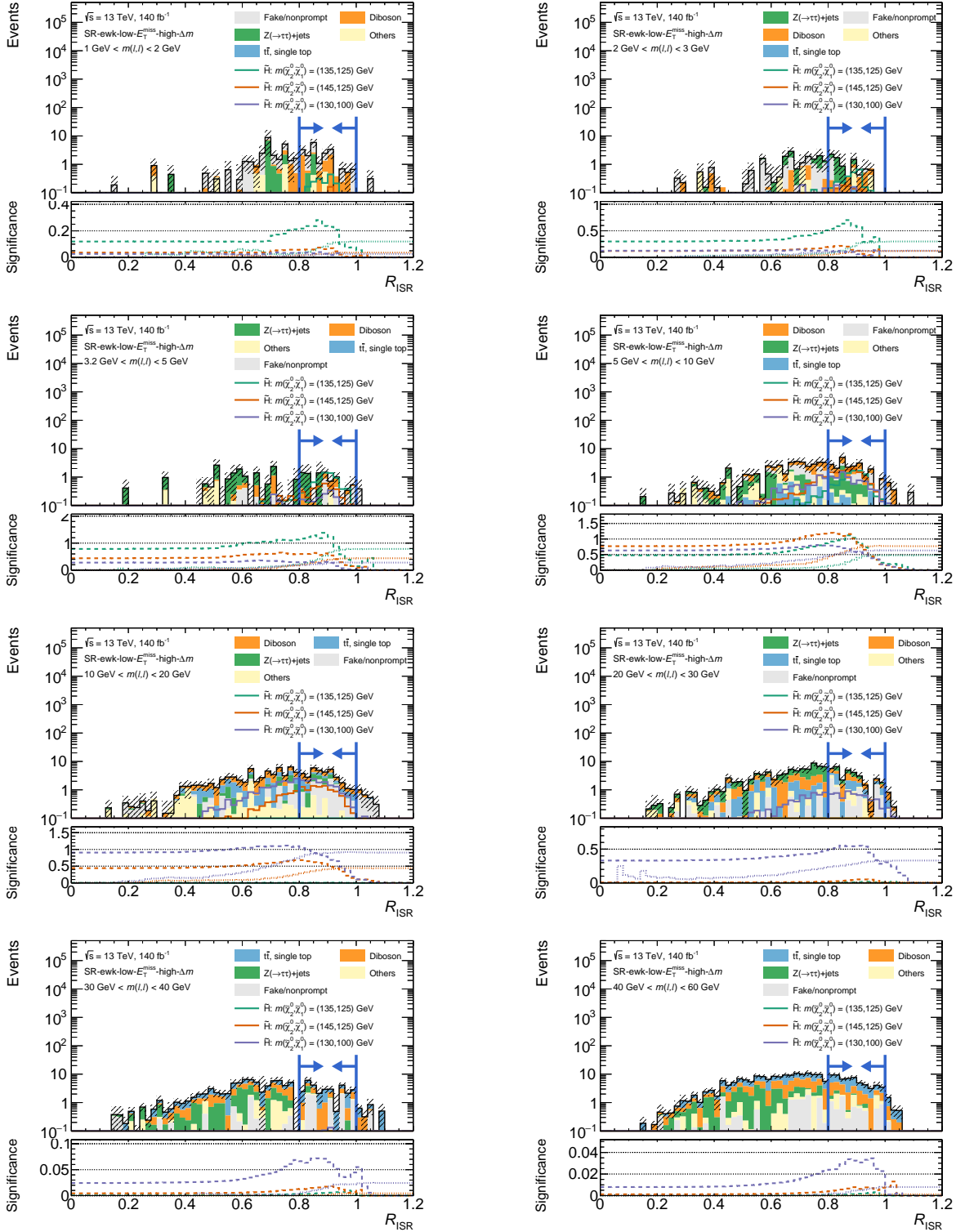
Figure D.5: N-1 plots of R_{ISR} in SR-ewk-low-$E_{\mathrm{T}}^{\mathrm{miss}}$-high-$\Delta m$ for the individual $m_{\ell\ell}$ bins. The blue arrows indicate the location and direction of the requirements on the variable shown. The bottom panel shows a significance scan with dotted (dashed) lines indicating the significance of a potential upper (lower) requirement at the shown position.
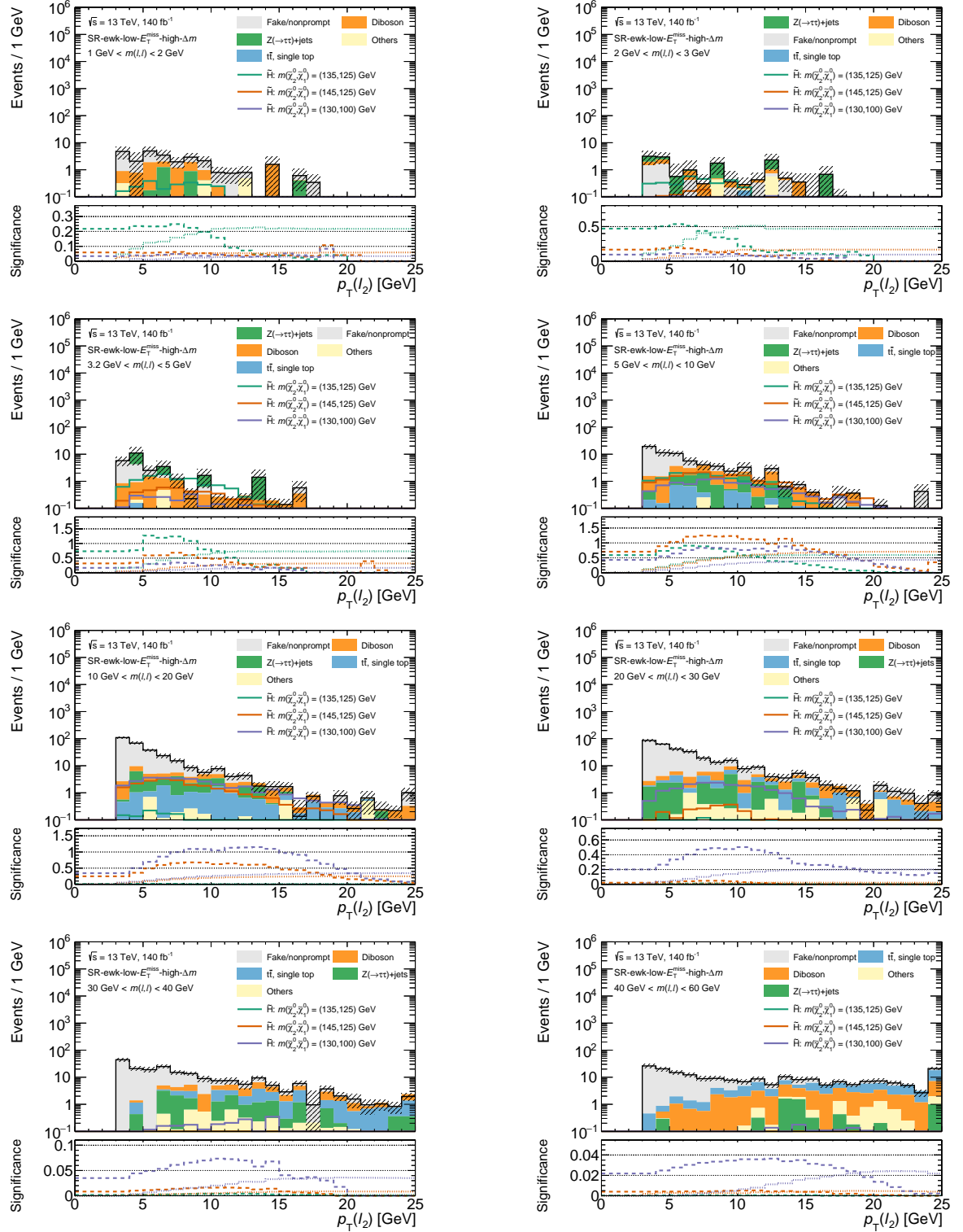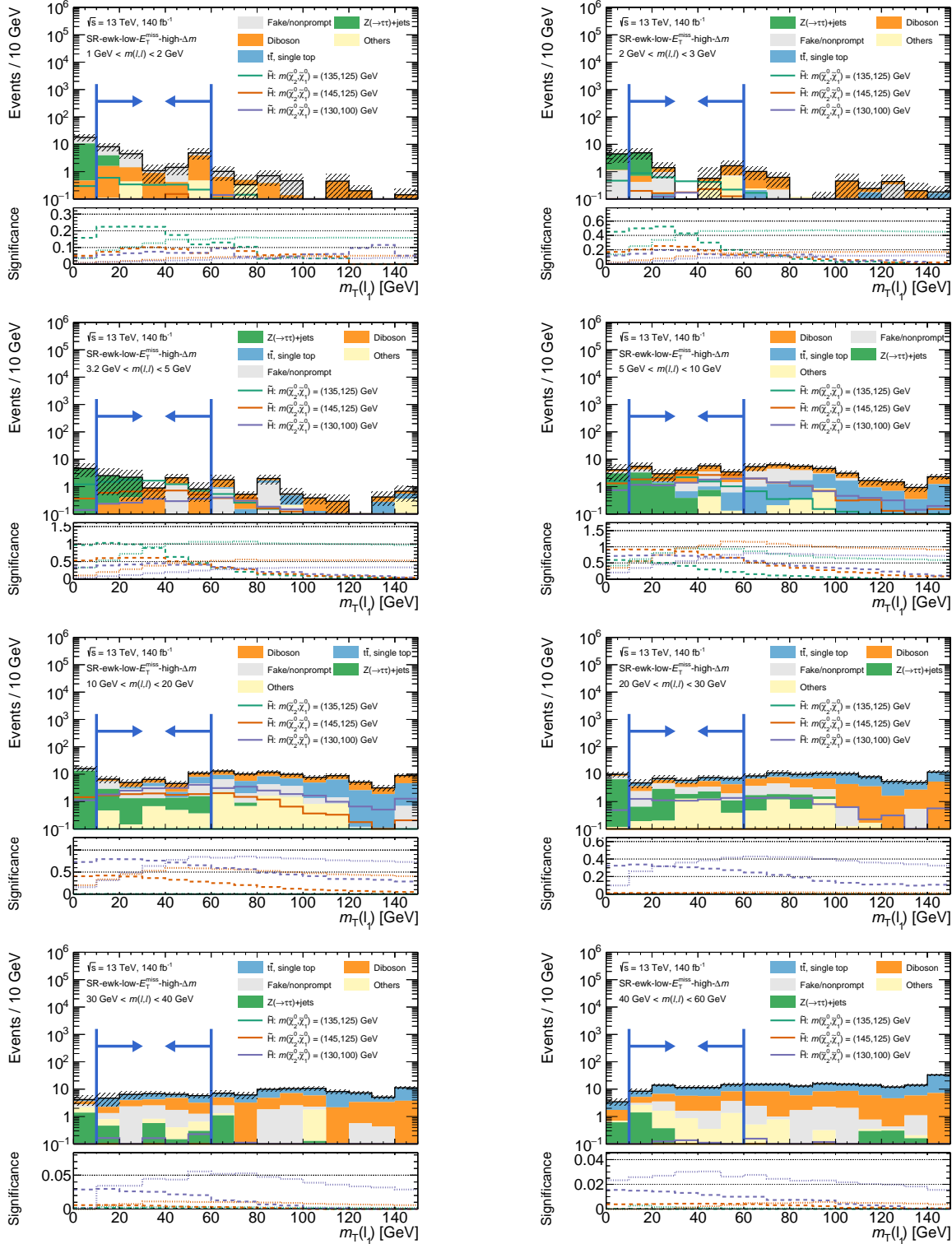
Figure D.6: N-1 plots of $p_\mathrm{T}(\ell_2)$ in SR-ewk-low-$E_\mathrm{T}^\mathrm{miss}$-high-$\Delta m$ for the individual $m_{\ell\ell}$ bins. The bottom panel shows a significance scan with dotted (dashed) lines indicating the significance of a potential upper (lower) requirement at the shown position.

Figure D.7: N-1 plots of $m_T^{\ell_1}$ in SR-ewk-low-E_T^{miss}-high-Δm for the individual $m_{\ell\ell}$ bins. The blue arrows indicate the location and direction of the requirements on the variable shown. The bottom panel shows a significance scan with dotted (dashed) lines indicating the significance of a potential upper (lower) requirement at the shown position.
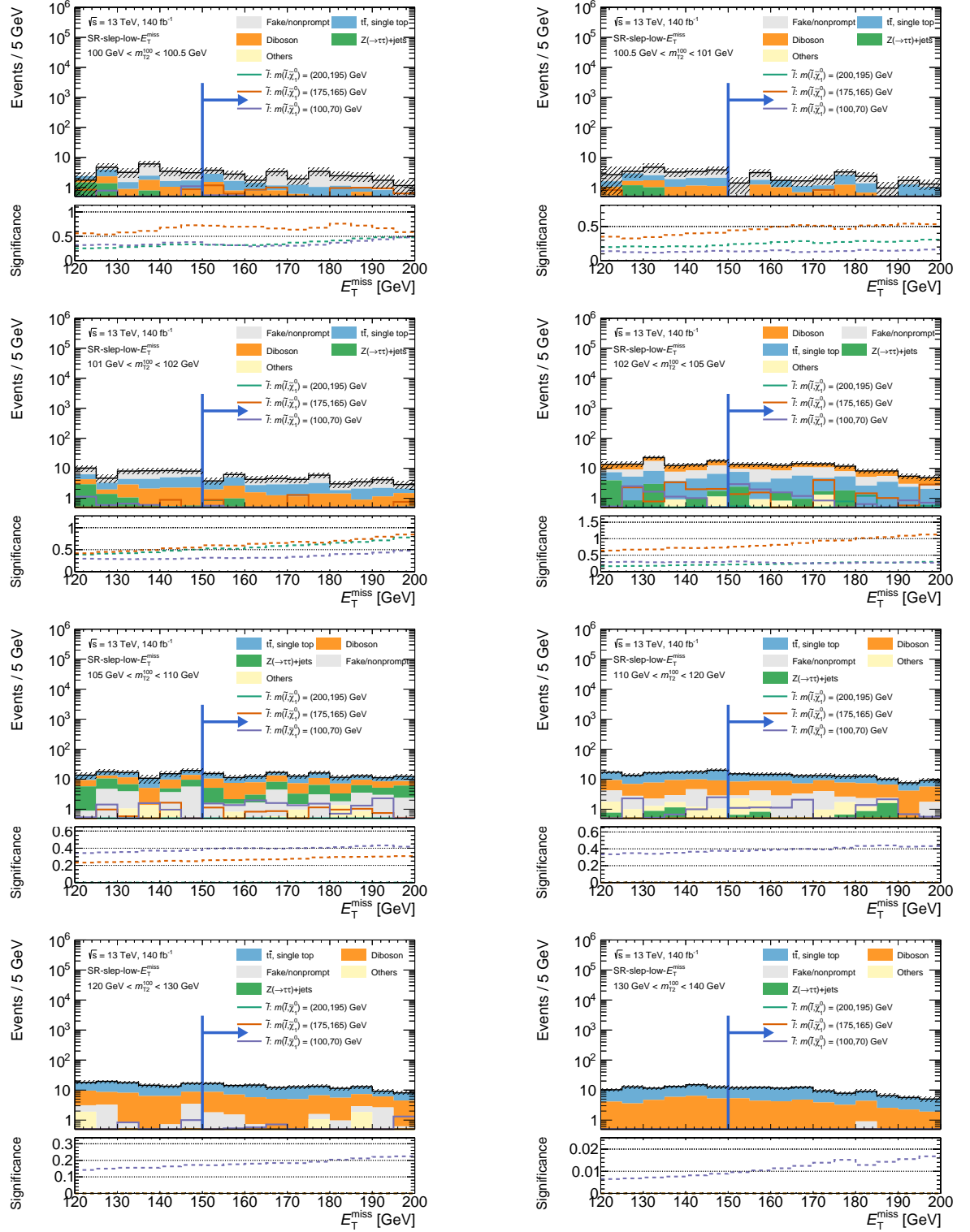
Figure D.8: N-1 plots of E_T^{miss} in SR-slep-low-E_T^{miss} for all m_{T2} bins. The last bin contains the overflow. The blue arrow indicates the location and direction of the requirement on the variable shown. The bottom panel shows a significance scan with dashed lines indicating the significance of a potential lower requirement at the shown position.
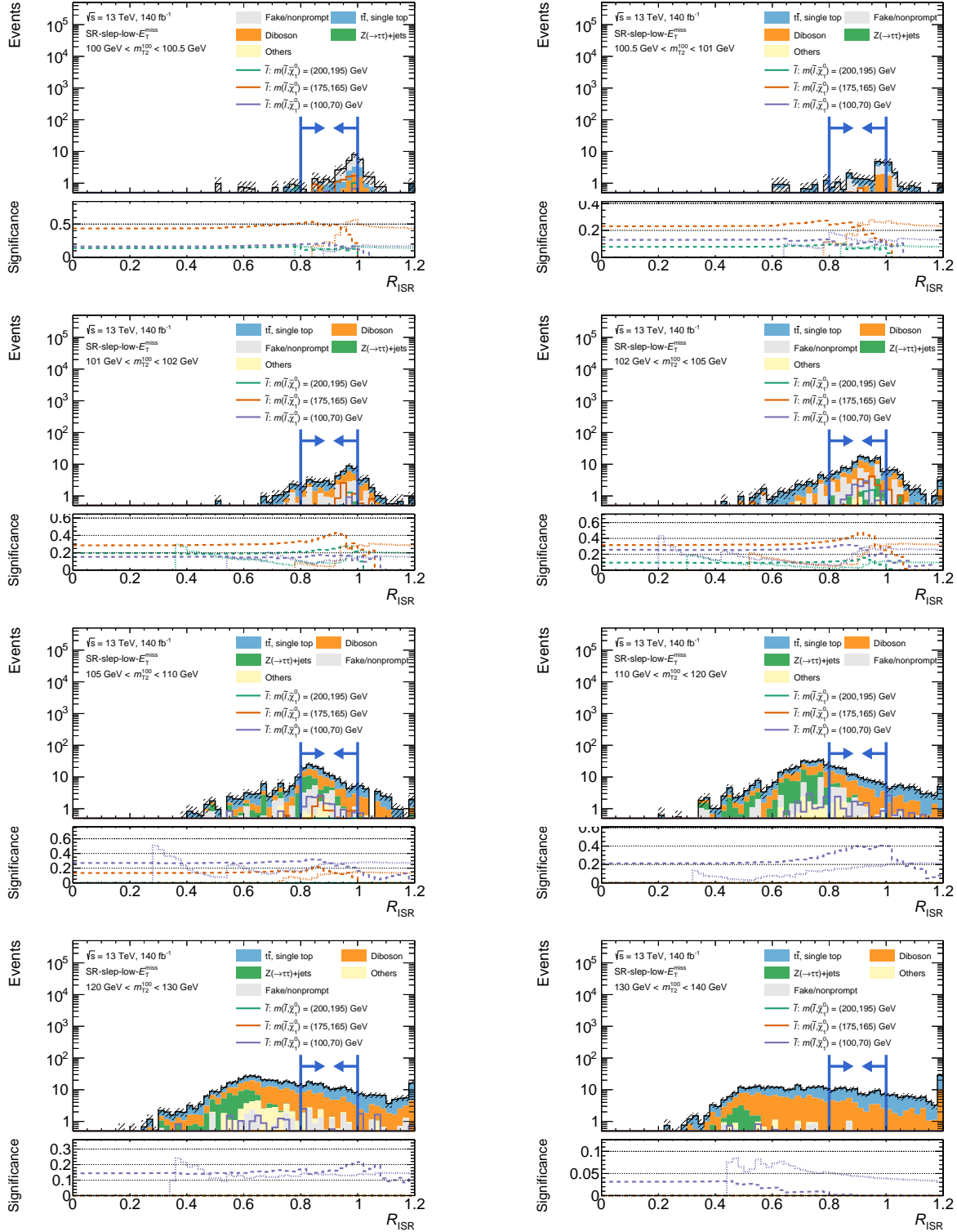
Figure D.9: N-1 plots of R_{ISR} in SR-slep-low-$E_{\mathrm{T}}^{\mathrm{miss}}$ for all m_{T2} bins. The last bin contains the overflow. The blue arrows indicates the location and direction of the requirement on the variable shown. The bottom panel shows a significance scan with dashed (dotted) lines indicating the significance of a potential lower (upper) requirement at the shown position.
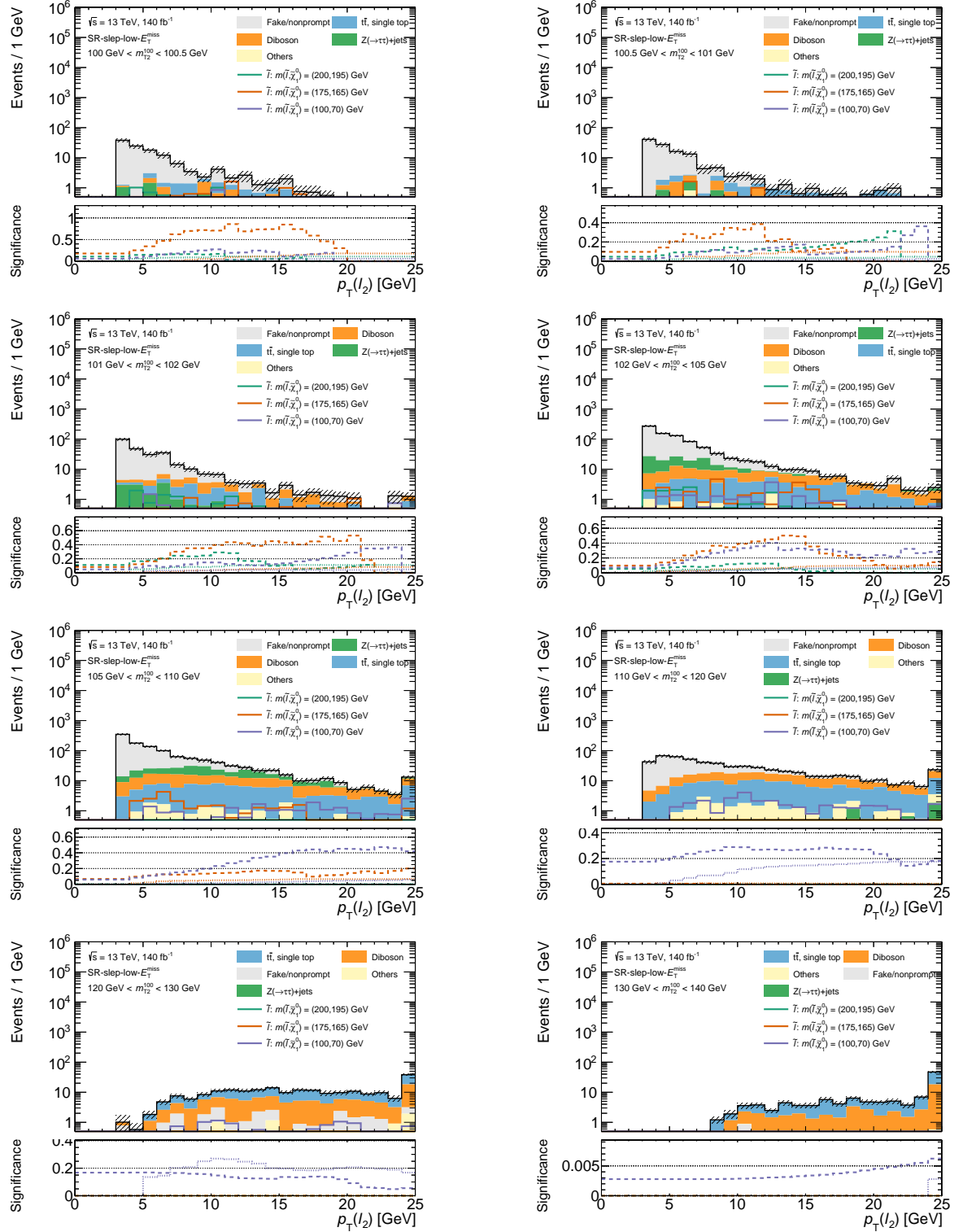
Figure D.10: N-1 plots of $p_\mathrm{T}(\ell_2)$ in SR-slep-low-$E_\mathrm{T}^\mathrm{miss}$ for all m_T2 bins. The last bin contains the overflow. The bottom panel shows a significance scan with dashed (dotted) lines indicating the significance of a potential lower (upper) requirement at the shown position.

Region	CR-top-ewk-low-$E_{\mathrm{T}}^{\mathrm{miss}}$	CR-tau-ewk-low-$E_{\mathrm{T}}^{\mathrm{miss}}$	CR-VV-ewk-low-$E_{\mathrm{T}}^{\mathrm{miss}}$
Observed	6164	2247	721
Fitted SM events	6163.90 ± 78.51	2247.00 ± 47.74	721.01 ± 26.92
Fake/nonprompt	231.23 ± 79.68	100.59 ± 71.43	68.12 ± 18.74
$t\bar{t}$, single top	5841.20 ± 114.27	83.80 ± 9.33	286.10 ± 37.77
Diboson	43.98 ± 11.69	73.36 ± 18.36	263.71 ± 63.98
$Z(\to \tau\tau)$+jets	21.41 ± 3.95	1955.98 ± 91.61	28.26 ± 8.80
Others	26.08 ± 12.94	33.27 ± 16.86	74.82 ± 38.22
Pre-fit SM events	6068.65 ± 994.71	2263.67 ± 276.29	822.30 ± 117.09
Fake/nonprompt	231.16 ± 80.13	100.59 ± 71.85	68.12 ± 18.87
$t\bar{t}$, single top	5728.30 ± 991.25	82.18 ± 20.51	280.59 ± 78.59
Diboson	61.82 ± 15.24	103.13 ± 19.64	370.68 ± 73.50
$Z(\to \tau\tau)$+jets	21.29 ± 5.69	1944.51 ± 264.26	28.09 ± 9.07
Others	26.08 ± 13.04	33.26 ± 16.99	74.82 ± 38.51

Table D.1: Pre-and post-fit event yields in the low-$E_{\mathrm{T}}^{\mathrm{miss}}$ electroweakino CRs for a background-only fit. Uncertainties in the background estimates combine statistical and systematic uncertainties.

D.2 Background Estimation

The following sections contain tables with event yields in the CRs, as well as additional plots for the low-$E_{\mathrm{T}}^{\mathrm{miss}}$ CRs.

D.2.1 Event Yields in Control Regions

Tables D.1 and D.2 present the event yields in the low-$E_{\mathrm{T}}^{\mathrm{miss}}$ electroweakino and slepton CRs, respectively. Both the pre- and post-fit yields after a background-only fit are shown, including all systematic uncertainties.

D.2.2 Additional Control Region Plots

Figures D.11 to D.13 show additional kinematic distributions of variables relevant for the analysis in the low-$E_{\mathrm{T}}^{\mathrm{miss}}$ electroweakino CRs. Likewise, Figures D.14 to D.16 depict kinematic distributions in the low-$E_{\mathrm{T}}^{\mathrm{miss}}$ slepton CRs. The plots do not include systematic uncertainties, such that the uncertainties bands represent only the statistical uncertainties. However, the MC estimates for top, $Z \to \tau\tau$ and diboson include the respective normalization parameters listed in Table 5.7.
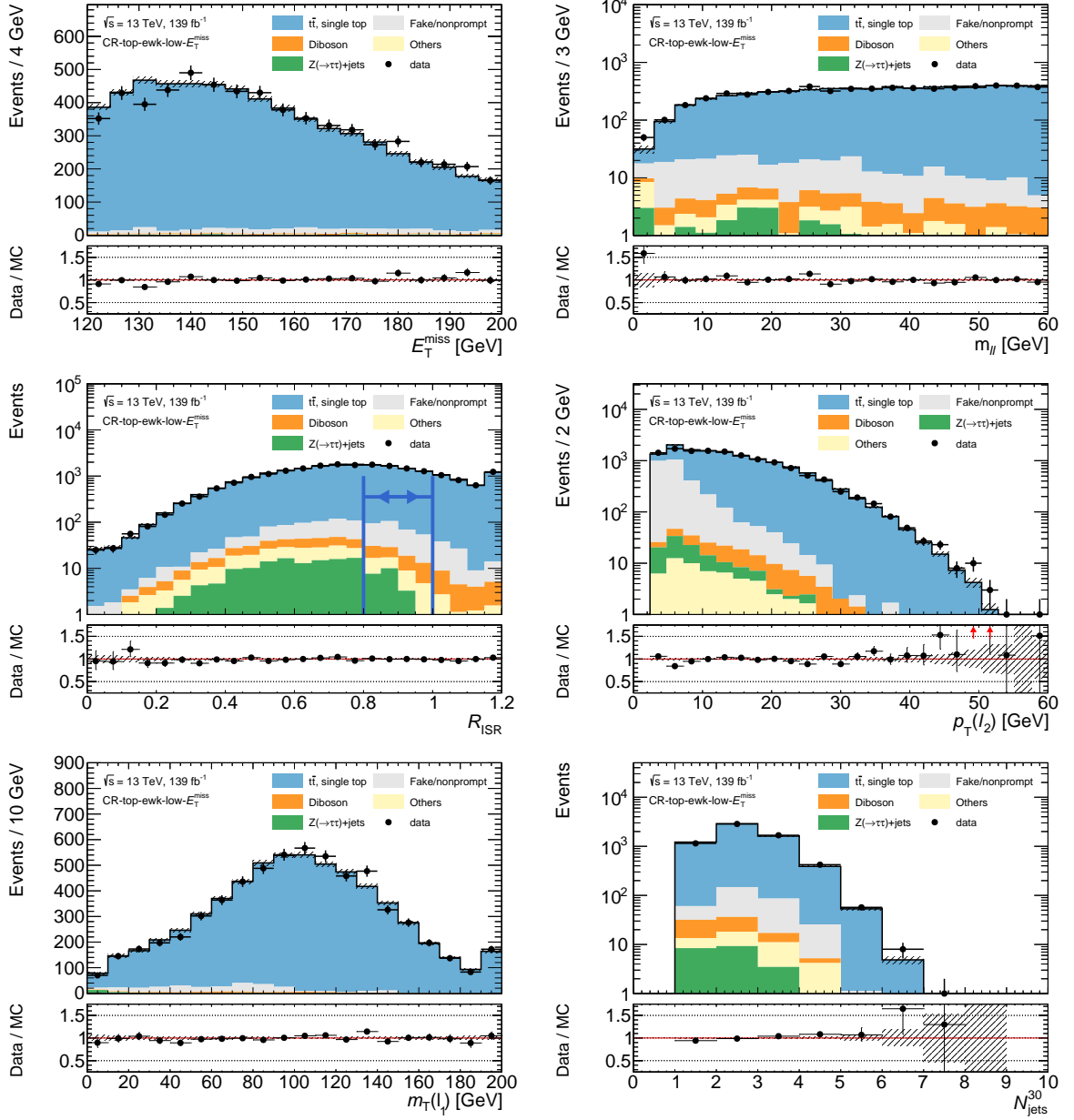
Figure D.11: Examples of kinematic distributions showing the data as well as the expected background in CR-top-ewk-low-E_T^{miss}. The full region definition is applied, except for the requirement imposed on the variable being plotted. The blue arrow indicates the requirement The first (last) bin contains the underflow (overflow). The uncertainty bands show only the statistical uncertainty.
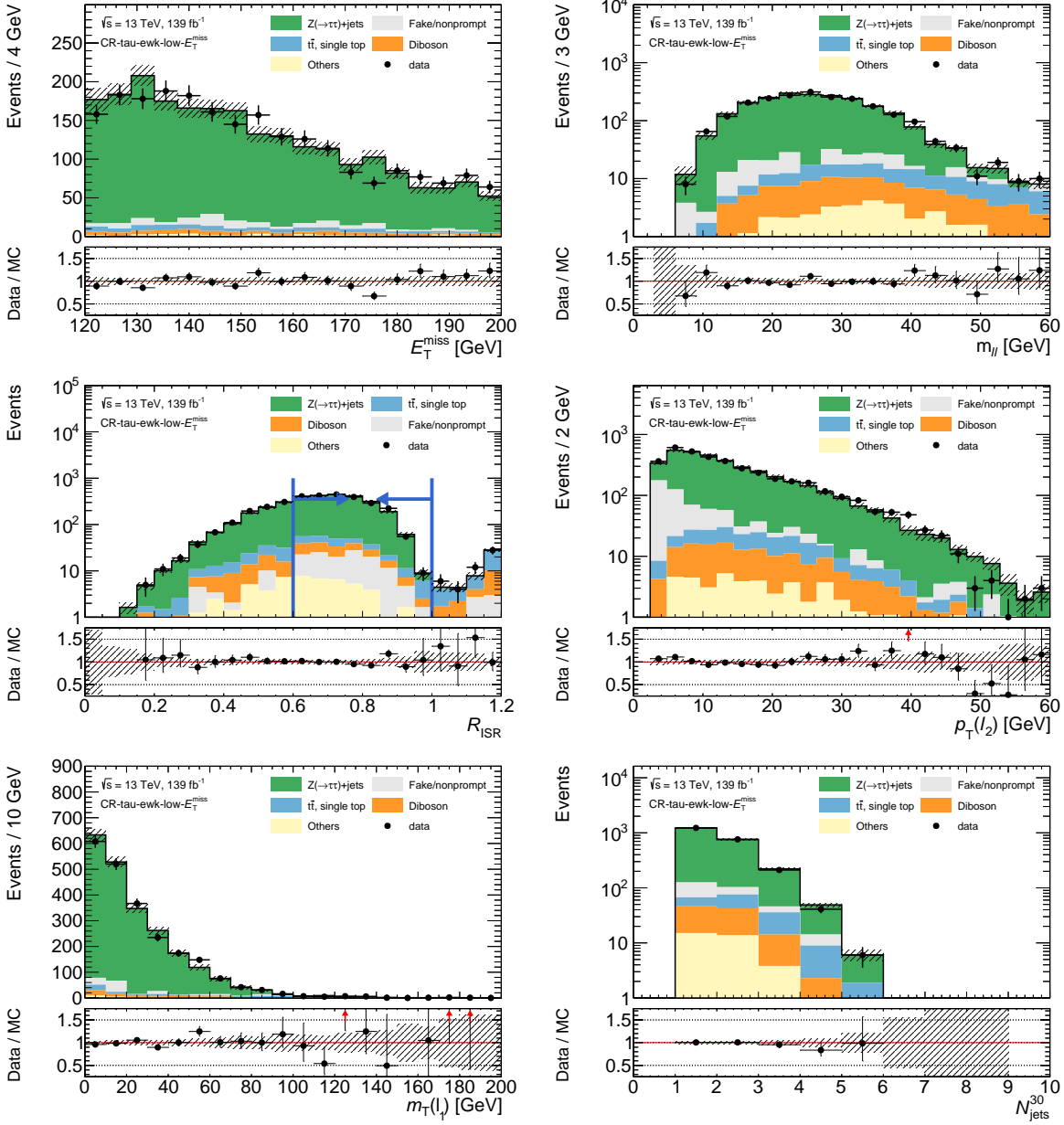
Figure D.12: Examples of kinematic distributions showing the data as well as the expected background in CR-tau-ewk-low-E_T^{miss}. The full region definition is applied, except for the requirement imposed on the variable being plotted. The blue arrow indicates the requirement The first (last) bin contains the underflow (overflow). The uncertainty bands show only the statistical uncertainty.
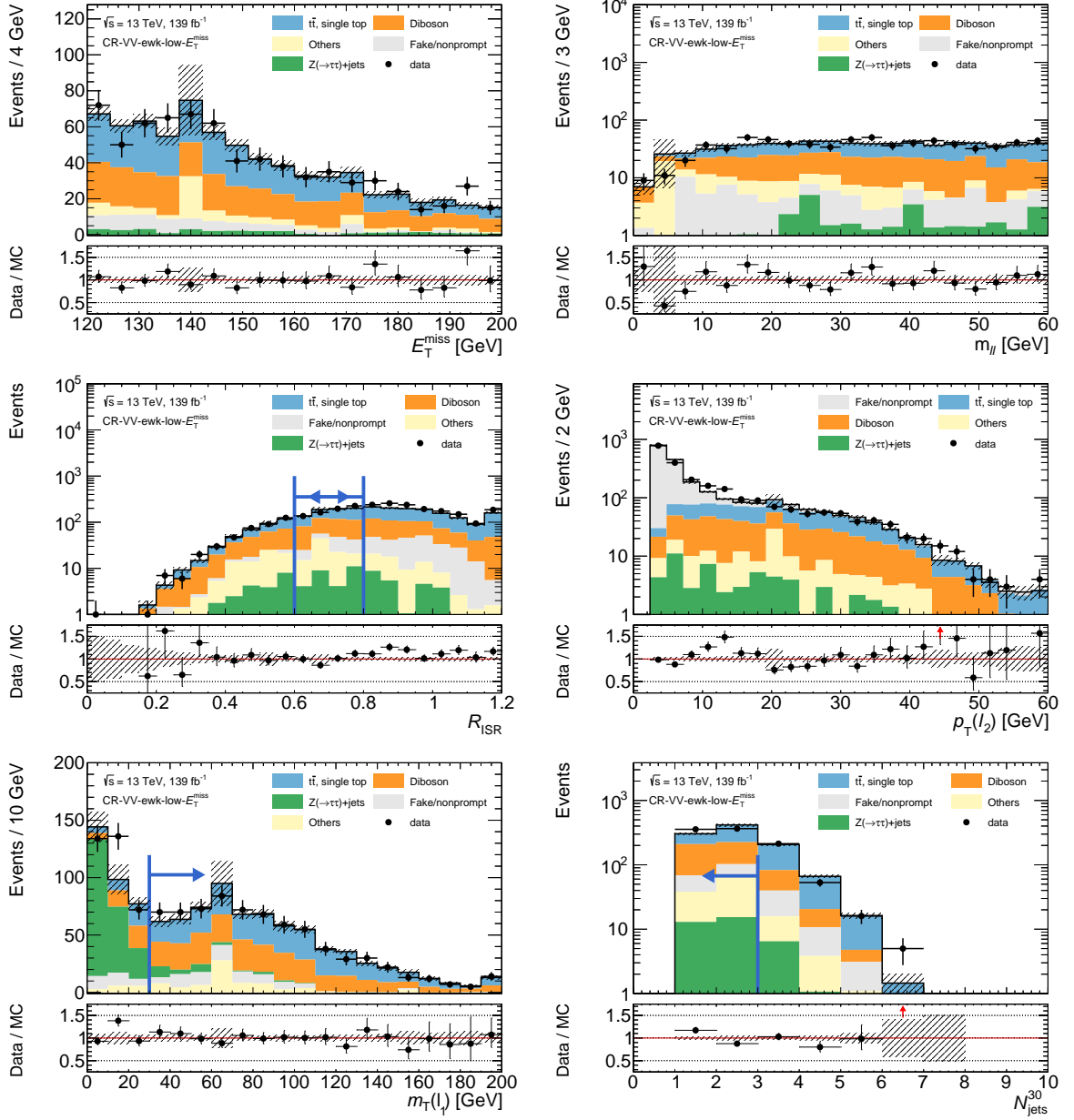
Figure D.13: Examples of kinematic distributions showing the data as well as the expected background in CR-VV-ewk-low-E_T^{miss}. The full region definition is applied, except for the requirement imposed on the variable being plotted. The blue arrow indicates the requirement The first (last) bin contains the underflow (overflow). The uncertainty bands show only the statistical uncertainty.

Figure D.14: Examples of kinematic distributions showing the data as well as the expected background in CR-top-slep-low-E_T^{miss}. The full region definition is applied, except for the requirement imposed on the variable being plotted. The blue arrow indicates the requirement The first (last) bin contains the underflow (overflow). The uncertainty bands show only the statistical uncertainty.
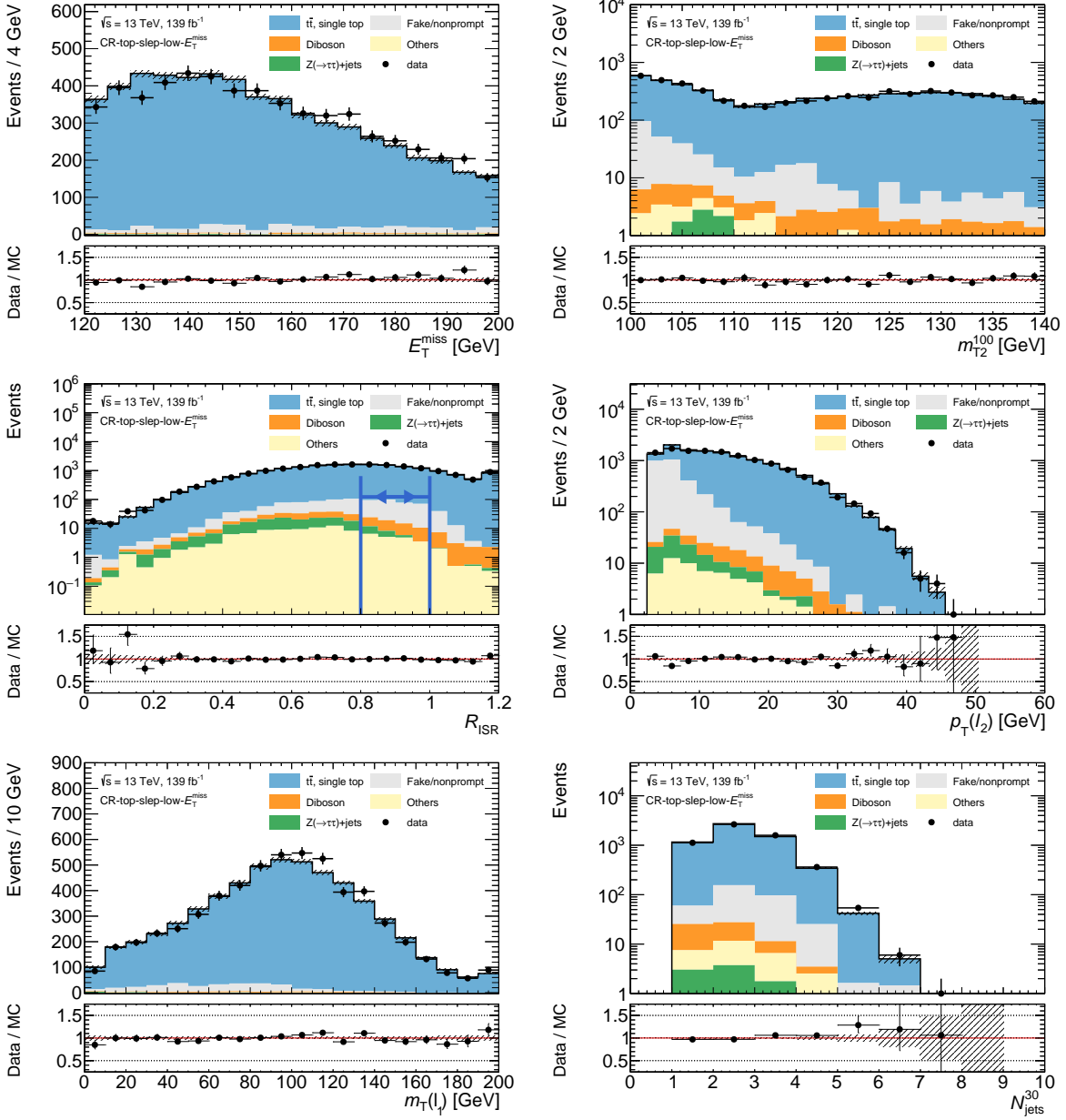
Figure D.15: Examples of kinematic distributions showing the data as well as the expected background in CR-tau-slep-low-E_T^{miss}. The full region definition is applied, except for the requirement imposed on the variable being plotted. The blue arrow indicates the requirement The first (last) bin contains the underflow (overflow). The uncertainty bands show only the statistical uncertainty.
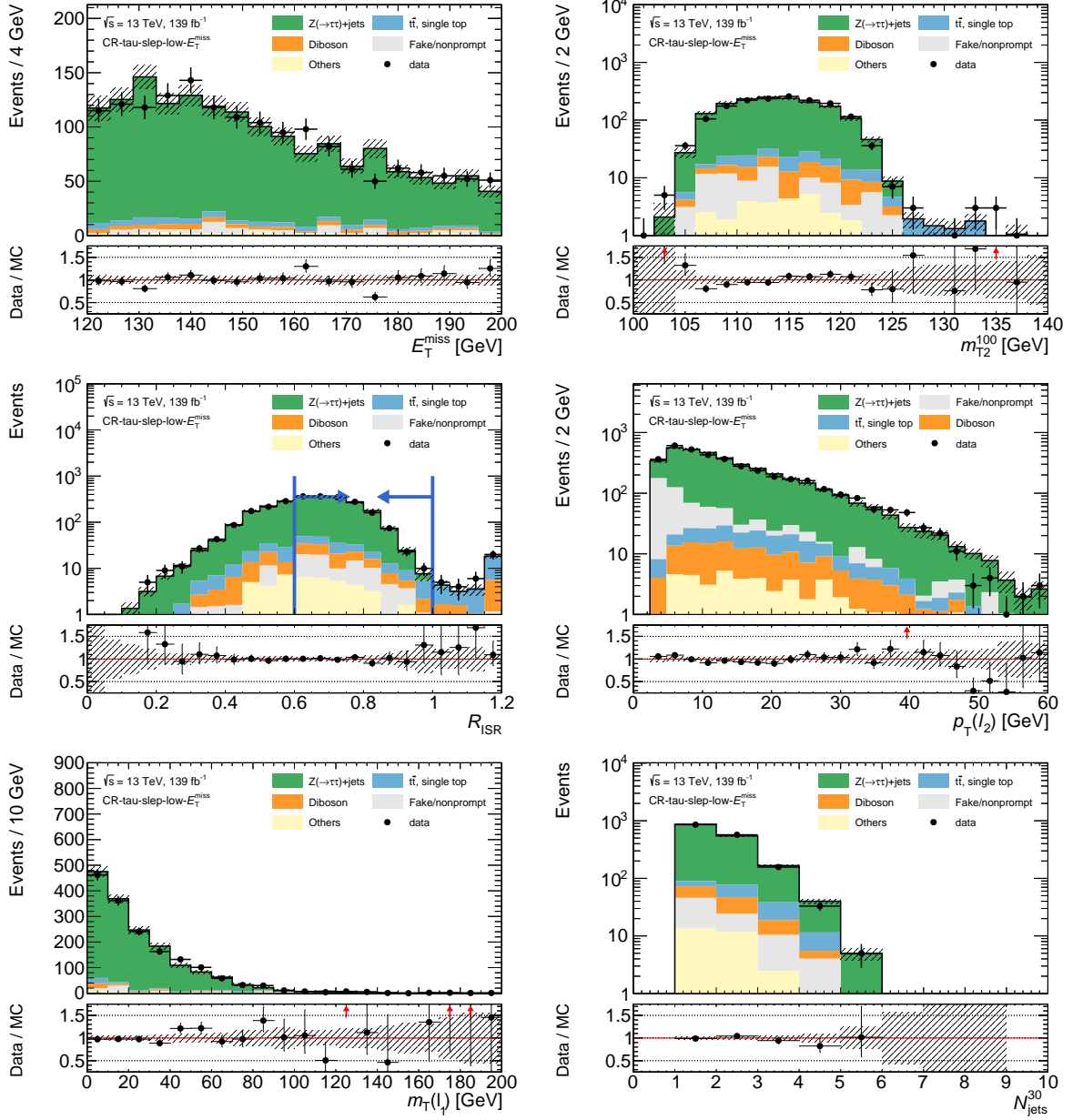
Figure D.16: Examples of kinematic distributions showing the data as well as the expected background in CR-VV-slep-low-E_T^{miss}. The full region definition is applied, except for the requirement imposed on the variable being plotted. The blue arrow indicates the requirement The first (last) bin contains the underflow (overflow). The uncertainty bands show only the statistical uncertainty.
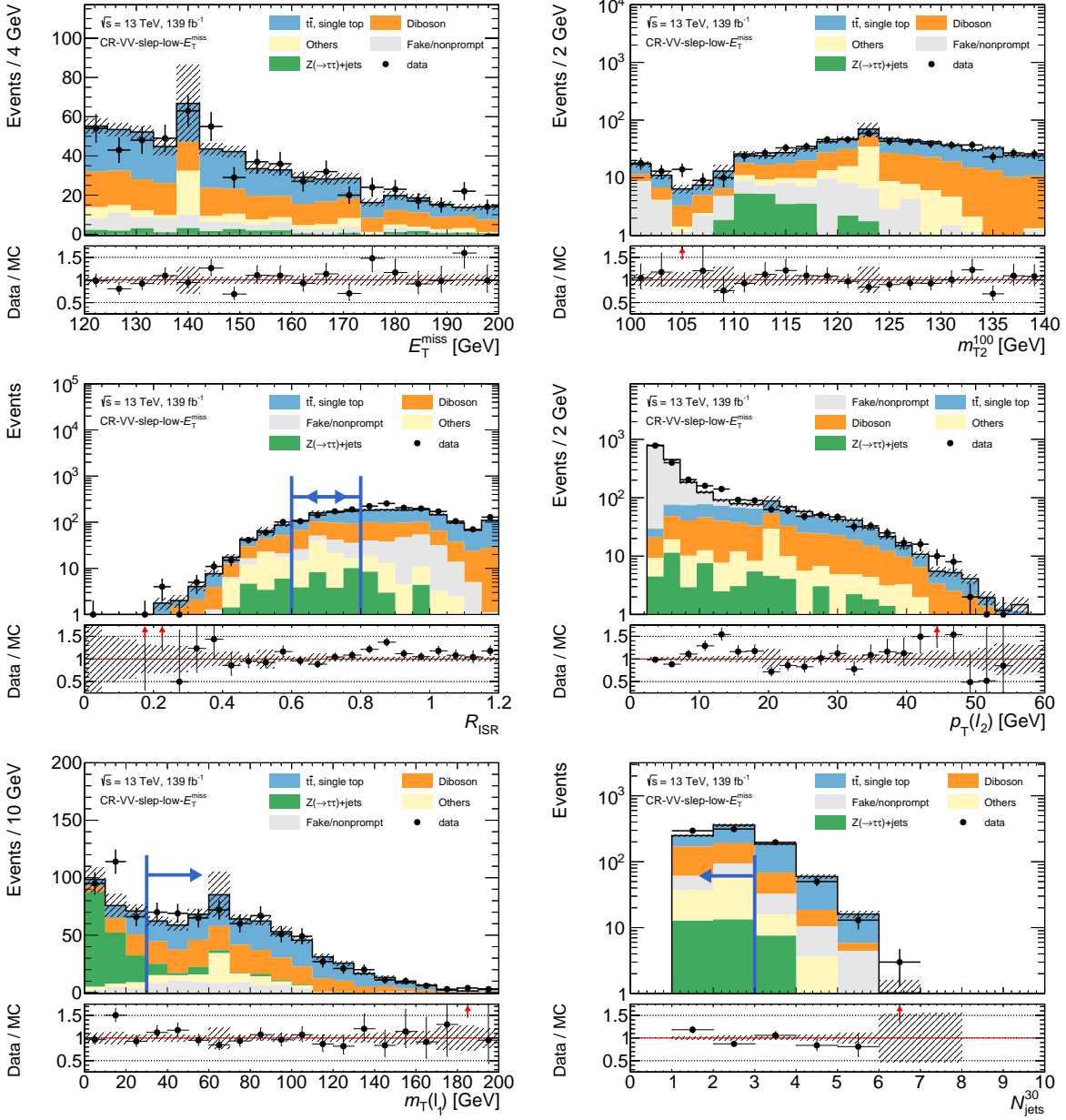
Region	CR-top-slep-low-$E_{\mathrm{T}}^{\mathrm{miss}}$	CR-tau-slep-low-$E_{\mathrm{T}}^{\mathrm{miss}}$	CR-VV-slep-low-$E_{\mathrm{T}}^{\mathrm{miss}}$
Observed	5779	1621	608
Fitted SM events	5778.98 ± 76.01	1620.90 ± 40.81	608.00 ± 24.72
Fake/nonprompt	272.62 ± 87.87	55.74 ± 49.67	61.88 ± 16.36
$t\bar{t}$, single top	5437.65 ± 118.74	74.41 ± 8.49	248.05 ± 32.44
Diboson	39.99 ± 12.41	59.74 ± 17.82	205.27 ± 59.37
Z($\to \tau\tau$)+jets	8.89 ± 3.13	1402.91 ± 70.42	25.96 ± 7.53
Others	19.82 ± 10.04	28.10 ± 14.80	66.85 ± 35.51
Pre-fit SM events	5736.50 ± 931.26	1599.02 ± 196.19	706.18 ± 102.62
Fake/nonprompt	272.61 ± 88.46	55.76 ± 49.98	61.88 ± 16.47
$t\bar{t}$, single top	5375.66 ± 926.87	73.56 ± 18.49	245.22 ± 69.31
Diboson	59.84 ± 14.00	89.42 ± 17.26	307.22 ± 60.84
Z($\to \tau\tau$)+jets	8.57 ± 3.53	1352.19 ± 186.91	25.02 ± 7.73
Others	19.82 ± 10.11	28.10 ± 14.91	66.85 ± 35.78

Table D.2: Pre-and post-fit event yields in the low-$E_{\mathrm{T}}^{\mathrm{miss}}$ slepton CRs for a background-only fit. Uncertainties in the background estimates combine statistical and systematic uncertainties.

D.3 Event Yields in low-$E_{\mathrm{T}}^{\mathrm{miss}}$ Signal Regions

The observed and expected event yields for the low-$E_{\mathrm{T}}^{\mathrm{miss}}$ electroweakino SR targeting low mass splittings, SR-ewk-low-$E_{\mathrm{T}}^{\mathrm{miss}}$-low-$\Delta m$, are shown in Tables D.3 and D.4 for $\mu\mu$ and ee events, respectively, and split into the individual $m_{\ell\ell}$ bins. Likewise, the observed and expected yields for SR-ewk-low-$E_{\mathrm{T}}^{\mathrm{miss}}$-high-$\Delta m$ are shown in Tables D.5 and D.6. The $\mu\mu$ and ee event yields for the low-$E_{\mathrm{T}}^{\mathrm{miss}}$ slepton SR are shown in Tables D.7 and D.8, respectively. The expected SM yields have been derived by a background-only fit, that include the associated SRs as constraining regions.

SR bin $m_{\ell\ell}$ [GeV]	[1,2]	[2,3]	[3,5]	[5,10]	[10,20]	[20,30]
Observed	16	8	6	41	59	21
Fitted SM events	14.4 ± 3.1	6.6 ± 1.9	4.9 ± 1.9	33 ± 4	50 ± 5	18.4 ± 3.2
Fake/nonprompt	6 ± 4	4.5 ± 1.9	3.3 ± 2.1	24 ± 4	43 ± 6	18.0 ± 3.1
$t\bar{t}$, single top	$0.01^{+0.06}_{-0.01}$	$0.01^{+0.06}_{-0.01}$	$0.01^{+0.05}_{-0.01}$	$0.16^{+0.18}_{-0.16}$	0.22 ± 0.06	0.15 ± 0.15
Diboson	2.3 ± 0.8	0.9 ± 0.4	0.77 ± 0.26	2.7 ± 1.0	0.82 ± 0.25	0.17 ± 0.09
$Z(\to \tau\tau)$+jets	5.4 ± 3.1	1.3 ± 0.6	0.8 ± 0.8	5.7 ± 2.0	5.5 ± 1.9	$0.02^{+0.28}_{-0.02}$
Others	0.40 ± 0.24	$0.000^{+0.005}_{-0.000}$	0.031 ± 0.029	0.016 ± 0.011	0.6 ± 0.4	0.0 ± 0.0
Pre-fit SM events	12 ± 6	5.9 ± 3.0	$2.9^{+3.1}_{-2.9}$	24 ± 6	41 ± 8	15 ± 4
Fake/nonprompt	6 ± 4	3.5 ± 2.8	$1.9^{+3.1}_{-1.9}$	17 ± 5	33 ± 7	15 ± 4
$t\bar{t}$, single top	$0.00^{+0.05}_{-0.00}$	$0.00^{+0.05}_{-0.00}$	$0.00^{+0.05}_{-0.00}$	$0.08^{+0.11}_{-0.08}$	0.20 ± 0.07	$0.09^{+0.10}_{-0.09}$
Diboson	2.5 ± 1.0	1.1 ± 0.6	0.87 ± 0.32	2.9 ± 1.1	0.92 ± 0.30	0.20 ± 0.10
$Z(\to \tau\tau)$+jets	3.3 ± 2.8	1.2 ± 0.6	$0.1^{+0.4}_{-0.1}$	4.1 ± 1.9	5.1 ± 2.3	$0.00^{+0.25}_{-0.00}$
Others	0.56 ± 0.33	0.012 ± 0.008	$0.04^{+0.05}_{-0.04}$	0.016 ± 0.012	0.8 ± 0.5	0.0 ± 0.0

Table D.3: Observed and expected yields in SR-ewk-low-E_T^{miss}-low-Δm for $\mu\mu$ events in the individual $m_{\ell\ell}$ bins using a background-only fit in which the SRs are added as constraining regions. Uncertainties in the background estimates combine statistical and systematic uncertainties.

SR bin $m_{\ell\ell}$ [GeV]	[3,5]	[5,10]	[10,20]	[20,30]
Observed	0	4	11	4
Fitted SM events	0.15 ± 0.10	4.7 ± 1.5	7.1 ± 1.7	2.0 ± 0.7
Fake/nonprompt	$0.000^{+0.007}_{-0.000}$	4.1 ± 1.5	6.7 ± 1.8	1.1 ± 0.7
$t\bar{t}$, single top	$0.00^{+0.04}_{-0.00}$	$0.000^{+0.033}_{-0.000}$	$0.01^{+0.06}_{-0.01}$	0.28 ± 0.16
Diboson	0.14 ± 0.08	$0.06^{+0.08}_{-0.06}$	0.24 ± 0.24	$0.05^{+0.19}_{-0.05}$
$Z(\to \tau\tau)$+jets	$0.000^{+0.015}_{-0.000}$	$0.5^{+0.8}_{-0.5}$	$0.1^{+0.4}_{-0.1}$	$0.5^{+0.6}_{-0.5}$
Others	$0.000^{+0.004}_{-0.000}$	0.0 ± 0.0	0.0 ± 0.0	0.0 ± 0.0
Pre-fit SM events	$0.17^{+0.31}_{-0.17}$	4.4 ± 2.6	4.1 ± 1.9	0.9 ± 0.7
Fake/nonprompt	$0.00^{+0.16}_{-0.00}$	3.3 ± 1.7	3.8 ± 1.9	$0.6^{+0.7}_{-0.6}$
$t\bar{t}$, single top	$0.00^{+0.05}_{-0.00}$	$0.00^{+0.05}_{-0.00}$	$0.00^{+0.05}_{-0.00}$	0.22 ± 0.16
Diboson	0.13 ± 0.09	$0.14^{+0.17}_{-0.14}$	0.29 ± 0.24	$0.00^{+0.13}_{-0.00}$
$Z(\to \tau\tau)$+jets	$0.00^{+0.25}_{-0.00}$	$1.0^{+1.8}_{-1.0}$	$0.00^{+0.25}_{-0.00}$	$0.00^{+0.25}_{-0.00}$
Others	$0.000^{+0.006}_{-0.000}$	0.0 ± 0.0	0.0 ± 0.0	0.0 ± 0.0

Table D.4: Observed and expected yields in SR-ewk-low-E_T^{miss}-low-Δm for ee events in the individual $m_{\ell\ell}$ bins using a background-only fit in which the SRs are added as constraining regions. Uncertainties in the background estimates combine statistical and systematic uncertainties.

SR bin $m_{\ell\ell}$ [GeV]	[1,2]	[2,3]	[3,5]	[5,10]	[10,20]	[20,30]	[30,40]	[40,60]
Observed	9	7	7	12	17	18	16	44
Fitted SM events	14.5 ± 2.8	7.5 ± 1.9	5.7 ± 1.8	11.7 ± 1.9	14.9 ± 2.2	16.6 ± 2.3	15.2 ± 2.0	35.4 ± 3.0
Fake/nonprompt leptons	7.7 ± 2.2	$0.00^{+0.12}_{-0.00}$	$0.02^{+0.24}_{-0.02}$	2.7 ± 1.3	5.1 ± 1.9	2.7 ± 1.7	2.9 ± 1.7	4.8 ± 2.1
$t\bar{t}$, single top	$0.00^{+0.04}_{-0.00}$	0.26 ± 0.07	$0.01^{+0.06}_{-0.01}$	1.3 ± 0.4	3.3 ± 0.7	5.1 ± 1.1	7.0 ± 1.0	17.8 ± 2.2
Diboson	4.6 ± 1.6	1.8 ± 0.5	3.0 ± 0.9	4.8 ± 1.2	4.3 ± 1.0	4.8 ± 1.1	4.7 ± 1.0	9.5 ± 1.9
$Z(\to \tau\tau)$+jets	1.8 ± 0.6	4.7 ± 1.5	2.3 ± 1.8	2.5 ± 1.1	1.4 ± 0.9	2.6 ± 1.0	$0.01^{+0.27}_{-0.01}$	1.6 ± 0.6
Others	0.4 ± 0.4	0.8 ± 0.5	0.39 ± 0.24	0.39 ± 0.25	0.9 ± 0.5	1.5 ± 0.8	0.63 ± 0.35	1.7 ± 1.0
Pre-fit SM events	20 ± 4	8.3 ± 3.2	6 ± 4	13.3 ± 3.2	16 ± 4	18 ± 4	16.1 ± 2.9	36 ± 6
Fake/nonprompt leptons	9.3 ± 2.5	$0.4^{+1.2}_{-0.4}$	$0.00^{+0.21}_{-0.00}$	2.5 ± 1.2	4.0 ± 1.8	2.1 ± 1.4	2.4 ± 1.5	3.4 ± 1.7
$t\bar{t}$, single top	$0.00^{+0.05}_{-0.00}$	0.26 ± 0.07	$0.00^{+0.05}_{-0.00}$	1.0 ± 0.5	3.1 ± 1.0	4.9 ± 1.7	7.3 ± 1.8	17 ± 4
Diboson	7.1 ± 2.5	2.3 ± 0.9	3.4 ± 1.2	5.9 ± 1.7	5.2 ± 1.5	5.9 ± 1.7	5.5 ± 1.4	11.3 ± 2.4
$Z(\to \tau\tau)$+jets	2.3 ± 0.8	4.2 ± 2.2	$2.2^{+3.5}_{-2.2}$	3.3 ± 1.9	2.1 ± 2.0	3.2 ± 1.4	$0.00^{+0.25}_{-0.00}$	1.6 ± 0.7
Others	$1.1^{+1.7}_{-1.1}$	1.0 ± 0.7	0.54 ± 0.31	0.54 ± 0.33	1.3 ± 0.7	2.1 ± 1.1	0.9 ± 0.5	2.5 ± 1.3

Table D.5: Observed and expected yields in SR-ewk-low-$E_{\mathrm{T}}^{\mathrm{miss}}$-high-$\Delta m$ for $\mu\mu$ events in the individual $m_{\ell\ell}$ bins using a background-only fit in which the SRs are added as constraining regions. Uncertainties in the background estimates combine statistical and systematic uncertainties.

SR bin $m_{\ell\ell}$ [GeV]	[3,5]	[5,10]	[10,20]	[20,30]	[30,40]	[40,60]
Observed	7	11	16	16	10	9
Fitted SM events	5.1 ± 1.4	9.2 ± 1.9	16.9 ± 2.6	15.9 ± 2.7	12.6 ± 2.4	17.7 ± 2.6
Fake/nonprompt leptons	1.6 ± 1.0	3.7 ± 1.7	6.4 ± 2.4	6.1 ± 2.5	3.8 ± 2.3	$1.7^{+2.0}_{-1.7}$
$t\bar{t}$, single top	0.014 ± 0.006	0.31 ± 0.20	2.9 ± 0.7	3.4 ± 1.1	4.6 ± 1.1	9.5 ± 1.4
Diboson	1.0 ± 0.5	3.1 ± 1.0	3.5 ± 0.8	2.5 ± 0.7	2.8 ± 0.7	5.1 ± 1.1
$Z(\to \tau\tau)$+jets	2.5 ± 1.0	2.0 ± 0.8	3.5 ± 1.3	3.3 ± 1.1	1.0 ± 0.9	$0.02^{+0.04}_{-0.02}$
Others	$0.013^{+0.020}_{-0.013}$	0.13 ± 0.08	0.55 ± 0.34	0.7 ± 0.4	0.37 ± 0.21	1.3 ± 0.8
Pre-fit SM events	3.9 ± 2.0	8.1 ± 2.6	18 ± 4	14 ± 4	14 ± 4	24 ± 5
Fake/nonprompt leptons	1.1 ± 0.9	2.4 ± 1.5	5.4 ± 2.8	4.8 ± 2.6	4.2 ± 2.6	3.3 ± 2.1
$t\bar{t}$, single top	$0.000^{+0.007}_{-0.000}$	0.31 ± 0.22	2.8 ± 1.0	3.0 ± 1.4	4.5 ± 1.8	11.0 ± 2.8
Diboson	1.0 ± 0.7	3.5 ± 1.3	4.4 ± 1.1	2.8 ± 1.0	3.6 ± 1.0	6.7 ± 1.7
$Z(\to \tau\tau)$+jets	1.8 ± 1.2	1.8 ± 1.1	4.3 ± 1.9	2.3 ± 1.0	$1.5^{+2.0}_{-1.5}$	$0.2^{+0.6}_{-0.2}$
Others	$0.012^{+0.020}_{-0.012}$	0.20 ± 0.11	0.8 ± 0.5	1.2 ± 0.6	0.59 ± 0.31	2.5 ± 1.7

Table D.6: Observed and expected yields in SR-ewk-low-$E_{\mathrm{T}}^{\mathrm{miss}}$-high-$\Delta m$ for ee events in the individual $m_{\ell\ell}$ bins using a background-only fit in which the SRs are added as constraining regions. Uncertainties in the background estimates combine statistical and systematic uncertainties.

SR-bin m_{T2}[GeV]	[100,100.5]	[100.5,101]	[101,102]	[102,105]	[105,110]	[110,120]	[120,130]	[130,140]
Observed	3	6	15	23	37	44	41	28
Fitted SM events	6.1 ± 1.2	4.7 ± 1.0	12.5 ± 1.7	25.1 ± 2.7	39 ± 4	39.5 ± 3.5	34.7 ± 3.0	26.2 ± 2.7
Fake/nonprompt	3.1 ± 1.1	0.7 ± 0.7	4.7 ± 1.4	5.9 ± 1.9	2.5 ± 2.0	3.6 ± 2.0	1.7 ± 1.2	$0.00^{+0.10}_{-0.00}$
$t\bar{t}$, single top	1.7 ± 0.4	2.1 ± 0.5	3.8 ± 0.7	8.5 ± 1.4	13.7 ± 2.5	20.6 ± 3.2	19.0 ± 2.2	17.5 ± 2.2
Diboson	1.10 ± 0.35	1.6 ± 0.4	3.1 ± 1.0	7.2 ± 1.9	9.6 ± 2.7	11.1 ± 2.9	12 ± 4	8.5 ± 2.5
$Z(\to \tau\tau)$+jets	$0.04^{+0.10}_{-0.04}$	$0.1^{+0.5}_{-0.1}$	0.62 ± 0.22	2.5 ± 1.0	9.4 ± 3.5	1.9 ± 1.0	$0.03^{+0.29}_{-0.03}$	$0.02^{+0.26}_{-0.02}$
Others	0.11 ± 0.07	0.18 ± 0.10	0.30 ± 0.17	1.0 ± 0.6	3.5 ± 2.1	2.3 ± 1.2	$2.3^{+3.4}_{-2.3}$	0.16 ± 0.09
Pre-fit SM events	7.2 ± 1.6	5.0 ± 1.4	12.5 ± 2.3	28 ± 5	38 ± 7	38 ± 6	36 ± 6	27 ± 5
Fake/nonprompt	3.7 ± 1.4	0.7 ± 0.7	4.5 ± 1.6	6.2 ± 2.2	2.9 ± 1.9	3.4 ± 2.0	1.6 ± 1.1	$0.00^{+0.10}_{-0.00}$
$t\bar{t}$, single top	1.7 ± 0.5	2.1 ± 0.8	3.5 ± 1.0	8.0 ± 2.1	11.7 ± 3.5	17 ± 5	19 ± 4	16 ± 4
Diboson	1.5 ± 0.4	1.9 ± 0.5	3.6 ± 1.0	9.9 ± 3.0	12.5 ± 3.0	13.9 ± 3.0	15 ± 4	11.0 ± 2.6
$Z(\to \tau\tau)$+jets	$0.17^{+0.22}_{-0.17}$	$0.1^{+0.4}_{-0.1}$	0.61 ± 0.29	2.8 ± 1.4	7.3 ± 3.3	1.3 ± 0.9	$0.00^{+0.25}_{-0.00}$	$0.00^{+0.25}_{-0.00}$
Others	0.12 ± 0.07	0.18 ± 0.10	0.29 ± 0.16	1.1 ± 0.7	3.5 ± 2.5	2.3 ± 1.2	$1.6^{+2.0}_{-1.6}$	0.14 ± 0.10

Table D.7: Observed and expected yields in SR-slep-low-E_T^{miss} for $\mu\mu$ events in the individual m_{T2} bins using a background-only fit in which the SRs are added as constraining regions. Uncertainties in the background estimates combine statistical and systematic uncertainties.

SR-bin m_{T2}[GeV]	[100,100.5]	[100.5,101]	[101,102]	[102,105]	[105,110]	[110,120]	[120,130]	[130,140]
Observed	8	5	15	19	30	24	32	11
Fitted SM events	5.9 ± 1.4	5.5 ± 1.8	11.6 ± 2.1	22.1 ± 3.1	27 ± 4	20.6 ± 2.7	28.1 ± 3.4	18.1 ± 3.2
Fake/nonprompt	2.6 ± 1.2	2.5 ± 1.3	4.7 ± 2.0	9.7 ± 3.0	7.2 ± 3.3	$1.7^{+2.1}_{-1.7}$	3.2 ± 2.3	$0.0^{+2.5}_{-0.0}$
$t\bar{t}$, single top	2.3 ± 1.0	1.9 ± 0.6	4.2 ± 1.6	5.9 ± 1.3	8.0 ± 1.3	8.3 ± 1.7	15.3 ± 3.2	12.6 ± 1.9
Diboson	0.8 ± 0.5	0.51 ± 0.22	2.1 ± 0.7	4.9 ± 1.4	5.9 ± 1.6	8.2 ± 2.3	8.8 ± 2.3	5.4 ± 1.4
$Z(\to \tau\tau)$+jets	$0.06^{+0.35}_{-0.06}$	$0.4^{+1.5}_{-0.4}$	$0.5^{+0.6}_{-0.5}$	$0.02^{+0.14}_{-0.02}$	5.1 ± 2.4	$0.02^{+0.29}_{-0.02}$	$0.02^{+0.28}_{-0.02}$	$0.00^{+0.20}_{-0.00}$
Others	0.09 ± 0.06	0.09 ± 0.05	0.21 ± 0.12	1.5 ± 0.8	$0.9^{+1.2}_{-0.9}$	2.3 ± 1.8	0.8 ± 0.4	0.10 ± 0.06
Pre-fit SM events	4.3 ± 1.5	5.3 ± 2.4	9.5 ± 2.8	23 ± 5	28 ± 7	20 ± 4	25 ± 5	20 ± 4
Fake/nonprompt	1.9 ± 1.2	2.4 ± 1.4	3.3 ± 1.9	9 ± 4	5.4 ± 3.3	$1.4^{+1.6}_{-1.4}$	2.2 ± 1.8	$1.0^{+1.2}_{-1.0}$
$t\bar{t}$, single top	1.3 ± 0.7	1.7 ± 0.7	3.0 ± 1.4	5.3 ± 1.7	8.7 ± 2.4	6.3 ± 1.9	11.9 ± 3.5	11.6 ± 3.0
Diboson	0.9 ± 0.5	0.67 ± 0.25	2.5 ± 0.7	6.5 ± 1.7	7.5 ± 1.9	9.7 ± 2.3	10.4 ± 2.4	7.7 ± 1.9
$Z(\to \tau\tau)$+jets	$0.00^{+0.25}_{-0.00}$	$0.4^{+1.7}_{-0.4}$	$0.5^{+0.6}_{-0.5}$	$0.2^{+1.1}_{-0.2}$	5.1 ± 3.2	$0.00^{+0.25}_{-0.00}$	$0.00^{+0.25}_{-0.00}$	$0.00^{+0.25}_{-0.00}$
Others	0.09 ± 0.06	0.09 ± 0.06	0.22 ± 0.13	1.7 ± 0.9	$1.2^{+1.8}_{-1.2}$	2.6 ± 2.1	0.8 ± 0.4	0.11 ± 0.06

Table D.8: Observed and expected yields in SR-slep-low-E_T^{miss} for ee events in the individual m_{T2} bins using a background-only fit in which the SRs are added as constraining regions. Uncertainties in the background estimates combine statistical and systematic uncertainties.

Acknowledgements

List of Abbreviations

pp proton–proton

AF any flavor

BSM beyond the Standard Model

CL confidence level

CP charge conjugation and parity symmetry

CR control region

CSC Cathode Strip Chamber

CT calorimeter-tagged

DAQ data acquisition system

DF different flavor

DM Dark Matter

FCC Future Circular Collider

FSR final state radiation

HLT high-level trigger

IBL Insertable B-Layer

ID Inner Detector

IP interaction point

ISR initial state radiation

JER jet energy resolution

JES jet energy scale

JVT jet vertex tagger

L1 level-1

LAr liquid argon

LHC Large Hadron Collider

LO leading order

LSP lightest supersymmetric particle

MC Monte Carlo

MDT Monitored Drift Tube

ME matrix element

MS Muon Spectrometer

MSSM minimal supersymmetric extension of the Standard Model

NLL next-to-leading-logarithm

NLO next-to-leading order

OS opposite sign

p.d.f. probability density function

PDF parton distribution function

PEB partial event building

QCD quantum chromodynamics

QED quantum electrodynamics

RF radio frequency

RJR Recursive Jigsaw Reconstruction

ROI Region of Interest

RPC Resistive Plate Chamber

SCT Silicon Microstrip Tracker

SF same flavor

SM Standard Model

SR signal region

SS same sign

SUSY supersymmetry

TGC Thin Gap Chamber

TRT Transition Radiation Tracker

VEV vacuum expectation value

VR validation region

WP working point

Bibliography

[1]   G. Arnison et al., *Experimental Observation of Isolated Large Transverse Energy Elec-trons with Associated Missing Energy at $\sqrt{s} = GeV\,540$*, Phys. Lett. **B122** (1983) 103.

[2]   G. Arnison et al., *Experimental Observation of Lepton Pairs of Invariant Mass Around 95 GeV/c^2 at the CERN SPS Collider*, Phys. Lett. **B126** (1983) 398.

[3]   Steven Weinberg, *A Model of Leptons*, Phys. Rev. Lett. **19** (1967) 1264.

[4]   ATLAS Collaboration, *Observation of a new particle in the search for the Standard Model Higgs boson with the ATLAS detector at the LHC*, Phys. Lett. B **716** (2012) 1, arXiv: 1207.7214 [hep-ex].

[5]   CMS Collaboration, *Observation of a new boson at a mass of 125 GeV with the CMS experiment at the LHC*, Phys. Lett. B **716** (2012) 30, arXiv: 1207.7235 [hep-ex].

[6]   C. N. Yang and R. L. Mills, *Conservation of Isotopic Spin and Isotopic Gauge In-variance*, Phys. Rev. **96** (1 1954) 191, URL: https://link.aps.org/doi/10.1103/PhysRev.96.191.

[7]   Michael E. Peskin and Daniel V. Schroeder, *An Introduction to quantum field theory*, Addison-Wesley, 1995, URL: http://www.slac.stanford.edu/~mpeskin/QFT.html.

[8]   Roman Pasechnik and Michal umbera, *Phenomenological Review on QuarkGluon Plasma: Concepts vs. Observations*, Universe **3** (2017) 7, arXiv: 1611.01533 [hep-ph].

[9]   M. Tanabashi et al., *Review of Particle Physics*, Phys. Rev. **D98** (2018) 030001.

[10] Ian C. Brock and Thomas Schörner-Sadenius, *Physics at the Terascale*, Wiley-VCH Verlag, 2011.

[11] Christopher C Tully, *Elementary particle physics in a nutshell*, Princeton Univ. Press, 2011, URL: https://cds.cern.ch/record/1417476.

[12] Emmy Noether, *Invariant variation problems*, Transport Theory and Statistical Physics **1** (1971) 186.

[13] David Griffiths, *Introduction to elementary particles*, Wiley-VCH, 2008.

[14] S. L. Glashow, *Partial Symmetries of Weak Interactions*, Nucl. Phys. **22** (1961) 579.

[15] M. Gell-Mann, *The interpretation of the new particles as displaced charge multiplets*, Nuovo Cim. **4** (1956) 848.

[16] Kazuhiko Nishijima, *Charge Independence Theory of V Particles*, Prog. Theor. Phys. **13** (1955) 285.

[17] F. Englert and R. Brout, *Broken Symmetry and the Mass of Gauge Vector Mesons*, Phys. Rev. Lett. **13** (1964) 321.

[18] Peter W. Higgs, *Broken Symmetries and the Masses of Gauge Bosons*, Phys. Rev. Lett. **13** (1964) 508.

[19] G. S. Guralnik, C. R. Hagen, and T. W. B. Kibble, *Global Conservation Laws and Massless Particles*, Phys. Rev. Lett. **13** (1964) 585.

[20] Jeffrey Goldstone, Abdus Salam, and Steven Weinberg, *Broken Symmetries*, Phys. Rev. **127** (1962) 965.

[21] Nicola Cabibbo, *Unitary Symmetry and Leptonic Decays*, Phys. Rev. Lett. **10** (1963) 531.

[22] Makoto Kobayashi and Toshihide Maskawa, *CP Violation in the Renormalizable Theory of Weak Interaction*, Prog. Theor. Phys. **49** (1973) 652.

[23] B. Pontecorvo, *Mesonium and anti-mesonium*, Sov. Phys. JETP **6** (1957) 429.

[24] Ziro Maki, Masami Nakagawa, and Shoichi Sakata, *Remarks on the unified model of elementary particles*, Prog. Theor. Phys. **28** (1962) 870.

[25] S. T. Petcov, *The Nature of Massive Neutrinos*, Adv. High Energy Phys. **2013** (2013) 852987, arXiv: `1303.5819 [hep-ph]`.

[26] Gerard 't Hooft, *Renormalizable Lagrangians for Massive Yang-Mills Fields*, Nucl. Phys. **B35** (1971) 167.

[27] G. W. Bennett et al., *Final Report of the Muon E821 Anomalous Magnetic Moment Measurement at BNL*, Phys. Rev. **D73** (2006) 072003, arXiv: `hep-ex/0602035 [hep-ex]`.

[28] H. Baer and X. Tata, *Weak scale supersymmetry: From superfields to scattering events*, Cambridge University Press, 2006, URL: `http://www.cambridge.org/9780521290319`.

[29] Andrzej Czarnecki and William J. Marciano, *The Muon anomalous magnetic moment: A Harbinger for 'new physics'*, Phys. Rev. **D64** (2001) 013014, arXiv: `hep-ph/0102122 [hep-ph]`.

[30] T. S. van Albada, J. N. Bahcall, K. Begeman, and R. Sancisi, *Distribution of dark matter in the spiral galaxy NGC 3198*, Astrophys. J. **295** (1985) 305.

[31] Gianfranco Bertone, Dan Hooper, and Joseph Silk, *Particle dark matter: Evidence, candidates and constraints*, Phys. Rept. **405** (2005) 279, arXiv: `hep-ph/0404175 [hep-ph]`.

[32] A. N. Taylor, S. Dye, Thomas J. Broadhurst, N. Benitez, and E. van Kampen, *Gravitational lens magnification and the mass of abell 1689*, Astrophys. J. **501** (1998) 539, arXiv: `astro-ph/9801158 [astro-ph]`.

[33] Wayne Hu and Scott Dodelson, *Cosmic microwave background anisotropies*, Ann. Rev. Astron. Astrophys. **40** (2002) 171, arXiv: `astro-ph/0110414 [astro-ph]`.

[34] P. A. R. Ade et al., *Planck 2013 results. XVI. Cosmological parameters*, Astron. Astrophys. **571** (2014) A16, arXiv: `1303.5076 [astro-ph.CO]`.

[35] I. J. R. Aitchison, *Supersymmetry in Particle Physics. An Elementary Introduction*, Cambridge University Press, 2007, ISBN: 9780511619250, URL: `http://www-public.slac.stanford.edu/sciDoc/docMeta.aspx?slacPubNumber=slac-r-865`.

[36] Stephen P. Martin, *A Supersymmetry Primer*, Adv. Ser. Direct. High Energy Phys. **18** (1998) 1, arXiv: `hep-ph/9709356`.

[37] Gian Francesco Giudice, *Naturally Speaking: The Naturalness Criterion and Physics at the LHC*, (2008) 155, arXiv: `0801.2562 [hep-ph]`.

[38] Yuri A Golfand and Evgeny P Likhtman, *Extension of the Algebra of Poincare Group Generators and Violation of p Invariance*, JETP Lett. **13** (1971) 323.

[39] D. V. Volkov and V. P. Akulov, *Is the Neutrino a Goldstone Particle?*, Phys. Lett. B **46** (1973) 109.

[40] J. Wess and B. Zumino, *Supergauge Transformations in Four-Dimensions*, Nucl. Phys. B **70** (1974) 39.

[41] J. Wess and B. Zumino, *Supergauge Invariant Extension of Quantum Electrodynamics*, Nucl. Phys. B **78** (1974) 1.

[42] S. Ferrara and B. Zumino, *Supergauge Invariant Yang-Mills Theories*, Nucl. Phys. B **79** (1974) 413.

[43] Abdus Salam and J. A. Strathdee, *Supersymmetry and Nonabelian Gauges*, Phys. Lett. B **51** (1974) 353.

[44] Steven Weinberg, *The quantum theory of fields. Vol. 3: Supersymmetry*, Cambridge University Press, 2013.

[45] Sidney R. Coleman and J. Mandula, *All Possible Symmetries of the S Matrix*, Phys. Rev. **159** (1967) 1251.

[46] Howard Georgi and Sheldon L. Glashow, *Gauge theories without anomalies*, Phys. Rev. **D6** (1972) 429.

[47] K. Abe et al., *Search for proton decay via $p \to e^+\pi^0$ and $p \to \mu^+\pi^0$ in 0.31 megatonůyears exposure of the Super-Kamiokande water Cherenkov detector*, Phys. Rev. **D95** (2017) 012004, arXiv: `1610.03597 [hep-ex]`.

[48] Glennys R. Farrar and Pierre Fayet, *Phenomenology of the Production, Decay, and Detection of New Hadronic States Associated with Supersymmetry*, Phys. Lett. B **76** (1978) 575.

[49] R. Barbier et al., *R-parity violating supersymmetry*, Phys. Rept. **420** (2005) 1, arXiv: `hep-ph/0406039 [hep-ph]`.

[50] S. Y. Choi, J. Kalinowski, Gudrid A. Moortgat-Pick, and P. M. Zerwas, *Analysis of the neutralino system in supersymmetric theories*, Eur. Phys. J. **C22** (2001) 563, arXiv: `hep-ph/0108117 [hep-ph]`.

[51] Riccardo Barbieri and G. F. Giudice, *Upper Bounds on Supersymmetric Particle Masses*, Nucl. Phys. B **306** (1988) 63.

[52] S. Dimopoulos, S. Raby, and Frank Wilczek, *Supersymmetry and the Scale of Unification*, Phys. Rev. D **24** (1981) 1681.

[53] Pran Nath and Richard L. Arnowitt, *Generalized Supergauge Symmetry as a New Framework for Unified Gauge Theories*, Phys. Lett. **56B** (1975) 177.

[54]   ATLAS Collaboration, *Mass reach of the ATLAS searches for Supersymmetry*, URL: http://atlas.web.cern.ch/Atlas/GROUPS/PHYSICS/CombinedSummaryPlots/SUSY/ATLAS_SUSY_Summary/ATLAS_SUSY_Summary_201803.png.

[55]   CMS Collaboration, *Summary plot Moriond 2017*, URL: https://twiki.cern.ch/twiki/pub/CMSPublic/SUSYSummary2017/Moriond2017_BarPlot.pdf.

[56]   Michele Papucci, Joshua T. Ruderman, and Andreas Weiler, *Natural SUSY Endures*, JHEP **09** (2012) 035, arXiv: 1110.6926 [hep-ph].

[57]   Zhenyu Han, Graham D. Kribs, Adam Martin, and Arjun Menon, *Hunting quaside-generate Higgsinos*, Phys. Rev. **D89** (2014) 075007, arXiv: 1401.1235 [hep-ph].

[58]   James D. Wells, *PeV-scale supersymmetry*, Phys. Rev. **D71** (2005) 015013, arXiv: hep-ph/0411041 [hep-ph].

[59]   Nima Arkani-Hamed and Savas Dimopoulos, *Supersymmetric unification without low energy supersymmetry and signatures for fine-tuning at the LHC*, JHEP **06** (2005) 073, arXiv: hep-th/0405159.

[60]   Kingman Cheung, Cheng-Wei Chiang, and Jeonghyeon Song, *A minimal supersymmetric scenario with only μ at the weak scale*, Journal of High Energy Physics **2006** (2006) 047.

[61]   Kwang Sik Jeong, *Light Higgsino for Gauge Coupling Unification*, Phys. Lett. **B769** (2017) 42, arXiv: 1701.06947 [hep-ph].

[62]   Natsumi Nagata and Satoshi Shirai, *Higgsino Dark Matter in High-Scale Supersymmetry*, JHEP **01** (2015) 029, arXiv: 1410.4549 [hep-ph].

[63]   Peter W. Graham, David E. Kaplan, and Surjeet Rajendran, *Cosmological Relaxation of the Electroweak Scale*, Phys. Rev. Lett. **115** (2015) 221801, arXiv: 1504.07551 [hep-ph].

[64]   V. A. Beylin, V. I. Kuksa, G. M. Vereshkov, and R. S. Pasechnik, *Neutralino-nucleon interaction in the Split Higgsino scenario of the Dark Matter*, Int. J. Mod. Phys. **A24** (2009) 6051, arXiv: 0903.4201 [hep-ph].

[65]   M. Adeel Ajaib, Bhaskar Dutta, Tathagata Ghosh, Ilia Gogoladze, and Qaisar Shafi, *Neutralinos and sleptons at the LHC in light of muon $(g-2)_\mu$*, Phys. Rev. **D92** (2015) 075033, arXiv: 1505.05896 [hep-ph].

[66]   Alexander S. Belyaev, Steve F. King, and Patrick B. Schaefers, *Muon g-2 and dark matter suggest nonuniversal gaugino masses:* $\mathbf{SU(5)} \times \mathbf{A_4}$ *case study at the LHC*, Phys. Rev. **D97** (2018) 115002, arXiv: 1801.00514 [hep-ph].

[67]   Johan Alwall, Philip Schuster, and Natalia Toro, *Simplified Models for a First Characterization of New Physics at the LHC*, Phys. Rev. D **79** (2009) 075020, arXiv: 0810.3921 [hep-ph].

[68]   Daniele Alves et al., *Simplified Models for LHC New Physics Searches*, J. Phys. G **39** (2012) 105005, arXiv: 1105.2838 [hep-ph].

[69]   ALICE Collaboration, *The ALICE experiment at the CERN LHC*, JINST **3** (2008) S08002.

[70] LHCb Collaboration, *The LHCb Detector at the LHC*, JINST **3** (2008) S08005.

[71] ATLAS Collaboration, *The ATLAS Experiment at the CERN Large Hadron Collider*, JINST **3** (2008) S08003.

[72] CMS Collaboration, *The CMS experiment at the CERN LHC*, JINST **3** (2008) S08004.

[73] TOTEM Collaboration, *The TOTEM experiment at the CERN Large Hadron Collider*, JINST **3** (2008) S08007.

[74] James Pinfold et al., *Technical Design Report of the MoEDAL Experiment*, (2009).

[75] O. Adriani et al., *Technical design report of the LHCf experiment: Measurement of photons and neutral pions in the very forward region of LHC*, (2006).

[76] Esma Mobs, *The CERN accelerator complex - August 2018*, General Photo, URL: https://cds.cern.ch/record/2636343.

[77] Lyndon R Evans and Philip Bryant, *LHC Machine*, JINST **3** (2008) S08001.

[78] R Scrivens et al., *Overview of the status and developments on primary ion sources at CERN*, 2nd International Particle Accelerator Conference, 2011, URL: http://cds.cern.ch/record/1382102.

[79] Maurizio Vretenar, "The radio-frequency quadrupole", *Proceedings, CERN Accelerator School on High Power Hadron Machines (CAS 2011): Bilbao, Spain, May 24-June 02, 2011*, 2013 207, arXiv: 1303.6762 [physics.acc-ph].

[80] CERN Education, Communications and Outreach Group, *LHC Guide*, 2017, URL: http://cds.cern.ch/record/2255762.

[81] Giles Barr, Robin Devenish, Roman Walczak, and Tony Weidberg, *Particle Physics in the LHC Era*, Oxford University Press, 2016.

[82] Corinne Pralavorio, *Record luminosity: well done LHC*, URL: https://home.cern/news/news/accelerators/record-luminosity-well-done-lhc (visited on 01/04/2019).

[83] CERN Press release, *First beam in the LHC - accelerating science*, URL: https://home.cern/news/press-release/cern/first-beam-lhc-accelerating-science (visited on 05/28/2019).

[84] ATLAS Collaboration, *Luminosity determination in pp collisions at $\sqrt{s} = 8$ TeV using the ATLAS detector at the LHC*, Eur. Phys. J. C **76** (2016) 653, arXiv: 1608.03953 [hep-ex].

[85] ATLAS Collaboration, *Luminosity Public Results Run 2*, URL: https://twiki.cern.ch/twiki/bin/view/AtlasPublic/LuminosityPublicResultsRun2 (visited on 05/28/2019).

[86] CERN Finance Committee, *Medium-Term Plan for the Period 2018-2022 and Draft Budget of the Organization for the Sixty-Fourth Financial Year 2018 (Director-General)*, 2017, URL: https://cds.cern.ch/record/2271005.

[87] G. Apollinari et al., *High-Luminosity Large Hadron Collider (HL-LHC)*, CERN Yellow Rep. Monogr. **4** (2017) 1.

[88] Zachary Marshall, *Simulation of Pile-up in the ATLAS Experiment*, J. Phys. Conf. Ser. **513** (2014) 022024.

[89] Joao Pequenao, *Computer generated image of the whole ATLAS detector*, 2008, URL: https://cds.cern.ch/record/1095924.

[90] Tomoya Iizawa, *The ATLAS Fast Tracker System*, PoS **TWEPP-17** (2017) 139.

[91] B. Abbott et al., *Production and integration of the ATLAS Insertable B-Layer*, JINST **13** (2018) T05008, arXiv: 1803.00844 [physics.ins-det].

[92] Karolos Potamianos, *The upgraded Pixel detector and the commissioning of the Inner Detector tracking of the ATLAS experiment for Run-2 at the Large Hadron Collider*, PoS **EPS-HEP2015** (2015) 261, arXiv: 1608.07850 [physics.ins-det].

[93] Joao Pequenao, *Computer generated image of the ATLAS inner detector*, 2008, URL: https://cds.cern.ch/record/1095926.

[94] P.L. Rosendahl, *ATLAS silicon microstrip tracker operation and performance*, Nucl. Instrum. Methods Phys. Res. A **718** (2013) 358.

[95] ATLAS Collaboration, *Particle Identification Performance of the ATLAS Transition Radiation Tracker*, ATLAS-CONF-2011-128, 2011, URL: https://cds.cern.ch/record/1383793.

[96] Adrian Vogel, *ATLAS Transition Radiation Tracker (TRT): Straw tube gaseous detectors at high rates*, Nucl. Instrum. Methods Phys. Res. A **732** (2013) 277.

[97] Henric Wilkens, *The ATLAS Liquid Argon calorimeter: An overview*, J. Phys. Conf. Ser. **160** (2009) 012043.

[98] Joao Pequenao, *Computer Generated image of the ATLAS calorimeter*, 2008, URL: https://cds.cern.ch/record/1095927.

[99] Joao Pequenao, *Computer generated image of the ATLAS Muons subsystem*, 2008, URL: https://cds.cern.ch/record/1095929.

[100] Hannah Elizabeth Herde, *Muon reconstruction performance in ATLAS at Run-II*, PoS **EPS-HEP2015** (2015) 285.

[101] Peter Jenni, Markus Nordberg, Marzio Nessi, and Kerstin Jon-And, *ATLAS Forward Detectors for Measurement of Elastic Scattering and Luminosity*, 2008, URL: http://cds.cern.ch/record/1095847.

[102] G. Avoni et al., *The new LUCID-2 detector for luminosity measurement and monitoring in ATLAS*, JINST **13** (2018) P07017.

[103] A. Ruiz Martínez, *The Run-2 ATLAS Trigger System*, J. Phys. Conf. Ser. **762** (2016) 012003.

[104] ATLAS Collaboration, *ATLAS level-1 trigger: Technical Design Report*, 1998, URL: http://cds.cern.ch/record/381429.

[105] Peter Jenni, Marzio Nessi, Markus Nordberg, and Kenway Smith, *ATLAS high-level trigger, data-acquisition and controls: Technical Design Report*, 2003, URL: http://cds.cern.ch/record/616089.

[106] William Panduro Vazquez, *The ATLAS Data Acquisition System: from Run 1 to Run 2*, Nucl. Part. Phys. Proc. **273-275** (2016) 939.

[107] ATLAS Collaboration, *Trigger Menu in 2017*, ATL-DAQ-PUB-2018-002, 2018, URL: https://cds.cern.ch/record/2625986.

[108] P. J. Laycock et al., *ATLAS data preparation in run 2*, J. Phys. Conf. Ser. **898** (2017) 042050.

[109] ATLAS Collaboration, *The ATLAS Simulation Infrastructure*, Eur. Phys. J. C **70** (2010) 823, arXiv: 1005.4568 [physics.ins-det].

[110] T. Gleisberg, S. Höche, F. Krauss, M. Schönherr, S. Schumann, et al., *Event generation with SHERPA 1.1*, JHEP **02** (2009) 007, arXiv: 0811.4622 [hep-ph].

[111] Andy Buckley et al., *General-purpose event generators for LHC physics*, Phys. Rept. **504** (2011) 145, arXiv: 1101.2599 [hep-ph].

[112] John C. Collins, Davison E. Soper, and George F. Sterman, *Factorization of Hard Processes in QCD*, Adv. Ser. Direct. High Energy Phys. **5** (1989) 1, arXiv: hep-ph/0409313 [hep-ph].

[113] Fabio Maltoni, Thomas McElmurry, Robert Putman, and Scott Willenbrock, *Choosing the Factorization Scale in Perturbative QCD*, (2007), arXiv: hep-ph/0703156 [HEP-PH].

[114] G. Cowan, *Statistical data analysis*, Oxford University Press, 1998.

[115] D. Amati and G. Veneziano, *Preconfinement as a Property of Perturbative QCD*, Phys. Lett. **83B** (1979) 87.

[116] Andy Buckley and Holger Schulz, *Tuning of MC generator MPI models*, Adv. Ser. Direct. High Energy Phys. **29** (2018) 281, arXiv: 1806.11182 [hep-ph].

[117] Andy Buckley, Hendrik Hoeth, Heiko Lacker, Holger Schulz, and Jan Eike von Seggern, *Systematic event generator tuning for the LHC*, Eur. Phys. J. **C65** (2010) 331, arXiv: 0907.2973 [hep-ph].

[118] S. Agostinelli et al., *GEANT4: A Simulation toolkit*, Nucl. Instrum. Meth. A **506** (2003) 250.

[119] John Allison et al., *Geant4 developments and applications*, IEEE Trans. Nucl. Sci. **53** (2006) 270.

[120] Wolfgang Lukas, *Fast Simulation for ATLAS: Atlfast-II and ISF*, Journal of Physics: Conference Series **396** (2012) 022031.

[121] Takashi Yamanaka, *The ATLAS calorimeter simulation FastCaloSim*, J. Phys. Conf. Ser. **331** (2011) 032053.

[122] ATLAS Collaboration, *Muon reconstruction performance of the ATLAS detector in proton–proton collision data at $\sqrt{s} = 13\,TeV$*, Eur. Phys. J. C **76** (2016) 292, arXiv: 1603.05598 [hep-ex].

[123] ATLAS Collaboration, *Muon Reconstruction and Identication: Studies with Simulated Monte Carlo Samples.*, ATL-PHYS-PUB-2009-008, 2009, URL: https://cds.cern.ch/record/1169053.

[124]   Zhi Zheng, Michael Holzbock, Stefano Zambito, Stefano Rosati, and Federico Sforza, *Low-pT Muon Selection Public Plots*, tech. rep. ATL-COM-PHYS-2018-844, CERN, 2018, URL: https://cds.cern.ch/record/2625138.

[125]   ATLAS Collaboration, *Muon reconstruction efficiency in reprocessed 2010 LHC proton–proton collision data recorded with the ATLAS detector*, ATLAS-CONF-2011-063, 2011, URL: https://cds.cern.ch/record/1345743.

[126]   Torbjörn Sjöstrand et al., *An Introduction to PYTHIA 8.2*, Comput. Phys. Commun. **191** (2015) 159, arXiv: 1410.3012 [hep-ph].

[127]   ATLAS Collaboration, *ATLAS Pythia 8 tunes to 7 TeV data*, ATL-PHYS-PUB-2014-021, 2014, URL: https://cds.cern.ch/record/1966419.

[128]   J. Pumplin et al., *New generation of parton distributions with uncertainties from global QCD analysis*, JHEP **07** (2002) 012, arXiv: hep-ph/0201195.

[129]   N. Davidson, T. Przedzinski, and Z. Was, *PHOTOS Interface in C++: Technical and Physics Documentation*, (2010), arXiv: 1011.0937 [hep-ph].

[130]   Gustavo Ordonez Sanz, "Muon identification in the ATLAS calorimeters", PhD thesis, 2009, URL: https://cds.cern.ch/record/1196071.

[131]   ATLAS Collaboration, *Performance of the ATLAS trigger system in 2015*, Eur. Phys. J. C **77** (2017) 317, arXiv: 1611.09661 [hep-ex].

[132]   ATLAS Collaboration, *Muons in the calorimeters: Energy loss corrections and muon tagging.*, ATL-PHYS-PUB-2009-009, 2009, URL: https://cds.cern.ch/record/1169055.

[133]   ATLAS Collaboration, *Muon identification and reconstruction efficiencies in full Run-2 dataset*, URL: https://atlas.web.cern.ch/Atlas/GROUPS/PHYSICS/PLOTS/MUON-2019-03/index.html.

[134]   ATLAS Collaboration, *Optimization of Isolation Selection at High-mu: Preliminary Public Plots*, URL: https://atlas.web.cern.ch/Atlas/GROUPS/PHYSICS/PLOTS/MUON-2018-002/index.html.

[135]   ATLAS Collaboration, *Searches for electroweak production of supersymmetric particles with compressed mass spectra in $\sqrt{s} = 13$ TeV pp collisions with the ATLAS detector*, ATLAS-CONF-2019-014, 2019, URL: https://cds.cern.ch/record/2675954.

[136]   ATLAS Collaboration, *Luminosity Public Results Run 2*, URL: https://twiki.cern.ch/twiki/bin/view/AtlasPublic/LuminosityPublicResultsRun2 (visited on 02/23/2019).

[137]   Kate Kahle and Rende Steerenberg, *LHC report: Something in the nothing*, URL: https://home.cern/news/news/accelerators/lhc-report-something-nothing (visited on 06/04/2019).

[138]   Jorg Wenninger, *LHC Report: operation with holes*, URL: https://home.cern/news/news/accelerators/lhc-report-operation-holes (visited on 06/04/2019).

[139]   S van der Meer, *Calibration of the effective beam height in the ISR*, CERN-ISR-PO-68-31, 1968, URL: https://cds.cern.ch/record/296752.

[140] V. Cindro et al., *The ATLAS beam conditions monitor*, JINST **3** (2008) P02004.

[141] ATLAS Collaboration, *Luminosity determination in pp collisions at $\sqrt{s} = 13$ TeV using the ATLAS detector at the LHC*, ATLAS-CONF-2019-021, 2019, URL: http://cds.cern.ch/record/2677054.

[142] C. G. Lester and D. J. Summers, *Measuring masses of semi-invisibly decaying particles pair produced at hadron colliders*, Phys. Lett. B **463** (1999) 99, arXiv: hep-ph/9906349.

[143] Alan Barr, Christopher Lester, and P. Stephens, *A variable for measuring masses at hadron colliders when missing energy is expected; m_{T2}: the truth behind the glamour*, J. Phys. G **29** (2003) 2343, arXiv: hep-ph/0304226.

[144] J. Alwall, R. Frederix, S. Frixione, V. Hirschi, F. Maltoni, et al., *The automated computation of tree-level and next-to-leading order differential cross sections, and their matching to parton shower simulations*, JHEP **07** (2014) 079, arXiv: 1405.0301 [hep-ph].

[145] Richard D. Ball et al., *Parton distributions with LHC data*, Nucl. Phys. B **867** (2013) 244, arXiv: 1207.1303 [hep-ph].

[146] Pierre Artoisenet, Rikkert Frederix, Olivier Mattelaer, and Robbert Rietkerk, *Automatic spin-entangled decays of heavy resonances in Monte Carlo simulations*, JHEP **03** (2013) 015, arXiv: 1212.3460 [hep-ph].

[147] Leif Lonnblad and Stefan Prestel, *Matching Tree-Level Matrix Elements with Interleaved Showers*, JHEP **03** (2012) 019, arXiv: 1109.4829 [hep-ph].

[148] ATLAS Collaboration, *The Pythia 8 A3 tune description of ATLAS minimum bias and inelastic measurements incorporating the Donnachie–Landshoff diffractive model*, ATL-PHYS-PUB-2016-017, 2016, URL: https://cds.cern.ch/record/2206965.

[149] A. D. Martin, W.J. Stirling, R. S. Thorne, and G. Watt, *Parton distributions for the LHC*, Eur. Phys. J. C **63** (2009) 189, arXiv: 0901.0002 [hep-ph].

[150] D. J. Lange, *The EvtGen particle decay simulation package*, Nucl. Instrum. Meth. A **462** (2001) 152.

[151] Benjamin Fuks, Michael Klasen, David R. Lamprea, and Marcel Rothering, *Gaugino production in proton-proton collisions at a center-of-mass energy of 8 TeV*, JHEP **10** (2012) 081, arXiv: 1207.2159 [hep-ph].

[152] Benjamin Fuks, Michael Klasen, David R. Lamprea, and Marcel Rothering, *Precision predictions for electroweak superpartner production at hadron colliders with Resummino*, Eur. Phys. J. C **73** (2013) 2480, arXiv: 1304.0790 [hep-ph].

[153] Benjamin Fuks, Michael Klasen, David R. Lamprea, and Marcel Rothering, *Revisiting slepton pair production at the Large Hadron Collider*, JHEP **01** (2014) 168, arXiv: 1310.2621 [hep-ph].

[154] Jon Butterworth et al., *PDF4LHC recommendations for LHC Run II*, J. Phys. G **43** (2016) 023001, arXiv: 1510.03865 [hep-ph].

[155] Pavel M. Nadolsky et al., *Implications of CTEQ global analysis for collider observation*, Phys. Rev. D **78** (2008) 013004, arXiv: 0802.0007 [hep-ph].

[156] Michael Krämer et al., *Supersymmetry production cross sections in pp collisions at* $\sqrt{s} = 7$ *TeV*, (2012), arXiv: `1206.2892 [hep-ph]`.

[157] A. Djouadi, M. M. Muhlleitner, and M. Spira, *Decays of supersymmetric particles: The Program SUSY-HIT (SUspect-SdecaY-Hdecay-InTerface)*, Acta Phys. Polon. **B38** (2007) 635, arXiv: `hep-ph/0609292 [hep-ph]`.

[158] Richard D. Ball et al., *Parton distributions for the LHC Run II*, JHEP **04** (2015) 040, arXiv: `1410.8849 [hep-ph]`.

[159] Charalampos Anastasiou, Lance J. Dixon, Kirill Melnikov, and Frank Petriello, *High precision QCD at hadron colliders: Electroweak gauge boson rapidity distributions at NNLO*, Phys. Rev. D **69** (2004) 094008, arXiv: `hep-ph/0312266`.

[160] D. de Florian et al., *Handbook of LHC Higgs Cross Sections: 4. Deciphering the Nature of the Higgs Sector*, CERN-2017-002-M (2016), arXiv: `1610.07922 [hep-ph]`.

[161] Matteo Cacciari, Michal Czakon, Michelangelo Mangano, Alexander Mitov, and Paolo Nason, *Top-pair production at hadron colliders with next-to-next-to-leading logarithmic soft-gluon resummation*, Phys. Lett. B **710** (2012) 612, arXiv: `1111.5869 [hep-ph]`.

[162] Michal Czakon and Alexander Mitov, *NNLO corrections to top-pair production at hadron colliders: the all-fermionic scattering channels*, JHEP **12** (2012) 054, arXiv: `1207.0236 [hep-ph]`.

[163] Michal Czakon and Alexander Mitov, *NNLO corrections to top pair production at hadron colliders: the quark-gluon reaction*, JHEP **01** (2013) 080, arXiv: `1210.6832 [hep-ph]`.

[164] Micha Czakon, Paul Fiedler, and Alexander Mitov, *Total Top-Quark Pair-Production Cross Section at Hadron Colliders Through* $O(\alpha_S^4)$, Phys. Rev. Lett. **110** (2013) 252004, arXiv: `1303.6254 [hep-ph]`.

[165] Michal Czakon and Alexander Mitov, *Top++: A Program for the Calculation of the Top-Pair Cross-Section at Hadron Colliders*, Comput. Phys. Commun. **185** (2014) 2930, arXiv: `1112.5675 [hep-ph]`.

[166] Nikolaos Kidonakis, *NNLL resummation for s-channel single top quark production*, Phys. Rev. D **81** (2010) 054028, arXiv: `1001.5034 [hep-ph]`.

[167] Nikolaos Kidonakis, *Next-to-next-to-leading-order collinear and soft gluon corrections for t-channel single top quark production*, Phys. Rev. D **83** (2011) 091503, arXiv: `1103.2792 [hep-ph]`.

[168] Rikkert Frederix, Emanuele Re, and Paolo Torrielli, *Single-top t-channel hadroproduction in the four-flavour scheme with POWHEG and aMC@NLO*, JHEP **09** (2012) 130, arXiv: `1207.5391 [hep-ph]`.

[169] Nikolaos Kidonakis, *Two-loop soft anomalous dimensions for single top quark associated production with a W- or H-*, Phys. Rev. D **82** (2010) 054018, arXiv: `1005.4451 [hep-ph]`.

[170] Simone Alioli, Paolo Nason, Carlo Oleari, and Emanuele Re, *A general framework for implementing NLO calculations in shower Monte Carlo programs: the POWHEG BOX*, JHEP **06** (2010) 043, arXiv: `1002.2581 [hep-ph]`.

[171] ATLAS Collaboration, *Multi-Boson Simulation for* 13 *TeV ATLAS Analyses*, ATL-PHYS-PUB-2017-005, 2017, URL: https://cds.cern.ch/record/2261933.

[172] ATLAS Collaboration, *ATLAS simulation of boson plus jets processes in Run 2*, ATL-PHYS-PUB-2017-006, 2017, URL: https://cds.cern.ch/record/2261937.

[173] ATLAS Collaboration, *Studies on top-quark Monte Carlo modelling with Sherpa and MG5_aMC@NLO*, ATL-PHYS-PUB-2017-007, 2017, URL: https://cds.cern.ch/record/2261938.

[174] ATLAS Collaboration, *A study of different colour reconnection settings for Pythia8 generator using underlying event observables*, ATL-PHYS-PUB-2017-008, 2017, URL: https://cds.cern.ch/record/2262253.

[175] ATLAS Collaboration, *Modelling of the $t\bar{t}H$ and $t\bar{t}V(V = W, Z)$ processes for $\sqrt{s} =$* 13 *TeV ATLAS analyses*, ATL-PHYS-PUB-2016-005, 2016, URL: https://cds.cern.ch/record/2120826.

[176] ATLAS Collaboration, *Search for electroweak production of supersymmetric states in scenarios with compressed mass spectra at $\sqrt{s} = 13$ TeV with the ATLAS detector*, Phys. Rev. D **97** (2018) 052010, arXiv: 1712.08119 [hep-ex].

[177] ALEPH, DELPHI, L3, OPAL Experiments, *Combined LEP Chargino Results, up to 208 GeV for low DM*, LEPSUSYWG/02-04.1, 2002, URL: http://lepsusy.web.cern.ch/lepsusy/www/inoslowdmsummer02/charginolowdm_pub.html.

[178] ALEPH, DELPHI, L3, OPAL Experiments, *Combined LEP Selectron/Smuon/Stau Results, 183-208 GeV*, LEPSUSYWG/04-01.1, 2004, URL: http://lepsusy.web.cern.ch/lepsusy/www/sleptons_summer04/slep_final.html.

[179] ALEPH Collaboration, *Search for scalar leptons in e^+e^- collisions at center-of-mass energies up to 209 GeV*, Phys. Lett. B **526** (2002) 206, arXiv: hep-ex/0112011.

[180] ALEPH Collaboration, *Search for charginos nearly mass degenerate with the lightest neutralino in e^+e^- collisions at center-of-mass energies up to 209 GeV*, Phys. Lett. B **533** (2002) 223, arXiv: hep-ex/0203020.

[181] ALEPH Collaboration, *Absolute mass lower limit for the lightest neutralino of the MSSM from e^+e^- data at $\sqrt{s}$ up to 209 GeV*, Phys. Lett. B **583** (2004) 247.

[182] DELPHI Collaboration, *Searches for supersymmetric particles in e^+e^- collisions up to 208 GeV and interpretation of the results within the MSSM*, Eur. Phys. J. C **31** (2003) 421, arXiv: hep-ex/0311019.

[183] L3 Collaboration, *Search for charginos with a small mass difference with the lightest supersymmetric particle at $\sqrt{s} = 189$ GeV*, Phys. Lett. B **482** (2000) 31, arXiv: hep-ex/0002043.

[184] L3 Collaboration, *Search for scalar leptons and scalar quarks at LEP*, Phys. Lett. B **580** (2004) 37, arXiv: hep-ex/0310007.

[185] OPAL Collaboration, *Search for anomalous production of dilepton events with missing transverse momentum in e^+e^- collisions at $\sqrt{s} = 183$ GeV to 209 GeV*, Eur. Phys. J. C **32** (2004) 453, arXiv: hep-ex/0309014.

[186] OPAL Collaboration, *Search for nearly mass degenerate charginos and neutralinos at LEP*, Eur. Phys. J. C **29** (2003) 479, arXiv: `hep-ex/0210043`.

[187] ALEPH Collaboration, *Absolute lower limits on the masses of selectrons and sneutrinos in the MSSM*, Phys. Lett. B **544** (2002) 73, arXiv: `hep-ex/0207056`.

[188] CMS Collaboration, *Search for new physics in events with two soft oppositely charged leptons and missing transverse momentum in proton–proton collisions at $\sqrt{s} = 13$ TeV*, Phys. Lett. B **782** (2018) 440, arXiv: `1801.01846 [hep-ex]`.

[189] CMS Collaboration, *Combined search for electroweak production of charginos and neutralinos in proton–proton collisions at $\sqrt{s} = 13$ TeV*, JHEP **03** (2018) 160, arXiv: `1801.03957 [hep-ex]`.

[190] ATLAS Collaboration, *Search for direct pair production of higgsinos by reinterpretation of the disappearing track analysis with 36.1 fb^{-1} of $\sqrt{s} = 13$ TeV data collected with the ATLAS experiment*, ATL-PHYS-PUB-2017-019, 2017, URL: `https://cds.cern.ch/record/2297480`.

[191] ATLAS Collaboration, *Search for long-lived charginos based on a disappearing-track signature in pp collisions at $\sqrt{s} = 13$ TeV with the ATLAS detector*, JHEP **06** (2018) 022, arXiv: `1712.02118 [hep-ex]`.

[192] M. Baak et al., *HistFitter software framework for statistical data analysis*, Eur. Phys. J. C **75** (2015) 153, arXiv: `1410.1280 [hep-ex]`.

[193] Kyle Cranmer, George Lewis, Lorenzo Moneta, Akira Shibata, and Wouter Verkerke, *HistFactory: A tool for creating statistical models for use with RooFit and RooStats*, (2012).

[194] Glen Cowan, Kyle Cranmer, Eilam Gross, and Ofer Vitells, *Asymptotic formulae for likelihood-based tests of new physics*, Eur. Phys. J. C **71** (2011) 1554, arXiv: `1007.1727 [physics.data-an]`, Erratum: Eur. Phys. J. C **73** (2013) 2501.

[195] Alexander L. Read, *Presentation of search results: the CL_S technique*, J. Phys. G **28** (2002) 2693.

[196] ATLAS Collaboration, *Performance of the ATLAS Inner Detector Track and Vertex Reconstruction in High Pile-Up LHC Environment*, ATLAS-CONF-2012-042, 2012, URL: `https://cds.cern.ch/record/1435196`.

[197] R. Fruhwirth, *Application of Kalman filtering to track and vertex fitting*, Nucl. Instrum. Meth. **A262** (1987) 444.

[198] T. Cornelissen et al., *The new ATLAS track reconstruction (NEWT)*, J. Phys. Conf. Ser. **119** (2008) 032014.

[199] ATLAS Collaboration, *Performance of the ATLAS track reconstruction algorithms in dense environments in LHC Run 2*, Eur. Phys. J. C **77** (2017) 673, arXiv: `1704.07983 [hep-ex]`.

[200] S. Boutle et al., *Primary vertex reconstruction at the ATLAS experiment*, J. Phys. Conf. Ser. **898** (2017) 042056.

[201] ATLAS Collaboration, *Vertex Reconstruction Performance of the ATLAS Detector at* $\sqrt{s}$ = 13 *TeV*, ATL-PHYS-PUB-2015-026, 2015, URL: https://cds.cern.ch/record/2037717.

[202] ATLAS Collaboration, *Reconstruction of primary vertices at the ATLAS experiment in Run 1 proton–proton collisions at the LHC*, Eur. Phys. J. C **77** (2017) 332, arXiv: 1611.10235 [hep-ex].

[203] ATLAS Collaboration, *Topological cell clustering in the ATLAS calorimeters and its performance in LHC Run 1*, Eur. Phys. J. C **77** (2017) 490, arXiv: 1603.02934 [hep-ex].

[204] ATLAS Collaboration, *Improved electron reconstruction in ATLAS using the Gaussian Sum Filter-based model for bremsstrahlung*, ATLAS-CONF-2012-047, 2012, URL: https://cds.cern.ch/record/1449796.

[205] ATLAS Collaboration, *Measurement of the photon identification efficiencies with the ATLAS detector using LHC Run 2 data collected in 2015 and 2016*, Eur. Phys. J. C **79** (2019) 205, arXiv: 1810.05087 [hep-ex].

[206] ATLAS Collaboration, *Electron and photon performance measurements with the ATLAS detector using the 2015-2017 LHC proton-proton collision data*, (2019), arXiv: 1908.00005 [hep-ex].

[207] ATLAS Collaboration, *Electron and photon energy calibration with the ATLAS detector using 2015–2016 LHC proton–proton collision data*, JINST **14** (2019) P03017, arXiv: 1812.03848 [hep-ex].

[208] ATLAS Collaboration, *Electron reconstruction and identification in the ATLAS experiment using the 2015 and 2016 LHC proton–proton collision data at* $\sqrt{s} = 13$ *TeV*, Eur. Phys. J. (2019), arXiv: 1902.04655 [hep-ex].

[209] Matteo Cacciari and Gavin P. Salam, *Pileup subtraction using jet areas*, Phys. Lett. **B659** (2008) 119, arXiv: 0707.1378 [hep-ph].

[210] Matteo Cacciari, Gavin P. Salam, and Gregory Soyez, *The anti-k_t jet clustering algorithm*, JHEP **04** (2008) 063, arXiv: 0802.1189 [hep-ph].

[211] Matteo Cacciari, Gavin P. Salam, and Gregory Soyez, *FastJet User Manual*, Eur. Phys. J. C **72** (2012) 1896, arXiv: 1111.6097 [hep-ph].

[212] Matteo Cacciari, Gavin P. Salam, and Gregory Soyez, *The Catchment Area of Jets*, JHEP **04** (2008) 005, arXiv: 0802.1188 [hep-ph].

[213] ATLAS Collaboration, *Jet energy scale measurements and their systematic uncertainties in proton–proton collisions at* $\sqrt{s} = 13$ *TeV with the ATLAS detector*, Phys. Rev. D **96** (2017) 072002, arXiv: 1703.09665 [hep-ex].

[214] ATLAS Collaboration, *Jet energy measurement with the ATLAS detector in proton–proton collisions at* $\sqrt{s} = 7$ *TeV*, Eur. Phys. J. C **73** (2013) 2304, arXiv: 1112.6426 [hep-ex].

[215] ATLAS Collaboration, *Jet energy resolution in proton–proton collisions at* $\sqrt{s} = 7$ *TeV recorded in 2010 with the ATLAS detector*, Eur. Phys. J. C **73** (2013) 2306, arXiv: 1210.6210 [hep-ex].

[216] ATLAS Collaboration, *Performance of pile-up mitigation techniques for jets in pp collisions at $\sqrt{s} = 8\,TeV$ using the ATLAS detector*, Eur. Phys. J. C **76** (2016) 581, arXiv: 1510.03823 [hep-ex].

[217] ATLAS Collaboration, *Performance of b-jet identification in the ATLAS experiment*, JINST **11** (2016) P04008, arXiv: 1512.01094 [hep-ex].

[218] ATLAS Collaboration, *Optimisation and performance studies of the ATLAS b-tagging algorithms for the 2017-18 LHC run*, ATL-PHYS-PUB-2017-013, 2017, URL: https://cds.cern.ch/record/2273281.

[219] D Adams et al., *Recommendations of the Physics Objects and Analysis Harmonisation Study Groups 2014*, tech. rep. ATL-PHYS-INT-2014-018, CERN, 2014, URL: https://cds.cern.ch/record/1743654.

[220] Jason Gallicchio and Yang-Ting Chien, *Quit Using Pseudorapidity, Transverse Energy, and Massless Constituents*, (2018), arXiv: 1802.05356 [hep-ph].

[221] ATLAS Collaboration, *Performance of missing transverse momentum reconstruction with the ATLAS detector using proton–proton collisions at $\sqrt{s} = 13\,TeV$*, Eur. Phys. J. C **78** (2018) 903, arXiv: 1802.08168 [hep-ex].

[222] ATLAS Collaboration, *E_T^{miss} performance in the ATLAS detector using 2015–2016 LHC pp collisions*, ATLAS-CONF-2018-023, 2018, URL: https://cds.cern.ch/record/2625233.

[223] Christopher G. Lester and Benjamin Nachman, *Bisection-based asymmetric M_{T2} computation: a higher precision calculator than existing symmetric methods*, JHEP **03** (2015) 100, arXiv: 1411.4312 [hep-ph].

[224] Howard Baer, Azar Mustafayev, and Xerxes Tata, *Monojet plus soft dilepton signal from light higgsino pair production at LHC14*, Phys. Rev. **D90** (2014) 115007, arXiv: 1409.7058 [hep-ph].

[225] Alan Barr and James Scoville, *A boost for the EW SUSY hunt: monojet-like search for compressed sleptons at LHC14 with 100 fb[1]*, JHEP **04** (2015) 147, arXiv: 1501.02511 [hep-ph].

[226] Paul Jackson and Christopher Rogan, *Recursive Jigsaw Reconstruction: HEP event analysis in the presence of kinematic and combinatoric ambiguities*, Phys. Rev. **D96** (2017) 112007, arXiv: 1705.10733 [hep-ph].

[227] Paul Jackson, Christopher Rogan, and Marco Santoni, *Sparticles in motion: Analyzing compressed SUSY scenarios with a new method of event reconstruction*, Phys. Rev. **D95** (2017) 035031, arXiv: 1607.08307 [hep-ph].

[228] C. Rogan, *RestFrames*, URL: http://RestFrames.com.

[229] ATLAS Collaboration, *Selection of jets produced in 13 TeV proton–proton collisions with the ATLAS detector*, ATLAS-CONF-2015-029, 2015, URL: https://cds.cern.ch/record/2037702.

[230] Robert D. Cousins, James T. Linnemann, and Jordan Tucker, *Evaluation of three methods for calculating statistical significance when incorporating a systematic uncertainty into a test of the background-only hypothesis for a Poisson process*, Nucl. Instrum. Meth. A **595** (2008) 480, arXiv: `physics/0702156 [physics.data-an]`.

[231] Aaron Roodman, *Blind analysis in particle physics*, eConf **C030908** (2003) TUIT001, arXiv: `physics/0312102 [physics.data-an]`.

[232] ATLAS Collaboration, *Observation and measurement of Higgs boson decays to WW^* with the ATLAS detector*, Phys. Rev. D **92** (2015) 012006, arXiv: `1412.2641 [hep-ex]`.

[233] ATLAS Collaboration, *Search for top squarks decaying to tau sleptons in pp collisions at $\sqrt{s} = 13\,TeV$ with the ATLAS detector*, Phys. Rev. D **98** (2018) 032008, arXiv: `1803.10178 [hep-ex]`.

[234] ATLAS Collaboration, *Jet energy measurement and its systematic uncertainty in proton–proton collisions at $\sqrt{s} = 7\,TeV$ with the ATLAS detector*, Eur. Phys. J. C **75** (2015) 17, arXiv: `1406.0076 [hep-ex]`.

[235] ATLAS Collaboration, *Tagging and suppression of pileup jets with the ATLAS detector*, ATLAS-CONF-2014-018, 2014, URL: `https://cds.cern.ch/record/1700870`.

[236] ATLAS Collaboration, *ATLAS b-jet identification performance and efficiency measurement with $t\bar{t}$ events in pp collisions at $\sqrt{s} = 13\,TeV$*, (2019), arXiv: `1907.05120 [hep-ex]`.

[237] ATLAS Collaboration, *Measurements of b-jet tagging efficiency with the ATLAS detector using $t\bar{t}$ events at $\sqrt{s} = 13\,TeV$*, JHEP **08** (2018) 089, arXiv: `1805.01845 [hep-ex]`.

[238] Sayipjamal Dulat et al., *New parton distribution functions from a global analysis of quantum chromodynamics*, Phys. Rev. **D93** (2016) 033006, arXiv: `1506.07443 [hep-ph]`.

[239] L. A. Harland-Lang, A. D. Martin, P. Motylinski, and R. S. Thorne, *Parton distributions in the LHC era: MMHT 2014 PDFs*, Eur. Phys. J. **C75** (2015) 204, arXiv: `1412.3989 [hep-ph]`.

[240] ATLAS Collaboration, *Search for direct production of charginos, neutralinos and sleptons in final states with two leptons and missing transverse momentum in pp collisions at $\sqrt{s} = 8\,TeV$ with the ATLAS detector*, JHEP **05** (2014) 071, arXiv: `1403.5294 [hep-ex]`.

[241] Ana Lopes, *ATLAS surveys new supersymmetry territory*, URL: `https://home.cern/news/news/physics/atlas-surveys-new-supersymmetry-territory` (visited on 09/19/2019).

[242] ATLAS Collaboration, *Searching for Electroweak SUSY: not because it is easy, but because it is hard*, URL: `https://atlas.cern/updates/physics-briefing/searching-electroweak-susy` (visited on 09/19/2019).

[243] ATLAS Collaboration, *SUSY July 2019 Summary Plot Update*, ATL-PHYS-PUB-2019-022, 2019, URL: `https://cds.cern.ch/record/2682063`.

[244] ATLAS Collaboration, *Summary of the ATLAS experiment's sensitivity to supersymmetry after LHC Run 1 — interpreted in the phenomenological MSSM*, JHEP **10** (2015) 134, arXiv: `1508.06608 [hep-ex]`.

[245] ATLAS Collaboration, *ATLAS sensitivity to winos and higgsinos with a highly compressed mass spectrum at the HL-LHC*, ATL-PHYS-PUB-2018-031, 2018, URL: `https://cds.cern.ch/record/2647294`.

[246] A. Abada et al., *FCC Physics Opportunities*, Eur. Phys. J. **C79** (2019) 474.

[247] A. Abada et al., *FCC-ee: The Lepton Collider*, Eur. Phys. J. ST **228** (2019) 261.

[248] A. Abada et al., *FCC-hh: The Hadron Collider*, Eur. Phys. J. ST **228** (2019) 755.

[249] M. J. Oreglia, "A study of the reactions $\psi' \to \gamma\gamma\psi$", Appendix D, PhD thesis, 1980.

[250] ATLAS Collaboration, *Performance of the ATLAS global transverse-momentum triggers at $\sqrt{s} = 8$ TeV*, ATL-DAQ-PUB-2018-001, 2018, URL: `https://cds.cern.ch/record/2311730`.

[251] ATLAS Collaboration, *Performance of the ATLAS muon trigger in pp collisions at $\sqrt{s} = 8$ TeV*, Eur. Phys. J. C **75** (2015) 120, arXiv: `1408.3179 [hep-ex]`.

[252] F. James and M. Roos, *Minuit: A System for Function Minimization and Analysis of the Parameter Errors and Correlations*, Comput. Phys. Commun. **10** (1975) 343.

[253] CMS Collaboration, *Search for top-squark pair production in the single-lepton final state in pp collisions at $\sqrt{s} = 8$ TeV*, Eur. Phys. J. C **73** (2013) 2677, arXiv: `1308.1586 [hep-ex]`.